THE UNIVERSITY *of* EDINBURGH

Surface atmosphere dynamics of reactive trace gases and water-soluble aerosol components above agricultural grassland and tropical rainforest

Robert Ramsay

THE UNIVERSITY
of EDINBURGH

Thesis submitted in fulfilment of
the requirements for the degree of
Doctor of Philosophy
to the
University of Edinburgh
February 2020

Declaration

I declare that this thesis was composed by myself, that the work contained herein is my own except where explicitly stated otherwise in the text, and that this work has not been submitted for any other degree or professional qualification except as specified.

Parts of this work have been published in

Ramsay, R., Di Marco, C. F., Heal, M. R., Twigg, M. M., Cowan, N., Jones, M. R., Leeson, S. R., Bloss, W. J., Kramer, L. J., Crilley, L., Srgel, M., Andreae, M. and Nemitz, E.: Surfaceatmosphere exchange of inorganic water-soluble gases and associated ions in bulk aerosol above agricultural grassland pre- and postfertilisation, *Atmos. Chem. Phys.*, 18(23), 1695316978, doi:10.5194/acp-18-16953-2018, 2018

Robert Ramsay

February 2020

Lay summary

The composition of our atmosphere is maintained by the biological processes that occur on the surface of the Earth. In turn, the surface is affected by chemical and physical processes that occur in the atmosphere. The delicate interactions that occur between the Earth and its atmosphere, termed "surface-atmosphere exchange", can be difficult to determine, especially with the changes wrought to the land and air by human activities. By accurately measuring the quantity and behaviour of the gases and particles that are deposited to and emitted from the surface of the Earth, it is possible to better understand these processes.

This work measured the quantities and behaviour of a selection of such gases and particles above two different landscapes — a Scottish pasture, and an area of the Amazon rainforest. For some of the gases or particles measured, this is the first time that their quantities and surface-exchange dynamics have been determined in real time over rainforest. The main conclusions that were drawn from the measurements made at the pasture site noted how human activities, such as fertiliser application, can perturb the atmosphere and lead to adverse consequences for the environment. Measurements over rainforest gained new insights into naturally occurring pathways, such as how the gases ammonia and nitrous acid can be emitted from forests. Episodes where pollution from around the globe arrived at the rainforest were also noted, highlighting how even remote areas of the Earth can be affected by human disruption to the atmosphere.

Abstract

The interaction between biosphere and atmosphere in the cycling of gas and aerosol species is of key importance in considering overall emission and deposition rates of nutrients and pollutants. Understanding of the biosphere-atmosphere processes that govern these cycles is critical to modelling overall global concentrations of atmospheric aerosols and trace gases, which in turn is vital to developing predictions for overall global climate and international pollution burdens.

However, to understand these processes, more measurements over a variety of different ecosystems are required, preferably measurements which are taken in real time, which are of high temporal resolution, and record a variety of species simultaneously and at potentially low background concentrations.

This thesis presents work in which the Gradient of Aerosols and Gases Online Registration (GRAEGOR), an instrument which employs a modified form of the aerodynamic gradient method (AGM) to determine fluxes from measured concentrations, was used to determine concentrations and fluxes of the trace gases NH_3, HCl, HONO, HNO_3 and SO_2 and the water-soluble aerosol species NH_4^+, Cl^-, NO_2^-, NO_3^- and SO_4^{2-} above agricultural grassland and tropical rainforest.

Measurements of the suite of trace gases and aerosols were conducted from May 2016 to June 2016 at the Easter Bush agricultural grassland site (Midlothian, United Kingdom). From these measurements, full time scale and diel profiles for

concentrations, fluxes and deposition velocities for each species were developed. Through the use the conservative exchange fluxes of tot-NH_4^- and tot-NO_3^-, it was found that a ground source of HNO_3 existed after a fertilisation event, which after scavenging by volatilised NH_3 formed ammonium nitrate aerosol. Diel cycle variation in HONO concentrations showed a background concentration of HONO during midday, contrary to expectations regarding the chemical behaviour of HONO. This suggests a potential daytime source of HONO at the site. A link between the deposition velocities for Cl^-, NO_3^- and SO_4^{2-} and a proxy for aerosol size provided evidence for the modelled link between increasing deposition velocity with increasing aerosol size. A comparison between the HONO concentrations measured by the GRAEGOR and the HONO concentrations measured by the Long Path Absorption Photometer (LOPAP) was also conducted, which found that the GRAEGOR records a higher concentration of HONO in comparison to the LOPAP, suggesting the presence of artefact factors within the GRAEGOR when measuring HONO. A modified form of a correction factor was developed to account for this HONO artefact. A similar comparison for NH_3 recorded by the GRAEGOR and NH_3 recorded by the Quantum Cascade Laser (QCL) was also conducted, finding that the QCL overestimated NH_3 concentrations.

Measurements of trace gases and aerosols above tropical rainforest were carried out from October 2017 to November 2017 at the Amazon Tall Tower Observatory (ATTO) site (Amazonas, Brazil). This was during the tropical dry season. Measurements of HONO concentration found that values remained above the detection limit of the instrument, even during daytime. Calculations of HONO flux found small but significant emissions of the trace gas in the early morning, suggesting formation of HONO below canopy during the evening followed by venting of the gas to above the canopy during the morning. It was found that local, regional and global sources of biomass burning led to periods of elevated SO_2 concentrations, with an associated increase in the dry deposition of SO_2

and associated SO_4^{2-} containing aerosol. Emissions of all measured aerosols, particularly Cl_, were observed throughout the campaign, which may be related to emissions of primary biological aerosol particles (PBAPs).

Bi-directional exchange of NH_3 was measured during the campaign at ATTO. In combination with ancillary measurements of leaf wetness data, a novel parameterisation of NH_3 emission and deposition to tropical rainforest was developed. This parameterisation was able to accurately simulate the bi-directional pattern of observed NH_3 fluxes at the rainforest site. Based on the observed pattern of NH_3 emissions occurring during periods where measured leaf wetness was low, it was concluded that emissions were driven by stomatal exchange of leaf NH_3 with the atmosphere.

This study has demonstrated that observed HONO concentrations above agricultural grassland are sometimes not consistent with predicted chemical pathways based on HONO photodissociation, and that there exists a potential source of HONO that affects overall daytime concentrations. Similarly, emissions of HONO have been demonstrated to exist from tropical rainforest, with a proposed pathway from soil emissions to the atmosphere. Furthermore, this study has conducted simultaneous measurements of the individual components of the NH_3-HNO_3-NH_4NO_3 triad, noting apparent formation of NH_4NO_3 from urea application to agricultural grassland. Finally, bi-directional exchange of NH_3 from the rainforest has been demonstrated to occur during the tropical dry season, particularly during the warm, dry periods at the canopy level that are characteristic of the hours immediately following noon.

Acknowledgements

I am deeply grateful for the support, encouragement and contribution of my supervisor at the University of Edinburgh, Prof. Mathew Heal. Prof. Heal, through many formal and informal meetings, has been a constant source of moral support and guidance. His edits and suggestions to the work presented in this thesis have been invaluable. I deem myself a better scientist after being under his tutelage.

I am very grateful to my supervisors based at the Centre for Ecology & Hydrology, Dr. Eiko Nemitz and Dr. Chiara Di Marco. Dr. Nemitz's overarching support and guidance for the study has been critical, and his ability to succinctly convey his extensive knowledge of atmospheric science has been deeply appreciated. For this, and for the many constructive meetings we have had, I am very thankful. Dr. Di Marco has taught me valuable skills in how to plan and carry out scientific field campaigns. Her guidance in instructing me in how to operate the GRAEGOR instrument in the first year of the study was exemplary. Our regular chats have been a source of encouragement during challenging periods of the study, and for this, and her wisdom and support throughout, I am extremely grateful.

I am very grateful for the support of my supervisors based at the Max Planck Institute for Chemistry, Dr. Matthias Sörgel, and Prof. Meinrat Andreae, both of whom were critical in organising the campaign at the Amazon Tall Tower

Observatory site. Dr. Sörgel's friendly, enthusiastic support throughout this study, especially during the Amazon campaign, is deeply appreciated. I am also thankful for Prof. Andreae's contributions and comments to the work.

I would like to thank the facility staff and research scientists at the Amazon Tall Tower Observatory site and the Centre for Ecology & Hydrology, for helping to organise, support and encourage my work throughout. In particular, I would like to thank Mr. Reiner Ditz, Dr. Stefann Wolff, Mr. Andrew Crozier, Dr. Marsailidh Twigg and Dr. Nicholas Cowan. I also thank the members of the MacAQUE (Modelling and measuring atmospheric chemistry and air quality at Edinburgh) group for their suggestions and support throughout the study

Finally, I dedicate this work to my mother, Ann, and to my sister, Lesleyanne. Thank you for your constant support and encouragement throughout my life and work.

Contents

List of Tables

List of Figures

Chapter 1

Introduction

This introduction first provides a broad overview of biosphere-atmosphere interactions with regards to agricultural grassland and tropical rainforest. A review of specific inorganic trace gases and their associated aerosol species which are exchanged between the surface and the atmosphere is then given, with descriptions of their effect on atmospheric chemistry and ecosystems upon their deposition provided. Considering the context provided by this review, justification for the measurement of the concentration and surface-atmosphere exchange of the inorganic trace gases and associated aerosols discussed is provided in a statement of the study aims and objectives.

1.1 Biosphere-atmosphere interactions the links between ecosystem and atmospheric composition

With the natural environment increasingly at risk from a variety of different pressures, principally anthropogenic driven climate change, increasing scientific focus has been given to determining the role of the natural world in providing the functions essential for continued life on Earth. Collectively termed ecosystem services (Costanza *et al.*, 1997), these functions which are carried out by the total environment, ranging from the lithosphere to the biosphere - account for such roles as the balanced regulation of water supplies, maintenance of soil fertility and the regulation of climate.

The last of these functions mentioned is of particular importance with regards to modelling and predicting the likely effects of anthropogenic driven climate change. There exists significant knowledge gaps with regards to how the environment as a whole affects the climate. The interplay between the biosphere and atmosphere, known overall as biosphere-atmosphere interactions, is known to be of significant importance with regards to some previously identified feedback loops. For example, the 1987 paper by Charlson, Lovelock, Andreae and Warren (Charlson *et al.*, 1987) outlined a negative feedback loop where oceanic phytoplankton were the source for the emission of dimethyl sulphide, which in the atmosphere formed a sulfate aerosol which acted as a cloud condensation nuclei (CCN), in turn precipitating the formation of clouds. Cloud formation increases the albedo in the atmosphere, causing greater reflectance of sunlight and thus causing a drop in surface temperature. As the emission of dimethyl sulphide by phytoplankton is affected by temperature, with warmer conditions increasing the rate of production, it was therefore suggested that, as temperature increased, the biosphere emitted

trace gas precursors which underwent oxidation to form particles, which in turn affected local and regional climate through the formation of CCN.

Biosphere-atmosphere feedback loops such as this may be key to understanding overall climate regulation in response to changing conditions. Arneth *et al.* (2010) gives an overview of some key interactions that are currently being investigated, such as the effect biogenic aerosols have on the global climate, including the conclusion that scattering aerosols (such as sulfates, nitrates and organic carbon) have a negative impact on radiative forcing, thus causing an overall cooling effect. Also of note in the review is discussion of the effect of secondary organic aerosols (SOA) and their precursor gases - biogenic volatile organic carbon (BVOC) species - which are estimated by Arneth *et al.* to have a significant overall effect on local and regional climates above forested areas from which BVOCs are principally emitted. Fowler *et al.* (2009) in an earlier review gives a comprehensive overview of the importance of ammonia fluxes to and from the biosphere, highlighting the effect of meteorological factors as temperature, humidity and soil moisture, as well as the underlying effect of biosphere composition.

1.1.1 Agriculture and biosphere-atmosphere interactions

As Arneth *et al.* (2010) note in the conclusion to their review, a greater number of measurements is required in order to effectively understand the underlying processes which are occurring in the interactions between biosphere and atmosphere. Furthermore, if the overall effect of these interactions is to be known, the gas and aerosol concentrations and fluxes which are measured must not be done in isolation, but rather as part of a comprehensive overview of a variety of different species simultaneously. Finally, in order to better comprehend the biosphere-atmosphere interactions which occurred prior to the Anthropocene (the current geological epoch, in which human activities have driven changes

to Earth systems), more measurements must be conducted in relatively pristine biospheres, where the overall exchange processes remain relatively unaffected by anthropogenic pressures. Similarly, to determine the impact of anthropogenic activity, measurements over a variety of biospheres shaped by human activity - such as agricultural areas, including grazed pastures - must also be conducted to determine the source, lifetime and impact of a variety of different pollutants.

1.1.2 The Amazon rainforest as a Biogeochemical Reactor

One particular biome of note which fulfils the near pristine requirements as outlined by Arneth *et al.*, and where there currently exists a lack of detailed measurements of the fluxes of a variety of trace gases and aerosol particles, is the Amazon rainforest. Considered a critical biome in consideration of biosphere-atmosphere exchange due to its large surface area, incorporation of almost 10% of global terrestrial vegetation (Houghton *et al.*, 2001), and its immense, hydroxyl radical led oxidative capacity driven by high levels of incoming solar radiation and water vapour, the Amazon is a key area for considering the cycling of a variety of gas and aerosol species. The remote location of some Amazon sites from human activity, combined with prevailing winds during the wet season which ensure near pristine atmospheric conditions, allow for any measured gas and aerosol concentrations taken at potential sites to be considered as close to a natural baseline as is feasibly possible. Furthermore, while measurements at Amazon sites remain limited, particular aspects of biosphere-atmosphere interactions above the rainforest are known to have direct effects on both climate (regionally and globally) and on the rainforest biosphere itself, particularly with regards to soil nutrient levels and leaf adsorption of particular trace gases. Therefore, as well as providing for the opportunity to study pristine atmospheric conditions in an area of intense atmospheric chemical production, measurements of trace gases

and aerosol particle concentrations taken within the Amazon rainforest can give greater insight to fundamental biosphere-atmosphere interactions that take place within this biome.

1.2 Tropospheric chemistry - overview of known pathways

Figure 1.1 highlights the fundamental interactions of importance when considering some of the trace gas and aerosol species present in the troposphere, with particular emphasis given on reduced and inorganic forms of nitrogen, hydroxyl radical formation, and inorganic trace gases such as sulfur dioxide and hydrogen chloride. The following sections discuss some of these reactions in more detail, with relevance to this projects aims and objectives.

1.2.1 Tropospheric oxidative capacity - the hydroxyl radical

Of crucial importance to overall tropospheric chemistry is the presence of the hydroxyl radical, OH. The hydroxyl radical is particularly present in plentiful quantities in the troposphere above the tropics (with an estimated daytime concentration of 1 $\times 10^7$ molecules cm^{-3}) due to high quantities of water vapour, intense solar irradiation, and a baseline source of ozone produced either in situ within the troposphere or transported from the stratosphere through convective mixing at the tropopause (Seinfeld and Pandis, 2006). Hydroxyl radicals act as a detergent, being the primary oxidant by which trace gases in the troposphere are oxidised. The overall concentration of OH is maintained by the reaction of the hydroperoxy radical (HO_2), which is a product of the terminal step reaction of

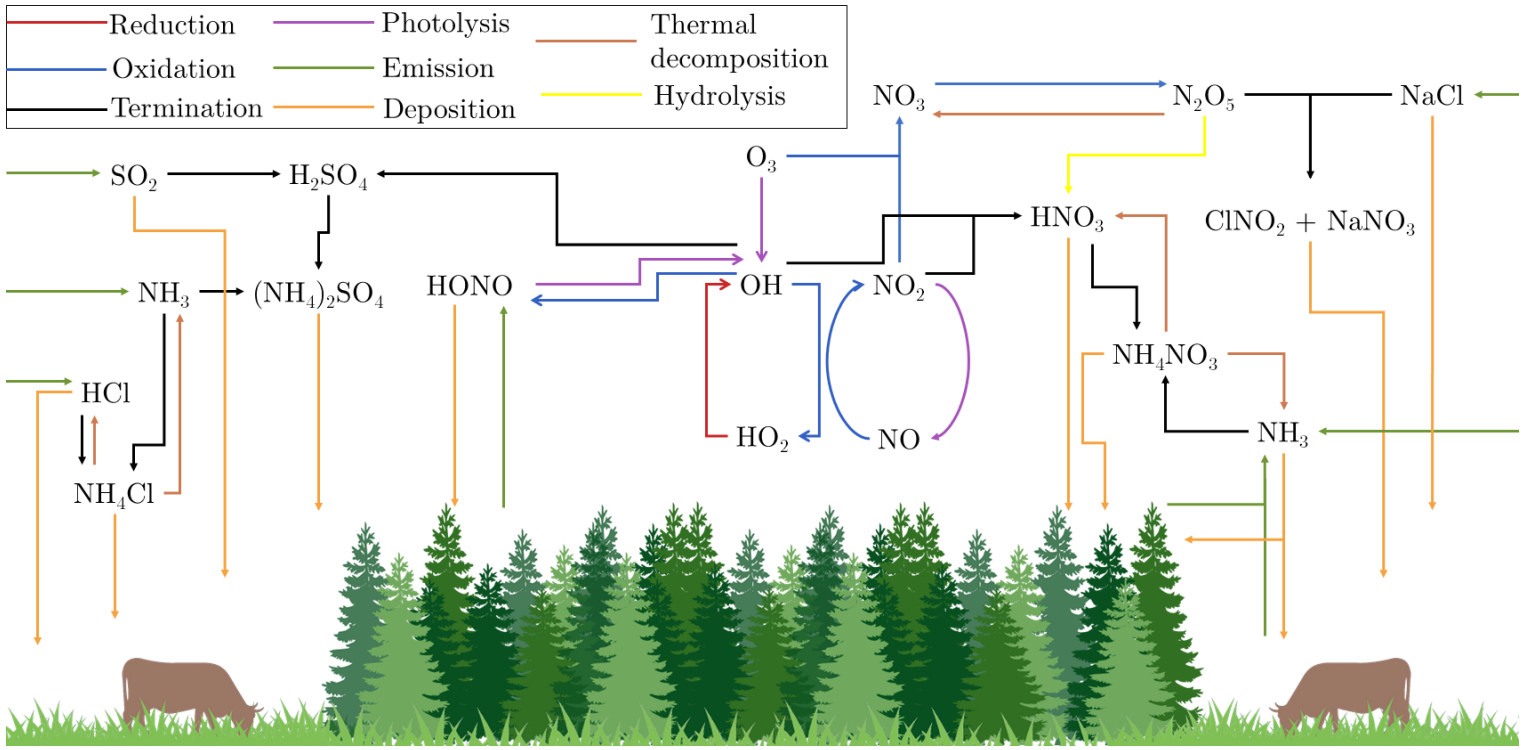

Figure 1.1: Selected chemical pathways and biosphere-atmosphere exchange of trace gases and reactive particles which occur over agricultural grassland and forest surfaces. The legend in the top left of the figure outlines the colour coding used to describe each pathway illustrated.

OH with carbon monoxide derived from full oxidation of biogenic volatile organic carbons, as illustrated in reactions 1.1 and 1.2

$$CO + OH \longrightarrow CO_2 + H \tag{1.1}$$

$$H + O_2 + M \longrightarrow HO_2 + M \tag{1.2}$$

HO_2 can react with tropospheric nitric oxide, to give an OH radical, as shown in 1.3

$$HO_2 + NO \longrightarrow NO_2 + OH \tag{1.3}$$

NO levels in turn are dependent on both soil emissions and nitrogen dioxide concentrations. Thus, the balance of OH is maintained by the presence of VOCs and NO_x (the collective name for NO and NO_2) (Thompson, 1992). This triumvirate of OH, BVOCs and NO_x species are the key components of chemistry within the free and planetary boundary layer of the troposphere, in turn acting as precursors or reactants with other species of note in determining the overall prevalence of trace gas species and aerosol particles.

1.2.2 The role of oxidised and reduced nitrogen

Reactive Odd Nitrogen, NO_y

Reactive odd nitrogen, or NO_y, is defined as the sum of NO_x and all of the oxidation products of NO_x. These species are of critical importance in overall

tropospheric chemistry in both remote and agricultural areas, and discussion of their formation, interaction with other species, and subsequent fate, is required for understanding overall biosphere-atmosphere exchange.

Considering first the progenitors of all other NO_y species, the NO_x species NO and and NO_2. The precursor gas to nitrogen dioxide in the troposphere is NO, itself an important reactant in the overall BVOC/NO_x cycle that regulates hydroxyl radical concentrations. In the Amazon rainforest, studies have found a positive flux (emission) of NO above the forest canopy (van Dijk and Meixner, 2001), even when factoring the effect of in-canopy transformation of NO to NO_2. In areas where human activity is present, such as agricultural grassland, NO has a variety of anthropogenic sources, principally from power station and diesel engine combustion. In pristine conditions such as the Amazon rainforest, production is driven by biogenic sources. The principal biogenic source is from the nitrification-denitrification cycle within soils, which is estimated to be responsible for the production of between 13 and 21 Tg Nitrogen yr^{-1} of NO (Davidson and Kingerlee, 1997). NO can be produced either through the oxidative process of soil nitrification catalysed by autotrophic *Nitrosobacteria* species

$$NH_4 \longrightarrow NH_2OH \longrightarrow HNO \longrightarrow NO \tag{1.4}$$

or through the reductive, denitrification soil cycle mediated principally under anaerobic conditions by a variety of different denitrifying bacteria species

$$NO_3 \longrightarrow NO_2 \longrightarrow NO \tag{1.5}$$

In addition, as reviewed by Medinets *et al.* (2015), NO production from soil is also driven by a process known as chemodenitrification, the abiotic, purely chemical

non enzyme related conversion of nitrite and nitrate to gaseous nitrogen species at low pH

$$3NO_2^- + 2H^+ \longrightarrow 2NO + NO_3^- + H_2O \tag{1.6}$$

Medinets *et al.* review also discussed the abiotic factors which affected overall emissions of soil NO. Referring to the work of Su *et al.* (2011) which found that a proportion of soil NO is generated from the dissociation of soil nitrous acid (HONO) under low pH conditions, Medinets *et al.* discussed the implications of soil moisture conditions, temperature and crucially soil pH, suggesting that the equilibrium of gaseous HONO with soil HONO was of critical importance in overall NO emissions. Furthermore, the degree of soil moisture content was identified as a key regulator of soil NO emissions, with waterlogged soils identified as impeding the overall diffusion of NO to the atmosphere. The overall effect of changing the soil moisture content of Amazon rainforest soils on NO fluxes was studied by Davidson *et al.* (2004), who found that in soil plots within the rainforest that were exposed to artificial drought, soil NO emissions were greater than the control sites that had a higher level of soil moisture content. With a changing climate that may induce more drought conditions within the Amazon (Duffy *et al.*, 2015), increased NO emissions is possible, which may have profound impacts on the production of NO_2, and, subsequently, on the formation of reactive odd nitrogen species and the regulation of overall hydroxyl concentrations.

One such species is the water soluble trace gas species nitrous acid (HONO), previously referred to in its formation of NO when under acidic soil conditions. In the troposphere, it can be formed by the homogeneous reaction of NO with OH to give

$$OH + NO \xrightarrow{M} HONO \tag{1.7}$$

This reaction is reversible, with HONO photodissociation yielding NO and OH (Pagsberg *et al.*, 1997)

$$HONO + h\nu \longrightarrow OH + NO \tag{1.8}$$

Alternatively, HONO can also react with OH to give -

$$HONO + OH \longrightarrow H_2O + NO_2 \tag{1.9}$$

As such, HONO formation from NO and OH occurs usually at night. HONO mixing ratios peak during the early morning, but then rapidly decrease at dawn when overnight HONO photodissociates into NO and OH. This photodissociation is particularly important as it injects a pulse of OH into the atmosphere at dawn, increasing oxidative capacity. The overall concentration of atmospheric HONO is therefore critical in determining associated concentrations of OH.

Nitrogen dioxide in the troposphere is formed from one of two reactions involving NO the oxidation by ozone of NO to form NO_2

$$O_3 + NO \longrightarrow NO_2 + O_2 \tag{1.10}$$

or the reaction of the hydroperoxy radical (HO_2) or peroxy radical (RO_2, where R is usually an organic group), which is formed from the termination of the BVOC oxidation cycle, with NO to give NO_2 (Stone *et al.*, 2012)

$$HO_2 + NO \longrightarrow NO_2 + OH \tag{1.11}$$

$$RO_2 + NO \longrightarrow RO + NO_2 \tag{1.12}$$

These three reactions are the main in situ reactions for the formation of NO_2 in the troposphere. NO_2 can then photodissociate at wavelengths shorter than 420 nm to give the $O(^3P)$ radical, which in turn is the progenitor of tropospheric ozone and thus the hydroxyl radical

$$NO_2 + h\nu \longrightarrow NO + O\left(^3P\right) \tag{1.13}$$

$$O\left(^3P\right) + O_2 + M \longrightarrow O_3 + M \tag{1.14}$$

NO_2 concentrations are therefore critical for the maintenance of the oxidative capacity of the troposphere, and thus for the continued oxidation of trace gases within the troposphere. NO_2 in itself acts as a reactant with a variety of other trace gas species to form other trace gas species present in the troposphere. For example, previously mentioned was the homogeneous reaction of NO and OH to form HONO. Similarly, the heterogeneous reaction of NO_2 with H_2O (Harrison *et al.*, 1996) also forms an important reaction with regards to overall HONO levels

$$2NO_2 + H_2O \longrightarrow HONO + HNO_3 \tag{1.15}$$

As previously noted, NO_2 photodissociates at wavelengths shorter than 420 nm.

During the night, therefore, the mixing ratio of NO_2 increases. Under these conditions, NO_2 reacts with any ozone present to give the nitrate radical (NO_3)

$$NO_2 + O_3 \longrightarrow NO_3 + O_2 \tag{1.16}$$

The NO_3 radical rapidly photodissociates and, depending on the wavelength of the incoming radiation, dissociates according to the following two reactions

$$NO_3 + h\nu\,(\lambda \leq_{700} \text{nm}) \longrightarrow NO + O_2 \tag{1.17}$$

$$NO_3 + h\nu\,(\lambda \leq_{580} \text{nm}) \longrightarrow NO_2 + O \tag{1.18}$$

The NO_3 radical is of critical importance as it acts the primary oxidative agent during night time (Brown and Stutz, 2012). It reacts with BVOCs to precipitate the formation of SOAs, as well as reacting with organic forms of sulfur to produce sulfate aerosols.

NO_3 can also combine with NO_2 to form the reservoir species dinitrogen pentoxide (N_2O_5), which can thermally decompose back to its original reactants

$$NO_3 + NO_2 + M \rightleftharpoons N_2O_5 + M \tag{1.19}$$

The N_2O_5 reservoir species can react with sodium chloride to give nitryl chloride ($ClNO_2$), therefore acting as an efficient remover of chloride species present in the troposphere. Of particular importance to this study is the hydrolysis reaction of

N_2O_5 within water droplets or on the surface of water containing aerosol particles, which results in the formation of nitric acid, HNO_3 -

$$N_2O_5 + H_2O \longrightarrow 2HNO_3 \tag{1.20}$$

During daytime, when N_2O_5 is absent, HNO_3 is formed at high OH radical concentrations by -

$$NO_2 + OH + M \longrightarrow HNO_3 \tag{1.21}$$

This leads to the overall termination of the OH/NO_x cycle, with HNO_3 being deposited from the troposphere to the biosphere. HNO_3 is extremely water soluble (with a Henrys Constant of 2.1×10^5 M atm^{-1}), and forms a nitric acid vapour. In the atmosphere, this vapour acts as a reactant with other atmospheric trace gases and aerosols to form a number of fine (particulate matter with a diameter under 2.5 μm, i.e. $PM_{2.5}$) and coarse (particulate matter with a diameter above 2.5 μm, i.e. PM_{10}) nitrate particulates of varying lifetime, and which are subsequently deposited to the surface, impacting overall biosphere function.

Reduced nitrogen species - NH_3 **and** NH_4^+

One of the most critical reactions involving HNO_3 is with the major basic gas of the tropsophere, NH_3. The gas phase equilibrium reaction of NH_3 with HNO_3 vapour, which is dependent upon temperature, relative humidity (Mozurkewich, 1993) and the relative concentrations of ions (such as sulfate) competing with HNO_3 for NH_3 (Wexler and Seinfeld, 1992), results in the formation of the fine nitrate particulate species, ammonium nitrate (NH_4NO_3)

$$NH_3 + HNO_3 \rightleftharpoons NH_4NO_3 \tag{1.22}$$

NH_4NO_3 is a semi volatile species that is deposited to the biosphere from the atmosphere. As a source of fine nitrate and ammonium (NH_4^+) aerosol in the atmosphere, it can have a range of atmospheric effects, such as through changes in overall radiative forcing caused by aerosol scattering (Adams *et al.*, 1999), or - through deposition to to nitrogen deficient fresh water systems - algal blooms, and, subsequently, eutrophication. Simultaneously, due to the fine nature of ammonium nitrate aerosol, it acts as a source of $PM_{2.5}$ airborne pollution, posing risks to human health. NH_4NO_3 is a major pollutant from agricultural areas.

Within the Amazon, due to high humidity and temperatures, the thermodynamic equilibrium favours the decomposition of NH_4NO_3 into NH_4^+ and NO_3^- upon evaporation. This is particularly important as this evaporation, which gives rise to smaller particles, can lead to changes in detected fluxes (Nemitz and Sutton, 2004). Furthermore, the introduction of ammonium and nitrate to the biosphere can increase chemical loading, leading to effects on overall vegetation composition (Verhoeven *et al.*, 2011).

As NH_3 is the dominant basic trace gas in the atmosphere, reacting with acidic trace gases to give a host of different aerosol particles, small changes in its overall atmospheric concentration can give rise to profound changes in overall mixing ratios and flux patterns. Understanding of its sources, emission factors and flux patterns is therefore important to understanding the complete cycle of tropospheric chemistry.

The majority of NH_3 emissions are anthropogenic in nature, originating primarily from agricultural sources or from biomass burning, but a significant proportion originate from biogenic sources, the majority of which are from the decomposition

of plant and animal matter (Behera *et al.*, 2013). Due to the near pristine conditions of the Amazon rainforest, overall ammonia concentrations are relatively low compared to agricultural areas, with episodes where significant increases occur associated with localised biomass burning.

Historically, it was assumed that the flux of ammonia was limited to a unidirectional deposition model in natural and semi-natural conditions, being restricted to bi-directional exchange only in areas where the surface concentration of NH_3 was high, such as on fertilised agricultural areas (Duyzer *et al.*, 1992). However, studies by Erisman and Wyers (1993) over heathland and then subsequently over coniferous forest (Wyers and Erisman, 1998) showed that a bi-directional flux of ammonia was present in unfertilised areas where surface or canopy concentrations of ammonia were low.

The bi-directional exchange of ammonia was considered by Schjoerring *et al.* (1998) to be a result of physiological parameters within the canopy of surface vegetation as well as the interplay between abiotic factors. Schjoerring *et al.* outlines some of the key considerations. Some critical factors identified include the canopy compensation point the value at which the NH_3 concentration balances outwards NH_3 loss and inward NH_3 absorption leaf chemistry (such as the presence of certain enzymes for NH_4^+ assimilation or root activity), soil nitrogen pools, relative humidity (related to stomatal conductance), temperature, and the life stage of the plant. More specifically, the compensation point is considered to be a balance, whereby when the stomatal concentration of NH_3 exceeds atmospheric concentrations, emission occurs and vice versa. Temperature also regulates emission and deposition by affecting the overall Henry and dissociation constants present in the apoplast (the space between the leaf cells and the leaf cuticle in which material can diffuse freely) which affects the total internal NH_3 concentrations in the leaf. Finally, the composition of reactive nitrogen in the soil

is also seen as critical soils which have a higher ratio of ammonium to nitrate generally leads to vegetation emitting greater amounts of NH_3.

The empirical evidence of bi-directional fluxes for NH_3 led to the development of associated models that simulated, in terms of analogy to electrical resistors and capacitors, the flux of NH_3 to and from surfaces. Sutton *et al.* (1998) develops the concept of the bi-directional model as a series of resistors such as atmospheric (R_a and R_b), cuticle (R_w) and stomatal (R_s) which affect overall NH_3 flux and have quantitative values based upon meteorological conditions. The direction of the flux is in turn mediated by the canopy compensation point (χ_c). Depending on the values of the cuticular and stomatal resistances, bi-directional exchange can occur, dependent on the value for the central pivot of the model - the canopy compensation point. Sutton *et al.* also introduced the concept of cuticular capacitance, which models the observed effect that NH_3 can be absorbed or desorbed from water films on leaf surfaces depending on relative humidity and temperature. Kruit *et al.* (2010) further refined this model by considering the existence also of a stomatal capacitance factor as well. Figure (1.2) illustrates a selection of models currently in use for simulating NH_3 fluxes, both unidirectional and bi-directional, over vegetated surfaces, with a description of their associated individual resistances.

The models for NH_3 bi-directional flux highlight the importance of the stomatal compensation point has on the overall flux direction, and that the stomatal compensation point itself is dependent upon temperature, relative humidity, and the concentration of both atmospheric and internal leaf NH_3. In the Amazon rainforest, where temperature and relative humidity is high, and where the overall atmospheric concentration of NH_3 is low, even small increases in temperature can lead to loss of leaf nitrogen in the form of emitted NH_3. It is therefore imperative to determine the overall conditions that affect NH_3 fluxes within the Amazon,

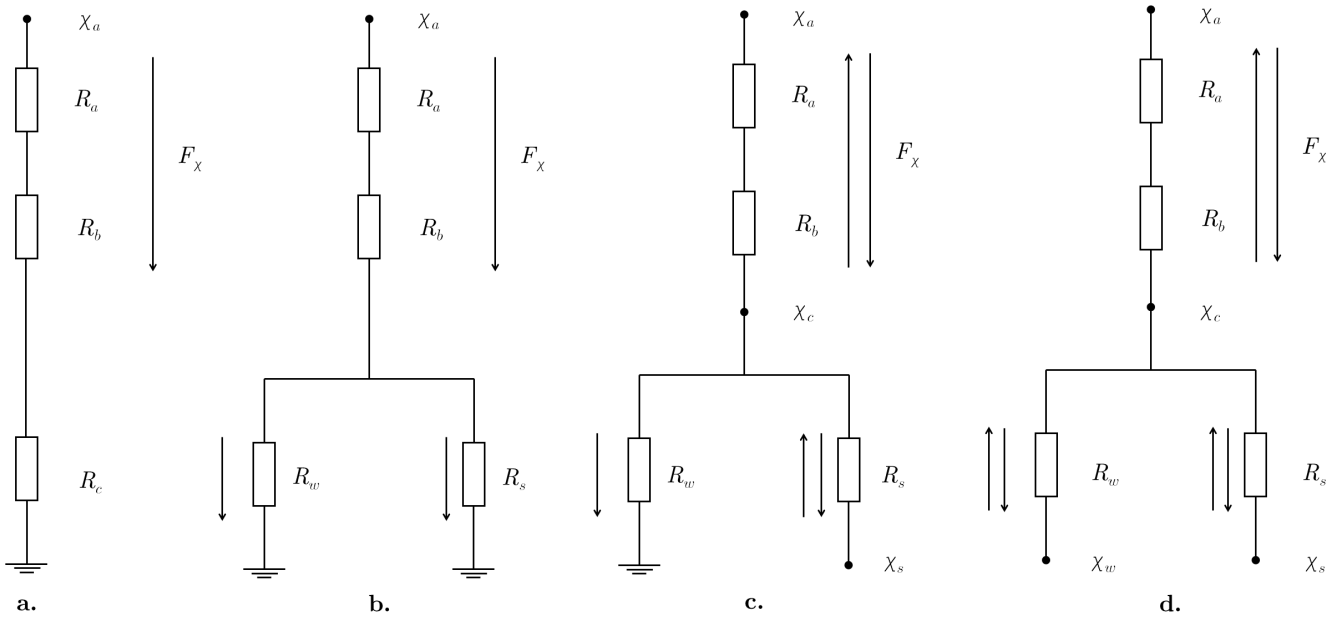

Figure 1.2: Selection of current single layer models for surface-atmosphere exchange of NH_3 over vegetation. From left to right - a., the simple canopy resistance model of aerodynamic resistance (R_a), quasi -laminar boundary layer resistance (R_b), and canopy resistance (R_c) in series; b., elaboration on a., with R_c subdivided into the stomatal (R_s) and cuticular (R_w) resistances; c., the "classic" canopy compensation (χ_c) point model, where surface-exchange of NH_3 is mediated by the stomatal compensation (χ_s) point; and d., the modified compensation point model with bi-directional exchange of NH_3 possible from both the stomata and cuticular surface.

with particular emphasis on temperature and relative humidity with regards to stomatal compensation points.

1.2.3 Sulfur dioxide and sulfate aerosol

One of the key determining factors for the formation of ammonium nitrate is the presence of competing acidic trace gases for neutralisation with the basic NH_3 gas, or anions which associate with the ammonium ion. Sulfur dioxide (SO_2) acts as a precursor trace gas in the troposphere for the formation of sulfuric acid (H_2SO_4), which can react with trace basic gases, such as ammonia, to generate sulfate (SO_4^{2-}) containing aerosols in the troposphere. Atmospheric SO_2 is principally generated through the combustion of fossil fuels and biomass burning. However, natural sources, which include volcanoes and the oxidation of trace sulfur containing gases such as dimethyl sulphide (Jardine *et al.*, 2015), can be important contributors to either background concentrations in remote areas or as periodic episodes of increased concentrations of SO_2. The dry deposition of SO_2 to the environment by itself can contribute to soil and forest acidification.

The formation of SO_4^{2-} from SO_2 occurs through an aqueous phase conversion SO_2 associates with water molecules, and undergoes an equilibrium reaction to produce bisulfite ions (HSO_3^-). In turn, bisulfite undergoes an equilibrium reaction forming the sulphite ion (SO_3^{2-}). Reactions 1.23, 1.24 and 1.25 outline these steps

$$SO_2 + H_2O \rightleftharpoons SO_2 \cdot H_2O \tag{1.23}$$

$$SO_2 \cdot H_2O \rightleftharpoons H^+ + HSO_3^- \tag{1.24}$$

$$HSO_3^- \rightleftharpoons H^+ + SO_3^{2-} \tag{1.25}$$

Further oxidation of sulphite gives SO_4^{2-}, although the dominant oxidative agent for this reaction is disputed. Ozone, hydrogen peroxide, and diatomic oxygen (catalysed by the presence of trace metals such as manganese and iron) have all been identified as a mechanism for this oxidation step. The SO_4^{2-} anion can then associate with ammonium ions in the atmosphere as an ionic mix which exists within rainwater or cloud droplets, ultimately being deposited through wet deposition to the biosphere.

Alternatively, SO_2 can be homogeneously oxidised in the gas phase by the OH radical

$$SO_2 + OH + M \longrightarrow HOSO_2 \cdot + M \tag{1.26}$$

which, upon further oxidation by O_2, results in sulfur trioxide (SO_3)

$$HOSO_2 \cdot + O_2 \longrightarrow HO_2 + SO_3 \tag{1.27}$$

Which rapidly converts to sulfuric acid in the presence of water vapour

$$SO_3 + H_2O + M \longrightarrow H_2SO_4 + M \tag{1.28}$$

In low NH_3 atmospheres, H_2SO_4 exists in the aerosol phase. As the concentration of NH_3 increases, it reacts with H_2SO_4 to give ammonium sulfate, $(NH_4)_2\,SO_4$

$$H_2SO_4 + 2NH_3 \longrightarrow (NH_4)_2\,SO_4 \tag{1.29}$$

$(NH_4)_2\,SO_4$ has several direct and indirect impacts on both the atmosphere and biosphere. Within the atmosphere, it acts as a scattering aerosol, decreasing the overall temperature and thus affecting local and regional climates. In the biosphere, its deposition affects vegetation, such as leading to the depletion of the waxy cuticle layer on the surface of coniferous trees (Van der Eerden *et al.*, 1992). Its deposition below the canopy can lead to increased pH within soils, as well as changes in the uptake of total nitrogen by vegetation.

1.2.4 Hydrogen chloride and chloride aerosol

Hydrogen chloride (HCl) is found in the atmosphere in the gaseous phase, with Pio and Harrison (1987) estimating a marine, pristine troposphere concentration of 0.08 to 0.3 $\mu g\,m^{-3}$. The dominant source for HCl is from anthropogenic combustion sources, particularly from the burning of chlorine rich coals or chlorine-containing wastes such as poly-vinyl-chloride plastic. It is also formed from the substitution reaction of sodium chloride, principally from sea spray, with the acidic trace gas nitric acid. In the troposphere, HCl reacts with ammonia to form the fine aerosol ammonium chloride, NH_4Cl, a semi-volatile species that is deposited to the biosphere, acting as a source of reduced nitrogen

$$HCl + NH_3 \rightleftharpoons NH_4Cl \tag{1.30}$$

However, although HCl may act as a precursor for secondary inorganic aerosol such as NH_4Cl, the vapour pressure of NH_4Cl is greater than that of NH_4NO_3. Consequently, HCl and its derivative NH_4Cl are not considered as important in

governing aerosol load in major chemical transport models. The major source of chloride (Cl^-) containing aerosol is therefore thought to be in the form of coarse sea-salt (NaCl). The substitution reaction between sea salt and nitric acid as previously mentioned results in not only HCl, but also the aerosol sodium nitrate $NaNO_3$, which when deposited acts as a source of coarse nitrate to the biosphere. This reaction, with consequently elevated levels of coarse nitrate aerosol, has been observed previously at coastal or near-coastal sites where marine air masses interact with polluted air masses (Yeatman *et al.*, 2001; Twigg *et al.*, 2015).

Over the Amazon, Trebs *et al.* (2004) made an extensive study on the concentrations of trace inorganics such as sulfide and chloride species. It was found that, in total, inorganic containing aerosols formed 20% of aerosol mass above the Amazon, with the observation that cations (such as potassium ions) formed half of inorganic aerosol mass, with anion aerosols (such as chloride and sulfide) constituting the remainder. Considering the importance of gas phase equilibrium reactions in the formation of sulfide, chloride and nitrate aerosols with ammonia, Trebs *et al.* stressed the importance of factoring temperature and relative humidity considerations into modelling for overall inorganic aerosol formation.

1.2.5 Primary biological aerosol particles (PBAPs)

Increasing focus has been given to aerosols which are directly emitted from the biosphere to the atmosphere. Termed primary biological aerosol particles (PBAPs), they comprise a whole category of ultrafine to coarse aerosol particles including pollen, animal and plant matter, viruses, and, of increasing importance in the study of cloud formation, fungal spores. Jaenicke (2005) estimates that, collectively, the total emissions of PBAs to the atmosphere is approximately 1000 $Tg\,yr^{-1}$.

In a study within the Amazon during the wet season of 2001, Elbert *et al.* (2007) concluded that fungal spores are a primary constituent of PBAPs in the rainforest, constituting over 45% of total coarse particulate matter. Of particular note was that two particular species groups of fungi accounting for the dominant fraction of total fungal spore PBA emissions. The first group, actively wet spore discharging *Basidiomycota* (ABM), comprised of mushroom and jelly fungi species, discharge their spores through a surface tension catapult, which is dependent upon relative humidity and the hygroscopic uptake of water vapour by the spore. The second group, termed actively wet spore discharging *Ascomycota* (AAM), constitute a variety of saprophyte species that discharge their spores through spore sacs called *asci*, which incorporates a fluid mixture of solutes including mannitol, potassium ions, nitrate ions and chloride ions. When the *asci* bursts to release its spore, the associated *asci* fluid is also discharged along with fragments of the spore.

Elbert *et al.* (2007) proposed that in the Amazon, due to the high photosynthetic rate, the emission of fungal spores was particularly important to overall aerosol budgets, and that the spores themselves, their *ascii* contents, or their fragments, could act as cloud condensation or ice nuclei in the upper troposphere. Poschl *et al.* (2010), in a study of CCN within the Amazon, also concluded that PBAPs acted as a source for ice nuclei. The study overall focused on the properties of CCN in the Amazon, concluding from electron microscopy measurements that CCN could be grouped into five classes pure SOA droplets, SOA-inorganic particles, primary biological aerosol particles such as spores, mineral dust from the Sahara, and pyrogenic carbon particles from biomass burning in Africa. Poschl *et al.* noted that during the initial stages of CCN formation, nucleation and Aitken mode, that pure SOA droplets dominated. However, this would require new particle formation to occur, which was not observed. Thus, even though CCN was observed as being composed of SOA, the initial impetus for formation of these droplets was considered enigmatic.

Pöhlker *et al.* (2012), in measurements of CCN composition over the Amazon using electron microscopy and secondary ion mass spectrometry, found that pronounced potassium spectra were detected in all SOA particles associated with CCN. Further observations found that the mass of potassium within each SOA particle was size dependent, with a greater mass composition in smaller particles that would be found in nucleation and Aitken mode, while a smaller composition in accumulation mode size particles. From this, Pöhlker *et al.* suggested that within each SOA composed CCN, there existed a potassium seed, which initiated CCN formation small potassium salt rich particles from primary emissions act as seeds for the condensation of organic material and that the primary potassium content is diluted upon particle growth. As a result, the route for SOA particle formation could be explained through potassium seeds for CCN. Linking to Elbert *et al.* (2007) review, Pöhlker *et al.* (2012) concluded that the potassium acting as CCN seeds were from the fungal emissions within the rainforest.

Further studies in remote, tropical rainforest areas have found that the fragments of AAM spores, which rupture in the troposphere under changing conditions of relative humidity, also contain inorganic ions. China *et al.* (2018) found that 40% to 60% of analysed spore fragments sampled above the Amazon rainforest contained Na^+ and Cl^-, principally in the form of NaCl. Crucially, it was found that the analysed coarse NaCl was "morphologically similar to dry sea-salt." Furthermore, it was observed that the spores themselves were emitted during wet, cool and calm ambient conditions.

It is therefore possible that a feedback loop exists whereby, under warmer conditions, the emissions of fungal spores increase due to higher photosynthetic activity, which causes the increased emission of fungal spores and associated ionic solutes found in AAM *asci*. Combined with increased emissions of BVOCs, and thus increased SOA formation, CCN formation is positively affected, leading to increased CCN particles and thus more cloud cover, which in turn would affect

surface temperatures. Measurements of Cl^- containing aerosol could therefore potentially act as a tracer for PBAPs.

1.3 Study aims, hypotheses, and thesis outline

The preceding sections have outlined the formation, lifetime and surface-atmosphere exchange of a selection of trace gases and aerosols, with a particular focus on the inorganic trace gases HCl, HONO, HNO_3, SO_2 and NH_3, and their associated counterparts, Cl^-, NO_2^-, NO_3^-, SO_4^{2-} and NH_4^+ containing aerosol. As stressed in the discussion of each individual species, concentration and flux measurements of these species are required over a variety of biospheres in order to better understand their surface-atmosphere exchange behaviour. In particular, measurements are required for biospheres with few or no measurements of these species (such as the Amazon rainforest).

This study was developed to meet this demand for more concentration and flux measurements of the trace gas and aerosol species discussed, and from those measurements, to further advance the knowledge of the processes governing the surface-atmosphere exchange of the trace gas and aerosol species measured. To achieve this, three principal aims, with associated research questions and hypotheses, were developed -

1. To measure the concentrations and fluxes of the inorganic trace gases HCl, HONO, HNO_3, SO_2 and NH_3 and their associated aerosol counterparts, Cl^-, NO_2^-, NO_3^-, SO_4^{2-} and NH_4^+ as taken over agricultural grassland.

This aim is discussed further in Chapter 4, which presents the measurements of concentrations and fluxes of the suite of inorganic trace gases and associated

aerosol counterparts mentioned, taken over the Easter Bush agricultural grassland site (Midlothian, United Kingdom) from May 2016 to June 2016. A detailed introduction on the concepts, measurement techniques, and the species measured during the campaign are given in the chapter, which expands on the material presented in this introduction. Furthermore, a literature review is presented which elucidates further upon the following research questions, and associated research hypotheses –

- Is there evidence of ammonium nitrate (NH_4NO_3) formation after the application of urea fertiliser to agricultural grassland, and can this be inferred through measuring each component of the NH_4NO_3 triad (NH_3, HNO_3, and the aerosol components of NH_4NO_3, NH_4^+ and NO_3^-) simultaneously? **Research hypothesis**– the application of urea fertiliser to agricultural grassland results in the formation of NH_4NO_3.

- Previous research has found evidence of emissions of the trace gas nitrous acid (HONO) from semi-natural sites, such as forests and grasslands. Are emissions of HONO from the agricultural grassland at Easter Bush observed? Are agricultural grassland sites an overall net source or net sink for HONO? **Research hypothesis 1** – emissions of HONO occur from the Easter Bush agricultural grassland site. **Research hypothesis 2** – The Easter Bush grassland site is a net source for HONO.

2. To measure the concentrations and fluxes of the inorganic trace gases HCl, HONO, HNO_3, SO_2 and NH_3 and their associated aerosol counterparts, Cl^-, NO_2^-, NO_3^-, SO_4^{2-} and NH_4^+ as taken over tropical rainforest.

This aim will be discussed in Chapter 5 and Chapter 6. Chapter 5 presents the concentration and flux measurements of the suite of inorganic trace gases and

associated aerosol counterparts mentioned, taken over the Amazon Tall Tower Observatory (ATTO) site (Amazonas, Brazil) from October 2017 to November 2017. Chapter 5 provides a detailed introduction to the ATTO site, measurement techniques used, and the species measured during the campaign, expanding on the material presented in this chapter. As with 4, a literature review expounds further on the following research questions, with associated research hypotheses –

- Is there evidence for the long range transport, either regionally or globally, and subsequent deposition of pollutants to the Amazon Tall Tower Observatory rainforest site? Can this be determined through the use of back trajectory analysis of air masses and concentration measurements of trace gases and aerosols? **Research hypothesis** – the deposition of regionally and globally transported pollutants is observed at the Amazon Tall Tower Observatory.
- Are emissions of trace gases and aerosols observed at the Amazon Tall Tower Observatory site, or are trace gases and aerosols uniformly deposited to the surface? **Research hypothesis** – emissions of trace gases and aerosols occur from the rainforest canopy to the atmosphere at the Amazon Tall Tower Observatory site.

Chapter 6 focuses particularly on the surface-atmosphere exchange of NH_3 over the ATTO site. The introduction to Chapter 6 expands on the material presented in Section 1.2.2, giving a more detailed overview of how NH_3 surface-atmosphere exchange is modelled. The research questions asked in this chapter, with associated hypotheses, are –

- Do emissions of NH_3 occur from the rainforest canopy to the atmosphere at the Amazon Tall Tower Observatory site ? **Research hypothesis** – the

deposition of regionally and globally transported pollutants is observed at the Amazon Tall Tower Observatory.

- If emissions do occur at the site, what are the meteorological conditions which drive them? A null and alternate hypothesis can be developed. H_0 – there is no relationship between the emissions of NH_3 at the Amazon Tall Tower Observatory site and any metrological condition, probability value (p-value) in linear regression analysis between meteorological conditions and NH_3 flux >0.05; H_a – there is a relationship between the emissions of NH_3 at the Amazon Tall Tower Observatory site and at least one metrological condition, probability value (p-value) in linear regression analysis between meteorological conditions and NH_3 flux <0.05

- Can the surface-atmosphere exchange behaviour of NH_3 be accurately modelled using 2D canopy models previously developed to model bi-directional surface exchange at other forest sites? As with the second question, a null and alternate hypothesis can be developed. H_0 – 2D canopy models do not simulate the observed fluxes of NH_3, p-value in linear regression analysis between all models and observed NH_3 fluxes >0.05; H_a – 2D canopy models do simulate the observed fluxes of NH_3, p-value in linear regression analysis between at least one model and observed NH_3 fluxes <0.05.

3. Through analysis and interpretation of the concentrations and fluxes gathered over agricultural grassland and tropical rainforest, further the understanding of processes governing the surface-atmosphere exchange of the inorganic trace gases HCl, HONO, HNO_3, SO_2 and NH_3 and their associated aerosol counterparts, Cl^-, NO_2^-, NO_3^-, SO_4^{2-} and NH_4^+.

Chapters 4, 5 and 6 provide discussion on the measurements of concentrations and fluxes taken over their respective study areas, and from this, draw conclusions

pertaining to the surface-atmosphere exchange of the trace gases and aerosols measured. Chapter 7 presents an overview of the conclusions drawn from Chapters 4, 5 and 6, with a synthesis of the results with existing literature to present novel insights into the surface-atmosphere behaviour of the species measured. This aim focuses on the exploratory aspects of this research, with the intention of developing of future research questions.

The following two chapters present an overview of the methods used throughout the rest of the thesis. Chapter 2 describes the micrometeorological methods and techniques which are used to measure the inorganic trace gases and associated aerosols as measured by this study. Chapter 3 outlines the instrument - the Gradient of Aerosols and Gases Online Registration (GRAEGOR) - which employs the methods outlined in Chapter 2 to measure the concentrations and fluxes of the inorganic trace gases HCl, HONO, HNO_3, SO_2 and NH_3 and their water-soluble aerosol counterparts Cl^-, NO_2^-, NO_3^-, SO_4^{2-} and NH_4^+.

Chapter 2

Micrometeorological theory and practice

2.1 The planetary boundary layer

The scope of micrometeorology concerns itself with phenomena that occur across small time and spatial scales relative to wider meteorology, principally, those that occur for less than 24 hours and over a distance spanning less than 1 km (Foken, 2008). As such, studies in micrometeorology focus on the lower layers of the troposphere where such transient and rapid processes occur. This area of the atmosphere, whose absolute height extends to an order of magnitude 10^3 m above surface but which varies according to atmospheric conditions, is termed the atmospheric boundary layer (ABL) or the planetary boundary layer (PBL). Defined as the part of the troposphere that is directly influenced by the presence of the Earths surface (Stull, 1988), it is characterised by its continuous mechanical (generated by wind shear) and thermal convective induced turbulent

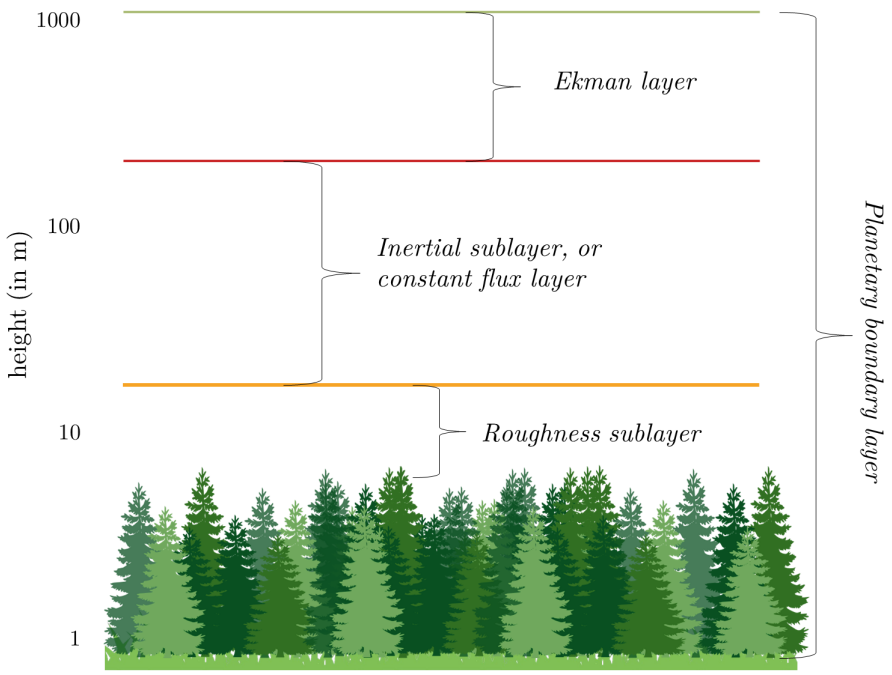

Figure 2.1: Extent of the planetary boundary layer (in m log scale), with subdivisions

flow, resulting in turbulence driven surface exchanges of heat, momentum, water vapour and trace gases.

The ABL can further be subdivided into a series of layers, as illustrated in Figure 2.1. At the lowest level exists the laminar boundary layer, extending a few millimetres above the surface. Here, molecular exchange of scalars (such as heat and momentum) dominates over turbulent exchange. The laminar layer gives way to a viscous sublayer that extends to about a centimetre above the surface. Here, too, molecular exchange of heat and momentum predominate. Above these layers where molecular exchange dominates extends the surface (or Prandtl) layer, whose extent varies with the degree of atmospheric stability but ranges from 10^1 to 10^2 m in orders of magnitude. Extending above the surface layer, from 10^2 m to 10^3 m in height, exists the Ekman layer, the uppermost level of the ABL. The relationship between flow and surface characteristics begins to decouple within the Ekman layer, as the increasing influence of the Coriolis effect becomes apparent.

Over rough land surfaces, the surface layer can further be subdivided into two regions the roughness sublayer and the inertial sublayer. The roughness layer is the region of air within and above the individual roughness elements (such as buildings, trees, and geological formations) which occupy the surface. The composition and canopy height (h_c) of the collective roughness elements have important ramifications for flux similarity theory, which underpins the micrometeorological technique used to measure the flux of trace gases and other scalars. A number of key variables, particularly aerodynamic roughness length and displacement height (the height above the surface roughness elements at which the logarithmic wind speed is extrapolated to be zero), are affected by the roughness sublayer. It therefore has a critical effect on the region above it, the inertial sublayer, which composes the second of the two subdivisions of the surface layer.

Within the inertial sublayer, shear stress is considered to be constant throughout. As a result, flux values are considered to deviate little with height, varying by approximately 10% from their surface values. For this reason, the inertial sublayer is also referred to as the constant flux layer. Based upon the logarithmic wind profiles that are displayed within this constant flux layer, micrometeorological techniques have been developed which allow for measurements of the surface exchange of trace gases and aerosols. It is important to note, however, that the underlying assumptions of these micrometeorological techniques include that the area of investigation has a homogeneous surface roughness area (termed the fetch), that there are neutral conditions, and that no chemical interaction of the species studied is occurring within the constant flux layer (Garratt, 1994).

2.2 Micrometeorological methods

A variety of different methods used in the measurement of biosphere to atmosphere surface exchanges of gases and aerosols, ranging from the micro scale flux of gases over a few square cm, such as cuvette measurements over leaf surfaces, to larger chamber measurements which can measure flux over several square metres. However, when considering the surface exchange over larger areas and vertical heights, micrometeorological methods grounded in measurements of turbulent exchange dominate. Broadly, these can be divided into direct methods, which sample air at one point above the surface and measure vertical wind speed, wind direction and the concentration of the species one wishes to measure (the eddy covariance method), or indirect methods which measure surface exchange by considering the rate of diffusion of the species measured along a concentration gradient sampled at two different heights (the aerodynamic gradient method, hereafter referred to as the AGM). Each method has its own distinct strengths and weaknesses, which will be considered in turn along with discussion of their theory and application in sensor development.

2.2.1 Direct methods - the eddy covariance method

The eddy covariance method is based on the concept that turbulent motion in wind speed and direction also generates variations in associated scalars such as sensible heat, latent heat, and the concentration of trace gases. For any trace gas species, the vertical flux can be described in terms of its mixing ratio (here expressed as χ), the vertical wind speed (w), and the density of air (ρ_a) -

$$F = \overline{\rho_a w \chi} \tag{2.1}$$

For every scalar considered in this turbulent situation, the value can be time decomposed through Reynolds decomposition (Stull, 1988) into its slowly varying mean and its instantaneous deviation from that mean. Therefore, the mixing ratio of the trace gas measured can be expressed as the product -

$$\chi = \overline{\chi} + \chi' \tag{2.2}$$

By establishing that the turbulent motion of air generates instantaneous variation in the scalar one wishes to measure (such as the mixing ratio of a trace gas) and thus its overall change in time and space, then it can be established that there is a common covariance between the instantaneous value variable of that scalar and that of the vertical wind speed component, w', which is the vertical measure of turbulent motion. Concordantly, the vertical flux of the concentration of an inorganic trace gas species as described by Eq. (2.1 can be expressed, through Reynolds decomposition, as -

$$F = \overline{(\overline{\rho}_a + \rho'_a)\,(\overline{w} + w')\,(\overline{\chi} + \chi')} \tag{2.3}$$

and thus -

$$F = \overline{(\overline{\rho}_a \overline{w}\ \overline{\chi} + \overline{\rho}_a \overline{w}\chi' + \overline{\rho}_a w'\overline{\chi} + \overline{\rho}_a w'\chi' + \rho'_a \overline{w}\ \overline{\chi} + \rho'_a \overline{w}\chi' + \rho'_a w'\overline{\chi} + \rho'_a w'\chi')} \tag{2.4}$$

The terms $\overline{\rho}_a \overline{w}\chi'$, $\overline{\rho}_a w'\overline{\chi}$ and $\rho'_a \overline{w}\ \overline{\chi}$ express average deviations from the mean. Consequently, they are equal to zero, and fall out of Eq. (2.4) to give -

$$F = (\overline{\rho}_a \overline{w}\ \overline{\chi} + \overline{\rho}_d w'\chi' + \rho'_a \overline{w}\chi' + \rho'_a w' \overline{\chi} + \rho'_a w'\chi') \tag{2.5}$$

Two assumptions of the eddy covariance method are that air density fluctuations are taken to be negligible, and that the mean vertical flow - for homogeneous, horizontal areas - is also negligible Consequently, Eq.(2.5) resolves, for any trace gas species, to -

$$F = \overline{\rho}_a \overline{w'\chi'} \tag{2.6}$$

The fluxes of other scalars such as heat and momentum can also be expressed in terms of covariance of the instantaneous variation of the scalar with the vertical wind speed component. For example, the flux of sensible heat, H, can be given as the covariance between the deviation in potential temperature (θ) and vertical wind speed (w), in combination with ρ_a and the specific heat capacity of air (c_P) -

$$H = \overline{\rho_a} C_p \overline{w'\theta'} \tag{2.7}$$

Therefore, sensors based on the eddy covariance method take online, rapid, and simultaneous measurements of the concentration of the scalar, plus the vertical wind speed, at one sample height. The averaging time used for the measured covariance is dependent on ensuring that it is longer than the lowest frequency variations which contribute to the vertical flux, but also ensuring that it is not so long that it exceeds the time scale at which changes in atmospheric stability would occur, thus violating the stationary requirements of the method. Generally, an averaging time of twenty to thirty minutes is required. Similarly, the sensors used

must be sensitive enough to measure low frequency eddies that may be present and which entrain the flux of the scalar measured. Eddy frequency is dependent on aerodynamic roughness length, and thus can vary substantially based on the roughness elements present in the area studied. Sensors which can detect eddy frequencies of approximately 10 Hz and greater are generally sufficient for most study areas.

While the eddy covariance method is direct and not reliant on semi-empirical values for its calculations and has the advantage of being a one point sensor, it has potential drawbacks. One problem is the introduction of large uncertainties in the measurements as a result of variations in air density caused by fluxes in sensible and latent heat. Most eddy covariance sensors rely on infrared analysers, which measure the density of trace gas species. Thus, changes to overall air density would affect the measured values, which can be particularly acute with gases whose fluxes are small in comparison to their background concentration. Furthermore, some gases such as NH_3, HNO_3 and HCl are prone to adsorption on the walls of the inlet-lines of the sensors used (Neuman *et al.*, 1999). As a consequence, fluxes of these gases as measured by eddy covariance are often dampened and unreliable.

2.2.2 Indirect methods - the classical aerodynamic gradient method

The AGM considers the turbulent transport of scalars to be analogous to that of molecular diffusion. Thus, the overall transport processes can be described in terms of a flux gradient format, where the flux of the given scalar is proportional to the local gradient. The flux of any given scalar, such as F_χ, can therefore be expressed in a format similar to Ficks First Law of Molecular Diffusion which is a product of the scalars concentration gradient and the transfer coefficient of that

scalar governing the diffusion process. The transfer coefficient (K_χ) is a function of z (the absolute distance above the ground, in m), d (the displacement height, in m), and L (the Obukhov length) -

$$F_\chi = -K_\chi \frac{\partial \chi}{\partial z} \tag{2.8}$$

Other scalars, such as shear stress and sensible heat, can similarly be expressed as -

$$\tau = -\rho_a K_M \frac{\partial u}{\partial z} \tag{2.9}$$

$$H = -\rho_a c_p K_H \frac{\partial T}{\partial z} \tag{2.10}$$

One of the assumptions of the AGM is that the processes governing the transport of one scalar is analogous to all other scalars. Thus, one of the implications is that the transfer coefficient for one scalar is equal to the transfer coefficient for all scalars. Consequently, the eddy diffusivity for species χ (K_χ) is the same as the diffusivity for sensible heat (K_H) and is analogous to that for momentum (K_M).

The eddy diffusivity for momentum can be expressed in terms of the friction velocity (u_*), a velocity scale which expresses the kinematic turbulent momentum flux in the inertial sublayer (Holton and Hakim, 2012) , where τ is the sheer stress and ρ_a is the density of air -

$$u_* = \sqrt{\frac{\tau}{\rho_a}} \tag{2.11}$$

Based on the paper by Monin and Obukhov (1954), which established the eponymous similarity theory, the transfer coefficient for momentum, K_M, can be expressed as -

$$K_M = \frac{\kappa(z-d)u_*}{\phi_M} \tag{2.12}$$

where κ is von Krmns constant, which has an approximate value of 0.4, ϕ_M is the stability correction for momentum, z is the absolute height above the ground (in m), and d is the displacement height. As the transfer coefficient for each scalar is considered analogous, the transfer coefficient for a given scalar (K_H) is therefore similar to that for momentum, with the stability correction function altered for sensible heat instead of momentum. Thus -

$$K_H = \frac{\kappa(z-d)u_*}{\phi_H} \tag{2.13}$$

where ϕ_H is the stability correction for sensible heat. With the effect of stability conditions considered, the flux of a species χ can be given as -

$$F_\chi = -\frac{\kappa(z-d)u_*}{\phi_H}\frac{\partial\chi}{\partial z} \tag{2.14}$$

For generic conditions, corrections must be made in order to account for atmospheric stability. This can be parameterised by considering the height at which the buoyancy of the air parcel (i.e. thermal convective production of turbulence) entraining the flux is equal to the turbulent kinetic energy of the air parcel generated by wind shear (i.e. mechanical production of turbulence). This height is known as the Obukhov length (Obukhov, 1946), and is given by Foken (Foken, 2006) as -

$$L = -\frac{u_*^3}{\kappa \frac{g}{T} \frac{H}{\rho_a c_p}} \tag{2.15}$$

where g is the acceleration due to gravity (9.8 $\mathrm{m\,s^{-2}}$), T is the absolute temperature (in K) and H is the sensible heat flux. As the Obukhov length is inversely proportional to the sensible heat flux, it follows that it is positive in stable conditions when there is a negative flux of sensible heat, is negative in unstable conditions when there is a positive flux of sensible heat, and infinite in neutral conditions when there is no flux of sensible heat. Alternatively, the gradient Richardson number (R_i), which expresses the gain in turbulent energy an air parcel entraining a flux achieves due to buoyancy and eddy motion, can be used to be measure atmospheric stability using the following equation

$$R_i = \frac{g}{T} \frac{\frac{\partial T}{\partial z}}{\left(\frac{\partial u}{\partial z}\right)^2} \tag{2.16}$$

If the boundary layer is unstable, then the Richardson number is less than zero and turbulence is sustained by convection. For stable conditions, where the Richardson number is greater than zero, turbulence is sustained by mechanical (shear) production. The gradient Richardson Number and the Obukhov Length are linked by the dimensionless stability parameter, ζ, expressed as (Prueger and Kustas, 2005) -

$$\zeta = \begin{array}{ll} \frac{R_i(z-d)}{1-5.2R_i(z-d)} & L > 0 \\ R_i(z-d) & L < 0 \end{array} \tag{2.17}$$

The stability parameter, ζ, can therefore be included in Eq.(2.14), to give the non-neutral stability corrected function for the flux of species χ, as

$$F_\chi = -K_H \left(\frac{z-d}{L}\right) \frac{\partial \chi}{\partial z} \tag{2.18}$$

By substituting Eq.(2.11) and Eq.(2.12) with associated stability parameter, into a rearranged form of Eq.(2.9) , the following expression for the partial derivative in horizontal mean wind velocity, ∂u, can be obtained -

$$\partial u = \frac{u_*}{\kappa(z-d)} \phi_M(\zeta) \partial z \tag{2.19}$$

By integrating this expression, a logarithmic profile for mean horizontal wind velocity is established (Thom, 1972) -

$$u(z-d) = \frac{u_*}{\kappa} \left[\ln \frac{(z-d)}{z_0} - \Psi_M(\zeta) \right] \tag{2.20}$$

where Ψ_M is the integrated form of the stability correction term for momentum, given by Panofsky (Panofsky, 1963) as

$$\Psi_M(\zeta) = \int_0^{z-d/L} \frac{1-\phi_M(\zeta)}{\zeta} \partial \zeta \tag{2.21}$$

and z_0 is the aerodynamic roughness length, the height at which the wind speed becomes zero. It is important to note that z_0 cannot be derived directly, but can be determined from extrapolating the logarithmic wind profile to its zero intercept, or by inference through the canopy height (z_0 is often expressed as approximately as $0.1 \times h_c$, where h_c is canopy height) (Shaw and Pereira, 1982). It therefore follows that z_0 is greater when the underlying surface of the sample

site is tall canopy, such as forest, in comparison to agricultural grassland areas, where h_c may extend for only a few cms.

Similarly, the integration of the expression for the concentration gradient for species χ yields

$$\chi(z-d) = \frac{\chi_*}{\kappa}\left[\ln\frac{(z-d)}{z_0'} - \Psi_H(\zeta)\right] \tag{2.22}$$

where Ψ_H is the integrated form of the stability correction term for heat, z_0' the mean height at which the exchange of the species occurs and χ_* the concentration profile of the species. As previously defined in Section 2.2.2, the flux of a species χ can be expressed as the product of the instantaneous deviation in vertical wind speed and the instantaneous variation in concentration of the species. Thus, substituting $w'\chi'$ with F_χ and rearranging gives -

$$F_\chi = -u_*\chi_* \tag{2.23}$$

Based on this framework, the flux of a species χ can be calculated from one of two methods. If the values for H and u_* are parameterised from gradients, then the gradient Richardson number can be found from Eq.(2.16), and subsequently L can be calculated from Eq.(2.15). The integrated stability correction functions from heat and momentum can then be determined based on each measurement height used. The values for u_* and χ_* in Eq.(2.23) can then be substituted from Eq.(2.20) and (2.22), to give the equation (Sutton *et al.*, 1992) -

$$F_\chi = -u_*\chi_* = -\kappa^2\frac{\partial u}{\partial\left[\ln(z-d) - \Psi_M(\zeta)\right.}\frac{\partial\chi}{\partial\left[\ln(z-d) - \Psi_H(\zeta)\right.} \tag{2.24}$$

Alternatively, if a sonic anemometer using the principles of eddy correlation is used, the values for u_* and H can be calculated directly using Eqs.(2.11). and (2.10) respectively, allowing for direct calculation of L. If $\partial\chi$ is calculated from measurements of the species at separate heights (e.g., z_2 and z_1), Eq.(2.22) can be substituted into Eq.(2.23), to give the "modified aerodynamic gradient method", as developed by Flechard (1998) -

$$F_\chi = -u_*\kappa \frac{\partial_\chi}{\ln\left(\frac{z_2-d}{z_1-d}\right) - \psi_{\mathrm{H}}\left(\frac{z_2-d}{L}\right) + \psi_{\mathrm{H}}\left(\frac{z_1-d}{L}\right)} \tag{2.25}$$

2.3 Considerations for aerodynamic gradient method measurements

2.3.1 The concept of fetch

For eddy covariance, the absolute height (z) at which to sample values for determining flux should be as large as possible, in order to avoid measuring within the roughness sub-layer where corrections for the flux similarity relationship are not as clearly understood, as well as to gain representative measurements of the area studied (Dellwik and Jensen, 2005). The overall height of the surface roughness layer is dependent on the canopy height, which is composed of individual roughness elements. Tall forest canopies therefore induce roughness sublayers that can extend for many tens of metres above the canopy, while grassland areas may have a roughness sub layer that extends only a few centimetres above the surface. Furthermore, different roughness elements have different internal properties - such as apoplast concentrations of ammonium ions - that can affect the deposition and emission rates of trace gases. Fluxes can therefore change substantially as one

area of vegetation is succeeded by another, such as when a forest area gives way to a grassland. New internal boundary layers form above different areas, and so sensors, if to be accurate, must be placed at a height that allows them to measure within an areas internal equilibrium layer.

It therefore follows that to measure an area accurately, the underlying surface area must be homogeneous with regards to its roughness elements. The upwind, horizontal distance between surface areas of differing homogeneity is termed the fetch, (x_F), and it affects the height at which samples should be taken by a factor of 100, so that a maximum sample height should be no more than $x_F/100$ (Monteith and Unsworth, 2013). For example, for a homogeneous forest that encompasses a fetch of 10,000 m upwind of the intended site for sampling, the sample height should be no more than 100 m, while for a homogeneous area of forest that encompasses a fetch of 20,000 m downwind of the sample site, the sample height should not exceed 200 m. This relationship is expressed graphically in Figure (2.2). For a two-point gradient method, the mean height between the two sampling points - for example, between 62 m and 40 m is 51 m - is taken as the sample height in the calculation of fetch.

However, it is important to note that the overall area for which the flux can be considered representative (termed the flux footprint) is dependent also on overall atmospheric stability, and can decrease in unstable conditions or increase in stable conditions (Horst and Weil, 1994).

This can present constraints to many studies of flux profiles, particularly in urban areas or landscapes defined ecologically by their heterogeneous mosaics of multiple patches. Studies have looked into correcting for this layer. For the intended study area at the ATTO site, however, the prevailing landscape ecology is uniformly homogeneous across large horizontal distances with regards to canopy height, allowing for measurements to be taken at large absolute heights.

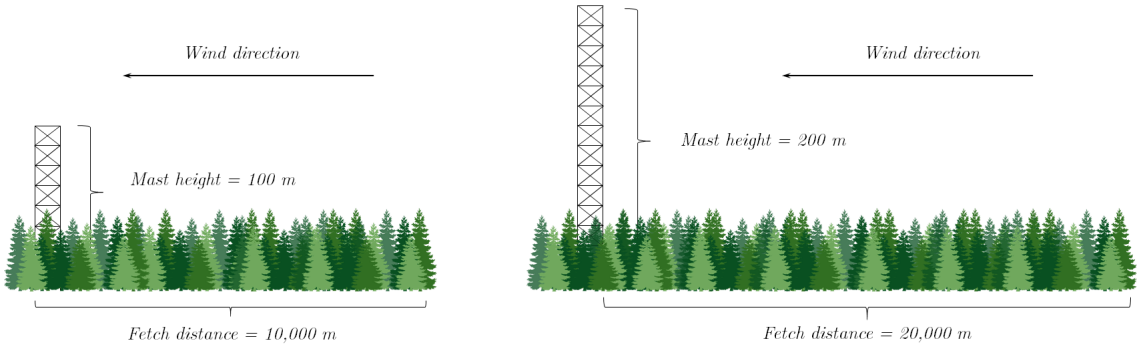

Figure 2.2: Illustration of relation between maximum measurement height on sensor masts with regards to fetch distance

2.3.2 Gas particle interconversion effects on flux measurements

It is important to note that the aerodynamic gradient method strictly applies for chemically inert tracers, and that when using this method to measure the fluxes of reactive species, potential sources or sinks within the atmosphere as a result of gas-particle interconversion (GPIC) must be taken into account. As an example, the NH_4NO_3 – NH_3 – HNO_3 triad previously discussed in 1.2.2 presents difficulties for flux measurements of the precursor trace gases (NH_3 and HNO_3), and the dissociation products of NH_4NO_3 (NH_4^+ and NO_4^-), due to the GPIC reactions occurring within the atmosphere leading to measured fluxes of these species deviating from their true values.

The use of the Damköhler Ratio (D_r) provides an estimate of how such chemical conversions may affect the surface-atmosphere exchange fluxes of the measured tracers, by considering the ratio of the transport time (or turbulent mixing time-scale) t_d to the reaction time of the chemical conversion (or chemical time-scale), t_c (Foken, 2008) –

$$D_{\mathrm{r}} = \frac{t_d}{t_c} \tag{2.26}$$

As an estimate, a value of $D_r > 0.1$ suggests that chemical interactions are affecting the surface-atmosphere exchange of the tracer (Nemitz *et al.*, 2009a).

The effect of GPIC on AGM flux measurements can also be assessed through the use of modelling, as outlined with regards to the NH_4NO_3 – NH_3 – HNO_3 triad by Kramm and Dlugi (1994) and Nemitz and Sutton (2004). Here, the flux profiles ($\mathrm{d}F_i/\mathrm{d}z$) of the precursor gases NH_3 and HNO_3 can be described, while accounting for GPIC, by considering the chemical source terms (Q_i) –

$$\frac{\mathrm{d}F_i}{\mathrm{d}z} = Q_i = \frac{(\chi_{\mathrm{eq},i} - \chi_i)}{t_{\mathrm{c}}} \tag{2.27}$$

with $\chi_{\mathrm{eq},i}$ and χ_i the theoretical concentration of the chemical tracer i and its actual, measured concentration respectively. Chapter 4 considers the concepts described in this section further, considering one particular method – the use of conservative exchange fluxes of total ammonium and total nitrate – to account for the flux divergence which occurs as the result of the application of fertiliser to an agricultural grassland, with focus on the NH_4NO_3 – NH_3 – HNO_3 triad.

2.4 Introduction of correction factors for rough surfaces such as forests

The flux similarity theory developed by Monin and Obukhov took as its study area a flat, smooth grassland site. Subsequent studies that further developed the theory, such as the the sites used by Swinbank and Dyer (1967), were also over

grassland or cropland areas where canopy height was low, and hence where the displacement height and roughness sub layer was limited.

Over areas such as forest, however, the roughness sub layer extends significantly above the canopy, and due to mast height and fetch limitations, most flux measurements above forests occur within the roughness sub layer. Assumptions that underlie the classical AGM cannot be made within the roughness sub layer (Högström, 1996), but the overall flux gradient relationship is still found to hold within the roughness sub layer to a high degree of confidence (Simpson *et al.*, 1998). In order to use the AGM within the roughness sub layer effectively and reliably, modifications may be made to the original theory in order to account for differences in scalar transport between the roughness sub layer and the inertial sub layer.

Work by Garratt (1980) established the concept of introducing roughness sub layer functions to the series of relationships defined by the AGM. These functions attempt to account for the deviations from the flux gradient similarity theory seen in the roughness sub layer, by introducing factors that account for said perturbations in the AGM observed in the roughness sublayer. A number of studies have attempted to formulate a variety of different correction functions for dense canopies such as forest. For example, Mölder *et al.* (1999) developed a semi-empirical correction factor for flux measurements above boreal forest. As Harman and Finnigan (2007) note, however, the majority of these roughness sub layer functions are not reasoned through physical principles and do not take a systemic approach to including the underlying surface properties. In the same study, Harman and Finnigan developed a physically based unified theory, which introduced the concept of vorticity thickness an additional mixing length to the AGM which accounts for the flow within the roughness sublayer to further develop a new form of correction factor.

Chapter 3

Gradient of Aerosols and Gases Online Registration (GRAEGOR)

3.1 Historical methods for determining the flux and concentration of trace gases and reactive aerosols

As the need for measurements of trace gases and their associated reactive particles grew, methods were developed in order to sample selected species both in the gaseous and the particulate phase. Some of the most commonly used methods in the past were based on filtration, whereby a sample of air passing through a selected filter would deposit any entrained particulate phase species upon the filter membrane, or would have its gaseous phase species adsorbed by a sorbent coated filter. As outlined by Ferm (1998), one of the most widespread methods based

upon filtration was the filter pack method (or tandem filter method), where an air sample would first pass through a prefilter which collected the particulate phase of the species, and then onwards to an impregnated filter where the sorption solution would adsorb the gas phase of the species. However, as mentioned by Ferm within the same paper, this method was hampered by gas-particle interactions that would occur on the filter membrane during sampling. Studies by Klockow *et al.* (1979) and Appel *et al.* (1980) had shown the significant presence of these interaction artefacts on filter membranes used in sampling. Furthermore, the limitation of the filter pack method prevented studying the concentrations of a species when its gas and particle phases are in equilibrium with each other, an important consideration in the measurement of ammonium nitrate particulate. As Chow (1995) also mentioned in their study of the methods available at the time for measuring trace gases and reactive aerosols, filter packs were characterised by their long sampling times (between 5 24 hours), poor calibration, and intensive labour management. Importantly, a major concern raised by Chow was the interaction between the gas phase and particulate phase species that would occur in filter packs. Measured gas concentrations, particularly of semi volatile species, would routinely be underestimated due to this effect.

The denuder tube sampler was developed in response to demands for a method that could isolate specific water soluble gas species for measurement. As outlined by Eatough *et al.* (1985) in a study on HNO_3 measurements using diffusion denuders, the denuder tube sampler works by adsorbing, and then chemically fixing, selected chemical species in the gas phase using a variety of chemical coatings on the walls of a denuder tube. Coatings are paired to the chemical species that one wishes to study Na_2CO_3 is used to collect HNO_3 (Ferm, 1986), while sodium fluoride is used to collect HCl (Dimmock and Marshall, 1987).

Significant disadvantages to the denuder tube sampler present themselves, however. Labour intensive gas extraction and re-coating procedures are required, and

due to each chemical coat being paired to only one chemical species, several denuder tubes are required in order to sample a wide range of gaseous species in one air sample simultaneously. In addition, sampling times can be large, ranging from 18 to 24 hours.

Instrumentation which could measure the concentration of a variety of both gaseous and aerosol species concurrently, without interference by the measuring medium or with other species, and which had a low sampling time in order to accurately determine the overall concentration gradient, was required in order to avoid the disadvantages posed by contemporary measurement methods.

3.2 The Wet Annular Rotating Denuder (WRD)

One such instrument that meets this criteria for measuring gaseous species is the Wet Annular Rotating Denuder (hereafter referred to as the WRD). The WRD was developed by the Netherlands Energy Research Foundation in the late 1980s. As described by Keuken *et al.* (1988), the WRD consists of two concentric glass tubes, one of which has a smaller diameter than the other. The narrower of the two tubes is placed within the wider tube to create the overall denuder. An aqueous solution is then pumped into the space between the two annular tubes (the annulus), thus coating both tube walls. The entire denuder is then rotated around its axis using a belt system, allowing for the entire annulus to be coated, during which air is then drawn through the annulus via a pump. Any gas species present within the sample then adsorbs onto the aqueous solution, and is siphoned off for sampling, which was at the time of creation done offline and through conductometry.

In Keuken *et al.* study, two WRDs were used simultaneously, with one WRD

having an aqueous solution consisting of a sorbent of formaldehyde and p-ydroxyphenylacetic acid in order to collect SO_2 and H_2O_2, and the other WRD having an aqueous solution containing a formic acid buffer to collect NH_3, HNO_3 and HCl. This allowed for multiple species to be measured concurrently by one WRD, overcoming one of the main limitations of previous denuder sampling techniques. The high sampling flow rate (of 32 $L\,min^{-1}$) allowed for relatively fast sampling periods compared to previous collection methods, and the final results gathered by Keuken suggested that the WRD was capable of low detection limits (0.2 to 0.5 μg for NH_3, HNO_3 and SO_2). One of the main difficulties encountered, however, was resolving issues with the gas phase equilibrium reaction between ammonium, nitric acid and ammonia nitrate, as well as issues concerning the measurement of sticky gases (such as HONO and HNO_3) that remained adhered to the denuder absorption solution. Furthermore, cleaning of the WRD was required after each sampling period via injection of cleaning solution.

Wyers *et al.* (1993) further refined the WRD by adding the capacity to measure NH_3 online using conductometry, by installing a sodium hydroxide flow which combined with the WRD eluent allowing for IC measurements to occur.

3.3 The Steam Jet Aerosol Collector (SJAC)

While trace gas species can be measured using a WRD, aerosols cannot. Thus, in order to determine both the aerosol and gaseous species in the atmosphere, additional instrumentation in conjunction with the WRD is required. One such instrument is the Steam Jet Aerosol Collector (SJAC), as developed by Khlystov *et al.* (1995).

The air sample to be analysed is first stripped of trace gases by a WRD. The sample is then fed into a mixing reservoir, where it is rapidly mixed with steam

provided by a heating element fed with a supply of double deionized water (DDI). This causes any aerosol particles contained within the air sample to become supersaturated and undergo deliquescence, forming droplets of at least 1 μm in diameter. Due to the high relative humidity in the mixing reservoir, droplets grow quickly, thus ensuring maximum possible deliquescence for nearly all aerosol particles present within the sample. The droplets are then collected by an arrangement of cyclones connected in series, and can then be collected using a peristaltic pump for either online or offline analysis by either ion chromatography (IC) or flow injection analysis (FIA). A condenser is also connected to the cyclones in order to reduce the amount of steam entering the pump system. The steam for the system is injected through what is termed the critical orifice at a rate of 5 $\mathrm{L\,min^{-1}}$. The high pressure injection, combined with the fixed volume of the SJAC, increases the temperature within the system allowing for the steam to remain above 100 °C. The high flow rate also insures that the steam is injected in the form of a fast jet, ensuring high turbulence and thus rapid mixing.

The Khlystov *et al.* study also investigated the efficiency of the SJAC for collection of total aerosol mass in comparison with filter packs. It was found that, with two cyclones present, the total collection efficiency for aerosol mass was close to 99.8% of that for filter packs. Additionally, the SJAC was tested for sampling efficiency and aerosol number collection in different aerosol size bands using a Differential Mobility Particle Sizer connected to the outlet of one of the cyclones. It was found that 99% of total aerosol particles within the 0.0019 to 0.886 μm diameter range were sampled with a steam injection rate of 3.5 g of water $\mathrm{min^{-1}}$.

This observation was confirmed by Slanina *et al.* (2001) during an inter-comparison study between the SJAC and other aerosol measuring techniques such as filter packs. Using a cloud chamber to generate a series of standardised aerosol mixtures, it was found that the SJAC had very good agreement in aerosol mass

with the filter packs used. It was also observed that the SJAC overcame some of the key limitations that were present in filter packs when used in the field, such as the ability to maintain semi volatile species, shorter sampling times, and the ability to measure aerosol concentrations for a variety of different chemical species online and continuously. Slanina *et al.* concluded that the SJAC is a reliable instrument that, in combination with online techniques such as IC and FIA, is capable of taking accurate measurements of aerosol concentrations for a variety of species over short periods of time. Additionally, with a detection limit of 0.02 $\mu g\,m^{-3}$ for ammonium and nitrate aerosols, the SJAC was suggested by Slanina *et al.* as a measurement technique that is capable of measuring ammonium and nitrate aerosols even in areas where the overall background concentrations of these species is low.

3.4 Overview of GRAEGOR instrument

The development of the WRD and SJAC enabled researchers to take measurements of the concentration of species in the gaseous and aerosol phases at high temporal resolution and at low detection limits. By combining these instruments into one comprehensive measurement tool, the concentration of both gas and aerosol phase particles could be determined at one measurement height.

This combination of both the WRD and SJAC as one combined instrument was first established by Trebs *et al.* (2004) for use in a campaign to measure the gaseous and aerosol phase concentrations of a variety of species on a pasture site in Northern Brazil. In this build, air is pumped through the horizontally aligned WRD, where soluble trace gas species are scavenged within the $NaHCO_3$ sorbent, and subsequently siphoned to a dedicated gas sample reservoir. From there, it is then analysed by IC and FIA. The trace gas-free air then leaves the WRD, and is

pumped to the SJAC mixing reservoir. After supersaturation and deliquescence, any aerosol particles gathered in the SJAC cyclone leave via the cyclone effluent to the dedicated aerosol sample reservoir for further analysis by IC and FIA.

Results from the study, conducted over a period 60 days covering the dry, transitional and wet seasons within the Inter Tropical Convergence Zone, arrived at a limit of detection (LOD) value of under 0.015 ppb for acidic trace gases and aerosol anions and under 0.118 for NH_3 and aerosol NH_4^+ (Trebs *et al.*, 2004), suggesting a high tolerance, making the combined WRD/SJAC particularly useful for measuring concentrations of species where the overall background concentration is low.

By using one pair of these instruments set at different measurement heights, the concentration gradient of a variety of different chemical species in either the gas or aerosol phase could be determined, and thus from that the flux as described in Chapter 2. This two-point system, using a combined SJAC/WRD system placed at two different measurement heights, was also used by Nemitz *et al.* (2004a) in a study above a Dutch heathland to determine the fluxes of the gaseous species NH_3, HNO_3, HONO, HCl and SO_2.

This two-point gradient method using two SJAC/WRD instruments was developed into the Gradient of Aerosols and Gases Online Registration (GRAEGOR), first described by Thomas *et al.* (2009) and based on the prototypes as developed by Nemitz *et al.* and Trebs *et al.* with alterations. Using the GRAEGOR, full flux profiles calculated using the aerodynamic gradient method and within a 1 hour time period can be developed for the gases HCl, HONO, HNO_3, SO_2 and NH_3 and their water-soluble aerosol counterparts Cl^-, NO_2^-, NO_3^-, SO_4^{2-} and NH_4^+, all in real time and with sufficient precision to allow calculation of surface atmosphere exchange fluxes under typical ambient concentrations (Thomas *et al.*, 2009).

A full schematic for the GRAEGOR is show in Fig. (3.1) , as taken from Thomas *et al.*. The GRAEGOR consists of an air pump, two sample boxes, a detector box, and a computer which regulates the program controlling the valve and syringe systems within the detector box. Each sample box contains a horizontally-aligned WRD and a SJAC, both of which are fed with a sorbent solution of DDI with 0.6 mL of H_2O_2 per 10 L DDI used as a biocide. The storage for this sorbent solution is placed above the sample boxes. Air is drawn first through the WRD at a rate of 16.7 $\mathrm{L\,min^{-1}}$ as regulated by the air pump. A high density polyethylene inlet (0.3 m length, and 1/3″ diameter) with a HDPE filter is placed at the inlet of the WRD where air is drawn, which is used to minimise the loss of HNO_3 and NH_3, as well as to ensure a particle cutoff diameter of 0.2 nm. Trace gases are scavenged by both sample boxes WRDs, and siphoned as effluent which is directed to the detector box. The trace gas free air then enters the mixing reservoir of the SJAC, where it undergoes supersaturation from steam generated in the associated steam generator. In the GRAEGOR, the steam generator is fed DDI at 1.1 $\mathrm{mL\,min^{-1}}$ and heated to 116 °C. The GRAEGOR has a modified SJAC system, where three sequential spirals are placed after the mixing reservoir and prior to the cyclone for droplet accumulation, in order to increase particle capture efficiency. The SJAC effluent for both sample boxes is then siphoned to the detector box for IC and FIA analysis.

The detector box itself contains an IC detection unit, a FIA system, and a central manifold system coordinated by solenoid valves that directs flow from the series of syringes arrayed at the front of the detector box system. The syringes system consists of a series of 10 mL syringes that collect effluent from both sample boxes, and directs them to the central manifold at a set flow rate of 0.333 $\mathrm{mL\,min^{-1}}$. Another series of 1 mL syringes directs the flow of reagents at a rate of 0.033 $\mathrm{mL\,min^{-1}}$. The reagents for the GRAEGOR are DDI, sodium hydroxide (0.1 M NaOH) and sodium bromide (NaBr, 500 ppb Br^-). The valve system operates

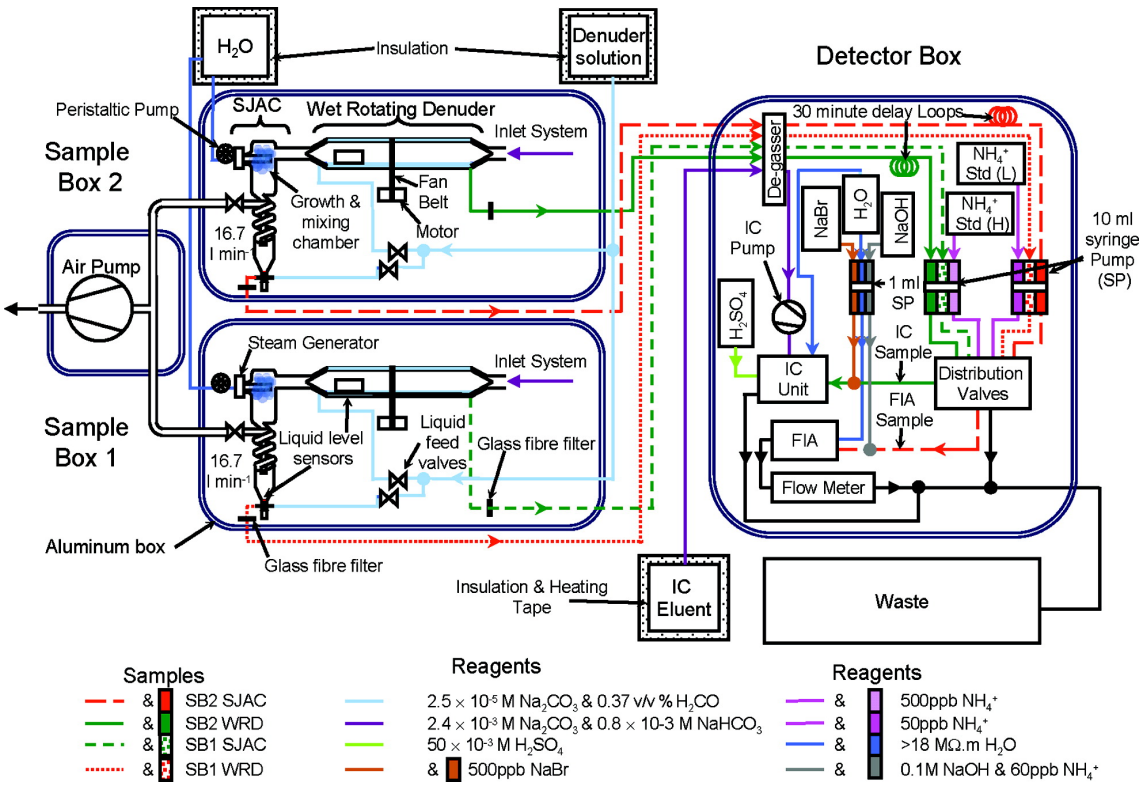

Figure 3.1: Schematic of the Gradient of Aerosols and Gases Online Registration. Reproduced from Thomas *et al.* (2009), with permission.

so that during each 15 minute cycle, SJAC and WAD effluents from both sample boxes are either being loaded in a pre-concentration system prior to analysis by IC, undergoing IC or FIA analysis, or being diverted to the waste flow.

3.4.1 Ammonia Flow Injection Analysis (AMFIA)

In order to determine the concentration of NH_3 gas and NH_4^+ aerosol particles, the GRAEGOR uses a FIA system termed Ammonia Flow Injection Analysis (or AMFIA). The principle of the AMFIA is based on the selective diffusion of NH_3 across a membrane at high pH, with subsequent analysis of NH_4^+ at reduced pH by conductivity (Sutton *et al.*, 2001). The AMFIA itself consists of a sample block and a detector block. A liquid sample enters the sample block,

and ammonia within the liquid is absorbed into an acid buffer through a gas permeable membrane. The reduced acid buffer, also termed the stripping solution, is then injected with sodium hydroxide, which subsequently raises the pH of the stripping solution (van Son *et al.*, 1983). The increase in pH causes the release of adsorbed NH_3, which passes through a second membrane in the detector block to be injected into a stream of pure deionized water whose flow is counter to that of the injected NH_3 sample. The subsequent solution is then analysed, with NH_4^+ concentration determined by conductivity (Norman *et al.*, 2009).

3.4.2 Ion Chromatography (IC) and analysis of flux

The liquid concentrations of the anions Cl^-, NO_2^-, NO_3^- and SO_4^{2-} are determined through IC. The IC unit used is a Metrohm 761 Compact Analyser with suppressor functionality, and the analytical column used is a Dionex AS12 with two associated Dionex TAC LP-1 pre-concentrator columns. The overall operation of the system is controlled using the Metrohm ICNet 2.3 software. The eluent used in the IC analytical column is composed of 30 mL of 1.0 M Na_2CO_3 and 8 mL of 1.0 M $NaHCO_3$ in 10 L of DDI.

During each 15 minute cycle, a sample of volume 4.56 mL is injected by the syringe system into the pre-concentrator column, and is backwashed with the Na_2CO_3 / $NaHCO_3$ eluent. An internal bromide standard of known concentration (consisting of the NaBr 500 ppb Br^- reagent previously mentioned) is also injected into the pre-concentrator along with the sample and eluent, allowing for the concentration of other detected anions to be determined through reference. With the proceeding 15 minute cycle, the overall solution consisting of sample, eluent and Br^- standard in the pre-concentrator column is injected into the IC analytical column, from where it enters the IC detector. With a set baseline conductivity controlled by the eluent and moderated by the use of chemical suppression using

H_2SO_4, and a reference conductivity peak provided by the Br^- standard, the conductivity of the anions Cl^-, NO_2^-, NO_3^- and SO_4^{2-} can be determined. The resulting chromatograms can then be analysed, with the concentration of each anion derived through integration of the areas under associated peaks. After analysis which is conducted over 15 minutes - the solution exits the IC detector as waste, and a new pre-concentrator sample solution is injected into the analytical column for analysis. In this manner, and with knowledge of whether the injected sample was from the WRD or SJAC, the concentrations of HCl, HONO, HNO_3 SO_2, Cl^-, NO_2^-, NO_3^- and SO_4^{2-}, at each sample box height for aerosol and gaseous species can be determined every hour, to give a total flux for gas and aerosol phase with one hour resolution.

3.5 Error analysis and validation of GRAEGOR

3.5.1 Suitability of GRAEGOR to measure concentrations and fluxes of trace gases and aerosols

Both Thomas *et al.* (2009) and Wolff *et al.* (2010a) have extensively tested the suitability of the GRAEGOR to resolve the vertical concentration gradients required in measuring fluxes. As outlined by Thomas *et al.* (2009), conducting side-by-side measurements (i.e., both sample boxes placed at one height and measuring concentrations concurrently) allows for the determination through linear regression analysis of the deviation in concentration measurements between sample boxes. From this, the resolvable vertical concentration gradients can be determined, with the first tests conducted by Thomas *et al.* (2009) suggesting that the GRAEGOR was highly suitable for resolving concentration gradients due to the high precision of the instrument. Wolff *et al.* (2010a) elaborates further on the

suitability of the GRAEGOR to resolve vertical concentration gradients, outlining the calculation of errors in concentration and flux measurements through Gaussian error propagation. From this, the minimum detectable fluxes of the trace gas and aerosol species measured can be determined, which is subsequently used as a data filter to eliminate measurements which do not meet the criteria for resolving vertical concentration gradients. The methods outlined by both Thomas *et al.* (2009) and Wolff *et al.* (2010a) are used in Chapters 4 and 5 to resolve the vertical concentration gradients measured at both field sites.

Artefacts in sampling can introduce errors in vertical concentration gradients. Pertinently, with regard to the GRAEGOR, the two trace gases that are impacted by artefact formation in WRDs are HONO and HNO_3. Under high NO and SO_2 ambient concentrations, HONO can form in WRDs, leading to artefact errors which affect the resolution of vertical concentration gradients. However, as will be outlined in both Chapter 4 and 5 of this thesis, this HONO artefact can be determined by the use of modelling, provided ambient concentrations of NO and SO_2 are available. For HNO_3, dinitrogen pentoxide (N_2O_5) can undergo an hydrolysis reaction on the surface of WRDs to form HNO_3, creating a positive artefact which introduces errors in the measured fluxes of HNO_3. This artefact formation occurs strictly at night due to the chemistry as discussed in Section 1.2.2. Measurements of the concentrations and subsequently fluxes of HNO_3 during the day are therefore unaffected.

3.5.2 Validation of GRAEGOR

Since its development by Thomas *et al.* (2009), the GRAEGOR has been involved in a number of intercomparison and validation campaigns. von Bobrutzki *et al.* (2010) outlines a campaign in which eleven measurement techniques of ammonia were compared. One of the instruments used was the GRAEGOR.

The average correlation between the techniques, which included quantum cascade laser spectroscopy, photo-acoustic spectrometers, and chemical ionisation mass spectrometers, was reported as $R^2 > 0.84$. The authors in particular highlighted the good performance of wet chemistry instruments, included the GRAEGOR, noting their good long term stability in measurements. The Exchange Process in Mountainous Regions, or EGER, campaign (Foken *et al.*, 2012), employed a GRAEGOR instrument in measuring reactive nitrogen gases, noting the capacity of the instrument to resolve vertical concentration gradients after thorough characterisation.

Chapter 4

Surfaceatmosphere exchange of inorganic watersoluble gases and associated ions in bulk aerosol above agricultural grassland pre and postfertilisation

This chapter is based on a research paper published in Atmospheric Chemistry and Physics (Ramsay, R., Di Marco, C. F., Heal, M. R., Twigg, M. M., Cowan, N., Jones, M. R., Leeson, S. R., Bloss, W. J., Kramer, L. J., Crilley, L., Srgel, M., Andreae, M. and Nemitz, E.: Surfaceatmosphere exchange of inorganic water-soluble gases and associated ions in bulk aerosol above agricultural grassland pre- and postfertilisation, Atmos. Chem. Phys., 18(23), 1695316978, doi:10.5194/acp-18-16953-2018, 2018). I took the GRAEGOR measurements, processed the data, and interpreted the results with help from Dr. C.F. Di Marco, Dr. E. Nemitz and Prof. M. Heal. LOPAP measurements of HONO were taken by Dr. C.F. Di Marco, Dr. M.M. Twigg, Dr. L.J. Kramer, and Dr. J. Crilley. QCL measurements of NH_3 *were taken by Dr. N. Cowan. I wrote the manuscript, with subsequent contributions from all co-authors.*

4.1 Introduction

As the demand for food production grows in line with an increasing global population, so too does the development of intensive agricultural practices. These can have deleterious impacts on the environment and human health (Godfray *et al.*, 2010; Foley *et al.*, 2011),particularly through the emission of trace gases and the formation of airborne particles generated by their reactive chemistry. It is therefore important that measurements be made of the surface–atmosphere exchange of trace gases and associated aerosol compounds to quantify the emissions from – and deposition to – land used for agriculture, in order to quantify the impact of agricultural activities on the atmosphere and environment. Such studies can inform the development of abatement strategies and legislation designed to control emissions from agricultural activities. This also provides important process understanding to represent better the dry deposition processes in chemistry and transport models used to predict air quality and climate change.

Of particular importance to the surface–atmosphere exchange over agricultural land is the formation of atmospheric reactive nitrogen (N_r) compounds. These include the gases ammonia (NH_3) and nitrous acid (HONO), the latter of which, together with nitric acid (HNO_3),also derives from the oxidation of nitrogen oxides (NO_x) emitted by combustion sources. NH_3 and HNO_3, and their aerosol equivalents NH_4^+ and NO_3^-, are the primary contributors to atmospheric reactive nitrogen (N_r) dry deposition (Andersen and Hovmand, 1999). The majority of NH_3 emissions originate from agricultural sources, either from direct point sources from the application of N-containing fertilisers or from long-term sources from livestock (Behera *et al.*, 2013). The use of urea as a fertiliser is associated with particularly large losses of NH_3 after application, due to the action of the urease enzyme present in soil, which leads to NH_3 volatilisation (Suter *et al.*, 2013). Ferm (1998) estimate that fertiliser losses as NH_3 average 14 % of the N applied.

Nitrogen losses from animal waste present on grassland used for sheep grazing have also been observed (Cowan *et al.*, 2015). While NH_3 is predominantly deposited close to the source, resulting NH_4^+ aerosol can be transported over large distances.

HNO_3 is primarily formed from the oxidation of nitrogen oxides (NO_x), which are principally anthropogenic in origin but also have a soil biogenic origin (Kim, 2013). HNO_3 is extremely water soluble and is rapidly removed from the atmosphere through deposition or by gas–particle interactions, leading to a high deposition velocity. The gas-phase equilibrium reaction of HNO_3 with NH_3, which is dependent upon temperature and relative humidity (RH) (Mozurkewich, 1993; Robertson *et al.*, 2013), gives rise to ammonium nitrate (4.1).

$$NH_3 + HNO_3 \rightleftharpoons NH_4NO_3 \tag{4.1}$$

The associated condensed-phase components of ammonium (NH_4^+) and nitrate (NO_3^-) exist in equilibrium (as ammonium nitrate (NH_4NO_3)) with NH_3 and HNO_3. Higher temperatures and lower humidity favour the decomposition of NH_4NO_3. The emission of these N_r species and their subsequent deposition by washout (wet deposition) or uptake on the surface (dry deposition) have high spatial and temporal variability and can have critical impacts on terrestrial and aquatic ecosystems, especially those which are nitrogen limited (Galloway *et al.*, 2003; Fowler *et al.*, 2013).

The interaction of NH_3 with HNO_3 can also lead to overestimation of the HNO_3 deposition rate, as the additional sink for HNO_3 deposition provided for by the reaction violates the maximum theoretical deposition rate modelled on a zero surface resistance model for HNO_3. The dissociation of NH_4NO_3 over vegetation can induce an opposite effect, with apparent emissions of HNO_3 occurring with associated high deposition rates for NO_3^- and NH_4^+ (Nemitz and Sutton, 2004).

The sums of the total ammonium (tot-$NH_4^+ = NH_3 + NH_4^+$) and of total nitrate (tot$-NO_3^- = HNO_3 + NO_3^-$), however, are conservative quantities (Kramm and Dlugi, 1994), and their use in the measurement of exchange fluxes can help to account for the $NH_3 - HNO_3 - NH_4NO_3$ triad on overall deposition rates.

HONO is similar to HNO_3 in that it can derive from oxidation of NO_x precursors. Although it can be formed homogeneously in the atmosphere by the reaction of the hydroxyl radical OH with NO (4.2) (Pagsberg *et al.*, 1997), the rate of this reaction is too slow to account for measured concentrations of HONO. Similarly, the heterogeneous reaction involving the reaction of NO_2 with H_2O on terrestrial surfaces, while potentially a contributory source to atmospheric HONO, has also been found to be too slow to account for measured concentrations (Kleffmann, 2007). HONO is photolysed during daytime, being a primary source of OH radicals depending on the source and sink mechanisms that govern its abundance (Sörgel *et al.*, 2015). However, a growing number of field measurements of non-zero HONO concentrations during the day points to the presence of daytime sources (Acker *et al.*, 2006), including the emissions of HONO from soils (Su *et al.*, 2011; Oswald *et al.*, 2013; Scharko *et al.*, 2015).

$$NO + OH \longrightarrow HONO \tag{4.2}$$

As the primary basic gas in the atmosphere, NH_3 also reacts with trace acidic gases, such as hydrogen chloride (HCl) and sulfuric acid (H_2SO_4). The products of these reactions give rise to the aerosols ammonium chloride (NH_4Cl) and ammonium sulfate ($(NH_4)_2SO_4$), which along with NH_4NO_3 act as scattering aerosols that alter the Earth's total albedo and contribute significantly to regional and global climate (Fiore et al., 2015). The ammonium salts make a significant contribution to inhalable particulate matter (PM) associated with human health impacts, with NH_4NO_3 often dominating PM pollution events in northern Europe

(Vieno *et al.*, 2014). Ammonium sulfate is particularly long lived, and its transport and subsequent deposition to surfaces such as agricultural soils can affect plant health (Van der Eerden *et al.*, 1992) and lower soil pH (Elliott *et al.*, 2008).

The dry deposition of the acidic gases themselves can also induce soil acidification, which on agricultural soils can limit the growth of crops through perturbation of the uptake of nutrients. HCl, like HNO_3, is highly water soluble; is deposited quickly to the surface; and consequently has a high deposition velocity. It can be formed by the reaction of other acidic gases, such as HNO_3 and SO_2, with sodium chloride found in sea spray (Pio and Harrison, 1987) SO_2, which is the precursor for H_2SO_4 in the atmosphere and is primarily anthropogenic in origin, being emitted via the burning of fossil fuels that contain sulfur.

Measurements of trace gases and associated aerosols are, however, restricted by the availability of appropriate instrumentation, complications in their measurement due to their reactivity and water solubility, and the potential interference of gas–particle interactions.

Techniques to measure concentrations and fluxes of these trace gas and associated aerosol components require multispecies quantification, low detection limits and fast temporal resolution. Eddy covariance, the most direct micrometeorological technique for the measurement of trace gas fluxes, requires fast-response sensors that are not available for some species (such as HNO_3) or are limited by the time-response and potential for chemical interferences of the inlet (Neuman *et al.*, 1999). While eddy covariance has been used to measure NH_3 concentrations using laser absorption spectroscopy, such as through the use of quantum cascade lasers (QCLs) (Famulari *et al.*, 2004; Zöll *et al.*, 2016), inter-comparisons with more established techniques are still lacking.

The aerodynamic gradient method (AGM) derives fluxes of a tracer from its vertical concentration gradient, which can be obtained from concentration measurements at two or more heights, avoiding the requirement for fast response measurement. Developments in automated wet-chemistry instrumentation have in turn led to the development of the Gradient of Aerosols and Gases Online Registration (GRAEGOR), a two-point gradient system that measures the concentrations of HCl, HONO, HNO_3, SO_2 and NH_3 as well as their associated aerosol counterparts Cl^-, NO_2^-, NO_3^-, SO_4^{2-} and NH_4^+ (Thomas *et al.*, 2009). One of the advantages of the modified aerodynamic gradient method is the ability to determine the deposition velocities (V_d) of chemical tracers, provided the flux and concentration at a reference height have been calculated. With the use of the GRAEGOR, which takes measurements of tracers at two heights over 1 h, high-resolution timescale measurements of deposition velocities can be acquired.

Other wet-chemistry instruments have also been developed to measure individual species at one height, such as the Long Path Absorption Photometer (LOPAP), which measures concentrations of HONO with fewer artefacts than the GRAEGOR (Heland et al., 2001). A comparison study between LOPAP HONO measurements and the Gas and Aerosol Collector (GAC) – an instrument which uses similar measurement techniques to the GRAEGOR – was conducted by (Dong *et al.*, 2012), but there has not yet been a published comparison between the LOPAP and GRAEGOR in measurements of HONO. Similarly, measurements of trace gases and aerosols above agricultural grassland using the GRAEGOR are limited, and previous studies above these land systems have been restricted to measurements of a limited number of species within a limited particle size range.

The aim of this study was to use the GRAEGOR to measure concentrations and fluxes of the trace gases HCl, HONO, HNO_3, SO_2 and NH_3 as well as their water-soluble aerosol counterparts Cl^-, NO_2^-, NO_3^-, SO_4^{2-} and NH_4^+ over agricultural grassland in Scotland during a period in early summer (May–June 2016) that

included a fertilisation event using urea pellets. The possible formation of NH_4NO_3 postfertilisation, a link between aerosol deposition velocity and size (specifically, a proxy for size based on the $PM_{2.5}/PM_{10}$ ratio from measurements nearby), and the potential ground source formation of HONO are discussed. A further aim of this study was to undertake inter-comparisons between the measurements of HONO by the GRAEGOR and two LOPAP instruments and between measurements of NH_3 recorded by a parallel quantum-cascade-laser eddy covariance system.

4.2 Methodology

4.2.1 Easter Bush site description

The campaign was conducted during the late spring–summer 2016 (21 May–24 June) at the Easter Bush measurement site (3°12′ W, 55°52′ N; 190 m above sea level), located 10 km south of Edinburgh, UK. Measurements were made at a 3 m tower situated on the boundary of two intensively managed grassland fields (hereafter referred to as the north and south field) of 16 ha total area, composed principally of *Lolium perenne* (perennial ryegrass) (Fig. 4.1). Due to the presence of the Pentland Hills close by to the west, local wind direction is channelled such that SW winds – the predominant wind direction at the site – yield flux footprints over the south field, while NE winds produce flux footprints over the north field.

Both fields are used for year-round (although not continuous) sheep grazing, in rotation with adjacent fields, but the south field also typically has an annual cutting for silage. Mineral fertilisation is carried out twice a year on both fields. During this study, fertilisation of the two fields occurred between 08:00 and 09:00 on 13 June, using urea mineral fertiliser at a rate of 69.9 kg Nitrogen ha^{-1}. In

preparation for this application, sheep that had been present in the fields since April were removed from the south field on 2 June and removed from the north field on 9 June. Sheep were reintroduced to the north field on 21 June.

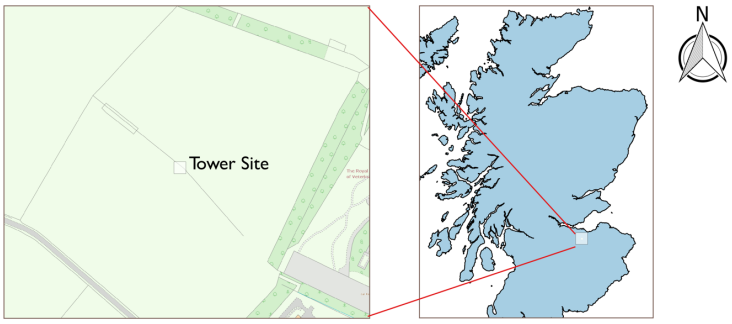

Figure 4.1: Location of the Bush Tower site (3°12′ W, 55°52′ N) in relation to surrounding agricultural land and within Scotland, UK.

Over the years the Easter Bush field site has hosted several long-term measurements of CO_2, CH_4 and NO_2 and has participated in a number of international projects, such as GRAMINAE (GRassland AMmonia INteractions Across Europe) (Sutton *et al.*, 2009), Greengrass (Soussana *et al.*, 2007) and NitroEurope (Sutton *et al.*, 2007). It has also supported several individual campaigns of trace gas measurements (Di Marco *et al.*, 2004; Famulari *et al.*, 2004; Jones *et al.*, 2017). In particular, fluxes of NH_3 were measured over an 18-month period (Milford *et al.*, 2001) and the GRAEGOR was operated during a period of manure application (Twigg *et al.*, 2011).

4.2.2 Instrumentation

Gradient of Aerosols and Gases Online Registration

The GRAEGOR (Energy Research Centre of the Netherlands) is a wet-chemistry instrument that measures the concentrations of reactive trace gases (HCl, HONO,

HNO_3, SO_2 and NH_3) and water-soluble aerosols (Cl^-, NO_2^-, NO_3^-, SO_4^{2-} and NH_4^+) continuously, semi-autonomously and with online analysis at hourly resolution (Thomas *et al.*, 2009; Wolff *et al.*, 2010b). The instrument consists of two sampling boxes placed at two heights (during this campaign, $z_1 = 0.6\,\mathrm{m}$, $z_2 = 2.4\,\mathrm{m}$), from which concentration gradients and hence fluxes can be derived.

Each sample box contains a horizontal wet rotating annular denuder (WRD) (Keuken *et al.*, 1988) and a steam jet aerosol collector (SJAC) (Khlystov *et al.*, 1995; Slanina *et al.*, 2001) connected in series. Air is drawn through each sample box simultaneously by an air pump at a rate of 16.7 $\mathrm{L\,min^{-1}}$, passing first through the WRD, which is continuously coated with a feeding solution of double-deionised water (DDI) of 18.2 MΩ resistance. Trace gases within the laminar airflow are absorbed into the sorption solution which is then fed from the sample box to a detection unit located at ground level. The trace-gas-free air then passes through the SJAC, where particles within the airflow are mixed with steam generated from the DDI water feeding solution, precipitating a supersaturation event causing the water-soluble particles to grow into droplets. The enlarged droplets are separated out of the air stream by a cyclone and fed as a liquid sample to the detection unit. Liquid samples from the SJAC and WRD of each sample box are analysed for NH_3/NH_4^+ using flow injection analysis (FIA) (Wyers *et al.*, 1993; Norman *et al.*, 2009). An ion chromatography (IC) unit equipped with a Dionex AS12 column quantifies the concentration of $HONO/NO_2^-$, HNO_3/NO_3^- and SO_2/SO_4^{2-} based on the measured conductivity of the respective anions within the liquid sample compared to a reference standard of 50 ppb Br^- added to the sample solution. Analysis by FIA and IC is carried out over 15 min, and using a flow control scheme a half-hourly averaged concentration of trace gases and water-soluble aerosols is generated for each height every hour.

A high-density polyethylene (HDPE) tube (0.3 m length, and 1/3″ outer diameter) with a HDPE filter is placed at the inlet of the WRD in order to minimise the loss

of HNO_3 and NH_3 and to ensure a particle diameter cutoff of 0.2 nm. A biocide of 0.6 mL of hydrogen peroxide (30 %) is added to every 1 L of the DDI water feeding solution to prevent biological contamination in the WRD of each sample box. Airflow is controlled using a critical orifice downstream of the SJAC.

Autonomous calibration of the FIA system was carried out 24 h after the beginning of the campaign and every 72 h thereafter, giving a total of five internal calibrations of this system. Calibration was conducted using three liquid NH_4^+ standards of 0, 50 and 500 ppb concentration. The IC unit is continuously checked for analytical performance by the addition of a liquid Br^- internal standard (50 ppb concentration) to each column injection. Calibration of the IC unit was conducted twice during the campaign (23 May and 28 June, prior to and after the campaign, respectively) using a mixed ionic liquid standard consisting of 25 ppb SO_4^{2-}, 20 ppb NO_3^- and 20 ppb Cl^-.

Measurements of the airflow into the sample boxes were conducted using an independent device (TSI Mass Flowmeter 4140) once every fortnight during the campaign. Additional checks of the field performance of the instrument included daily checks of the WRD tubes and sample box air inlets for signs of visible contamination.

The GRAEGOR sampling boxes have very short inlets with no size selection. Consequently, the aerosol concentration reflects water-soluble total suspended particles (TSP). It detects any compound that dissociates to form the measured ions and therefore has a number of artefacts. These include interferences in HONO measurements through NO_2, particularly during periods of high SO_2 concentrations (Spindler *et al.*, 2003); the inclusion of dinitrogen pentoxide (N_2O_5) concentrations in measurements of HNO_3 during the nighttime measurement periods, though the magnitude of this unclear in rural environments (Phillips

et al., 2013); and the potential for organic chloride compounds to be included in measurements of overall Cl^- aerosol (Nemitz *et al.*, 2000b).

The GRAEGOR has been demonstrated to be capable of measuring fluxes in a number of studies both in identical form to the one used here (Wolff *et al.*, 2010b; Twigg *et al.*, 2011) and in related variants (Nemitz *et al.*, 2004a; Rumsey and Walker, 2016). Ammonia-specific instruments based on the same technology (AMANDA, GRAHAM, ECN, Petten, the Netherlands) (Wyers *et al.*, 1993) represent the most commonly used instrument for the automated measurement of ammonia fluxes.

Supplementary measurements

Vertical profiles of temperature were measured at the tower using fine-thread, custom-made, shielded thermocouples set at the same heights as the GRAEGOR sample boxes. Located 0.4 m from the tower, an eddy covariance system (Gill Anemometer R01012 with LI-COR-7000) at a height of 2.6 m measured three-dimensional wind speed, sensible heat flux (H), frictional velocity (u_*) and wind direction. Ongoing, long-term measurements of relative humidity (Vaisala 50/Y Humitter), global radiation (Skye Instruments SKS 110 pyranometer) and total rainfall (Campbell Scientific ARG110 tipping bucket rain gauge) were also available at the site for the campaign period. Measurements of HONO taken by a LOPAP (QUMA Elektronik & Analytik, Wuppertal, Germany) and NH_3 measurements taken by a quantum cascade laser (Aerodyne Research Inc., Billerica, USA) during the campaign period were used for comparison studies with GRAEGOR measurements. Measurements of NO_2 concentration, used in Sect. 3.4.4 to quantify an artefact in GRAEGOR HONO measurements, were recorded by a chemiluminescence NO_2 detector (200E, Teledyne API, San Diego, California, USA) located 300 m south-east of the Easter Bush site.

4.2.3 Micrometeorological theory

Aerodynamic gradient method

The aerodynamic gradient method (AGM), based upon flux–gradient similarity theory, calculates the flux of a tracer (χ, such as a gas or aerosol species) based on its vertical concentration gradient coupled with turbulence parameters (Foken, 2008). In this chapter, a hybrid version of the AGM is used, in which the flux is calculated as (Flechard, 1998)

$$F_\chi = -u_* \kappa \frac{\chi_2 - \chi_1}{\ln\left(\frac{z_2-d}{z_1-d}\right) - \psi_\mathrm{H}\left(\frac{z_2-d}{L}\right) + \psi_\mathrm{H}\left(\frac{z_1-d}{L}\right)}, \tag{4.3}$$

where the friction velocity (u_*) is derived from eddy covariance measurements with a sonic anemometer; κ is the von Karman constant ($\kappa = 0.41$); z_2 and z_1 are the heights of the sample boxes; d is the displacement height; and ζ is a dimensionless stability parameter expressing the ratio $(z-d)/L$, where L is the Obukhov length, a measure for atmospheric stability. The parameter Ψ_H, an integrated form of the heat stability correction term, accounts for deviations from the log-linear profile under non-neutral stratification. By convention, negative and positive flux values denote deposition and emission, respectively.

Choice of displacement height, d, value

A temperature gradient profile for the campaign was derived from measurements of air temperature at the two heights at which concentrations were measured (0.6 and 2.4 m). Sensible heat flux (H) was calculated from the temperature gradient as per Wang and Bras (1998):

$$H = -\rho_{\text{air}} c_p K_{\text{H}} (z-d) \frac{\mathrm{d}T}{\mathrm{d}z}, \tag{4.4}$$

where c_p is the heat capacity of air, ρ_{air} is the density of air, and K_{H} is the eddy diffusivity constant for heat. K_{H} can be calculated as

$$K_{\text{H}} (z-d) = \frac{(z-d)\, u_*}{\phi_{\text{H}} \left(\frac{z-d}{L}\right)}, \tag{4.5}$$

where z is the absolute height above ground, d is the displacement height, u_* is the friction velocity, and Φ_{H} is the stability correction for sensible heat. Sensible heat flux and, by extension, the flux of the trace gas and aerosol species, are dependent upon the value of d. In order to ensure that the correct displacement height was chosen, the sensible heat flux based upon the temperature gradient developed from thermocouple measurements was calculated using a variety of different values for displacement height. The resulting values for the sensible heat flux were then compared through linear regression to the value for the sensible heat flux recorded by the eddy covariance system also present. A displacement height value of 0.14 m gave the closest agreement between the sensible heat fluxes derived by the aerodynamic gradient approach and eddy covariance, with a linear regression slope of 0.997 and $R^2 = 0.945$.

Determination of dry deposition velocities

The dry deposition velocity (V_{d}) of a tracer is the negative ratio of its flux to its concentration (χ) at height $z - d$:

$$V_{\text{d}} (z-d) = -\frac{F_\chi}{\chi_z (z-d)}. \tag{4.6}$$

The V_{d} for gas species may also be expressed as the reciprocal of the total resistance for deposition, which is composed of R_{a} (the aerodynamic resistance), R_{b} (the quasi-laminar boundary layer resistance) and R_{c} (the canopy resistance) as per the resistance analogy for dry deposition (Fowler and Unsworth, 1979; Wesely, 1989). R_{a} and R_{b} were calculated from Eqs.(4.7) and (4.8) using meteorological measurements taken at the site using (Garland, 1977)

$$R_{\mathrm{a}}\left(z-d\right)=\frac{u(z-d)}{u_{*}^{2}}-\frac{\psi_{\mathrm{H}}\left(\zeta\right)-\psi_{\mathrm{M}}\left(\zeta\right)}{\kappa u_{*}}\,, \tag{4.7}$$

$$R_{\mathrm{b}}=\left(Bu_{*}\right)^{-1}, \tag{4.8}$$

where B^{-1}, B being the Stanton number, is parameterised by the turbulent Reynolds number, Re_{*} (the ratio of the frictional force to the kinematic velocity of air) and the Schmidt number, Sc (the ratio of kinematic velocity of air to the molecular diffusivity coefficient of the gas species):

$$B^{-1}=1.45Re_{*}^{0.24}Sc^{0.8}. \tag{4.9}$$

If R_{a} and R_{b} are calculated from measurements, R_{c} can be inferred via

$$R_{\mathrm{c}}=\frac{1}{V_{\mathrm{d}}(z-d)}-R_{\mathrm{a}}\left(z-d\right)-R_{\mathrm{b}}. \tag{4.10}$$

For gases, a theoretical maximum deposition velocity can be calculated when it is assumed that the gas is completely absorbed by the canopy (i.e. for $R_{\mathrm{c}}=0$):

$$V_{\max} = \frac{1}{(R_a + R_b)}. \tag{4.11}$$

The canopy resistance approach can only describe deposition and fails when the exchange of a gas is bidirectional, such as is often the case with NH_3. In this case, the canopy compensation point model can be adopted, which considers the surface interaction of NH_3 in terms of parallel resistance pathways, composed of individual resistances such as stomatal resistance and cuticular resistance (Nemitz *et al.*, 2000a; Flechard *et al.*, 2015).

The gradient technique is only applicable for inert species whose flux is constant with height. Most studies of surface exchange fluxes of reactive compounds do not have the information to assess whether chemical reactions might interfere with the flux measurement, but in this study the behaviour of HNO_3 and HCl allows us to draw conclusions on flux divergence (see Section 4.4.2 below). Following precedence in the literature (Nemitz and Sutton, 2004, e.g.) we initially evaluate fluxes assuming that chemistry can be ignored, and then discuss the validity of this discussion based on the results.

Limits of detection and estimation of uncertainties in concentration measurements and flux calculations

The concentration limit of detection (LOD) of the instrument for each of the species measured was quantified from a field blank test. The field blank test was carried out prior to the campaign on the 20 March over 24 h by switching off the sample box air pump and sealing the air inlets, but leaving the rest of the system unaltered, as per Thomas *et al.* (2009). Limits of detection were then calculated as 3 standard deviations from the average background signal. Results from this

Table 4.1: Limit of detection (LOD, determined as 3 standard deviations from average baseline signal), mean (μ_A), median (μ_M), min, max and arithmetic standard deviation (σ_A) for concentrations measured at 2.4 m for trace gases and water-soluble aerosols measured during the Easter Bush campaign, calculated from hourly data. Number of measurements (N) for each compound is also shown.

	LOD	μ_A	μ_M	Min	Max	σ_A	N
(2.4 m)	ng m^{-3}	μg m^{-3}	μg m^{-3}	μg m^{-3}	μg m^{-3}	μg m^{-3}	
NH_4^+	190	0.74	0.64	< LOD	2.33	0.43	580
Cl^-	15	0.91	0.36	< LOD	7.88	1.31	515
NO_2^-	17	0.02	0.02	< LOD	0.05	0.01	373
NO_3^-	47	1.53	1.32	< LOD	6.27	1.18	538
SO_4^{2-}	109	1.29	1.22	< LOD	6.26	0.83	540
NH_3	172	1.48	1.15	< LOD	13.8	1.5	602
HCl	67	0.2	0.15	< LOD	1.4	0.18	544
HONO	30	0.04	0.04	< LOD	0.12	0.02	410
HNO_3	97	0.19	0.16	< LOD	0.68	0.12	509
SO_2	120	0.24	0.18	< LOD	1.48	0.21	480

test are presented in Table 4.1, expressed as LOD values for each trace gas and corresponding water-soluble aerosol species.

The minimum detectable flux for each aerosol and gas species measured by the GRAEGOR is dependent upon atmospheric stability and the ambient concentration of the given trace gas or aerosol species. Based on the method described by Thomas *et al.* (2009), median minimum detectable fluxes (F_{LOD}) were calculated for each trace gas and aerosol species measured and are detailed in Tables 4.2 and 4.3, respectively.

Table 4.2: Mean (μ_{A}), median (μ_{M}), minimum and maximum values for flux, deposition velocity (V_{d}), maximum deposition velocity (V_{max}) and canopy resistances (R_{c}) for trace gases measured during the Easter Bush campaign, based on hourly values. Also shown are the median relative standard error (σ_F), the flux limit of detection (F_{LOD}) evaluated for typical conditions (median u_* and median concentration) and the fraction of the hourly flux value that exceeds the flux detection limit evaluated for that hour (f_{LOD}).

		NH_3	HCl	HONO	HNO_3	SO_2
Flux ($\mathrm{ng\,m^{-2}\,s^{-1}}$)	μ_{A}	15.2	−3.51	−0.3	−2.66	−3.04
	μ_{M}	5.65	−1.98	−0.29	−1.99	−1.68
	Min	−324	−61.2	−2.46	−18.6	−35.6
	Max	1460	−0.03	4.92	0.82	−0.03
	No. of measurements	577	506	384	500	465
	σ_F (%)	32	58	56	42	67
	F_{LOD}	1.28	0.75	0.18	0.89	0.97
	f_{LOD} (%)	94	84	78	87	89
V_{d} ($\mathrm{mm\,s^{-1}}$)	μ_{A}	−8.99	15.1	8.8	13.6	11.7
	μ_{M}	−6.1	14.5	7.69	12.9	10.0
	Min	−215	0.01	−55.6	−4.72	0.34
	Max	92.9	52.8	59.8	56.8	55.4
V_{max} ($\mathrm{mm\,s^{-1}}$)	μ_{A}	19.5	15.3	14.1	13.9	14.2
	μ_{M}	18.8	15.3	14.0	13.8	14.0
	Min	1.7	0.04	0.04	0.04	0.45
	Max	57	40.4	37.0	36.90	37.0
R_{c} ($\mathrm{s\,m^{-1}}$)	μ_{A}	0	33.8	331	23.3	49.2
	μ_{M}	0	1.82	13.1	5.71	27.6

Table 4.3: Mean (μ_{A}), median (μ_{M}), minimum and maximum values for flux and deposition velocity (V_{d}) for water-soluble aerosols measured during the Easter Bush campaign. Also shown are the median relative standard error (σ_F), the flux limit of detection (F_{LOD}) evaluated for typical conditions (median u_* and median concentration) and the fraction of the hourly flux value that exceeds the flux detection limit evaluated for that hour (f_{LOD}).

		NH_4^+	Cl^-	NO_3^-	SO_4^{2-}
Flux ($\mathrm{ng\,m^{-2}\,s^{-1}}$)	μ_{A}	−3.55	−4	−3.34	−3.56
	μ_{M}	−2.97	−1.11	−1.76	−2.19
	Min	−42.2	−60.0	−89.3	−59.7
	Max	18.2	−1.06	31.9	−0.95
	No. of measurements	224	484	477	482
	σ_F (%)	58	41	48	45
	F_{LOD}	2.21	0.85	1.28	1.78
	f_{LOD} (%)	91	81	84	87
$V_{\mathbf{d}}$ ($\mathrm{mm\,s^{-1}}$)	μ_{A}	0.93	3.65	1.97	1.89
	μ_{M}	0.37	3.14	1.52	1.45
	Min	−0.04	−0.92	−9.43	−2.48
	Max	7.57	21.3	9.8	9.53

When calculating the flux of a species using the aerodynamic gradient method, it is apparent that errors in individual concentration measurements propagate into an error in the concentration differences and, subsequently, affect the accuracy of the calculated vertical concentration gradient. Some errors systematically affect both heights and therefore affect the gradient to a lesser extent than systemic errors in sampling efficiency at a single height, such as the difference in capture efficiency of the WRD tubes or slight differences in airflow caused by differences in the critical orifices, which may impact the accuracy of concentration

measurements and resultantly affect the precision in the error of the concentration difference.

The overall random error in the measurements of the trace gas and water-soluble aerosol concentrations (σ_{m}) can be determined using a Gaussian error propagation approach, in which the concentration error is expressed as a product of several individual measurement errors with the mixing ratio, m (Trebs *et al.*, 2004) (4.12)

-

$$\sigma_{\mathrm{m}} = m\sqrt{\left(\frac{\sigma_{\mathrm{m_{liq}}}}{m_{\mathrm{liq}}}\right)^2 + \left(\frac{\sigma_{\mathrm{Br_{(std)}}}}{\mathrm{Br_{(std)}}}\right)^2 + \left(\frac{\sigma_{Q_{\mathrm{Br}}}}{Q_{\mathrm{Br}}}\right)^2 + \left(\frac{\sigma_{\mathrm{m_{Br}}}}{m_{\mathrm{Br}}}\right)^2 + \left(\frac{\sigma_{Q_{\mathrm{air}}}}{Q_{\mathrm{air}}}\right)^2}. \tag{4.12}$$

Here, m_{liq} is the mixing ratio of the compounds found in the analysed liquid sample in ppb, $\mathrm{Br_{(std)}}$ the stated mixing ratio of the internal $\mathrm{Br^-}$ standard, Q_{Br} the flow rate of the internal $\mathrm{Br^-}$ standard, m_{Br} the analysed $\mathrm{Br^-}$ mixing ratio and Q_{air} the air mass flow through the system. All values have an associated standard deviation, σ_x. This formulation holds strictly for the species measured by ion chromatography; for $\mathrm{NH_3}$ and $\mathrm{NH_4^+}$, the equation is altered by omitting the factor relating to $\mathrm{Br^-}$ addition and substituting the factor for Q_{Br} and its associated standard deviation with the term Q_{S}, the flow of the analysed liquid sample of $\mathrm{NH_3}$ or $\mathrm{NH_4^+}$.

Uncertainties for the trace gases and water-soluble aerosols measured calculated by error propagation ranged from 8 % to 18 % (3σ) throughout the campaign, varying primarily due to fluctuations in the measured flow rate and analysed concentration of the internal $\mathrm{Br^-}$ standard.

The error in the concentration difference ($\sigma_{\Delta c}$) can be characterised experimentally, by placing both sample boxes at one height or – provided that the absolute difference between sample heights is small – by using one common air inlet at a specified height, with the instrument operated normally. From this side-by-side measurement, linear regression analysis accompanied by orthogonal best fit between the concentrations measured by each sample box can be conducted, with deviation from a 1 : 1 fit between sample heights defined as a systemic error. Using the calculated orthogonal fit equation, corrections in the concentrations can then be applied, accounting for the systemic bias (Wolff *et al.*, 2010a). After correction using the orthogonal fit, the remaining scatter – termed the residuals – was used to determine the error in the concentration difference. During this campaign, one side-by-side measurement was conducted on 8 June for 16 h by connecting a common air inlet set at $z = 1.2$ m between each sample box. From the results obtained, it was found that for the gases NH_3, HCl, HONO, HNO_3 and SO_2 that deviation from the 1 : 1 fit resulted in a precision of measurements $< 4\,\%$ (3σ). For the aerosol species Cl^-, NO_3^- and SO_4^{2-}, precision was calculated as $< 8\,\%$ (3σ), while for NH_4^+ it was calculated as $< 9\,\%$ (3σ).

Errors in flux calculations can similarly be determined through the Gaussian error propagation method applied to Eq. 4.1. Wolff *et al.* (2010a), using an analogous form of this equation, showed that total error in the flux is composed of ($\sigma_{\Delta c}$) and the error in the flux–gradient relationship (expressed as a transport velocity by Wolff *et al.*), which is dominated by the error in u_* (σ_{u*}).

$$\sigma_F = F\sqrt{\left(\frac{\sigma_{vu_*}}{u_*}\right)^2 + \left(\frac{\sigma_{\Delta c}}{\Delta c}\right)^2} \tag{4.13}$$

This simplification neglects the detailed secondary errors associated with the stability correction which to quantify fully is beyond the scope of this study.

σ_{u*} is dependent upon the sonic anemometer used and whether conditions are neutral or non-neutral Foken, 2008; Nemitz *et al.*, 2009b. For neutral conditions, and based on the sonic anemometer used, σ_{u*} was estimated at $\leq 10\,\%$. For non-neutral conditions, σ_{u*} was estimated at 12 % median, which, in combination with $\sigma_{\Delta c}$, was used to calculate σ_F.

Throughout this chapter, stated errors for concentration measurements are derived from the measurement uncertainty as calculated by Eq.4.12, while stated errors for flux calculations are derived from the flux uncertainty as calculated by Eq.4.13. Calculated errors for the uncertainty in concentration measurements, the error in the concentration difference and the error in the calculated fluxes for all species measured are similar to values determined by previous studies which have used the GRAEGOR successfully to measure flux gradients (Thomas *et al.*, 2009; Wolff *et al.*, 2010b; Twigg *et al.*, 2011).

Data postprocessing

Concentrations that were less than 3 times the limit of detection as calculated before the campaign began (20 March) were discarded. Calculated fluxes were filtered according to a standard protocol. Fluxes were not calculated for periods of low wind speed ($u < 1\,\mathrm{m\,s^{-1}}$), low friction velocity ($u < 0.15\,\mathrm{m\,s^{-1}}$) and very stable conditions as indicated by the Obukhov length absolute value ($|L| < 5\,\mathrm{m}$). Fluxes were also discarded for periods when the wind was obstructed by the measurement cabin and other towers ($270° > wd < 320°$, and $120° > wd < 160°$). Calculated fluxes which were below the minimum detectable flux value for their respective trace gas or aerosol species were discarded.

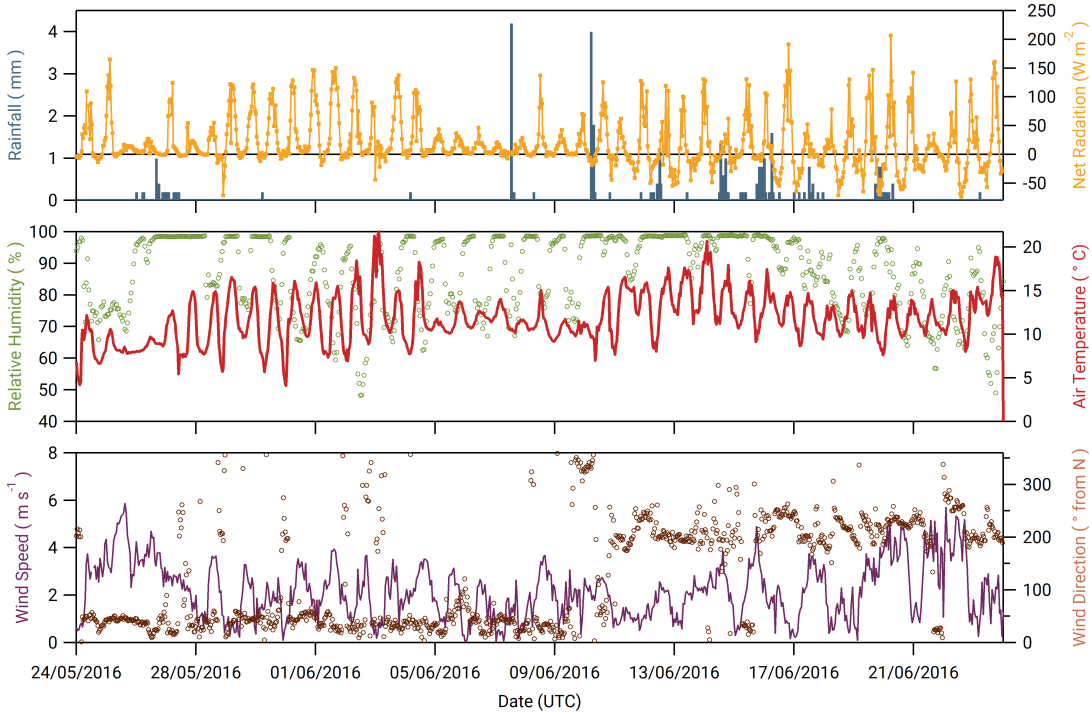

Figure 4.2: Time series of hourly concentrations of the water-soluble aerosol species measured during the Easter Bush campaign. Results smoothed using a 5 h moving point average.

4.3 Results

4.3.1 Meteorology

Figure 4.2 shows time series of the rainfall, net radiation, relative humidity, air temperature, and wind speed and direction measured during the campaign. The meteorology splits into two episodes. From 24 May to 5 June 2016, the dominant prevailing wind direction was north-easterly, accompanied by dry and sunny conditions with air temperature displaying a characteristic diel cycle that increased each day. Following a period of cloudier conditions from 6 to 10 June, the prevailing wind direction shifted to south-westerly for the

remainder of the measurement period. Conditions became wetter and the diel air temperature amplitude was reduced. Relative humidity remained high throughout the campaign, with only occasional periods $< 70\,\%$, such as 3–4 June and 21–23 June. Wind speed was variable throughout, ranging between 0.05 and $5.87\,\mathrm{m\,s^{-1}}$, with a median value of $2.16\,\mathrm{m\,s^{-1}}$. During the fertilisation period, the prevailing wind direction was from the SW, and therefore over the south field, with no precipitation but high ($> 90\,\%$) relative humidity.

4.3.2 Concentrations of trace gases and water-soluble aerosols

Summary statistics for the concentrations of the trace gas and water-soluble aerosol species measured at 2.4 m during the campaign are presented in Table 4.1. Median values for the concentrations of water-soluble aerosol species were similar to those measured in PM_{10} at the nearby rural background monitoring site of Auchencorth Moss (Twigg *et al.*, 2015). The time series of the measured aerosol and trace gas concentrations are displayed in Figs.4.3 and 4.4, respectively. Data gaps in the time series are due to in-field calibrations, poor chromatograms, or instability in liquid or airflow.

Mean concentrations of NO_3^- were $1.53\,\mu\mathrm{g\,m^{-3}}$ (2.4 m), whereas its gaseous counterpart, HNO_3, had mean concentrations of $0.19\,\mu\mathrm{g\,m^{-3}}$ (2.4 m). The mean particulate NO_3^- concentrations were therefore almost 6 times greater than the gaseous HNO_3 counterpart. The same dominance of particulate SO_4^{2-} concentrations over gaseous SO_2 concentrations was also observed.

Median concentrations of particulate Cl^- were 0.37 and $0.36\,\mu\mathrm{g\,m^{-3}}$ at 0.6 and 2.4 m, respectively. The mean concentrations of Cl^- were also similar at both heights at 0.89 and $0.91\,\mu\mathrm{g\,m^{-3}}$, respectively. Variation in HCl concentrations at

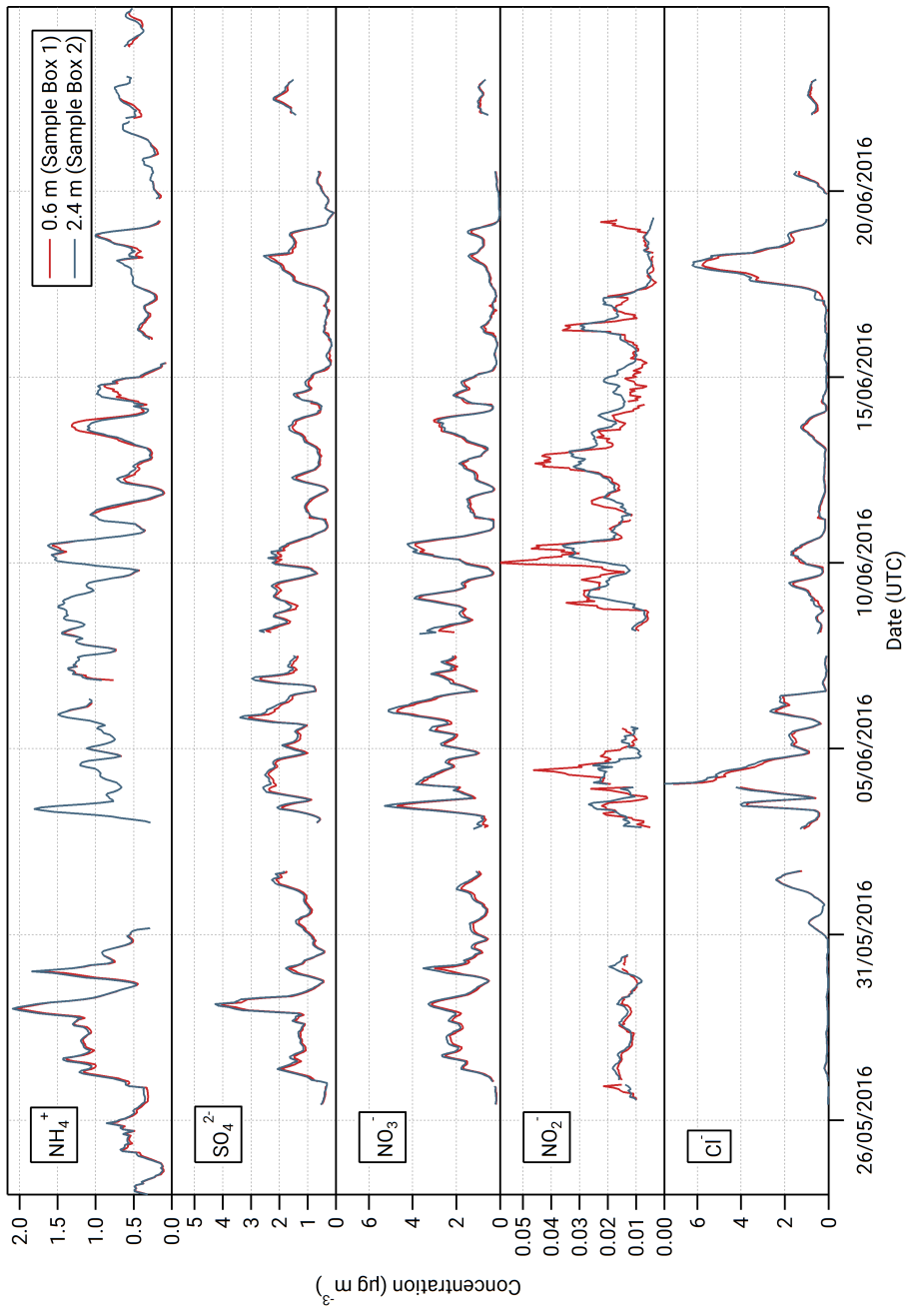

Figure 4.3: Time series of hourly concentrations of the water-soluble aerosol species measured during the Easter Bush campaign. Results smoothed using a 5 h moving point average.

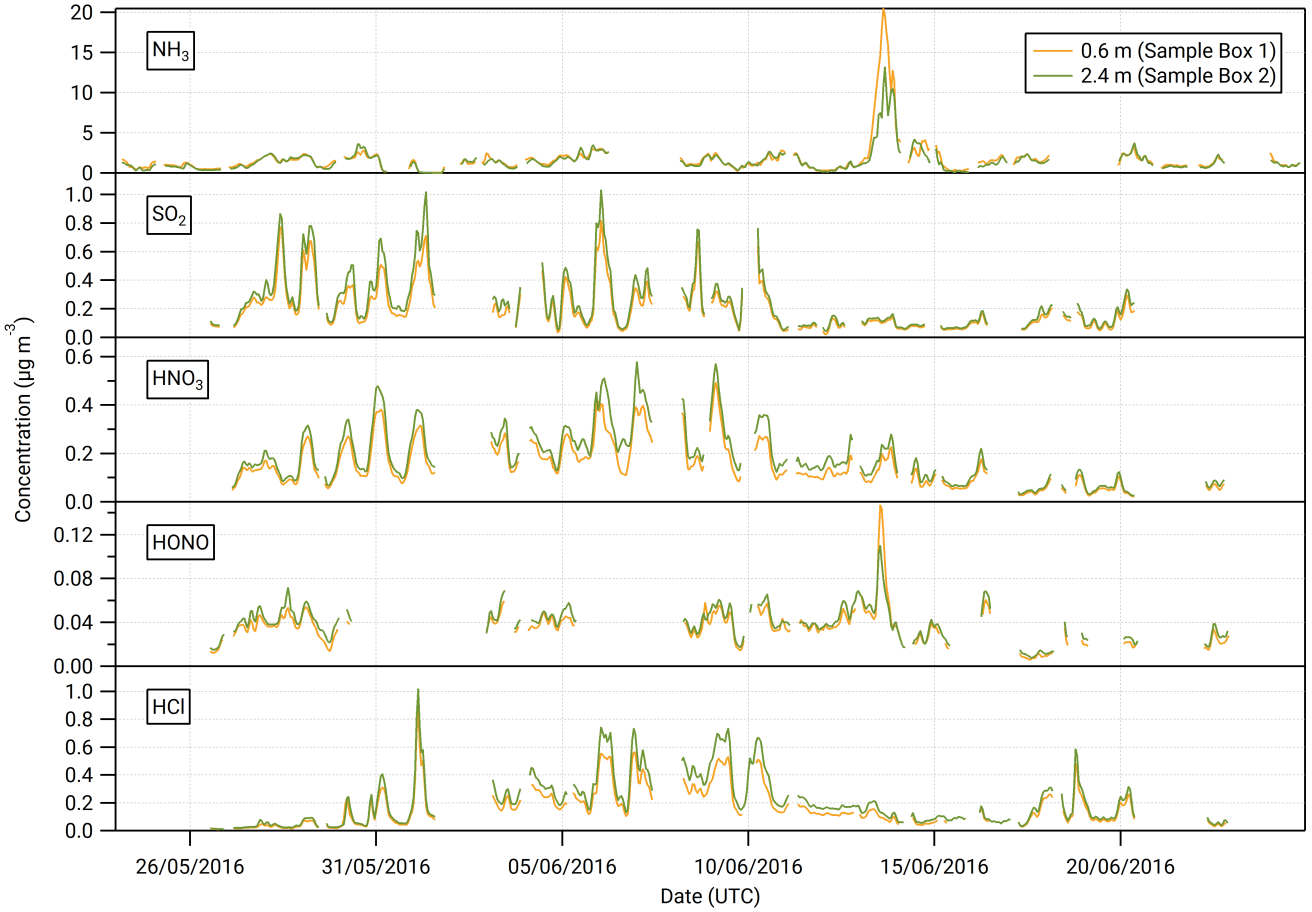

Figure 4.4: Time series of hourly concentrations of the gaseous species measured during the Easter Bush campaign. Results smoothed using a 5 h moving point average.

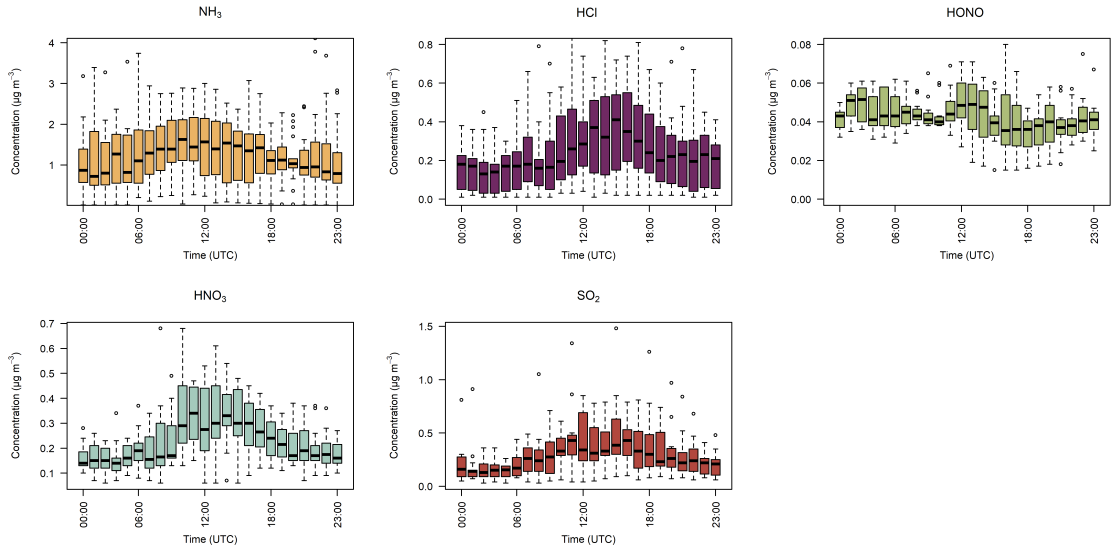

Figure 4.5: Hourly median diel trace gas concentrations measured by the GRAEGOR at 2.4 m prior to fertilisation. Boxes show the lower and upper quartiles and whiskers the 5 % to 95 % range, with outliers shown as circles.

each height was more pronounced, with a mean value of 0.16 μg m^{-3} at 0.6 m and 0.20 μg m^{-3} at 2.4 m, and a median value of 0.12 μg m^{-3} at 0.6 m and 0.15 μg m^{-3} at 2.4 m. As for particulate NO_3^- and gaseous HNO_3, measured particulate Cl^- concentrations were greater than those of gaseous HCl, by about a factor of 2 at each height.

In contrast, NH_3 concentrations were larger than those of particulate NH_4^+; median concentrations of NH_3 were 1.15 μg m^{-3} (2.4 m), while median concentrations of NH_4^+ were 0.64 μg m^{-3} (2.4 m). The average concentrations of NH_3 were similar to those reported previously at the same site for the same time of year (Milford *et al.*, 2001). Similarly, the average concentrations of HONO are higher than those of its particulate counterpart, NO_2^-, with median concentrations for HONO of 0.04 μg m^{-3} (2.4 m) and corresponding concentrations for NO_2^- of 0.02 μg m^{-3} (2.4 m), respectively.

Maximum concentrations for NH_3 and HONO at 0.6 m were 21.4 and 0.15 μg m^{-3}.

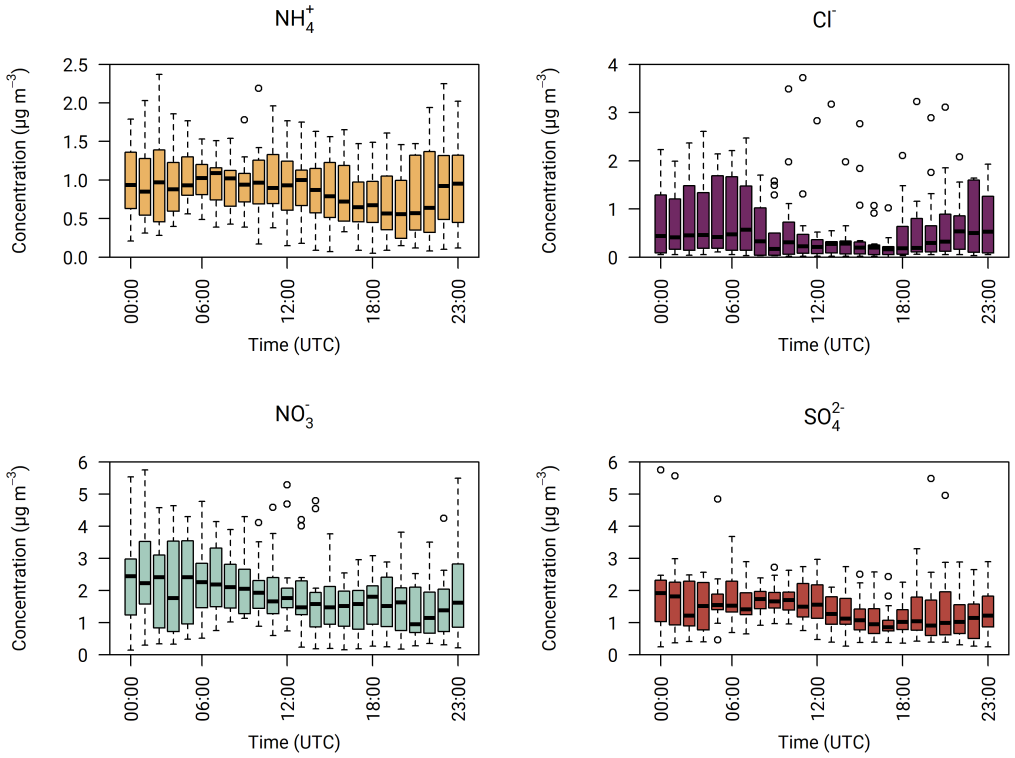

Figure 4.6: Hourly median diel water-soluble aerosol concentrations measured by the GRAEGOR at 2.4 m prior to fertilisation. Boxes show the lower and upper quartiles and whiskers the 5 % to 95 % range, with outliers shown as circles.

At 2.4 m, the maximum concentrations for NH_3 and HONO were 13.8 and 0.12 $\mu g\,m^{-3}$. The maximum values at each height occurred at 11:00 on the 13 June for NH_3, 1 h after fertilisation of the south field, and at 13:00 on 13 June for HONO, 4 h after fertilisation of the south field.

The time series of measurements presented in Figs.4.3 and 4.4 show that both aerosol and trace gas concentrations are affected by prevailing meteorological conditions, with larger concentrations for each species during the drier, warmer period of 28 May to 6 June, followed by decreased concentrations from 6 to 10 June when precipitation increased and temperature decreased. Concentrations were lower – except for the peaks in NH_3 and HONO after fertilisation on the 13 June

– during the period from 10 June to the end of the campaign, concurrent with the change in prevailing wind direction from the NE to the SW.

The concentrations of HNO_3 and SO_2 showed a strong diel cycle (Fig.4.4) from 26 May to 9 June, with maxima at both measurement heights occurring between 11:00 and 14:00 and minima occurring at night between 03:00 and 06:00. A similar, but weaker, inverted pattern was exhibited by their particulate counterparts, with NO_3^- concentrations at both heights (Fig.4.3) having maxima between 02:00 and 04:00 and minima between 12:00 and 15:00.

Figure 4.5 shows the median diel concentrations of NH_3, HCl, HONO, HNO_3 and SO_2 at 2.4 m prior to fertilisation. The median concentrations of HONO remained above the detection limits of the instrument even during daytime, contrary to its expected photochemistry. While concentrations of HONO peaked during nighttime and decreased during the day as incoming solar radiation increased, there remained a detectable concentration of HONO at both heights even for the measurement minima at 15:00. The median diel concentrations for HCl, HNO_3 and SO_2 show a shared pattern, with concentrations peaking during the day to reach a maximum between 11:00 and 14:00, followed by a decrease during the night, reaching minima between 02:00 and 04:00. The concentrations of NH_3 showed little variation across the day. Figure 4.6 shows the median diel concentrations of NH_4^+, Cl^-, NO_3^- and SO_4^{2-} at 2.4 m prior to fertilisation. The median diel concentrations of NH_4^+ reach a minimum at 20:00, with a maximum at 07:00. The concentrations of NO_3^- show a similar pattern of early morning median maxima (04:00) and evening minima (20:00). The median diel SO_4^{2-} concentrations had maxima at midnight and a minimum at 16:00. The Cl^- concentrations reached a maximum at 03:00 and a minimum at 13:00; however, the upper quartile range was high across all hours, with the maximum concentration of 7.88 $\mu g\,m^{-3}$ recorded at 03:00 (median at this time is 0.5 $\mu g\,m^{-3}$).

4.3.3 Fluxes, deposition velocities and canopy resistance

Fluxes of trace gases

Figure 4.7 shows the time series of the fluxes for the traces gases measured during the campaign. Data gaps are due to either absent data points (unpaired concentrations) or periods where data were filtered (refer to Sect. 4.3.4).

Bidirectional fluxes were present for both NH_3 and HONO, with emission events for each gas occurring during the period of fertilisation of the south field. For the other trace gases – HCl, HNO_3 and SO_2 – the flux was unidirectional, with deposition occurring throughout the campaign. The deposition for HCl, HNO_3 and SO_2 varied, with larger deposition fluxes occurring during the warmer, drier periods, particularly during the period 1–8 June, and smaller deposition fluxes close to zero during the colder, wetter period at the end of the campaign (15–24 June).

Summary statistics for the trace gas fluxes, deposition velocities, theoretical maximum deposition velocities and canopy resistance values are presented in Table 4.2. The maximum NH_3 flux was $+1460\,\mathrm{ng\,m^{-2}\,s^{-1}}$, recorded at 12:00 on 13 June, 3 h after fertilisation. The mean flux for NH_3 was $+15.2\,\mathrm{ng\,m^{-2}\,s^{-1}}$, suggesting that emission was the predominant flux for NH_3 during this campaign. For all other gases, the mean flux values were negative, suggesting that deposition was the net flux process overall. However, a maximum flux for HONO of $+4.92\,\mathrm{ng\,m^{-2}\,s^{-1}}$, recorded 5 h after fertilisation, highlights the bidirectional flux pattern for HONO during the campaign. The maximum HONO flux measured here was particularly large. Nitrous acid emissions have previously been reported postfertilisation of grassland using cattle slurry at the same field site ranging from +1.0 to $+1.5\,\mathrm{ng\,m^{-2}\,s^{-1}}$ (Twigg *et al.*, 2011). Table 4.2 also shows the median relative flux error, the typical flux detection limits (F_{LOD}) and the fraction

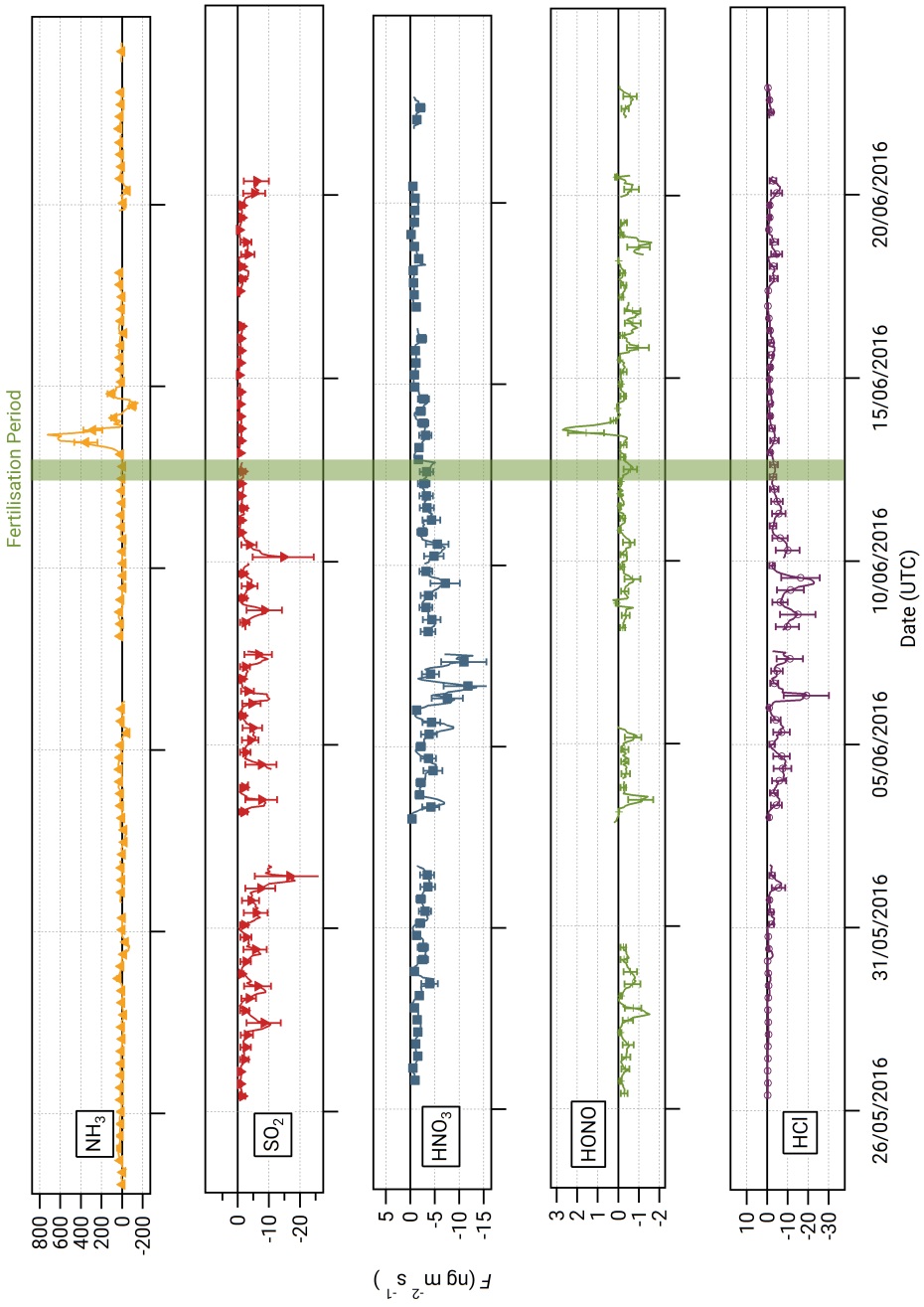

Figure 4.7: Time series of hourly trace gas fluxes measured during the Easter Bush campaign. Results smoothed using a 5 h moving point average. The fertilisation period was 08:00–09:00 on 13 June and is highlighted in green. Flux uncertainties for each trace gas are included as error bars.

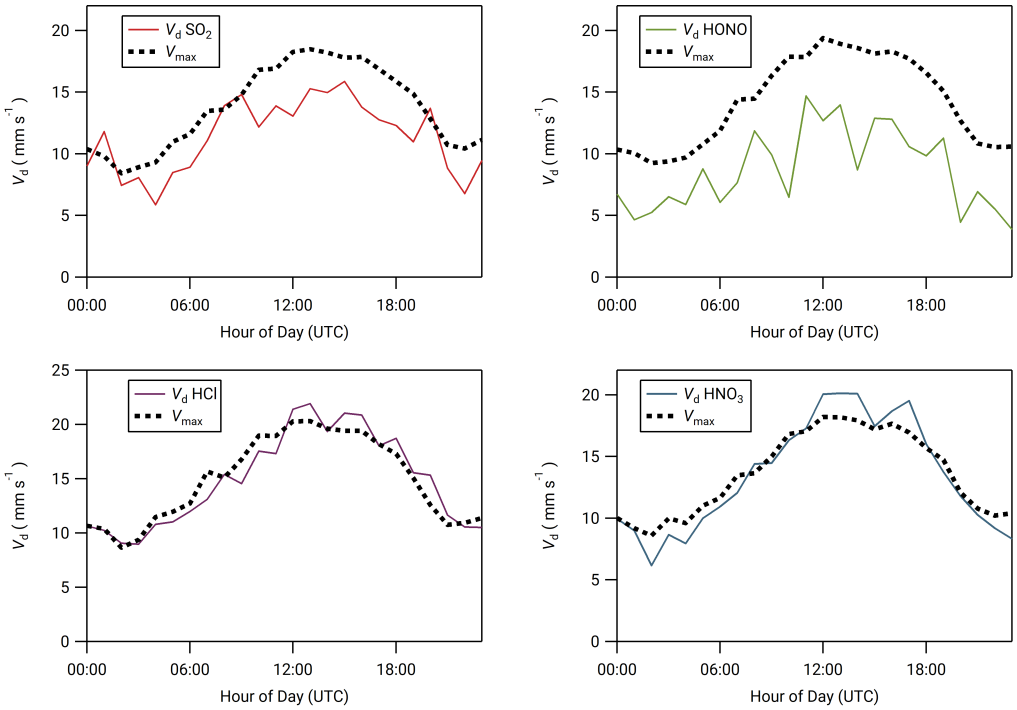

Figure 4.8: Median diel cycles prior to fertilisation for deposition velocity (V_d) and maximum deposition velocity (V_{max}) for (top row from left) SO_2 and HONO; and (bottom row from left) HCl and HNO_3.

of 60 min flux values that exceed the F_{LOD} of that period, based on actual concentration and turbulence. It should be noted that the uncertainty of the campaign averages is much smaller as random uncertainty reduces with the square root of the number of observation that enter the calculation of the ensemble average (Langford *et al.*, 2015).

Median diel cycles for the deposition velocity and calculated theoretical maximum deposition velocity for the trace gases HCl, HONO, HNO_3 and SO_2 are shown in Fig.4.8 The calculation of median diel values for trace gas deposition velocities and canopy resistances excludes the period of flux divergence which occurred during fertilisation. The diurnal deposition velocities for HCl and HNO_3 were very close to the calculated maximum deposition velocities, which is expected

as a result of their reactivity and high water solubility. The deposition velocity for SO_2 is near the theoretical maximum during nighttime but is lower during daytime. The deposition velocity for HONO was consistently lower than its theoretical maximum throughout the entire day. While median values for the V_d for HNO_3 are close to the values for V_{max}, deposition velocities that exceeded their corresponding theoretical maximum were recorded. While most exceedances fall within the uncertainty range of the measurement, a maximum deposition velocity of $56.8\,mm\,s^{-1}$ was recorded at 14:00 on 13 June, 4 h after fertilisation.

Fluxes of water-soluble aerosol components

The measured surface fluxes of the aerosol species Cl^-, NO_3^-, SO_4^{2-} and NH_4^+ are shown in Fig. 4.9, as well as the summary statistics for the fluxes and deposition velocities in Table 4.3. A large data gap in NH_4^+ fluxes from 31 May to 10 June 2016 was due to NH_4^+ only being measured at one height on account of unreliable data for NH_4^+ at the lower height of 0.6 m.

Pre-fertilisation, all aerosol species exhibited deposition fluxes. The deposition fluxes were larger during the drier, warmer period from 31 May to 6 June and close to zero during the wetter conditions at the end of the campaign. An important exception was the apparent emission of NH_4^+ and NO_3^- from 13:00 on 13 June to 02:00 on 14 June, starting 4 h after fertilisation of the south field.

Summary statistics for the fluxes and deposition velocities for the aerosol species measured are shown in Table 4.3. As for the trace gases, the median deposition velocities for the aerosol species exclude the period of flux divergence which occurred during fertilisation. The maximum flux for NH_4^+ of $+18.16\,ng\,m^{-2}\,s^{-1}$ was recorded at 16:00 on 13 June, 7 h after fertilisation of the south field. Similarly, the maximum flux for NO_3^- ($+31.84\,ng\,m^{-2}\,s^{-1}$) was also recorded soon

after fertilisation, at 18:00 on the 13 June. Overall, however, the mean fluxes for all aerosol species were negative, confirming a predominant net deposition to the surface.

4.3.4 HONO and NH_3 GRAEGOR measurement comparisons with LOPAP and QCL

HONO comparison study between GRAEGOR and LOPAP

A comparison of HONO measurements from the GRAEGOR and two LOPAP instruments was conducted from 26 May to 6 June to investigate the potential artefacts in the WRD method used by the GRAEGOR. The LOPAPs were part of a study to investigate the mechanisms controlling HONO fluxes over managed grassland, including investigating the potential ground sources of HONO, details of which are presented in Di Marco *et al.* (2019). A series of simple linear regression analyses was conducted to determine the level of agreement between the concentrations of HONO measured by each sample box of the GRAEGOR and each of the LOPAPs. The two LOPAP instruments were operated at the two heights of 0.6 and 2.0 m (hereafter referred to as LOPAP (0.6 m) and LOPAP (2.0 m), respectively). In all comparisons, the GRAEGOR recorded a higher concentration of HONO than either of the LOPAPs. The linear regressions suggest that there is a consistent offset in all GRAEGOR concentrations, varying between 0.01 and 0.02 $\mu g\,m^{-3}$. In comparisons between the GRAEGOR sample box 1 at 0.6 m and both LOPAPs, the linear regression slope for HONO varies from 0.92 to 0.97. The comparisons between the GRAEGOR sample box 2 (2.4 m) and the LOPAPs suggest that the linear regression slope for HONO is 1.06 and 1.01 for LOPAP (2.0 m) and LOPAP (0.6 m), respectively. In all comparisons, however, there exists a constant concentration offset, which results in a constant higher

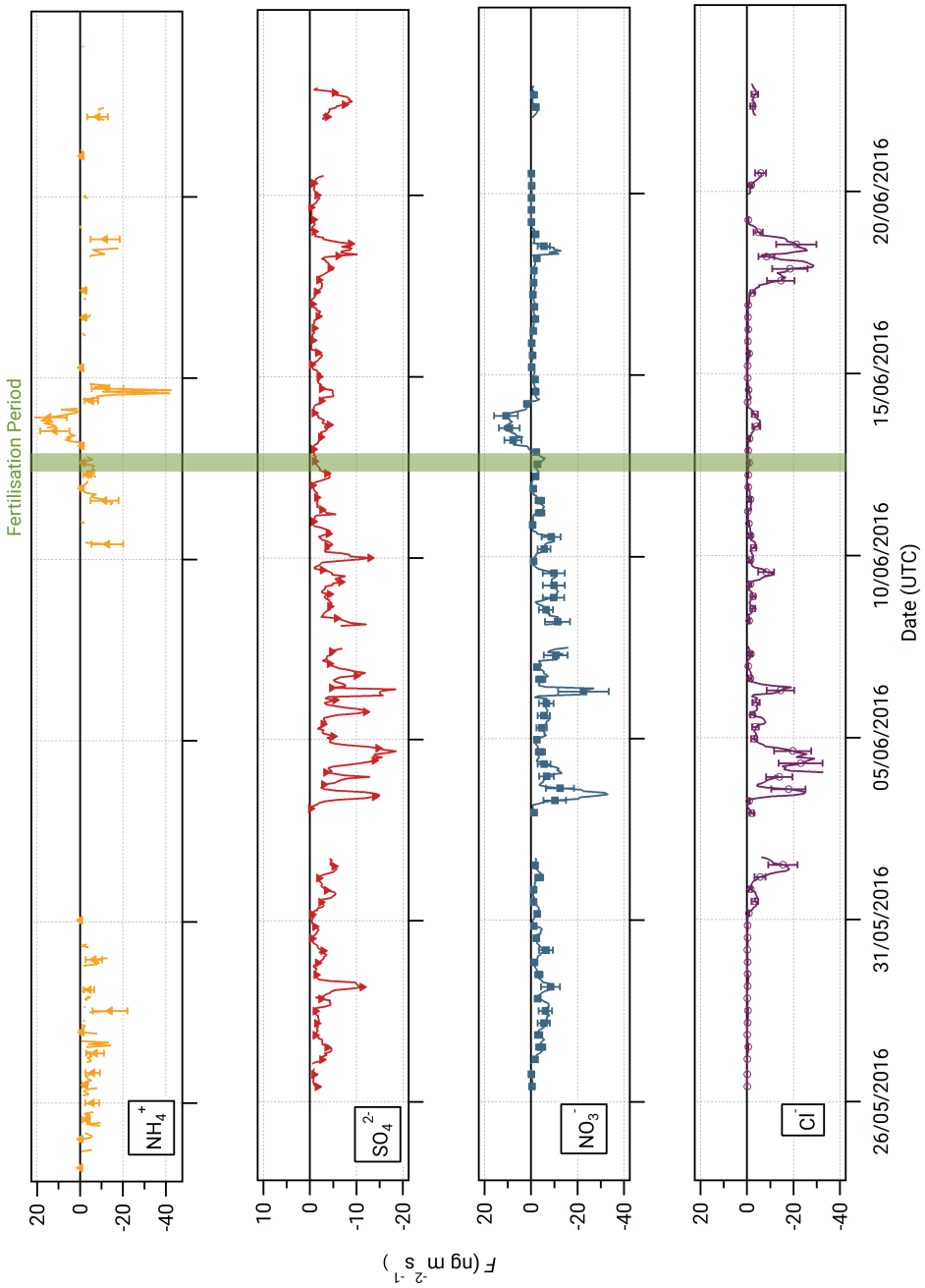

Figure 4.9: Time series of hourly fluxes of water-soluble aerosol species measured during the Easter Bush campaign. Results smoothed using a 5 h moving point average. The fertilisation period was 10:00 on 13 June and is highlighted in green. Flux uncertainties for each aerosol are included as error bars.

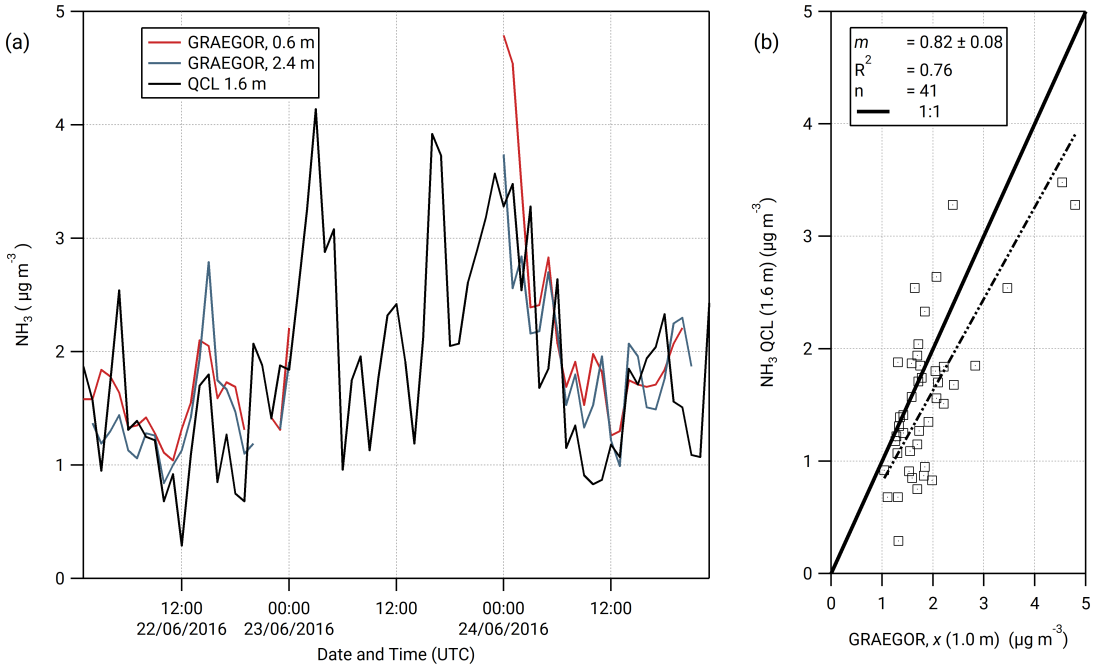

Figure 4.10: **(a)** Time series of hourly averages of NH_3 measurements recorded by GRAEGOR (0.6 and 2.4 m) and QCL. **(b)** Linear regression analysis between QCL NH_3 measurements and GRAEGOR (derived averaged concentration at 1.0 m) NH_3 measurements.

concentration recorded by both GRAEGOR sample boxes. The closest agreement is between GRAEGOR sample box 2 (set at height 2.4 m) and LOPAP (2.0 m), where the HONO concentration recorded by the GRAEGOR sample box 2 (2.4 m) is 1.06 that of LOPAP (2.0 m). This comparison also has the best statistical agreement, with an R^2 value of 0.67, suggesting a reasonable agreement between the GRAEGOR sample box 2 and LOPAP (2.0 m) measurements.

NH_3 comparison study between GRAEGOR and QCL

On 7 June, a QCL with inlet at height 1.6 m was installed at the Easter Bush site and took measurements of NH_3 from 19 June to 7 August. A total of 3 days of concurrent NH_3 measurements taken by the GRAEGOR and the QCL were

recorded in the period 21–24 June. The time series of the NH_3 measurements by each instrument are shown in Fig. 10a. An averaged NH_3 concentration at 1.0 m (χ (1 m)) taken by the GRAEGOR was compared with the NH_3 concentrations taken by the QCL in a simple linear regression analysis, displayed in Fig.4.10. The linear regression shows that the GRAEGOR recorded a factor of 1.22 higher concentrations of NH_3 than the QCL, with an associated R^2 value of 0.76. However, the number of concurrent measurements is small, with only 41 shared hourly measurement values across 3 days and a period of 19 continuous hours missing between 02:00 and 23:00 of 23 June.

4.4 Discussion

4.4.1 Ion balance

The ion balance for the hourly-measured cation (NH_4^+) and anion (NO_3^- and SO_4^{2-}) aerosol species pre-fertilisation is shown in Fig.4.11. Values are shown as molar equivalent concentration, derived from aerosol mass concentrations converted to molar concentrations and subsequently multiplied by their charge. Cl^- charge was not included, under the assumption that it would be entirely associated, in the form of sea salt, with Na^+ which was not measured by the GRAEGOR. While the correlation between cation and anion species is very good ($R^2 = 0.71$), the linear regression suggests a deficit of NH_4^+, suggesting that some of the NO_3^- and/or SO_4^{2-} was balanced by ions other than NH_4^+. A likely candidate is Na^+: some of the SO_4^{2-} is likely to have represented sea-salt SO_4^{2-} and some $NaNO_3$ is formed by reaction of NaCl with HNO_3. Figure 4.11 is coloured by Cl^- concentration, and periods of anion excess tend to be associated with elevated Cl^- concentrations.

The formation of $NaNO_3$ through the reaction of HNO_3 or NO_x with sea salt has

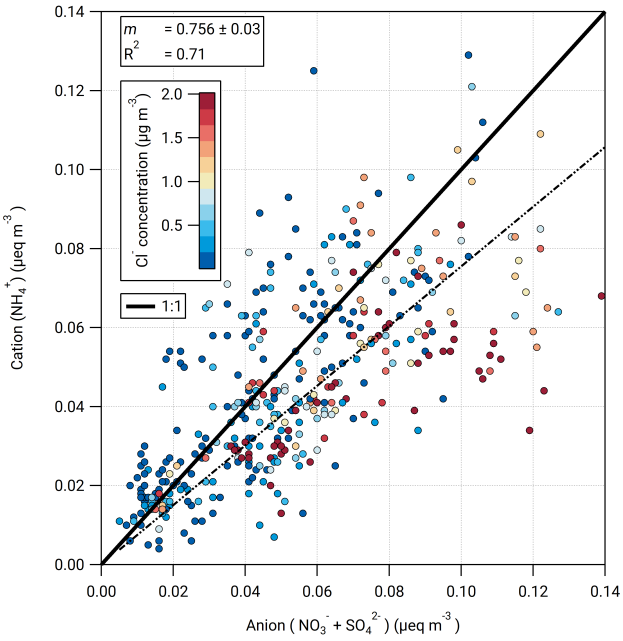

Figure 4.11: The ion balance of measured selected anions ($NO_3^- + SO_4^{2-}$) and measured cations (NH_4^+) in $\mu eq\,m^{-3}$. The colour scale is capped at $2\,\mu eq\,m^{-3}$ Cl^- to highlight the association of anion excess with periods of sea-salt influence.

been previously observed in coastal sites (Andreae *et al.*, 1999; Bardouki *et al.*, 2003; Dasgupta *et al.*, 2007; Kutsuna and Ibusuki, 1994) and within the UK and Ireland, where the interaction of marine air with polluted air masses at coastal sites was shown to significantly shift the aerosol NO_3^- to the coarse mode (Yeatman *et al.*, 2001; Twigg *et al.*, 2015). Scavenging of atmospheric H_2SO_4, formed from SO_2 (O'Dowd and de Leeuw, 2007), by sea salt may also be occurring, which would also shift some of the SO_4^{2-} from the fine to the coarse mode.

4.4.2 Deposition velocities and fluxes of water-soluble aerosol and trace gas species

Fluxes of water-soluble aerosols and trace gases

Fluxes of SO_4^{2-} and Cl^- throughout the campaign were deposited unidirectionally towards the canopy surface. However, during the fertilisation period of the south field, bidirectional fluxes of NH_4^+ and NO_3^- were observed. Prior to fertilisation these species were deposited to the site. An apparent emission flux of NO_3^- is consistent with the possibility of NH_4NO_3 formation above grassland suggested by the divergence of $HNO_3 V_d$ from V_{max} (Nemitz *et al.*, 2009a) in the presence of high concentrations of NH_3 near the surface. Concentrations of NH_3 peak at 21.4 $\mu g\,m^{-3}$ on 13 June, 11:00, which occurs 3 h before peak HNO_3 V_d and 7 h prior to the apparent peak in emissions of NO_3^- at 18:00.

Fluxes for the trace gases were bidirectional for NH_3 and HONO, with deposition for all other species measured. Emissions of NH_3 and HONO occurred throughout the campaign, with HONO emissions particularly present during the early morning. Both species reached peak emissions soon after fertilisation. Increases in atmospheric NH_3 concentration and emissions of NH_3 resulting from the application of solid urea fertiliser have been previously established (Akiyama *et al.*, 2004; Sommer and Hutchings, 2001), with losses from volatilisation increasing if the urea pellets are poorly mixed into the soil and if conditions are dry and warm. While conditions prior to the fertilisation event were cool, temperatures increased quickly throughout the day, peaking at 19.2 °C at 13:00, 4 h after fertilisation. Volatilisation was likely exacerbated by the dry conditions throughout 13 June. The increase in concentration and upward flux of NH_3 provides the source for the formation of NH_4NO_3 in the presence of HNO_3.

Aerosol deposition velocities

Deposition velocities for NO_3^- reached a maximum value of $9.8\,mm\,s^{-1}$ during daytime and a minimum of $0.2\,mm\,s^{-1}$ outside the period of apparent emission fluxes at night. A similar pattern was observed for sulfate, which reached a maximum value of $9.5\,mm\,s^{-1}$ during daytime and a minimum value, outside of apparent emission events, of $0.15\,mm\,s^{-1}$ during night. Median V_d values for NO_3^- and SO_4^{2-} were 1.52 and $1.45\,mm\,s^{-1}$, respectively. For Cl^-, the median V_d was $3.14\,mm\,s^{-1}$. The deposition velocities for SO_4^{2-} where larger than those previously observed and derived for accumulation mode particles from theoretical considerations (Petroff *et al.*, 2008). For sulfate in the fine ($< 2.5\,\mu m$ diameter) range, Allen *et al.* (1991) recorded a mean value of $1\,mm\,s^{-1}$ for deposition velocity over short grass, similar to observations made by Gallagher *et al.* (2002), who reported a mean value of $0.9\,mm\,s^{-1}$.

The dry deposition of particles can be modelled using a process-orientated approach, which describes the deposition velocity as a function of particle size based on removal mechanisms acting within the vegetation canopy, such as Brownian diffusion, impaction, interception and sedimentation (Slinn and Slinn, 1980; Davidson *et al.*, 1982; Slinn, 1982). The models predict that for particles $> 0.1\,\mu m$ in diameter deposition velocity increases with increasing particle size. Vong *et al.* (2004) recorded deposition velocities greater than $2\,mm\,s^{-1}$ for PM_{10} particles over grassland. If the sulfate and chloride were in particularly coarse particles, deposition velocities would potentially be skewed towards a higher deposition velocity.

Secondary ammonium compounds are typically found in the accumulation mode (0.1 to $1\,\mu m$), while sea salt is found in super-micron particles (Myhre *et al.*, 2006). Although measurements of particle size were not made during this campaign, measurements of aerosol species (including Cl^- and SO_4^{2-}) in the $PM_{2.5}$ and

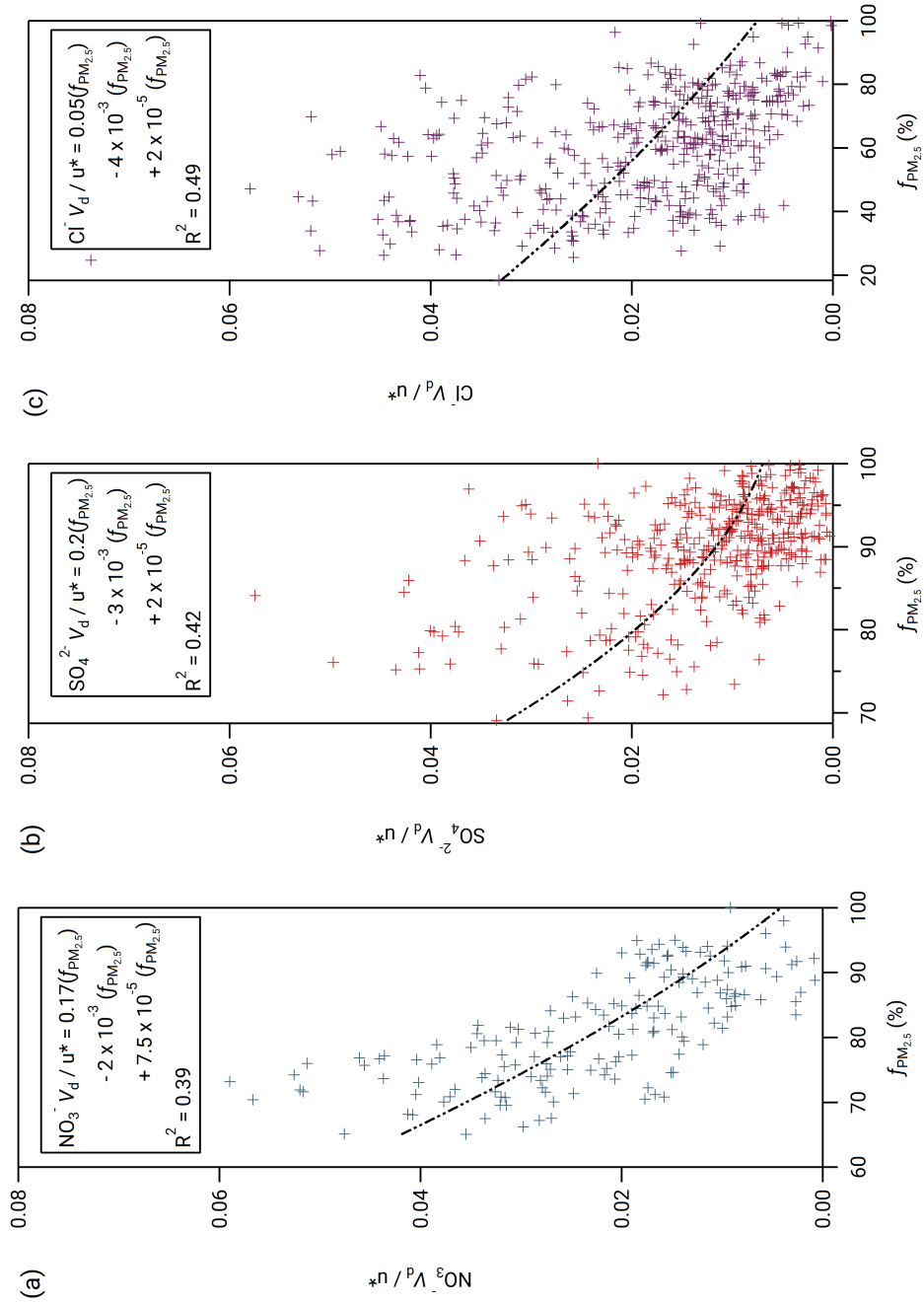

Figure 4.12: The normalised deposition velocity as a function of $f_{\mathrm{PM2.5}}$ (expressed as a %) for **(a)** nitrate, **(b)** sulfate and **(c)** chloride, derived from the MARGA measurements at Auchencorth Moss.

PM_{10} size fractions were taken by a two-channel Monitor for Aerosols and Gases in Ambient Air (MARGA, Applikon B.V., the Netherlands) instrument located at Auchencorth Moss, 12 km south-west of Easter Bush. Aerosol concentration data were taken from an online database of MARGA measurements (DEFRA, 2018). Agreement between MARGA and GRAEGOR aerosol concentrations was excellent (with correlations for SO_4^{2-} with $R^2 = 0.95$, and for Cl^- with $R^2 = 0.91$ between MARGA PM_{10} and GRAEGOR TSP). As proxy for a particle size measurement, the proportion of $PM_{2.5}$ to PM_{10} was used, with a lower proportion of $PM_{2.5}$ indicating a greater proportion of coarse aerosol and a corresponding larger deposition velocity based on process-orientated modelling. To a first-order approximation, particle deposition velocities scale with u_* (Pryor et al., 2008). Figure 4.12 shows plots of the normalised deposition velocities (V_d/u_*) against the fraction of the PM_{10} mass contained in $PM_{2.5}$ at Auchencorth Moss ($f_{PM_{2.5}} = PM_{2.5}/PM_{10}$) for nitrate (a), sulfate (b) and chloride (c).

While the dynamic range of $f_{PM_{2.5}}$ varied between compounds, third-order polynomial curves consistently describe the relation between the proportion of $PM_{2.5}$ to overall PM and the normalised V_d for nitrate, sulfate and chloride, suggesting – in line with Slinn (1982) – that deposition velocity increases strongly with increasing particle size above 0.1 μm particle diameter. However, the relationship – although statistically significant – shows significant variability, which may be due to measurement uncertainty, but might also reflect the additional effect of atmospheric stability on particle fluxes (Wesely *et al.*, 1985; Petroff *et al.*, 2008) or differences in the size distribution between the Auchencorth and Easter Bush measurement sites. It must be stressed that the proportion of $PM_{2.5}$ to PM_{10} is a proxy measurement for particle size and can only differentiate the proportions of aerosol of diameter less than or greater than 2.5 μm.

By contrast, the median deposition velocity of 0.37 mm s^{-1} for NH_4^+ was much smaller and within the range of previous measurements of dry deposition velocities

of accumulation mode particles to grassland. The average $f_{PM_{2.5}}$ for NH_4^+ recorded was 96 %, compared to 78 % for NO_3^- and 86 % for SO_4^{2-}, suggesting that virtually all of the NH_4^+ measured was contained in fine particles, within the measurement error. The average normalised deposition velocity (V_d/u_*) of NH_4^+ of 0.04 was in the range of the values for the other compounds evaluated at $f_{PM_{2.5}} = 100\,\%$.

Thus, the relatively high deposition velocities for Cl^-, NO_3^- and SO_4^{2-} (compared with NH_4^+) are a result of some of these compounds being contained in coarse aerosol. This is consistent with the ion balance (Fig 4.11), which suggests that some of these compounds are balanced by sea-salt Na^+, which is found mostly in the coarse fraction.

It should be noted that the increase in V_d with increasing contribution of coarse aerosol only accounts for the size dependence of the processes of impaction and interception. As a non-turbulent process, gravitational sedimentation is not reflected in micrometeorological flux measurements and the sedimentation velocity would need to be added to the deposition velocity derived here.

Trace gas deposition velocities

Median diel deposition velocities for HNO_3 and HCl closely matched the theoretical maximum deposition velocities within the uncertainty of the measurement (Fig.4.8), which closely conforms to their expected physico-chemical behaviour. Both HNO_3 and HCl are reactive and highly water soluble, and consequently it is expected that their deposition velocities should equal the theoretical maximum and that the canopy resistance for these species should be equal to zero Dollard *et al.* (1987). The close agreement between V_d and V_{max} during most of the campaign suggests that chemistry is not affecting the fluxes and that the standard

aerodynamic gradient method is therefore applicable. However, significant deviations of the calculated deposition velocity from the theoretical maximum for HNO_3 exist: R_c values for HNO_3 were particularly large 40 h after fertilisation, from 15 to 16 June, when the mean R_c value was 14.8 s m^{-1}. Conversely, there were periods when the V_d for HNO_3 exceeded the V_{max}, such as on 13 June at 13:00 h, when V_d for HNO_3 was recorded as 56.8 mm s^{-1} compared with a calculated maximum of 17.5 mm s^{-1}.

Reductions in V_d for HNO_3 (or in other words a non-zero R_c) have been linked to ground-level sources or non-zero vapour pressures of HNO_3 over nitrate-containing aerosol (particularly, NH_4NO_3), which may evaporate from aerosol within the air space below the measurements or previously deposited to leaf surfaces (Brost *et al.*, 1988; Kramm and Dlugi, 1994; Nemitz and Sutton, 2004). By contrast, values of V_d for HNO_3 that exceed the theoretical maximum could suggest the presence of an additional sink for HNO_3, which would potentially arise as the result of NH_3 reactions with HNO_3 to form NH_4NO_3 (Nemitz *et al.*, 2000b; Van Oss *et al.*, 1998). The higher V_d values for HNO_3 during the fertilisation period, followed by a higher R_c value 40 h afterwards, could suggest the formation of NH_4NO_3 immediately following fertilisation followed by its volatilisation soon after. Indeed, the exceedance of V_{max} coincided with upward fluxes of NH_4^+ and NO_3^- (Fig.4.9) and this suggests that, during the period after fertilisation, the increase in NH_3 concentration led to an exceedance of the equilibrium vapour pressures of NH_4NO_3 near the ground, resulting in partitioning of NH_3 and HNO_3 into the aerosol phase. This would have constituted an additional airborne sink for HNO_3 ($V_d > V_{max}$) as well as a source (apparent emission) for NH_4^+ and NO_3^- as previously reported by Nemitz et al. (2009a). Additionally, NH_4NO_3 formation can also be investigated by comparing the gas phase concentration product of the precursor gases, i.e, $K_M = [NH_3][HNO_3]$ with theoretical equilibrium constant

of NH_4NO_3, K_e Twigg *et al.* (2011). If K_M exceeds K_e, then there exists the potential for aerosol formation.

It should be noted that during this period the aerodynamic gradient method does not derive accurate fluxes because the condition of flux conservation is not met (Wolff *et al.*, 2010b), and this period has therefore not been included in the diel cycles and summary statistics presented above.

By contrast, fluxes of total ammonium (tot-NH_4^+ = NH_4^+ + NH_3) and total nitrate (tot-NO_3^- = NO_3^- + HNO_3) would be conserved, as the effect of gas–particle interactions are not considered, and their assessment provides additional information on the processes occurring during periods when fluxes are not conserved with height. By using this method of converting to conservative exchange fluxes, periods of flux divergence can be identified.

Prior to the fertilisation event on 13 June, the fluxes for tot-NO_3^- were universally depositional to the surface, while fluxes of tot-NH_4^+ were bidirectional with significant variation. Consequently, flux divergence is not considered to have occurred prior to fertilisation on the 13 June. However, 6 h after fertilisation, a significant emission event of tot-NO_3^- was observed lasting for 6 h. Interestingly, this indicates that the apparent NO_3^- emission during this period (Fig.4.9) exceeded the measured deposition of HNO_3 and that there must have been a net source of NO_3^- at the surface during this period.

Upward fluxes have previously been reported in the literature where they were attributed to the volatilisation of NH_4NO_3 from leaf surfaces (Neftel *et al.*, 1996) or alkyl nitrate chemistry (Farmer and Cohen, 2008). Primary emissions of HNO_3 could arise from the heterogeneous reaction of NO_2 with water (Harrison *et al.*, 1996):

$$2NO_2 + H_2O \longrightarrow HONO + HNO_3. \quad (4.14)$$

Kleffmann (2007) suggests that HNO_3 could be formed by the reduction of NO_2 on organic sources of humic acid, a process that would also lead to the production of HONO. The formation of HNO_3 inferred from observations coincided with emissions of HONO postfertilisation. However, as discussed previously, this reaction is slow and, while possibly contributing to some of the observed HONO emission, may not be able to account for the majority of observed emissions.

A second potential pathway is the emission of HONO from the soil. As described by Scharko *et al.* (2015), the oxidation of ammonium by microbes in soils with high nitrification rates can lead to biogenic emissions of HONO. The addition of urea to the agricultural soil at Easter Bush would lead to an increase in soil NH_4^+ concentrations and subsequently, through oxidation by soil microbes, the observed emission of HONO.

4.4.3 Daytime source of HONO

As shown in Fig.4.5, the median diel concentrations for HONO recorded by the GRAEGOR at 2.4 m do not drop below the detection limits of the instrument, determined to be 30 ng m^{-3} from calibrations carried out during the campaign. This is contrary to what would be expected based solely on the photolysis rate of HONO, which would suggest that, after accumulation of HONO during nighttime, rapid photolysis should reduce concentrations to below the detectable levels for measurement during early morning (Pagsberg *et al.*, 1997). As measurement approaches have improved over the past 10 years, a growing number of measurements have revealed non-negligible HONO daytime concentrations at rural (Acker *et al.*, 2006; Su *et al.*, 2008; Sörgel *et al.*, 2011), agricultural (Laufs

et al., 2017) and urban (Lee *et al.*, 2016) sites, including previous studies at the Easter Bush site (Twigg *et al.*, 2011).

4.4.4 Comparison of GRAEGOR with other instrumentation

Comparison of nitrous acid measurement between GRAEGOR and LOPAP

The comparison between the LOPAPs and the GRAEGOR revealed that both sample boxes of the GRAEGOR measured higher HONO concentrations than the LOPAP, principally due to the presence of a constant concentration offset of 0.01 to 0.02 $\mu g\,m^{-3}$ of HONO. Previous comparisons of measurements of HONO have been between the wet annular rotating denuder, as used in the GRAEGOR, and optical absorption techniques, primarily differential optical absorption spectroscopy (DOAS) instruments. In those comparisons, it has been found that HONO measurements by WRD, particularly during daytime and at low concentrations, tend to be significantly higher than DOAS measurements (Appel *et al.*, 1990). By comparison, the LOPAP shows good agreement in HONO measurements with the DOAS (Kleffmann *et al.*, 2006), as the DOAS method is a molecule-specific method and the LOPAP method measures any potential NO_x artefact.

The higher concentrations recorded by the GRAEGOR can be explained by the presence of chemical interferences that occur on the inlet, at the air–liquid interface and within the sampling solution. As the WRD uses a liquid film to sample HONO, and as HONO can form heterogeneously on such surfaces, overestimation of HONO can occur. Furthermore, interferences by chemical reactions of NO_2 with hydrocarbons within the sampler can lead to a further

interference (Gutzwiller *et al.*, 2002), particularly in proximity to diesel emissions. It has also been shown that, in high-alkalinity sampling solutions, mixtures of SO_2 and NO_2 can add a further interference to measurements (Spindler *et al.*, 2003). Finally, photolytically induced artefacts can be introduced in the sampling lines that connect the GRAEGOR sampling box to the detector unit (Kleffmann and Wiesen, 2008). The LOPAP, which is also a wet-chemistry-based instrument, is designed to minimise the chemical interferences and artefacts that can be introduced in other wet-chemistry instruments.

A comparison between daytime (06:00 to 18:00) GRAEGOR HONO concentrations and LOPAP HONO concentrations found only a slightly greater difference than the comparison between nighttime (19:00 to 05:00) concentrations recorded by the GRAEGOR and LOPAP. While previous comparisons between the DOAS and the WRD found that daytime concentrations measured by the WRD were higher than the DOAS compared to nighttime measurements, these studies were generally conducted in urban areas where both HONO and NO_x concentrations were high (Febo *et al.*, 1996), in contrast to the low concentrations at Easter Bush. The implementation of thermal insulation material around the GRAEGOR sampling lines may have also reduced the influence of photolytic artefacts in exposed sampling lines during the day, which would have elevated daytime HONO measurements recorded by the GRAEGOR.

Spindler *et al.* (2003) developed the following quantification of the chemical artefact produced by the mixing of NO_2 and SO_2 in highly alkaline sampling solutions for HONO measurements in their investigation of SO_2 and NO_2 chemical interference, with all concentrations measured in ppb.

$$[\mathrm{HONO}]_{\mathrm{artefact}} = 0.0056\,[\mathrm{NO_2}] + 0.0022\,\mathrm{ppb}^{-1}\,[\mathrm{NO_2}]\,[\mathrm{SO_2}] \qquad (4.15)$$

The first term describes the heterogeneous formation of HONO by reaction of NO_2 with water alone, and the second describes the aqueous-phase reaction of NO_2 and SO_2. Using measurements of SO_2 and NO_2 concentrations, the HONO artefact for the period of the GRAEGOR–LOPAP comparison was calculated and subtracted from the HONO concentrations recorded by the GRAEGOR. A linear regression between the concentrations recorded by GRAEGOR sample box 2 and LOPAP (2.0 m), which had the best agreement without artefact reduction, indicated better agreement after the correction for the artefact ($\mathrm{GRAEGOR}_{\mathrm{artefact}}$ (2.4 m) = 1.02 · HONO(HONO(LOPAP(2.0 m))), intercept = $5 \times 10^{-3}\,\mu\mathrm{g\,m^{-3}}$, $R^2 = 0.72$). Coefficient values were altered to produce the best possible agreement between GRAEGOR and LOPAP HONO values, arriving at a final artefact quantification of:

$$[\mathrm{HONO}]_{\mathrm{artefact}} = 0.0090\,[\mathrm{NO_2}] + 0.0034\,\mathrm{ppb^{-1}}\,[\mathrm{NO_2}]\,[\mathrm{SO_2}]\,. \tag{4.16}$$

Use of these altered coefficients further reduced the offset in GRAEGOR HONO measurements but also reduced the statistical agreement between GRAEGOR and LOPAP HONO measurements ($\mathrm{GRAEGOR}_{\mathrm{artefact}}$ (2.4 m) = 0.98 · HONO(HONO(LOPAP(2.0 m))), intercept = $2 \times 10^{-3}\,\mu\mathrm{g\,m^{-3}}$, $R^2 = 0.57$). Figure 4.13 shows the results of these analyses, with the linear regression between GRAEGOR sample box 2 (2.4 m) and LOPAP (2.0 m) without the artefact reduction applied to GRAEGOR sample box 2 (2.4 m) HONO concentrations, with Spindler's artefact reduction and with the modified Spindler's artefact reduction. While the agreement between the LOPAP and GRAEGOR is improved by the introduction of an artefact reduction value, it does not fully close the gap even with altered coefficient values, with a constant concentration offset still present in measurements. The possibility that a further artefact is introduced from NO_2

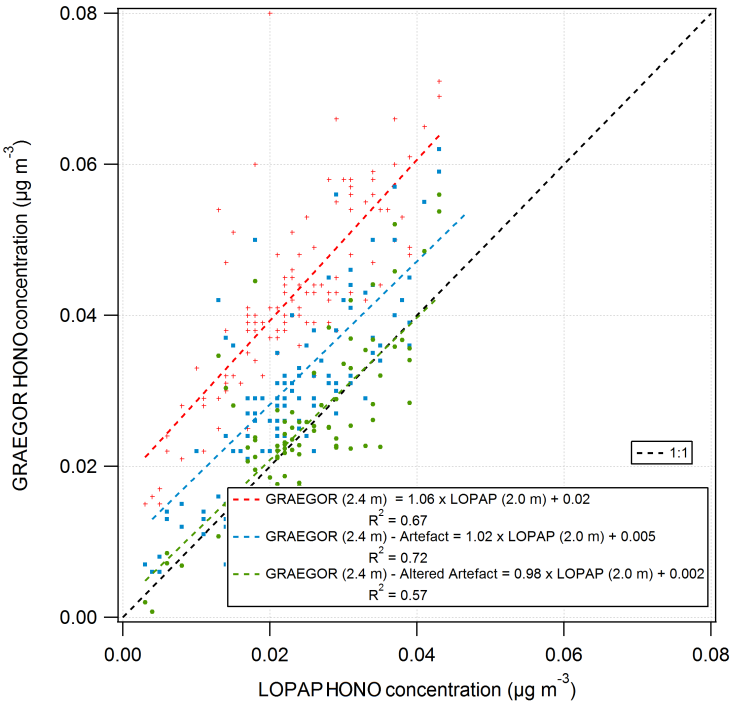

Figure 4.13: Simple linear regression analyses between GRAEGOR (2.4 m) and LOPAP (2.0 m) without artefact reduction (red), with Spindler's artefact reduction (blue) and with a modified Spindler's artefact reduction (green) applied to GRAEGOR (2.4 m) HONO concentration.

mixing with hydrocarbons would require further investigation, with concurrent measurements of hydrocarbons.

To determine whether the HONO concentration offset in the GRAEGOR measurements impacted on the measurements of HONO flux, a comparison between the HONO flux values derived from GRAEGOR and LOPAP measurements was conducted. Concurrent fluxes of HONO derived from LOPAP and GRAEGOR measurements exist for 72 hourly measurements, from 26 May to 6 June. Figure 4.14 shows (a) the full time series of concurrent HONO flux values derived from GRAEGOR and LOPAP measurements and (b) a scatter plot of GRAEGOR against LOPAP HONO flux values. Overall, GRAEGOR HONO fluxes are biased towards deposition, with greater deposition values and lesser emission values

compared to concurrent LOPAP values. This pattern would be consistent with the concept of an artefact formation dependent upon SO_2 and NO_2. SO_2 fluxes were unidirectionally depositional at Easter Bush during the campaign as measured by the GRAEGOR. Deposition of SO_2 would lead to greater formation of artefacts within the sample box set at a higher height, which is consistent with comparisons of HONO concentrations between each sample box of the GRAEGOR and each LOPAP instrument. In turn, this would lead to a bias in HONO flux values, resulting in a skew towards deposition. It should be noted that the sample size of concurrent measurements of HONO flux from GRAEGOR and LOPAP measurements is limited ($n = 72$).

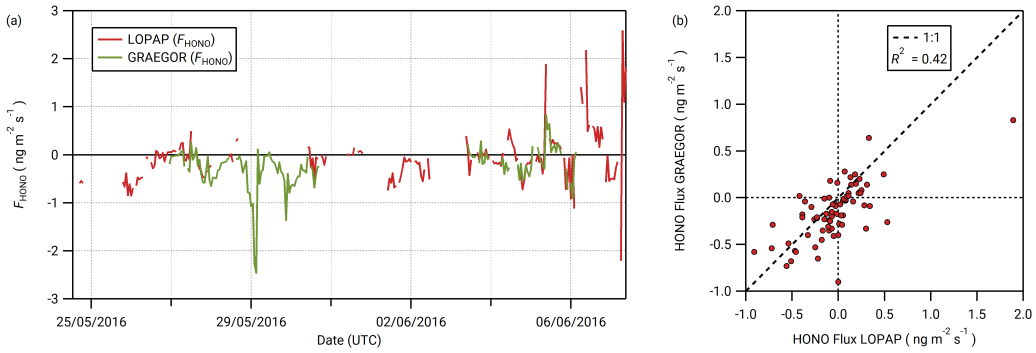

Figure 4.14: (a) Time series of concurrent flux measurements of HONO derived from LOPAP (red) and GRAEGOR (green) measurements. **(b)** Scatter plot of GRAEGOR HONO flux values against LOPAP HONO flux values.

Comparison of ammonia measurements with GRAEGOR and QCL

The comparison between the GRAEGOR and QCL found that, while there was reasonable agreement between the instruments, the GRAEGOR measured somewhat higher NH_3 concentrations than the QCL, by a factor of 1.2. Due to a lack of ancillary micrometeorological data during this campaign, the short overlap in measurements and necessary filtering of unreliable data, there are too few concurrent measurements (15 h) of flux between the QCL and the GRAEGOR

for a reliable comparison. There are also only 41 h of concurrent concentration measurements between the two instruments, which overlapped with a period of low NH_3 concentrations.

A similar comparison between a WRD system (the Ammonia Measurement by Annular Denuder with Online Analysis, AMANDA) and the QCL system was conducted at the same site in 2004 and 2005 by Whitehead *et al.* (2008). This comparison also found that the WRD system measured higher concentrations of NH_3 compared to the QCL, but at a far greater factor of 1.67. This difference was particularly pronounced during periods of low NH_3 concentrations, with better agreement recorded during a fertilisation and cutting event that occurred during that study. The older (pumped) QCL used during the earlier campaign did not derive its concentrations from first principles, in contrast to the QCL used during the comparison with the GRAEGOR reported here, which should be within 3 % of the absolute value without further calibration, according to the manufacturer. An inter-comparison between 11 different measurement techniques for NH_3 – including the AMANDA and two QCL instruments (the DUAL-QCLAS and the compact-QCLAS) – was conducted at the Easter Bush site in 2008 (von Bobrutzki *et al.*, 2010). While good statistical agreement was found in linear regression between the AMANDA and both QCL instruments for NH_3 concentrations throughout the entirety of the campaign ($R^2 = 0.92$ and $R^2 = 0.97$ for the compact-QCL and DUAL-QCLAS, respectively), there was less agreement between the instruments during periods of low (< 10 ppb) NH_3 concentrations ($R^2 = 0.81$ and $R^2 = 0.52$ for the compact-QCL and DUAL-QCLAS, respectively). During periods of low concentration, the QCL systems also underestimated NH_3 concentrations compared to the AMANDA.

Any errors in the GRAEGOR's internal NH_3 calibration system are unlikely to have an effect at low NH_3 concentrations. As a test, the calibration values obtained from all the internal calibration checks which were carried out through the

campaign (total calibrations = 5) were used to calculate the NH_3 concentrations during the period of QCL measurements. No significant concentration difference was found between the concentrations obtained by different calibration values, due to no systematic difference in agreement between the different calibration periods.

While there remain significant differences in measured NH_3 concentrations between the GRAEGOR and QCL, the improved agreement between those concentrations, particularly at low values, compared with the results from 2004 and 2005 suggests an improved methodology in use by the QCL system in place at Easter Bush. Further measurements, particularly of fluxes and during periods of high NH_3 concentrations, would be required for a more detailed analysis.

4.5 Conclusions

In this chapter, simultaneous measurements of the trace gases HCl, HONO, HNO_3, SO_2 and NH_3 as well as their associated water-soluble aerosols counterparts Cl^-, NO_2^-, NO_3^-, SO_4^{2-} and NH_4^+, before and after urea fertilisation of an agricultural grassland have been presented. The main findings for this study are described as follows.

1. Simultaneous measurements of the components of the $NH_3 - HNO_3 - NH_4NO_3$ triad suggested formation of ammonium nitrate postfertilisation. The use of the conservative exchange fluxes tot-NH_4^+ and tot-NO_3^- indicates the presence of a ground source of HNO_3 postfertilisation, which would be rapidly scavenged by high postfertilisation concentrations of NH_3 to form NH_4NO_3. Through this mechanism, use of urea fertiliser becomes a source of regional, rather than local, pollution.

2. The deposition velocities measured for the aerosol compounds Cl^-, NO_3^- and SO_4^{2-} were significantly larger than those measured for NH_4^+. After normalisation by turbulence, the measurements suggested a clear relationship between deposition velocity and particle size for Cl^-, NO_3^- and SO_4^{2-}, as parameterised using the proxy of compound in $PM_{2.5}/PM_{10}$, although the relationship shows significant variability. Therefore, the high deposition velocities for aerosol compounds recorded at the site are a result of a fraction of the compounds being contained in super-micron aerosol, such as sea-salt sulfate and sodium nitrate.

3. Evidence for a HONO daytime source at the site throughout the campaign adds to the growing body of past measurements that has found evidence for HONO daytime formation in rural, urban and agricultural areas. There is also evidence for the emission of HONO postfertilisation at the site.

This also appears to be the first time a comparison between measurements of HONO concentrations determined by the LOPAP and the GRAEGOR instruments has been documented. While good linear agreement exists between HONO measurements taken by GRAEGOR and LOPAP at both measurement heights, a consistent offset in GRAEGOR HONO measurements suggests the presence of chemically induced artefacts within the GRAEGOR system. This is potentially linked to atmospheric SO_x and NO_x concentrations.

Furthermore, this chapter presents a comparison between measurements of NH_3 concentration determined by the GRAEGOR and a QCL system. While changes to the QCL operation system compared to previous studies conducted at the site have resulted in better agreement between the GRAEGOR and QCL, particularly for low NH_3 concentrations, there still remain significant differences in NH_3 concentrations with larger values reported by the denuder system.

Future measurements of aerosol deposition velocities should aim to investigate the

effect of particle size upon deposition velocity, using a more robust measurement of particle size than used here. In addition, the ability of urea pellets to act as a potential surface on which heterogeneous formation of HONO and HNO_3 occurs should be investigated, particularly as the formation of these compounds can give rise to the formation of the regional pollutant NH_4NO_3.

Chapter 5

Concentrations and biosphere-atmosphere fluxes of inorganic trace gases and associated ionic aerosol counterparts over the Amazon rainforest

This chapter is based on a research paper currently in preparation for submission to the journal Atmospheric Chemistry and Physics. I took the GRAEGOR measurements, processed the data, and interpreted the results with help from Dr. C.F. Di Marco, Dr. E. Nemitz and Prof. M. Heal. Aerosol Chemical Species Monitor (ACSM) measurements of the concentrations of the water-soluble aerosols Cl^-, NO_3^-, SO_4^{2-} *and* NH_4^+ *were taken by Dr. S. Carbone. Meteorological data used in the campaign was taken by Dr. M. Sá and Dr. A. Arujo. I wrote the manuscript, with subsequent contributions from all co-authors.*

5.1 Introduction

The Amazon rainforest is one of the last remaining wildernesses on Earth, which through a select combination of environmental and geographical factors acts as a critical, living driver of global climate (Malhi *et al.*, 2008). A vast region of near-undisturbed verdant growth, covering almost 60% of the total land coverage of Brazil, it incorporates almost 40% of global tropical forest cover (Baccini *et al.*, 2012), stores an estimated 160 Pg of organic carbon in its soils (Gloor *et al.*, 2012), and harbours an immense atmospheric oxidative capacity driven by a powerful hydrological cycle (Lelieveld *et al.*, 2008). The strong coupling between the forest and the atmosphere, and the acutely sensitive feedback loops between them that regulates atmospheric composition, has earned the Amazon rainforest the sobriquets of the Green Ocean (Martin *et al.*, 2016; Roberts *et al.*, 2001; Williams *et al.*, 2002) and the biogeochemical reactor (Pöhlker *et al.*, 2012). It is therefore not only a near pristine microcosm of the pre-Anthropocene, but also acts as a continental natural laboratory to study unmodified surface-atmosphere exchange processes.

However, the combination of global climate change and the intensification of human development within and on the periphery of the rainforest has left the Amazonian biosphere in a precarious situation (Davidson *et al.*, 2012). Emissions of pollutants from agricultural activities, biomass burning and deforestation in the vicinity of the rainforest can perturb its surface-atmosphere exchange processes (Ganzeveld and Lelieveld, 2004) and cause changes in the local, regional, and even global climate (Lenton *et al.*, 2008).

While measurements of the atmospheric composition and surface-atmosphere exchanges process of the Amazon rainforest have been conducted since the late 1980s (Andreae and Andreae, 1988; Artaxo *et al.*, 2013; Harriss *et al.*, 1990; Martin *et al.*, 2010a), there remain significant knowledge gaps. Fundamental

questions such as the quantification of inorganic trace gas fluxes and the chemical speciation of coarse aerosols remain partially unanswered. Most pressingly, the need for long term, baseline measurements of gases and aerosols is required to quantify the impact of changing, anthropogenic conditions.

This latter point has been addressed by the establishment of the Amazon Tall Tower Observatory (ATTO). Located in a pristine, remote rainforest site 150 km NE of the city of Manaus, the site provides the baseline measurements of meteorology, trace gases and aerosol required to quantify the impact of natural and anthropogenic change (Andreae *et al.*, 2015). Recent output has included a long-term overview of cloud condensation nuclei over the Amazon Rainforest (Pöhlker *et al.*, 2016, 2018), observations of the enhancement of deep convection over the rainforest by ultra-fine particles (Fan *et al.*, 2018), and the influence of African volcanic emissions on long-range transport of pollutants to the ATTO site (Saturno *et al.*, 2018a). However, several inorganic trace gases and their aerosol counterparts, are currently not routinely measured due to the intense labour and resource requirements. The aim of this work was to make such measurements via an intensive observation campaign (IOC); in particular the aim was to derive the first time-series of simultaneous flux measurements of these species at this tropical rainforest site.

The gas species of interest for investigation at the ATTO site, but of which there are currently few short or long measurements of for tropical rainforest as a whole, include ammonia (NH_3), nitrous acid (HONO), hydrogen chloride (HCl), nitric acid (HNO_3) and the precursor to atmospheric sulfuric acid, sulfur dioxide (SO_2). As the primary basic gas in the atmosphere, NH_3 is important as the precursor of various ammonium salts, particularly NH_4NO_3, formed from the temperature and humidity dependent reaction between NH_3 and HNO_3. These salts act as light-scattering aerosols in the atmosphere, altering the Earths total albedo and consequently affecting regional and global climate (Fiore *et al.*, 2015).

Depending on environmental conditions, ammonium salts can be particularly long lived, and their eventual decomposition above nitrogen-limited ecosystems such as the Amazon rainforest can lead to disturbances in soil fertility, vegetation composition, and pollution of groundwater sources (Fowler *et al.*, 2013). The dynamic equilibrium between NH_3, HNO_3, and HNO_3 makes it difficult to determine the surface-atmosphere exchange of the individual members of the triad. To date, very few simultaneous measurements of each component in real time and with high time resolution exist (Trebs *et al.*, 2004; Wolff *et al.*, 2010a; Twigg *et al.*, 2011), with none over tropical rainforest.

Measurements of HONO are also critically required due to its potential contribution to atmospheric hydroxyl radical (OH) concentrations. OH radicals act as the primary daytime oxidant in the Amazon rainforest, and its formation is driven by photodissociation of ozone by UV radiation in the presence of water vapour. In the tropics, where there is intense incoming solar radiation and high humidity, concentrations of the OH radical are elevated relative to the global median (Kuhn *et al.*, 2007; Lelieveld *et al.*, 2002; Taraborrelli *et al.*, 2012). The photodissociation of HONO also results in the formation of OH radicals, and its contribution to sustaining the overall atmospheric oxidative capacity above the Amazon rainforest may therefore be critical. Non-negligible concentrations of HONO have been reported at urban (Lee *et al.*, 2016), agricultural (Laufs *et al.*, 2017; Twigg *et al.*, 2011) and rural European forest sites (Sörgel *et al.*, 2011) but there are currently no published measurements of HONO concentrations or fluxes above tropical rainforest.

In addition to the need for increased measurements of inorganic trace gases is the requirement for more observations of aerosols, particularly concentrations of chemically separated particulate in the coarse fraction, aerosol deposition velocities, and surface-atmosphere exchange behaviour. The majority of aerosol measurements made at the ATTO site have so far focused on the sub-micron (<

PM$_1$) size fraction, reflecting the importance of these particles in seeding cloud condensation nuclei and its seasonal and temporal variability driven by biomass burning (Artaxo *et al.*, 2013; Martin *et al.*, 2010b; Poschl *et al.*, 2010). Studies of coarse fraction aerosols, in contrast, are limited (Moran-Zuloaga *et al.*, 2018; Whitehead *et al.*, 2016), but have confirmed that coarse fraction aerosols are driven by the transport of dust, sea salt, primary biogenic aerosols, and particles transported in smoke from biomass burning. While number concentrations and chemically-speciated sub-micron aerosol particles have been measured, there are currently no flux or deposition velocity data for chemically-speciated fine or coarse-mode particles for the Amazon rainforest.

Determination of concentrations and fluxes of trace gases and aerosol components requires precise, high-time resolution measurements. Instruments must also be sensitive to the often very low concentrations in remote locations such as the Amazon rainforest. Compounding these requirements is the potential impact of gas-particle interactions that must be considered for accurate descriptions of surface-atmosphere exchange. This requires concurrent, multi-species measurements.

To address these demands, development in automated wet-chemistry instruments has led to the construction of the Gradient of Aerosols and Gases Online Registration (GRAEGOR), which is capable of measuring the concentrations of the inorganic trace gases NH_3, HCl, HONO, HNO_3 and SO_2 and their associated water-soluble aerosol counterparts NH_4^+, Cl^-, NO_2^-, NO_3^- and SO_4^{2-}, at two separate heights at hourly resolution (Thomas *et al.*, 2009). Fluxes for each of these species can then be derived from the two concentrations using a modified version of the aerodynamic gradient method (AGM), from which hourly values for the deposition velocities (V_d) of each species can also be determined. A number of campaigns have now confirmed the suitability of the GRAEGOR for

measuring vertical concentration gradients and fluxes of these trace gases and aerosol components (Thomas *et al.*, 2009; Twigg *et al.*, 2011; Wolff *et al.*, 2010b).

The overall aim of this study was to resolve some of the knowledge gaps in the biosphere-atmosphere exchange of inorganic trace gases and aerosols to and from tropical rainforest. We present here the concentrations, fluxes and deposition velocities of the trace gases NH_3, HCl, HONO, HNO_3 and SO_2 and their associated aerosol counterparts NH_4^+, Cl^-, NO_2^-, NO_3^- and SO_4^{2-}, as measured by the GRAEGOR wet-chemistry, two-point gradient system during a period of the 2017 dry season at the ATTO site. Using supplementary measurements of non-refractory, chemically differentiated sub-micron aerosol and concentrations of atmospheric elemental black carbon, we elucidate the lifetime, behaviour and origins of the trace gases and aerosols measured.

5.2 Methodology

5.2.1 Site Description

The measurements presented in this study are from an IOC conducted at the ATTO site from 6 October to 5 November. Situated on a level plateau located 12 km northwest of the Uatum River, the ATTO site lies 150 km northeast of the Manaus urban region. The site lies within the Amazon Time Zone (UTC 4 hours). All times presented in this work are given as local time. The vegetation is composed of dense, undisturbed upland rainforest (*terra firme*), with a rich tree species diversity (140 tree species ha^{-1}) (Andreae *et al.*, 2015). Based on the height of the tallest trees, the canopy height (h_c) is 37.5 m (Chor *et al.*, 2017). The site lies within the central Amazonian region, and experiences an annual oscillation between wet and dry seasons with transitional periods, driven by the

position of the inter-tropical convergence zone (ICTZ). The wet season, typically lasting between February and May when the ICTZ is south of the ATTO site, is characterised by north-easterly (NE) trade winds bringing air masses from the North Atlantic. These travel over hundreds of kilometres of untouched rainforest, leading to near pristine atmospheric conditions. Conversely, the dry season (which lasts from August to November), is characterised by air masses arriving from the south east, predominately travelling over urban and agricultural areas of Brazil. As a result, they often bring anthropogenic emissions of trace gases and associated aerosols to the ATTO site, leading to elevated concentrations of such species as black carbon and carbon monoxide (Saturno *et al.*, 2018b).

In addition to a base camp, electrical installations and various container units which house instruments, the site is composed of three measurement towers: an 80 m mast used for aerosol measurements; an 80 m walk-up tower (2°08.637 S, 58°59.992 W, 120 m a.s.l) which can accommodate larger instrumentation; and a 325 m tower (2°08.602′ S, 59°00.003′ W, 120 m a.sl.), on which instruments for long-term measurements are installed. The GRAEGOR system for this campaign was installed on the 80 m walk-up tower.

For the consideration of flux fetch distance, wherein accurate measures of fluxes for a surface are limited by the homogenous extent of the surfaces roughness elements, the 80 m walk up tower has a calculated fetch distance of 8 km based on the formulation given by Monteith and Unsworth (2013). While the region of *terra firme* forest extends for more than 10 km in all directions from the tower, and for several hundreds of kilometres in the north-east direction, it extends for only 5 km to the south, after which campina shrub-forest predominates to the edge of the Uatum River. Consequently, while the measured fluxes can be considered representative of the surrounding surface for most directions, fluxes from the south should be considered with some care.

5.2.2 Instrumentation

Gradient of Aerosols and Gases Online Registration (GRAEGOR)

The GRAEGOR (ECN, The Netherlands) is a semi-autonomous, wet chemistry instrument capable of online measurement of the concentrations of the water-soluble inorganic trace gases NH_3, HCl, HONO, HNO_3 and SO_2, and their associated aerosol counterparts NH_4^+, Cl^-, NO_2^-, NO_3^- and SO_4^{2-}, at hourly resolution at two separate heights (Thomas *et al.*, 2009). It consists of two sample boxes, set at two discrete heights, and a detector box at ground level. For this study, the sample boxes were set at two heights on the 80 m walk up tower $z_1 = 42\,\mathrm{m}$,and $z_2 = 60\,\mathrm{m}$.

Each sample box consists of a horizontally-aligned wet rotating annular denuder (WRD) (Keuken *et al.*, 1988) and a steam jet aerosol collector (SJAC) (Slanina *et al.*, 2001) connected in series. Air is simultaneously drawn through both sample boxes at a rate of 16.7 $\mathrm{L\,min^{-1}}$, kept constant through critical orifices located downstream of the SJACs. The inlets of the sample boxes are directly connected to the WRDs via a 0.3 m length high-density polyethylene (HDPE) tubing and a HDPE filter, which ensures a particle diameter cut-off of 0.2 nm as well as minimising losses of HNO_3 and NH_3. The air streams first pass through the WRDs, which are coated in a continuously replenishing sorption solution of 18.2 MΩ double deionized (DDI) water. Water-soluble trace gases contained within the laminar air flows diffuse into the liquid sorption solution, which is then fed to the detector box at ground level for analysis. Free of trace gases, the air streams then enter the SJACs and is mixed with water vapour fed from the DDI solution. This precipitates a supersaturation event, such that any particles contained in the air streams rapidly (0.1 s) grow to droplets of 2 μm diameter. The particle-containing droplets are then separated from the air steams by use of a cyclone, and are fed

as liquid samples to the detector box. To prevent biological contamination of the WRDs, the DDI feeding solution includes 0.6 mL of 30% hydrogen peroxide H_2O_2 (9.8 M) per 10 L of DDI.

A series of liquid pressure regulators were placed in the path of the liquid samples being fed to the detector box in order to prevent high hydrostatic pressures damaging the detector box, generated by the 40 m and 60 m liquid sample water columns. Liquid samples from the SJACs and WRDs are analysed for NH_4^+ and NH_3 respectively by a flow injection analysis (FIA) unit (Norman *et al.*, 2009; Wyers *et al.*, 1993). An 761 compact ion chromatography (IC) unit (Metrohm, Switzerland), equipped with a Dionex AS12 column, determines the concentrations of HCl/Cl^-, $HONO/NO_2^-$, HNO_3/NO_3^- and SO_2/SO_4^{2-} in the WRD and SJAC liquid streams respectively based on the measured anion conductivity of the samples compared to a 50 ppb Br^- reference standard added to the sample solution, taking into account the specific conductivities of the various ions compared with Br. Through a flow control scheme that enables continuous analysis of samples, the GRAEGOR provides a half hourly averaged measurement of trace gas and aerosol concentrations for each height and species.

Calibration of the FIA unit is autonomous, conducted 24 hours after the GRAEGOR begins measurement after start up and every 72 hours afterwards. The calibration uses three liquid NH_4^+ samples of 0, 50, and 500 ppb concentration. For this study, a total of 10 autonomous internal calibrations took place. The IC unit is continuously calibrated by the addition of the 50 ppb Br^- internal standard which is added to every liquid IC sample.

Sample box airflows were monitored continuously via the pressure drop across a flow restrictor, calibrated every five days using a 4140 Mass Flowmeter (TSI, USA). Additional checks of the instrument performance were conducted daily, for example visual checks that the WRDs or SJACs were not contaminated.

Due to the short inlet length and absence of any size selection, measurements of aerosol taken by the GRAEGOR are of water-soluble total suspended particulate (TSP). Furthermore, as the instrument measures any compound that dissociates to form the measured anion, the GRAEGOR has a number of potential artefacts. These include interferences in HONO measurements from NO_2 during periods of high SO_2 concentrations (discussed in detail in Section 5.4.3) (Spindler *et al.*, 2003) and interference in HNO_3 measurements at night from dinitrogen pentoxide (N_2O_5). Nevertheless, the GRAEGOR has proven capable of time-resolved flux measurements in previous campaigns (Twigg *et al.*, 2011; Wolff *et al.*, 2010b).

Supplementary Measurements

The ATTO site is equipped with an extensive suite of other instruments that provide long-term observations of meteorology, gases and particle properties. Wind speed, wind direction, sensible heat (H), and frictional velocity (u_*) were measured at 46 m on the 80 m walk-up tower using an eddy covariance system (Gill WindMaster). Continuous measurements of relative humidity and air temperature (both measured using a Vaisala HMP45C-L), rainfall (HS Hyquist TB4-L rain gauge), and net radiation (Kipp and Zonnen Net Radiometer) were also available. Concentrations of elemental black carbon (BC) were measured by an aethalometer (Magee Scientific AE33) at 325 m on the ATTO Tall Tower, and concentrations of carbon monoxide (CO) were measured at 52 m by a Picarro CKADS18. Also presented in this study are concentrations of NH_4^+, Cl^-, NO_3^- and SO_4^{2-} recorded by a Time of Flight Aerosol Chemical Species Monitor (ToF-ACSM, Aerodyne Inc.) at 321 m on the ATTO Tall Tower.

5.2.3 Micrometeorology

Modified Aerodynamic Gradient Method

The aerodynamic gradient method (AGM) is based upon flux-gradient similarity theory, which assumes that the flux of a tracer χ (such as a gas or particle) can be determined if its vertical concentration gradient and its diffusion coefficient are known (Foken, 2008). In this study, a modified hybrid form of the AGM is used, whereby the flux of a trace gas or aerosol species can be determined from the vertical concentration difference of the species (∂_χ), and a series of stability parameters (Flechard, 1998) and the friction velocity (u_*) derived by eddy-covariance from fast-response ultrasonic anemometry:

$$F_\chi = -u_* \kappa \frac{\chi_2 - \chi_1}{\ln\left(\frac{z_2-d}{z_1-d}\right) - \Psi_H\left(\frac{z_2-d}{L}\right) + \Psi_H\left(\frac{z_1-d}{L}\right)} \tag{5.1}$$

Here, κ is the dimensionless von Krmn constant ($\kappa = 0.41$); z_2 and z_1 are the heights at which the concentrations were measured (60 m and 42 m, respectively, in this study); d is the zero-plane displacement height in m; Ψ_H is the integrated form of the heat stability correction term, included to account for deviations from the log-linear profile; and z/L, also termed ζ, is a dimensionless constant of atmospheric stability that uses L, the Obukhov length. By convention, a negative flux value denotes deposition to the surface while a positive flux an emission from the surface.

The zero-plane displacement height, d, is a critical parameter for calculation of the flux, and for a closed canopy is related to the canopy height, $\mathrm{h_c}$ ($d = 0.66$ to $0.9 \times \mathrm{h_c}$). The analysis of this campaign uses a the value of $d = 33.4$ m as

determined by Chor *et al.* (2017) from measurements of the logarithmic wind profile.

Calculation of dry deposition velocities

The dry deposition velocity (V_{d}) of a trace species is the negative ratio of the flux of the species to its concentration at a reference height (z) with consideration to the zero-plane displacement height:

$$V_d(z-d) = -\frac{F_\chi}{\chi_z(z-d)} \tag{5.2}$$

For gases, the deposition velocity can also be determined from the resistance analogy for dry deposition (Fowler and Unsworth, 1979; Wesely, 1989). Here, V_{d} is the reciprocal of the sum of the aerodynamic resistance R_a, the quasi-laminar boundary layer resistance R_b, and the canopy resistance R_c:

$$V_d(z-d) = \frac{1}{R_a(z-d) + R_b + R_c} \tag{5.3}$$

R_a and R_b can be calculated from Eq.(5.4) and (5.5) Garland (1977):

$$R_a(z-d) = \frac{u(z-d)}{u_*^2} - \frac{\Psi_H(\zeta) - \Psi_M(\zeta)}{\kappa u_*} \tag{5.4}$$

$$R_b = (Bu_*)^{-1} \tag{5.5}$$

Where Ψ_M is the integrated form of the momentum stability correction term; and

B is the sub-layer Stanton number Foken (2008), the product of the turbulent Reynolds number and the Schmidt number.

If the V_{d} of a trace gas is known from its flux via Eq. (5.2), and R_a and R_b are calculated using micrometeorological data, the canopy resistance R_c can be inferred from rearranging Eq. (5.3). Similarly, a theoretical maximum deposition velocity (V_{max}) for a trace gas can be determined if R_a and R_b are known, by setting $R_c = 0$, which is equivalent to assuming perfect absorption of the gas by the canopy:

$$V_{\mathrm{max}}(z-d) = \frac{1}{R_a(z-d) + R_b} \tag{5.6}$$

The deposition of particles is more difficult to parameterise using the dry deposition resistance analogy, due to the different behaviour of particles compared to gases. In particular, the physical transport of particles through the quasi-laminar boundary layer is dependent on other processes than Brownian diffusion, such as impaction and interception. Consequently, although aerosol deposition velocities can be calculated as per Eq. (5.2), associated theoretical V_{max} which depends on measurements of R_b - cannot. Furthermore, due to the complexity in modelling the deposition process for larger particles, the deposition velocity for a particle is often replaced by an associated surface deposition velocity (V_{ds}) value, parameterised by (Wesely *et al.*, 1985):

$$V_{ds} = \frac{1}{\left(\frac{1}{V_d} - R_a\right)} \tag{5.7}$$

Correction factors for AGM in roughness sub-layer

The aerodynamic gradient method is ultimately on Monin-Obukhov similarity theory (MOST). One of the assumptions of MOST is that fluxes are measured in the inertial sub-layer, where fluxes deviate little with height. For this reason, the inertial sub-layer is often termed the constant flux layer (CFL). However, in the roughness sub-layer (RSL) which extends over the individual roughness elements of the surface, MOST does not strictly hold (Garratt, 1980). As a result, one of the underlying assumptions of the AGM is invalid, and consequently flux measurements using AGM can be erroneous (De Ridder, 2010).

Over forests, the roughness sub-layer can extend to almost three times the height of the canopy. Indeed, it is virtually impossible making gradient flux measurements that avoid measuring within the roughness sublayer, both for logistical reasons, but also because gradients become increasingly weak at higher height and because of the limitations of the CFL (Dias-Jnior *et al.*, 2019). As with other studies, the flux measurements presented here were made at least partially within the RSL of the rainforest, where the height of the canopy was 37.1 m and the roughness sublayer height therefore extended to an estimated 111 m.

As the profiles of concentrations and turbulence deviate from the logarithmic shape assumed by Eq. (5.1) within the RSL, fluxes calculated with the standard approach are likely to be underestimated compared to the true flux value (Raupach and Legg, 1984). However, the overall flux gradient relationship within the roughness sublayer can still hold (Simpson *et al.*, 1998) and be used to determine fluxes, but correction factors (also termed enhancement factors) must be implemented to account for measuring within the roughness sub-layer.

Work by Chor *et al.* (2017) at the ATTO site has led to development of such a correction factor, hereby termed γ_F, that can be applied to flux measurements made

using AGM above tropical rainforest. γ_F is dependent upon atmospheric stability, with a larger correction factor applied during stable atmospheric conditions compared to unstable conditions. This reflects the findings made by Zahn *et al.* (2016) over tropical rainforest that the solar zenith angle alters the predictions of scalars by MOST in the roughness sub-layer, with best agreement between observations and predictions at noon. Using measurements of L as a parameter for stable and unstable atmospheric stability, the values of γ_F developed by Chor *et al.* (2017) were applied to AGM flux calculations throughout this study, after it was verified that they provide good agreement between measured and theoretically derived deposition velocities for HCl and HNO_3 (cf Section 5.3.3 below).

5.2.4 Estimation of errors

GRAEGOR Limits of Detection (LOD)

The concentration limit of detection (LOD) (defined as 3σ above the background signal, where σ is the standard deviation) is of critical importance when measuring in regions of very low concentrations such as the Amazon rainforest. The LOD for each species measured by the GRAEGOR was determined from a field blank test, which was conducted during the campaign over a 22 hour period from 18:00 local time on 23 October to 16:00 local time on 24 October 2017. As detailed by Thomas *et al.* (2009), the field blank test to determine concentration LODs involves switching off the sample box air pump and sealing the air inlets of the samples boxes, while leaving the rest of the system operating under measurement conditions. LODs are then determined as 3σ from the resulting background signal. Concentration LODs determined during this campaign are presented in Table 5.1 for individual trace gas and associated aerosol species, respectively.

Error in concentration measurements

The overall error in concentration measurements (σ_m) for the trace gases and aerosol components can be expressed as the product of the mixing ratio (m) with the individual error measurements, estimated by using a Gaussian Error Propagation approach (Trebs *et al.*, 2004):

$$\sigma_{\mathrm{m}} = m\sqrt{\left(\frac{\sigma_{\mathrm{m_{liq}}}}{m_{\mathrm{liq}}}\right)^2 + \left(\frac{\sigma_{\mathrm{Br_{(std)}}}}{\mathrm{Br_{(std)}}}\right)^2 + \left(\frac{\sigma_{Q_{\mathrm{Br}}}}{Q_{\mathrm{Br}}}\right)^2 + \left(\frac{\sigma_{\mathrm{m_{Br}}}}{m_{\mathrm{Br}}}\right)^2 + \left(\frac{\sigma_{Q_{\mathrm{air}}}}{Q_{\mathrm{air}}}\right)^2}. \quad (5.8)$$

Each term in the propagation product denotes a measurement parameter and its associated standard deviation (σ_χ). In order, these are the mixing ratio of the compounds found in the liquid sample (m_{liq}), the mixing ratio of the Br^- standard ($Br_{(std)}$), the flow rate of the internal Br^- standard (Q_{Br}), the mixing ratio (as analysed by the IC system) of the Br^- standard (m_{Br}) and the air mass flow through the system (Q_{air}). This formulation applies strictly for calculating the error in concentration measurement of species measured using IC. For NH_3 and NH_4^+, which were analysed using FIA, the error in concentration measurement can also be determined by using Eq. (5.8) by omitting the terms for $Br_{(std)}$ and m_{Br} (and their associated σ_χ values), and replacing the factor Q_{Br} with Q_S, the flow rate of the NH_3/NH_4^+ liquid sample. Calculated uncertainties ranged from 9-19%, with Q_S, Q_{Br}, and m_{Br} the largest contributors (in ranked order) to total measurement uncertainty.

Error in flux measurements

As outlined by Wolff *et al.* (2010a) and in Chapter 4 of this work, the flux measurement error (σ_F) for a trace gas or aerosol is composed of two terms, the product of the error in the concentration difference (Δ_C) and its associated standard deviation (σ_{Δ_c}) with the error in the flux-gradient relationship (here, expressed as a transfer velocity), which is dominated by the error in u_* (σ_{u_*}); and the flux (F) of the trace gas or aerosol measured:

$$\sigma_F = F\sqrt{\left(\frac{\sigma_{u_*}}{u_*}\right)^2 + \left(\frac{\sigma_{\Delta_C}}{\Delta_c}\right)^2} \tag{5.9}$$

The error in the concentration difference can be determined through extended side-by-side measurements, where both sample boxes are placed at the same height and are supplied with a common air inlet. The instrument is then allowed to operate normally. The concentrations measured by both sampling boxes during this side-by-side sampling period are plotted against each other and fit with orthogonal regression. Using the orthogonal fit equation, the concentrations for the side-by-side sampling period and the wider campaign can then be corrected to account for systematic errors between each sample box. After correction, the remaining scatter in the side-by-side sampling concentrations (the residuals) is used to determine the error in the concentration difference. For the ATTO campaign, extended side-by-side measurements were conducted on 6 November at the end of the measurement period, with both sample boxes placed at 60 m.

The standard deviation in the measurement of u_* (σ_{u_*}) is dependent upon the sonic anemometer used to measure u_* and the atmospheric stability at the time of measurement (Foken, 2008; Nemitz *et al.*, 2009b). For this campaign, a value of 10% for σ_{u_*} was used during non-neutral conditions, and 12% for neutral conditions.

The median error values in flux calculations, as a percentage of flux values, is presented for trace gases and aerosol components in Tables 5.2 and 5.3, respectively. These values are in line with those calculated for previous studies (Thomas *et al.*, 2009; Wolff *et al.*, 2010a).

Table 5.1: Mean (μ_A), median (μ_M), arithmetic standard deviation (σ_A), maximum, minimum and number of measurements for water soluble aerosol and inorganic trace gas concentration measurements taken at 60 m on the 80 m tower, with associated limits of detection (LOD) values for each species based on 30-minute values.

(60 m)	μ_A $\mu g\,m^{-3}$	μ_M $\mu g\,m^{-3}$	σ_A $\mu g\,m^{-3}$	Max $\mu g\,m^{-3}$	Min $\mu g\,m^{-3}$	No. of Measurements	LOD $ng\,m^{-3}$
NH_4^+	0.30	0.30	0.16	0.73	0.01	508	190
Cl^-	0.23	0.14	0.22	1.35	0.01	516	15
NO_2^-	0.01	0.01	0.01	0.09	0.00	577	17
NO_3^-	0.47	0.41	0.33	2.07	0.05	489	147
SO_4^{2-}	0.51	0.49	0.25	1.12	0.07	528	109
NH_3	0.28	0.25	0.18	1.94	0.01	558	173
HCl	0.13	0.11	0.09	0.47	0.03	526	67
HONO	0.07	0.06	0.04	0.38	0.01	599	30
HNO_3	0.25	0.23	0.14	1.04	0.03	579	147
SO_2	0.23	0.21	0.11	0.84	0.01	549	156

5.3 Results

5.3.1 Meteorology and indicators of pollution

Figure 5.1 presents hourly time series of the net radiation, rainfall, relative humidity, air temperature, wind direction and wind speed measured during the

campaign. Presented in addition to the meteorological conditions are the mass concentrations of black carbon (M_{BC}) and carbon monoxide (c_{CO}). The values of M_{BC} and c_{CO} have been used in previous studies at ATTO as markers to demarcate periods of near-pristine and polluted conditions. Thus Pöhlker *et al.* (2018) defined pristine rainforest (PR) conditions as periods when M_{BC} values are <0.01 $\mu g\,m^{-3}$ for over 6 hours. Alternatively, or in combination with M_{BC}, periods when c_{CO} values are below the monthly background CO concentrations recorded at the Cape Point hemispheric background reference station (https://www.esrl.noaa.gov/gmd/ dv/site/CPT.html; last access: 21 November 2018) are also considered PR conditions. However, during this campaign, there were no recorded periods when M_{BC} or c_{CO} met these criteria, and therefore no period of PR conditions. This is typical for dry season conditions (Pöhlker *et al.*, 2016).

While PR conditions (according to the above definition) were not observed, there were periods when M_{BC} over a 6 hour period was close to falling below 0.01 $\mu g\,m^{-3}$. For example, between 12:00 on the 8 October and 09:00 on the 9 October, M_{BC} values varied between 0.01 and 0.02 $\mu g\,m^{-3}$. Periods where M_{BC} values approach the PR criterion were associated with periods of rainfall and north to north-easterly winds. For the remainder of this chapter, periods when the values of M_{BC} and c_{CO} approached conditions for PR status (0.01 $\mu g\,m^{-3}$ and 150 ppb, respectively, over 6 hours) are termed near-PR conditions.

Conversely, there are periods where M_{BC} and c_{CO} values notably exceed their mean values (0.04 $\mu g\,m^{-3}$ and 280 ppb respectively), as for example the period between 21 and the 25 October. During this time, values of M_{BC} increase steadily from 0.04 $\mu g\,m^{-3}$ to a final maximum of 0.12 $\mu g\,m^{-3}$ at 00:00 on the 25 October. A sharp decrease in M_{BC} occurs at 04:00 on the same day, coinciding with a period of precipitation, the first since the 18 October. This 5-day period is also noted for comparatively drier, warmer conditions and a prevailing wind direction

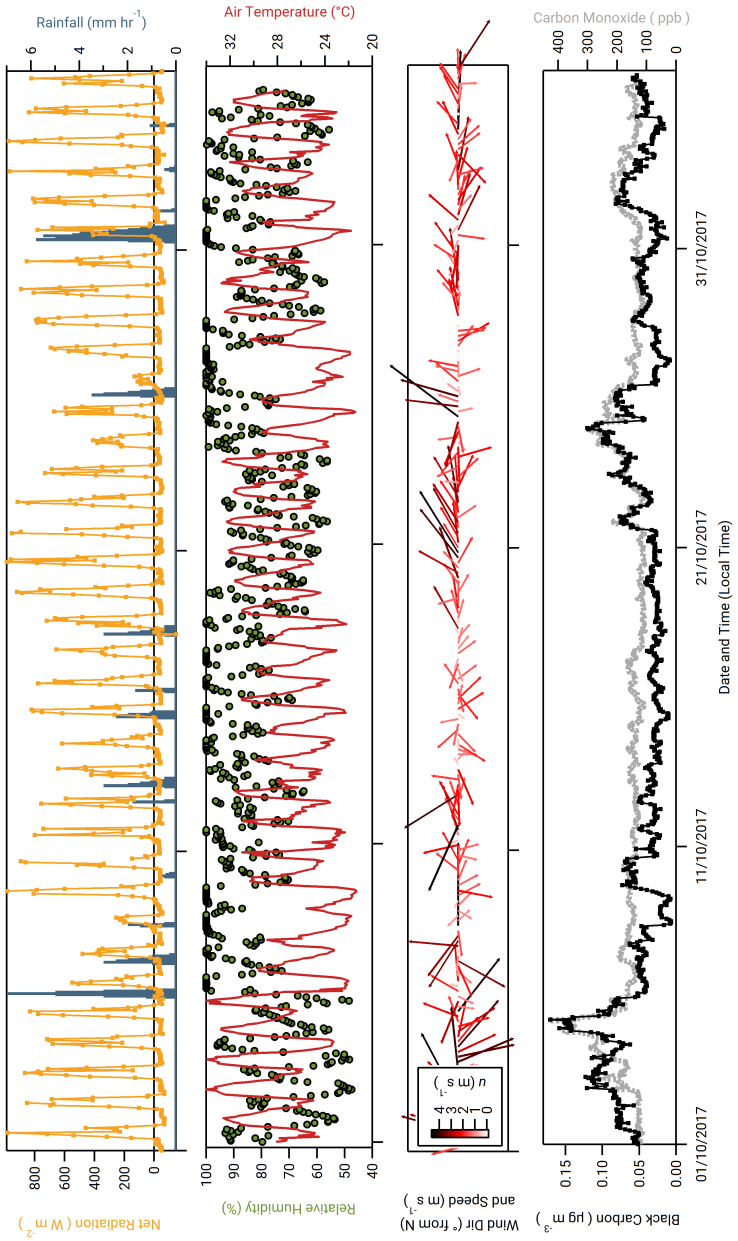

Figure 5.1: Meteorological and supplementary measurements taken during the campaign. From top, net radiation, hourly rainfall, relative humidity, air temperature, wind speed and wind direction (barbs scaled to wind speed, and orientated from 0° North) , and concentrations of black carbon and carbon monoxide.

from the east to south-east. Periods where there was a 6 hour exceedance of the mean value of M_{BC} (0.04 $\mu g\,m^{-3}$) with associated drier, warmer conditions are referred to hereafter as polluted conditions.

5.3.2 Concentrations of inorganic trace gases and associated aerosol counterparts

Summary statistics for the inorganic trace gases and associated aerosol counterparts measured at 60 m is presented in Table 5.1. The table also includes the associated limit of detection values, in $ng\,m^{-3}$. The times series of inorganic trace gas concentrations at 42 m and 60 m are shown in Figure 5.2, and the corresponding time series of associated aerosol counterpart concentrations are shown in Figure 5.3. For comparison, Figure 5.3 also presents the concentrations of particulate NH_4^+, Cl^-, NO_3^- and SO_4^{2-} measured by the ToF-ACSM taken at 321 m on the Amazon Tall Tower. Gaps in the GRAEGOR time series are due to automated calibrations of the instrument, instrument failure, and periods where liquid or air flow were unstable

Table 5.1 shows that the mean and median concentrations of all trace gases and associated aerosol species exceeded their limit of detection except for nitrite (NO_2^-). Concentrations of particulate NO_2^- are particularly difficult to measure using wet chemistry methods owing to its low ambient concentrations. Previous attempts to measure NO_2^- using the GRAEGOR at rural sites have also been unsuccessful (Wolff *et al.*, 2010b). Consequently, NO_2^- data are not discussed further in this chapter.

All aerosol species (with the exception of NO_2^-) had mean and median concentrations greater than the associated inorganic trace gas. This was the case at both measurement heights. For example, the mean and median concentration values of

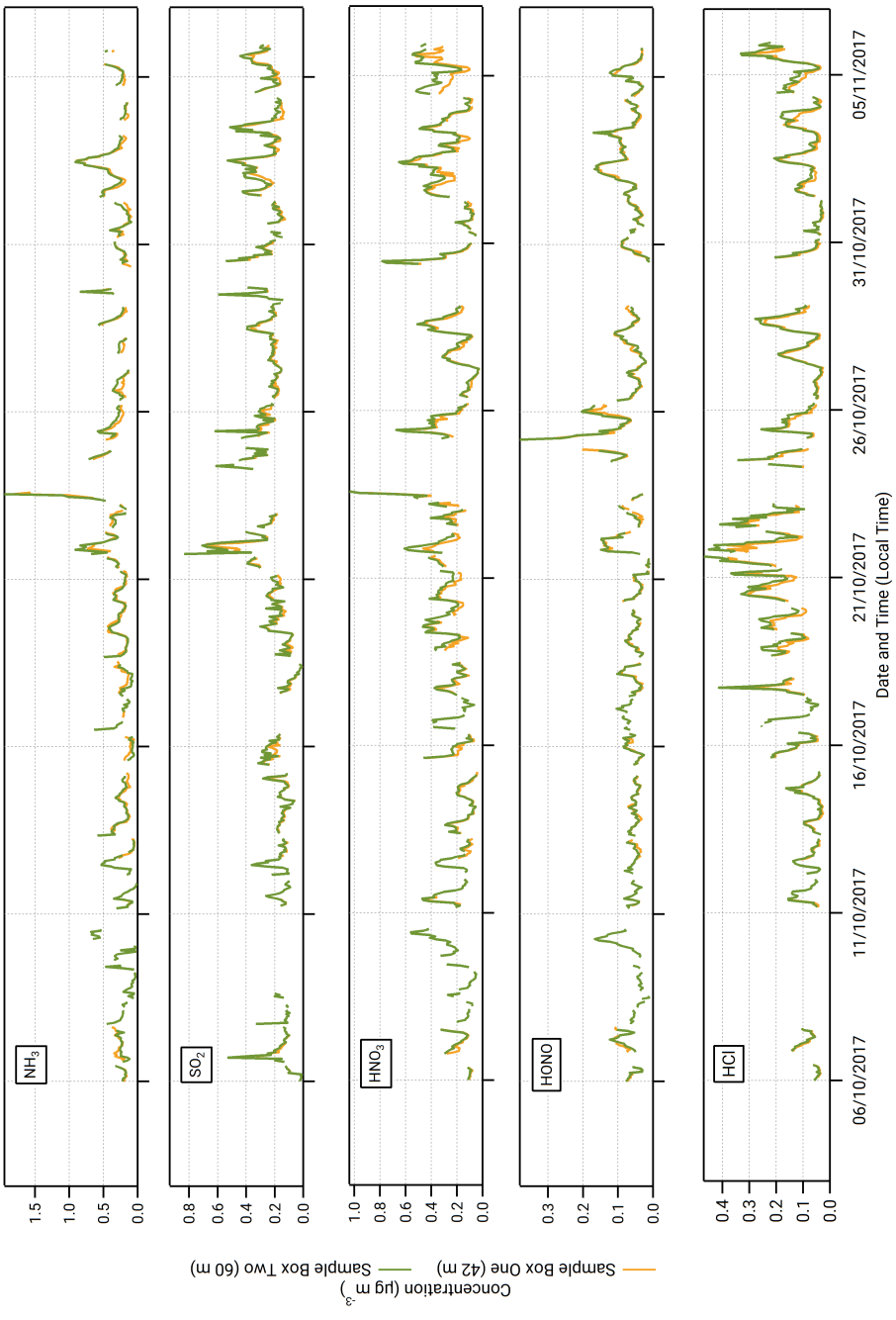

Figure 5.2: Time series of hourly concentrations of inorganic trace gas species measured by the GRAEGOR at 42 m (yellow) and 60 m (green) on the 80 m tower at the Amazon Tall Tower Observatory site.

NH_4^+ at 42 m (0.30 $\mu g\,m^{-3}$ and 0.28 $\mu g\,m^{-3}$ respectively) exceeded those recorded for NH_3 at the same height (0.27 and 0.22 $\mu g\,m^{-3}$). The difference is most pronounced between NO_3^- and HNO_3, and SO_4^{2-} and SO_2, with a mean value of 0.47 $\mu g\,m^{-3}$ for NO_3^- at 60 m compared to a corresponding mean value of 0.25 $\mu g\,m^{-3}$ at the same height for HNO_3; and a mean value of 0.51 $\mu g\,m^{-3}$ for SO_4^{2-} at 60 m compared to a mean value of 0.23 $\mu g\,m^{-3}$ for SO_2 at the same height. The predominance of aerosol phase over gas phase for these species has been noted at other rural and forest sites; for example Wolff *et al.* (2010b) reported median NO_3^- and HNO_3 concentrations of 0.48 $\mu g\,m^{-3}$ and 0.12 $\mu g\,m^{-3}$ using the GRAEGOR above a rural forest in SE Germany.

Concentrations varied between near-PR and polluted periods. Minimum values for all aerosol and gas species which fall below their respective instrumental LODs occurred during near-PR conditions. Conversely, the maximum concentration values recorded for all species occurred during the longest polluted period of the campaign (21 - 25 October). In particular, Cl^- and NO_3^- reach their respective maximum concentrations of 1.35 $\mu g\,m^{-3}$ and 2.07 $\mu g\,m^{-3}$ at 23:00 on 21 October. Concentrations of NH_3 and HNO_3 increase from 21 October to reach maximum values of 1.94 $\mu g\,m^{-3}$ and 1.04 $\mu g\,m^{-3}$ respectively at noon of 23 October.

Aerosol concentrations as recorded by a ToF-ACSM at 321 m and GRAEGOR show either good agreement or divergence, depending on the species. Of the aerosols measured, SO_4^{2-} has the best agreement in measurements between the ToF-ACSM and GRAEGOR. Linear regression analysis for the full campaign showed a near 1:1 agreement between SO_4^{2-} measured at 60 m by GRAEGOR and at 321 m by the ToF-ACSM, with marginally higher concentrations recorded by the GRAEGOR ($m = 0.89$, $R^2 = 0.45$). During the period from 18 to 26 October, agreement was particularly good ($m = 0.97$, $R^2 = 0.65$). Similarly, although not as statistically robust as for the SO_4^{2-} measurements, there is a near-linear agreement between NH_4^+ concentrations measured by GRAEGOR at

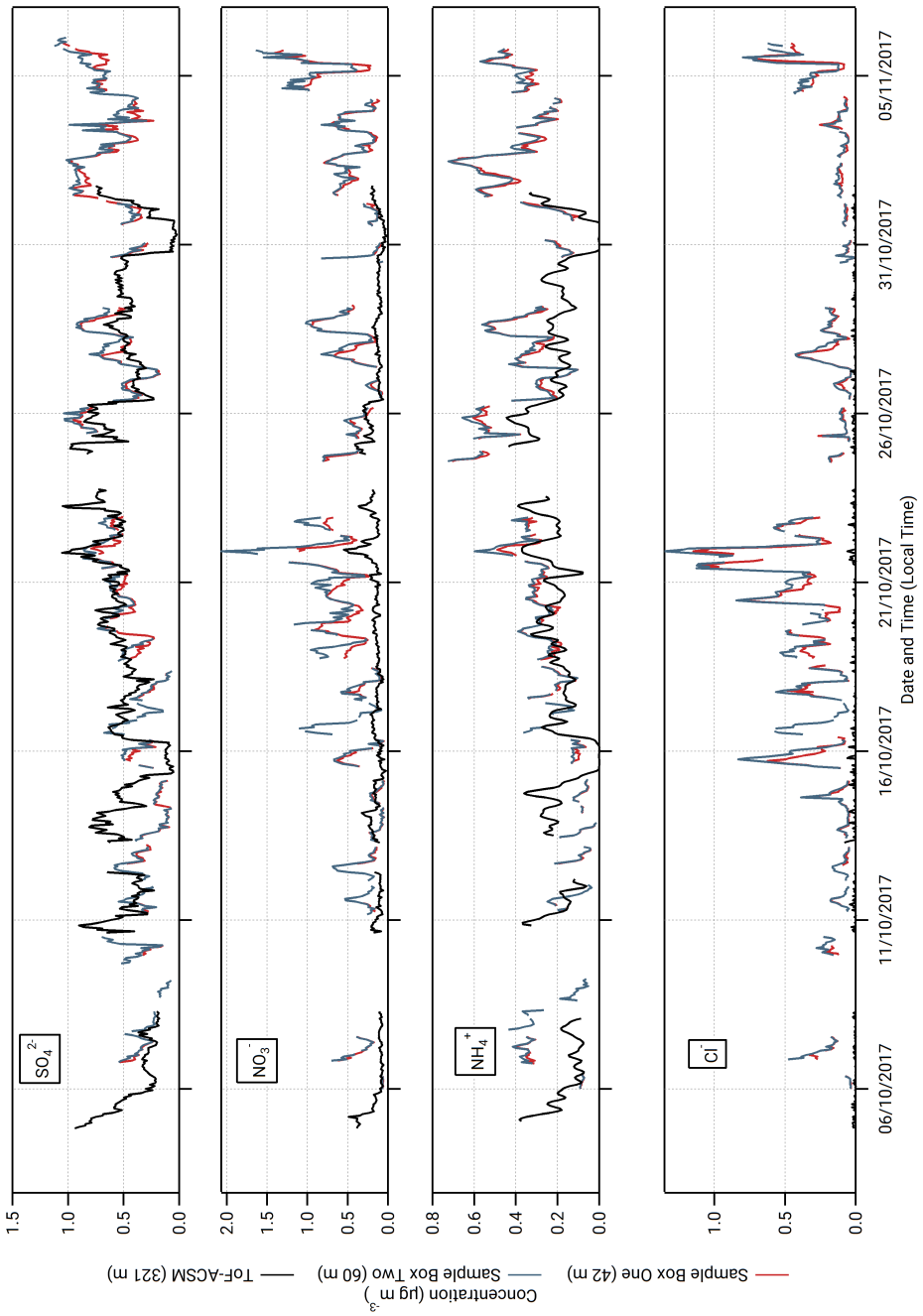

Figure 5.3: Time series of hourly concentrations of water-soluble aerosol species measured by the GRAEGOR at 42 m (red) and 60 m (blue) on the 80 m tower, and ToF-ACSM at 321 m (black) on the Main Amazon Tall Tower, at the Amazon Tall Tower Observatory site

60 m and ToF-ACSM at 321 m ($m = 0.85$, $R^2 = 0.35$). As with the comparison between SO_4^{2-} measurements, the GRAEGOR records higher concentration values for NH_4^+.

In contrast, there are significant differences between GRAEGOR and ToF-ACSM measurements for both NO_3^- and Cl^-. While there is some agreement in overall trends between GRAEGOR and ToF-ACSM measurements of NO_3^-, with both instruments recording a simultaneous maximum in NO_3^- (ToF-ACSM = 0.54 $\mu g\,m^{-3}$, GRAEGOR, 60 m = 2.07 $\mu g\,m^{-3}$ on 21 October 2018 23:00), in general the GRAEGOR measurements of NO_3^- are a factor of 3-4 greater than those from the ToF-ACSM. The difference in Cl^- concentration is even more pronounced. The median concentration for Cl^- from the ToF-ACSM is 0.02 $\mu g\,m^{-3}$; in comparison, the median value from the GRAEGOR at 60 m is 0.14 $\mu g\,m^{-3}$. At several points during the campaign, the ToF-ACSM does not record a value for Cl^-. In comparison, 93% of all measurements of Cl^- recorded by the GRAEGOR are above the detection limit of the instrument.

The median (0.06 $\mu g\,m^{-3}$) and mean (0.07 $\mu g\,m^{-3}$) values for the inorganic trace gas counterpart of NO_2^-- - nitrous acid, HONO - remained above the detection limit of the instrument (30 $ng\,m^{-3}$) at both sampling heights. Although the diel cycle of HONO exhibited a maximum during night and minimum during the day (0.02 $\mu g\,m^{-3}$ at 14:00), it remained above the detection limit even during daylight hours (Figure 5.4), which, given the high photolysis of HONO during daytime, implies the presence of a daytime source. Similarly, median diel SO_2 concentrations remained above the detection limit of the instrument throughout the campaign. SO_2 is usually considered a marker for anthropogenic emissions, and but its presence at concentrations above detectable limits during near-PR conditions might be at least in part supported by biogenic sources. Previous measurements had found SO_2 concentrations close to the lowest values observed in this study and had attributed them partly to biogenic emissions (Andreae

and Andreae, 1988; Andreae *et al.*, 1990). There are also periods where the trace gas HCl another marker of anthropogenic emissions - which originates from combustion activities and the reaction of sea-salt with HNO_3 - is recorded in elevated concentrations above its detection limit.

5.3.3 Fluxes, Deposition Velocities, and Canopy Resistances

Fluxes of inorganic trace gases

Figure 5.5 shows the average diel cycles of the deposition velocities in comparison with those of V_{max} for HCl and HNO_3. Two sets of values are presented values calculated using the standard modified aerodynamic gradient method discussed previously in Section 5.2.3 without the application of a correction factor for measuring within the roughness sublayer, termed pre-correction values; and values calculated with the application of a flux correction factor developed by Chor *et al.* (2017), γ_F, discussed previously in Section 5.2.3, which adjusts values obtained using the aerodynamic gradient method for measuring in the roughness sublayer, termed post-correction values. Due to their high water solubility (and resulting large effective Henry coefficient), HCl and HNO_3 are expected to deposit at V_{max} (Lelieveld and Crutzen, 1991), unless chemical conversions affect their fluxes (Nemitz *et al.*, 2000a; Twigg *et al.*, 2011). The correction brings the V_d for these gases in close agreement with V_{max}, within the measurement error. The correction increases the average V_d of HNO_3 from 10.2 to 12.4 mm s^{-1} (average V_{max} = 12.3 mm s^{-1}) and that of HCl from 12.5 to 15.2 mm s^{-1} (average V_{max} = 15.3 mm s^{-1}). This suggests that overall the Chor correction works well, and the remainder of the chapter will discuss post-correction values only. With this consideration in mind, Figure 5.6 shows the average diurnal cycles of the post-γ_F

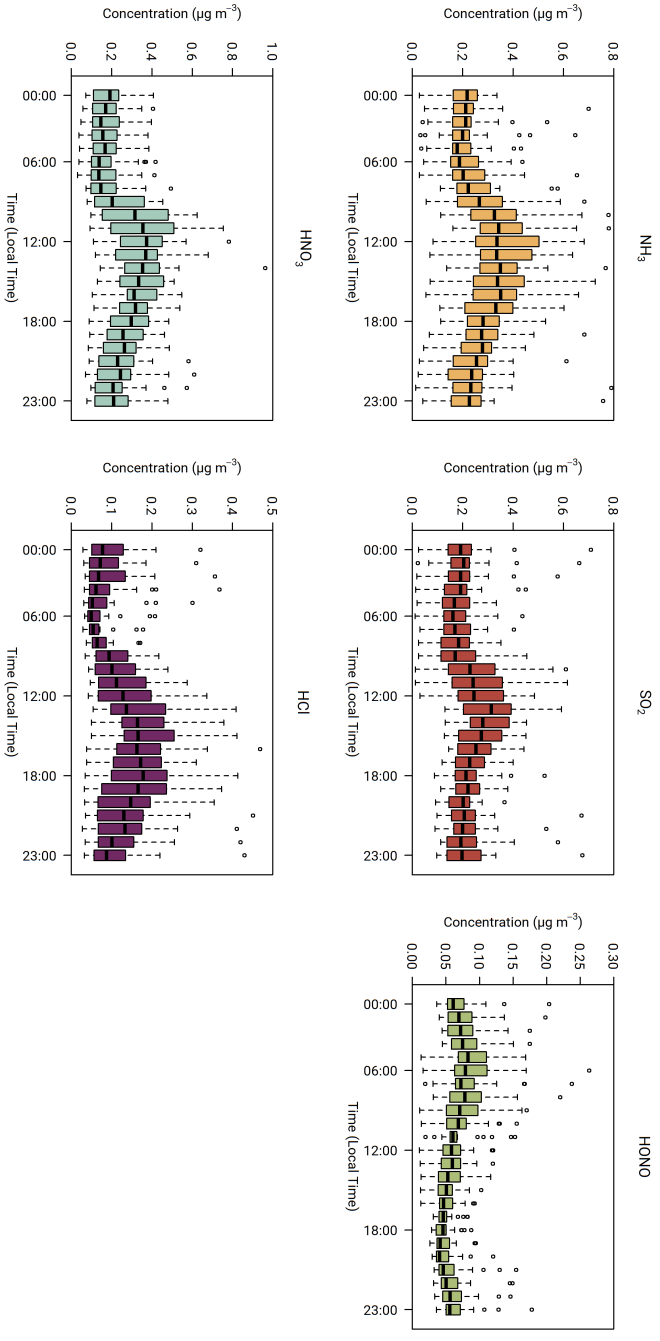

Figure 5.4: Median hourly diel concentrations for the inorganic trace gases (from left) NH_3, SO_2, HONO, HNO_3 and HCl at the 60 m sampling height measured during the campaign.

corrected deposition velocity in comparison with that of V_{max} for the remaining trace gases measured NH_3, HONO and SO_2.

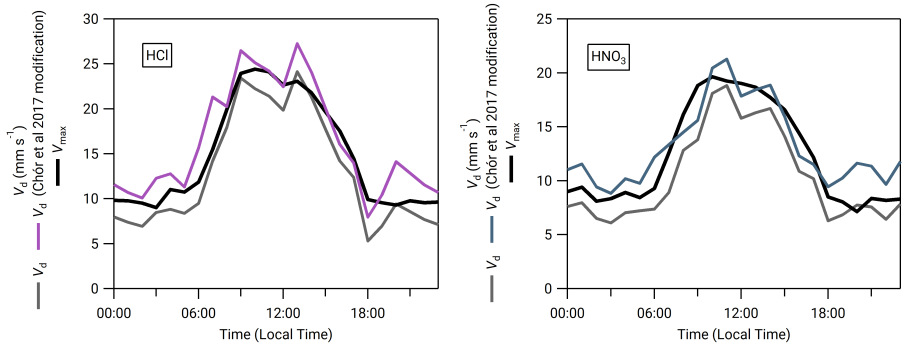

Figure 5.5: Inorganic trace gas deposition velocities (V_d) pre- and post- correction with γ_F (Chor *et al.*, 2017) and calculated theoretical maximum deposition velocities (V_{max}) for HCl and HNO_3.

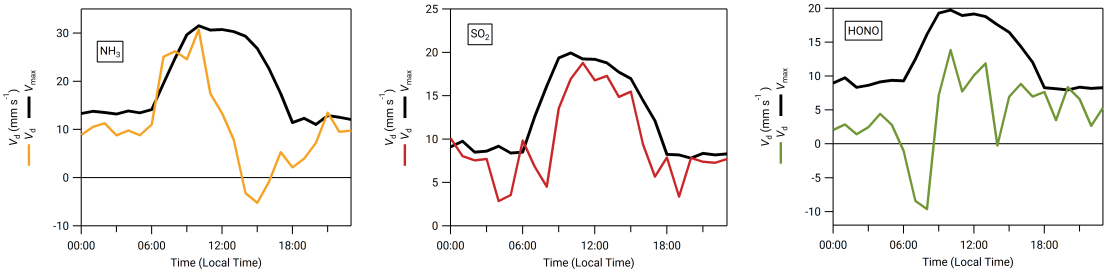

Figure 5.6: Inorganic trace gas deposition velocities (V_d) post correction with γ_F (Chor *et al.*, 2017) and calculated theoretical maximum deposition velocities (V_{max}) for NH_3, SO_2 and HONO.

Table 5.2 presents a statistical summary of the calculations for fluxes, deposition velocities (V_d), theoretical maximum deposition velocities (V_{max}) and canopy resistances (R_c) for the inorganic trace gases measured during the campaign. As already alluded to, with the roughness sublayer correction of Chor *et al.* (2017), HCl and HNO_3 both deposit at V_{max} within the error of the measurement, with a canopy resistance $< 3\ \mathrm{s\,m^{-1}}$.

Time series for the post-filtered, post-corrected fluxes of the inorganic trace gases measured are shown in Figure 5.7. The inorganic trace gases HNO_3, SO_2 and

Table 5.2: Mean (μ_{A}), median (μ_{M}), maximum and minimum values post-roughness sub layer correction for fluxes, deposition velocities (V_{d}), theoretical maximum deposition velocities (V_{max}) and canopy resistances (R_{c}) for the inorganic trace gases measured during Amazon Tall Tower Observatory campaign. The number of fluxes calculated is quoted as number of measurements, and the median error in flux measurements as a percentage of flux values for each individual trace gas species (σ_F) is included as part of the statistical summary for fluxes.

		NH_3	HCl	HONO	HNO_3	SO_2
Flux ($\mathrm{ng\,m^{-2}\,s^{-1}}$)	μ_{A}	-2.83	-2.30	-0.34	-3.56	-2.41
	μ_{M}	-1.81	-1.44	-0.23	-2.29	-1.22
	Max	9.47	0.67	3.97	2.39	1.17
	Min	-30.2	-16.9	-7.10	-25.2	-33.1
	No. of measurements	434	400	422	405	405
	σ_F (%)	33	56	54	45	63
V_{d} ($\mathrm{mm\,s^{-1}}$)	μ_{A}	10.5	15.2	4.49	12.4	10.4
	μ_{M}	8.26	14.3	4.08	11.9	7.08
	Max	79.8	78.3	63.9	63.3	74.3
	Min	-36.3	-9.76	-141	-21.9	-3.43
V_{max} ($\mathrm{mm\,s^{-1}}$)	μ_{A}	19.3	15.3	12.6	12.3	12.9
	μ_{M}	18.1	14.5	12.1	11.9	12.4
	Max	49.9	39.1	31.8	31.2	32.5
	Min	0.75	0.60	0.49	0.49	0.52
R_{c} ($\mathrm{s\,m^{-1}}$)	μ_{A}	52.7	2.92	165	1.42	16.8
	μ_{M}	64.0	1.57	164.8	1.81	33.5

HCl were almost entirely deposited to the surface. Any upward fluxes calculated for these gases lay within their respective error ranges. Fluxes which exceed the median values for these gases, and the maximum calculated fluxes for these species, were recorded during the drier, warmer polluted conditions that prevailed from 18 October to 26 October 2017. For example, the maximum calculated flux for SO_2 , and the largest flux of any species measured during the campaign, was -33.2 $ng\,m^{-2}\,s^{-1}$ which occurred on 21 October at 11:00. Conversely, while increased deposition fluxes are observed for NH_3 and HONO during this same period, multiple periods of emission were recorded for these gases throughout the campaign. Although the predominant pattern of surface-atmosphere exchange throughout the campaign for HONO and NH_3 was deposition to the surface, as reflected in their respective median flux and V_d values, periods of emission are a significant proportion of overall surface-atmosphere exchange. 26% of calculated flux values for HONO, and 19% for NH_3, were positive i.e. emissions from the surface. The diel pattern of emissions is highlighted in Figure 5.8, which presents median diel values for the inorganic trace gas species measured. HONO emissions are concentrated in the early morning, with positive median values indicating a prevalent pattern of emission present at 07:00 and 08:00. In contrast, NH_3 emissions were found in the afternoon, from 14:00 to 16:00 hours. The remaining trace gases HCl, HNO_3 and SO_2 recorded maximum deposition fluxes in the afternoon, with decreased fluxes during the night and early morning hours.

Fluxes of associated ionic aerosol counterparts

A statistical summary of fluxes and deposition velocities for the aerosol species measured during the campaign is presented in Table 5.3. As for the inorganic trace gas fluxes, Table 5.3 presents aerosol flux and deposition velocity values pre- and post- correction with γ_F. Also included for each species is the minimum

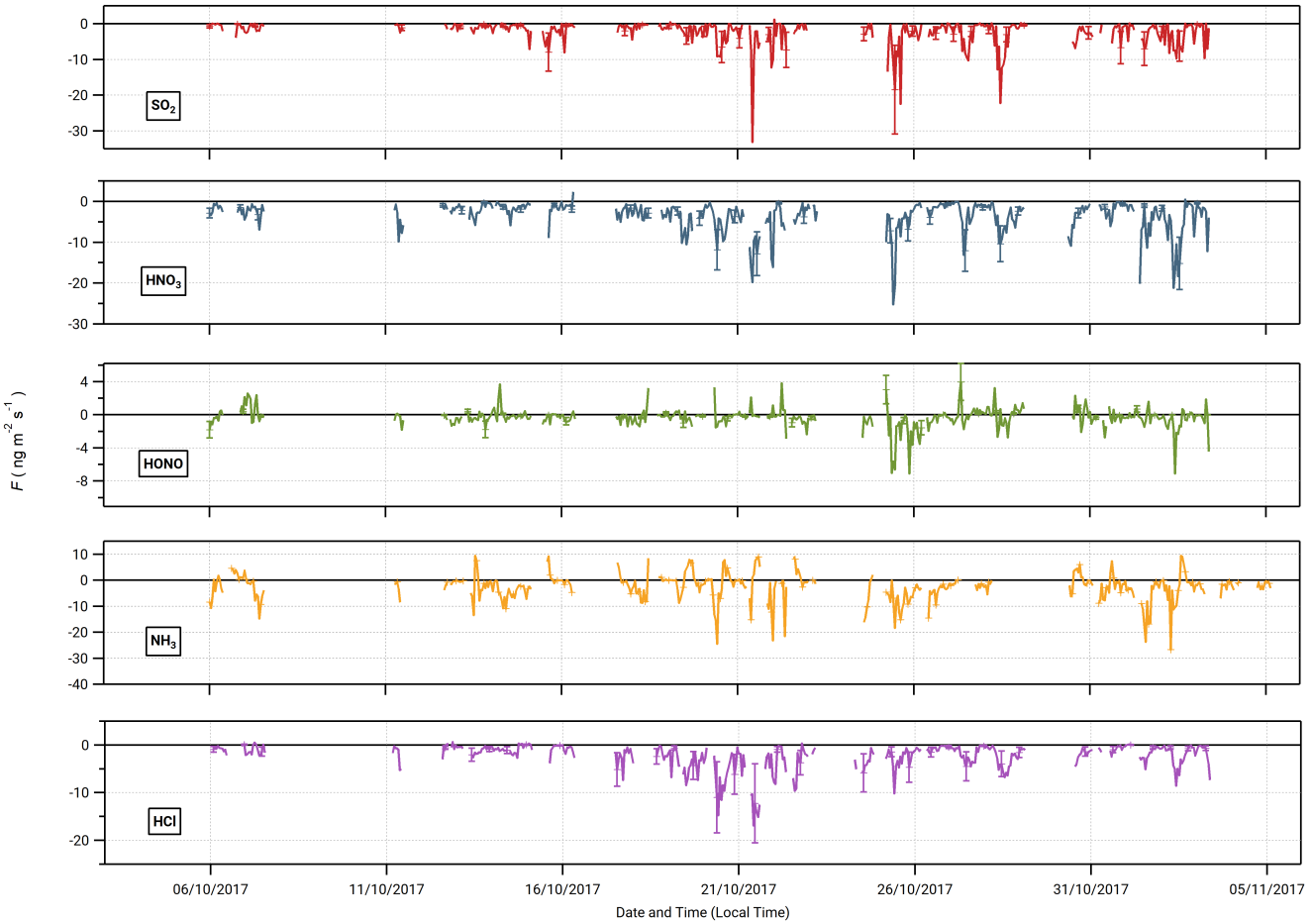

Figure 5.7: Time series of post-filtered, post- γ_F corrected calculated fluxes for the inorganic trace gas species measured during the campaign.

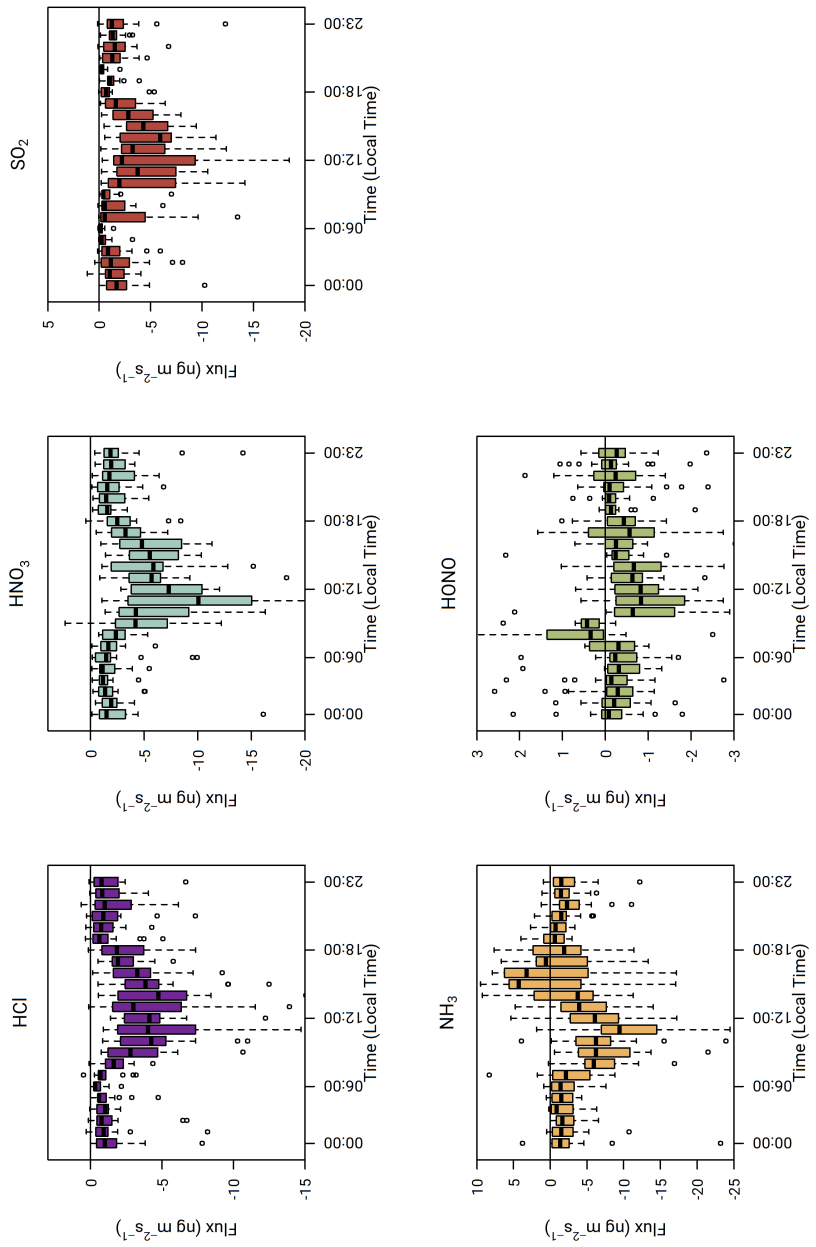

Figure 5.8: Calculated median diel fluxes of inorganic trace gas species measured during the campaign. From top left (clockwise) HCl, HNO_3, SO_2, HONO and NH_3.

detectable flux (F_{LOD}), and the percentage of calculated fluxes which exceed this value (f_{LOD} %).

Pre-correction median V_d values for NH_4^+ and SO_4^{2-} were 1.73 and 1.91 mm s^{-1} respectively. In the comparison of GRAEGOR and ToF-ACSM concentration measurements outlined in Section 5.3.2, it was found that, considering the difference in measurement height, there was reasonable agreement between the instruments for measurements of NH_4^+ and SO_4^{2-} concentrations. This suggested, due to the ToF-ACSM measuring in the sub-micron ($< \mu$m particle diameter) range, that the NH_4^+ and SO_4^{2-} aerosol counterparts measured by the GRAEGOR were also in the sub-micron range. From process-orientated modelling of aerosol V_d, it has been suggested that particle V_d increases over increasingly rough surfaces. Gallagher *et al.* (2002) parameterises this relationship as a function of the surface deposition velocity, V_{ds}, and the surface roughness (given as the surface roughness length, z_0, in m):

$$V_{ds} = 0.581 \log (z_0) + 1.86 \tag{5.10}$$

Using the median value of the surface roughness lengths calculated at the site (and including only lengths with a valid calculated value of aerosol V_d) yields a value of 2.86 m for z_0. Substituting this into the Eq.(5.10) parameterisation suggests a V_{ds} of 2.12 mm s^{-1} for sub-micron particles. The pre-corrected values for NH_4^+ and SO_4^{2-} are lower than this parameterised value. Values of NH_4^+ and SO_4^{2-} V_d converted to V_{ds} using Eq.(5.7) results in a median V_{ds} value for NH_4^+ and SO_4^{2-} of 2.94 and 3.27 mm s^{-1}, respectively. Although these values are higher than the parameterised value, Eq. (5.10) was derived specifically for particles in the range 0.1 to 0.2 μm. Larger particle sizes, correcting for frictional velocity, would have higher V_{ds} (Davidson *et al.*, 1982; Slinn, 1982). Thus, if the particle

size range for NH_4^+ and SO_4^{2-} exceeds 0.2 μm, but remains in the sub-micron range, the measured median V_d would exceed the parametrised value.

Table 5.3: Mean (μ_A), median (μ_M), maximum and minimum values post-roughness sub layer correction for fluxes and deposition velocities (V_d) for the water soluble aerosols measured during the Amazon Tall Observatory campaign. The number of fluxes calculated is quoted as number of measurements, and the median error in flux measurements as a percentage of flux values for each individual aerosol species (σ_F) is included as part of the statistical summary for fluxes.

		NH_4^+	Cl^-	NO_3^-	SO_4^{2-}
Flux ($ng\,m^{-2}\,s^{-1}$)	μ_A	-1.67	-2.25	-4.40	-3.49
	μ_M	-1.23	-1.25	-2.67	-2.77
	Max	0.70	3.63	2.94	4.31
	Min	-10.9	-22.8	-23.8	-21.8
	No. of measurements	427	371	342	360
	σ_F (%)	56	43	44	41
V_d ($mm\,s^{-1}$)	μ_A	2.86	7.83	7.04	3.72
	μ_M	2.64	7.32	5.83	2.81
	Max	25.2	53.6	48.6	33.0
	Min	-2.58	-12.5	-8.1	-7.56

In contrast to post-corrected V_{ds} values for NH_4^+ and SO_4^{2-}, which are in the range for parameterised values for the site, the median V_{ds} values for Cl^- and NO_3^- are 2 to 3 times greater than the parametrised value of 2.12 $mm\,s^{-1}$. The post-corrected median V_{ds} value for Cl^- is 10.2 $mm\,s^{-1}$ while for NO_3^- it is 7.59 $mm\,s^{-1}$. As the parameterised value holds only for particle diameters between 0.1 0.2 μm, and considering that modelling indicates an increase in V_{ds} with increasing particle size, the larger median V_{ds} values for Cl^- and NO_3^- suggest

that these aerosol counterparts were measured by the GRAEGOR in the coarse ($>$ $\mathbf{PM}_{2.5}$) fraction.

A time series of post-γ_F aerosol counterpart fluxes is presented in Figure 5.9. The predominant direction of surface-atmosphere exchange for all aerosol species was deposition, as reflected in median flux values recorded in Table 5.3. However, individual emission fluxes were recorded for all species, with the maximum emission values for Cl^- and SO_4^{2-} ($+3.63$ ng m^{-2} s^{-1} and $+4.31$ ng m^{-2} s^{-1}, respectively) being particularly large. The time series of values is filtered for errors in measurement and for micrometeorological values that fall outside specified limits (Section 5.2.4). These emissions fluxes are therefore unlikely to be caused by instrumentation faults or calculation errors. They are, however, limited in duration and overall extent positive particle emissions are never observed consecutively, occurring exclusively within one hour periods, and constitute between only $<$1% (NH_4^+) to 5% (Cl^-) of total fluxes. While particle emission fluxes have previously been observed with the GRAEGOR (Nemitz *et al.*, 2004b; Twigg *et al.*, 2011), these previous observations have occurred during periods of known flux divergence.

5.4 Discussion

5.4.1 Concentration levels and their controls

Proportional contribution of acidic inorganic trace gases to total atmospheric acidity

The proportion of inorganic trace gases over the ATTO site during the campaign can give important insight into the overall atmospheric chemistry. As the primary

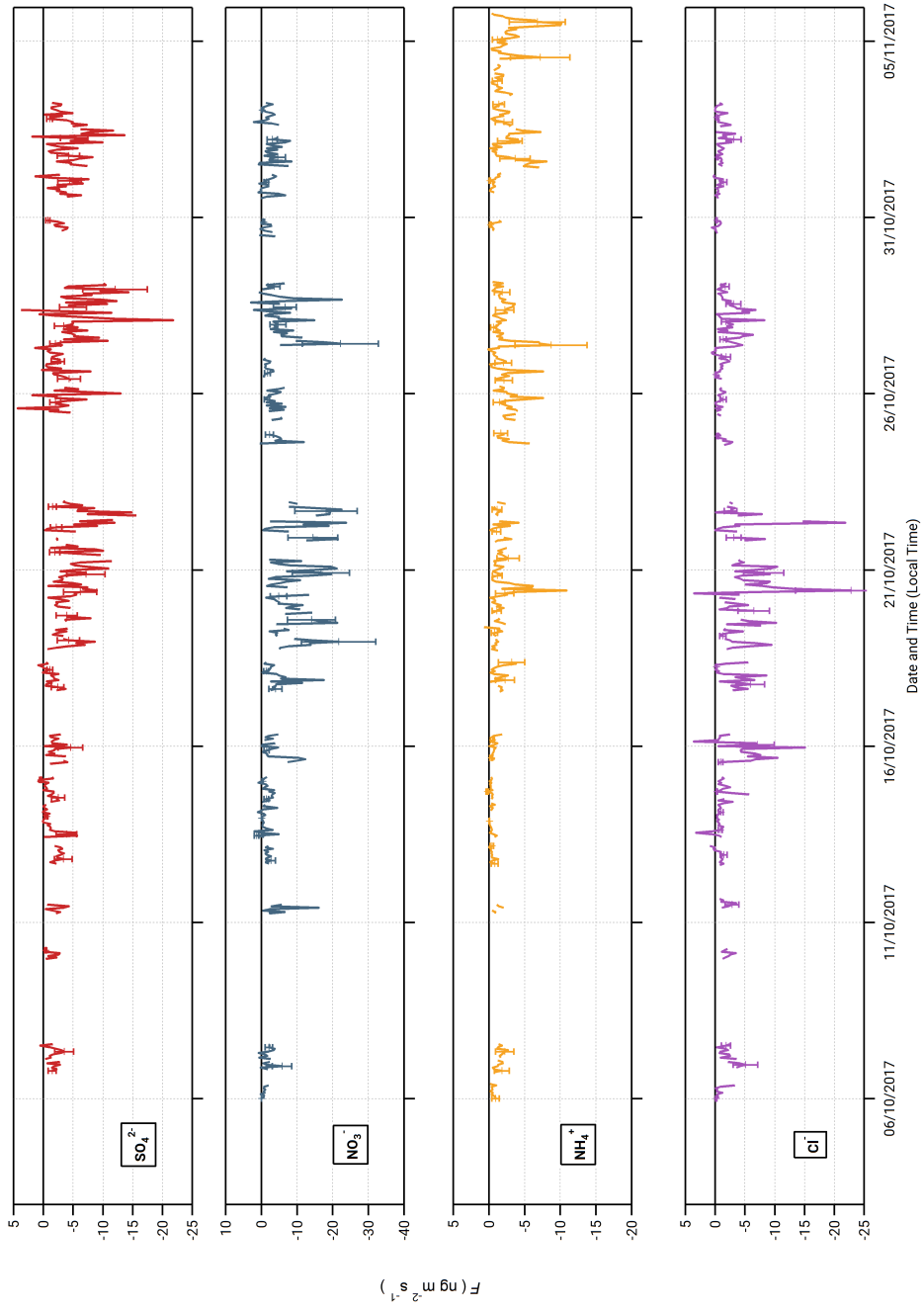

Figure 5.9: Time series of post-filtered, post- γ_F corrected calculated fluxes for the aerosol counterpart species measured during the campaign.

basic gas in the atmosphere, NH_3 can react with the acidic inorganic trace gases HCl, HNO_3 and (formed through the oxidation of SO_2) H_2SO_4 to form a selection of ammonium salts whose lifetime and behaviour are dependent upon their associated inorganic trace gas. In the industrialised world, SO_2 is commonly thought to be the dominant acidic gas in the atmosphere. To investigate the importance of the various acidic gases to total acidity at this remote Amazon site, the fractional contribution to total inorganic acid loading for HCl, HONO, HNO_3 and SO_2 as measured by the GRAEGOR was determined in units of μeq m^{-3} (Figure 5.10). Taken as an arithmetic mean value, the fractional contributions of SO_2, HNO_3 and HCl are similar. While not as significant as a contributor in comparison, HONO also contributes at an average of 0.13, which remains consistent throughout the duration of the campaign. The contributions of SO_2 and HNO_3 average at 0.31 and 0.30, respectively, whilst the contribution of HCl averages at 0.26 but fluctuates throughout the campaign, varying between 0.05 0.10 during near-pristine conditions to almost 0.40 during the polluted period from 19 to 25 October.

Long range transport of pollutants the influence of biomass burning on measurements

The concentrations of all measured inorganic trace gases and associated aerosol species show significant differences between near-pristine and polluted periods (Figures 5.2 and 5.3). The minimum recorded concentrations for all species are recorded during periods where BC < 0.02 μg m^{-3} and $c_{CO} < 150$ ppb. Conversely, the maximum concentrations recorded for all species occur during the period between 21 to 25 October 2017, during which time the concentration of BC peaks at 0.14 μg m^{-3} at midnight on the 25 October along with a peak in c_{CO} of 300 ppb. Calculated fluxes exhibit the same behaviour, with maximum deposition fluxes occurring during the relatively polluted period of the campaign. The gases

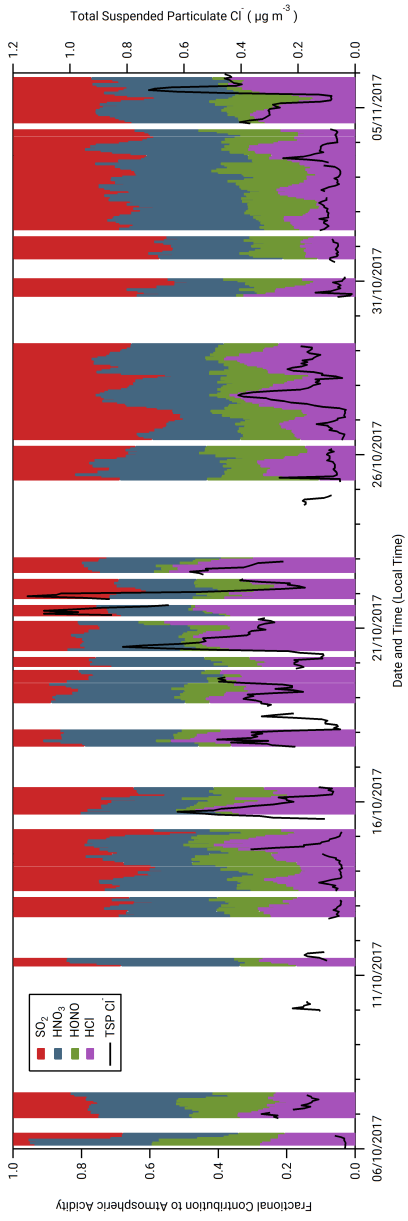

Figure 5.10: Fractional contribution to total measured inorganic acidity from SO_2, HNO_3, HONO and HCl as measured by the GRAEGOR at 60 m (hourly resolution). The concentration of total suspended particulate Cl^- is included as an indicator of periods where sea salt or chloride containing particulate was present at the ATTO site.

NH_3, HCl and SO_2 all have maximum deposition values on 21 October, with a pronounced deposition of -33.2 $ng\,m^{-2}\,s^{-1}$ for SO_2 at 11:00 on this day. While HNO_3 also records a large deposition flux on 21 and 22 October, it peaks at a maximum deposition value on 25, during which time the HONO flux is also at its maximum deposition value.

For the relatively polluted period from 21 October to 25 October, there is evidently a marked increase in concentrations and fluxes above the average, dry-season background levels. Anthropogenic activity, principally biomass burning, may be the driver for this observed increase. Consequently, it is important to determine whether measurements of trace gases and associated aerosol concentrations correlate with the measured concentrations of BC, which acts as a marker for biomass burning and for anthropogenic emissions in general. Determining the strength of the correlation between black carbon and each of the inorganic trace gases with their associated aerosols measured provides an indication of whether their concentrations were driven by anthropogenic activity such as biomass burning, or other possible causes. To investigate this correlation, a ranked Spearman coefficient test was conducted. For all species, Spearman correlation coefficients were statistically significant (p <0.05), suggesting a monotonic relation between all inorganic trace gases and associated aerosols with BC. Correlations with BC were strongest for NH_3 ($r_s = 0.60$) and SO_2 (r_s of 0.51), which was also the case for the aerosol phases of both gases. The weakest correlation between an inorganic trace gas and BC was found for HCl ($r_s = 0.29$). HONO and HNO_3, while not as strongly correlated with BC as NH_3 and SO_2, showed a moderate monotonic positive correlation. Conversely, there was a weak positive correlation between NO_3^- and BC, with a very weak positive correlation for Cl^-.

To determine the origin of the polluted air masses arriving at the ATTO site during the relatively polluted period of the campaign when BC concentrations

were greatest, back trajectory analysis was conducted. Ten-day air-mass back-trajectories which arrived every 3 hours at a height of 500 m a.s.l during the period from 18 October to 25 October 2017 were modelled using the HYSPLIT-4 air trajectory model (Stein *et al.*, 2015) and the Global Data Assimilation System (GDAS) meteorology data set at $1° \times 1°$ resolution using the OpenAir package for R (Carslaw and Ropkins, 2012). The ensemble of back trajectories per week of the campaign is shown in Figure 5.11. Trajectories arriving during the third week of the campaign (20 - 26 October), which coincides with increased concentrations of pollutants, are noticeable for their origin over the south west coast of Africa. They are also characterized - in comparison to other weekly grouped trajectories - by travelling further south over the interior of Brazil, veering sharply to arrive at the site from a southerly direction and thus from over the populated areas to the east of Manaus. Figure 5.12 focuses on the path of the daily trajectories grouped by week in the regional area surrounding the ATTO site, with the location of fires (recorded by the National Aeronautics and Space Administrations Fire Information for Resource Management Service) overlaid. During the period of increased concentrations from 19 to 24 October, trajectories travel over areas where frequent fires are recorded.

This back-trajectory analysis provides some insight into the origins of the polluted air masses during 21 to 25 October. During the dry season, a mixture of regional and remote sources contribute to the pollution over the Amazon Basin, with local sources from deforestation and biomass burning being predominant (Andreae *et al.*, 2012). Pollution from the densely populated north-east coast of Brazil contributes to the pollution burden (Andreae *et al.*, 2018) throughout the relatively polluted period. In addition to this dry season background pollution, there are periods when the long-range transport of pollutants contributes to the overall pollution burden observed at the ATTO site. The source for the majority of these episodes during the dry season has been determined to originate from the

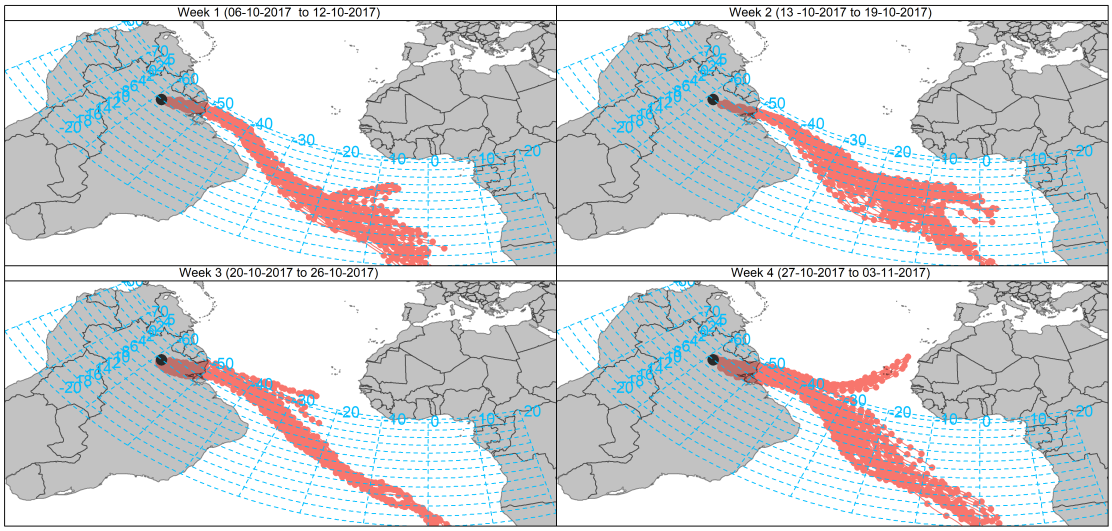

Figure 5.11: Air-mass back-trajectories arriving at the 80 m walk up tower on each day every three hours from 00:00 over the period from 6 October 2017 to 3 November 2017, grouped by week. The duration of each trajectory is 240 hours, marks indicate 12 hour intervals. Modelled using NOAA HYSPLIT 4 using GDAS1 meteorology.

west coast, or the interior, of southern Africa, with volcanic eruptions (Saturno *et al.*, 2018a) and biomass burning (Pöhlker *et al.*, 2018; Andreae *et al.*, 2018) as two of the attributed causes. Biomass burning occurs predominately from June to October in southern Africa, with savannah burning in Zambia and the North West and Limpopo provinces of South Africa usually peaking during October (Roberts *et al.*, 2009). As the backward trajectories for 21 to 24 October come from the west coast of southern Africa, it is likely that the increased concentrations and fluxes of the longer-lived aerosols species are due to the long-range transport of biomass burning pollution from southern Africa.

Investigations into the chemical constituents of smoke from biomass burning in laboratory studies (McMeeking *et al.*, 2009), field studies from atmospheric monitoring stations located near biomass burning point sources (Aurela *et al.*, 2016), and aircraft measurements of plumes from biomass burning (Andreae

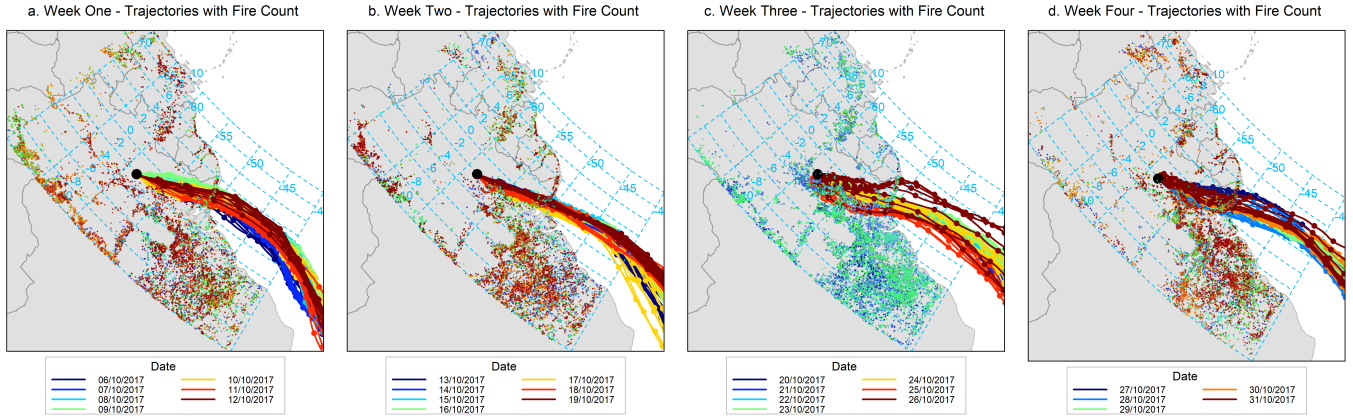

Figure 5.12: Air-mass back-trajectories arriving at the 80 m walk up tower on each day every three hours from 00:00 over the period from 6 October 2017 to 31 October 2017, grouped by week, and further subdivided by day, for the regional area surrounding the ATTO site. Fire count data is included as an overlay to each weekly plot, with fire count coloured according to the date on which the fire was recorded by satellite imagery.

et al., 2018; Aruffo *et al.*, 2016; Fiedler *et al.*, 2011) have confirmed elevated emissions of the inorganic gases and aerosol species measured during the ATTO campaign. Biomass burning is an important source of reactive nitrogen emissions, and emissions of NH_3 from biomass burning are the second most important source of global emissions behind agriculture, accounting for 14% of total terrestrial emissions (VanDamme *et al.*, 2014; Whitburn *et al.*, 2015). Furthermore, emissions of NO_x the precursor gas to atmospheric HNO_3 and HONO from burning during the southern African biomass burning season is a significant contributor to free tropospheric NO_x in the southern hemisphere ((Adon *et al.*, 2010; Galanter *et al.*, 2000)). Finally, SO_2 and HCl emissions from biomass burning (Burling *et al.*, 2010; Yokelson *et al.*, 2011) and elevated counts of sub-micron particles such as SO_4^{2-} and NH_4^+ (Aurela *et al.*, 2016) have previously been measured from both ground and aircraft measurements of biomass burning plumes.

The evidence from the correlation and back-trajectory analyses suggests that the presence of SO_2 and NH_3 (and their associated aerosol counterparts, NH_4^+ and SO_4^{2-}) was primarily driven by biomass burning. For the period from 21 to 24 October, concentrations of NH_4^+ and SO_4^{2-} may have been elevated due to biomass burning in the region surrounding the ATTO site, with the possible complement of plumes from biomass burning originating in southern Africa. Figure 5.13 highlights this link by presenting concentration weighted trajectory analyses, which determine the geographic origin for concentration levels of a select species, for BC, SO_4^{2-} and NH_4^+. Areas determined as the source for the highest measured concentration of these three species align with areas in which the most intense (as determined by the fire radiative power of each fire count) biomass burning occurs regionally.

While this holds partly for HONO and HNO_3, it only weakly holds for their associated aerosol counterparts (NO_3^- and Cl^-) and the trace gas HCl. An

alternative origin for these species must therefore be considered and will be discussed further in Section 5.4.1 and Section 5.4.2 for the trace gas HCl and the aerosols NO_3^- and Cl^- respectively.

Urban Plumes, NO_x and reactive nitrogen formation

The increase in HNO_3 concentrations on 25 October, coinciding with increased deposition fluxes, could be due to air masses that arrived from the south and south-east of the site on the same day, that may have brought emissions of NO_x (NO_2 + NO) trace gases from the urban areas of Manaus and Santarm. The predominant source for the production of HNO_3 in the troposphere is the OH driven oxidation of NO_2, which occurs in conditions of elevated NO_2 concentrations. In remote areas, where background levels of NO_2 are low, the production of HNO_3 is limited. However, with injections of anthropogenically derived NO_2 into the atmosphere above remote areas, the efficient scavenging of OH by elevated NO_2 concentrations leads to the formation, and subsequent deposition, of HNO_3 (Mannschreck *et al.*, 2004). Fossil fuel combustion is the primary anthropogenic, and overall predominant, source for NO_2 in the troposphere. Air masses which have passed over the large urban areas to the south and south east of the site may therefore bring elevated NO_2 concentrations, which combined with the high number concentrations of the OH radical present at the site, would result in increased concentrations of HNO_3. Kuhn *et al.* (2010) and Trebs *et al.* (2012) conducted measurements of NO_2 downwind and west of the Manaus urban area, and reported elevated NO_2 concentrations in remote areas affected by NO_2 emission plumes from the city. With air masses arriving at the site from the south and south east, and which travelled over the eastern suburbs of Manaus and the city of Santarm respectively, it is possible that NO_2 emission plumes are therefore responsible for the elevated concentrations of HNO_3 observed on 25 October.

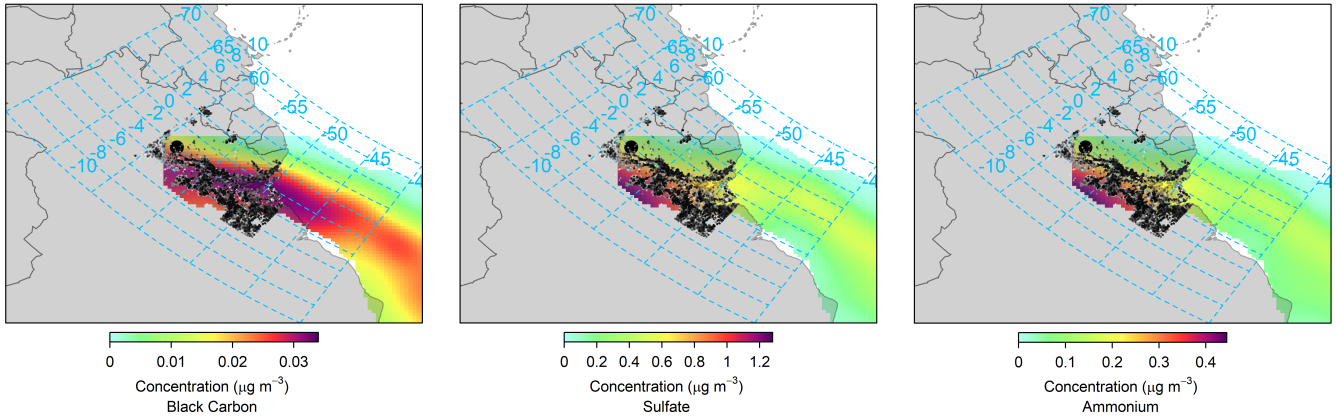

Figure 5.13: Concentration weighted trajectory analysis for (from left) BC, SO_4^{2-} and NH_4^+, with fire data overlaid. Fire data is coloured (scale, from light grey to black) by fire intensity, a measure of the fire radiative power of the individual fire.

Biogenic drivers of HCl concentrations

While a moderate, positive monotonic relation exists between concentrations of HCl and BC, it is unlikely that the presence of HCl above the detection limit of the GRAEGOR could be sustained throughout the campaign solely through anthropogenic emissions. HCl is highly reactive and water soluble, with a mean lifetime of 36 hours (Graedel and Keene, 1995; Kritz and Rancher, 1980). Consequently, it is unlikely that regional or global biomass burning could contribute meaningfully to the HCl concentrations observed at this remote site. The peak in HCl concentrations observed during the relatively polluted periods of the campaign could be a result of biomass burning from local sources in close proximity, but an alternative explanation must be considered for the measured background concentrations.

A potential contributor for the sustenance of HCl concentrations is the oxidation of methyl chloride (CH_3Cl). The predominant natural source of CH_3Cl is tropical forest (Yokouchi *et al.*, 2002), with emissions driven by a select group of plant species principally, dipterocarps and ferns (Blei *et al.*, 2010) whose emission rates are unaffected by abiotic conditions (Yokouchi *et al.*, 2015). Gebhardt *et al.* (2008) measured an average emission for CH_3Cl of 9.5 $\mu g\, m^{-2} hr^{-1}$ over Guyanese and Surinamese rainforest, while Moore *et al.* (2005) reported the existence of CH_3Cl concentrations above a rainforest canopy in Rodônia, Brazil, confirming that the Amazon rainforest region is a net regional source for CH_3Cl.

Sanhueza (2001) proposes an OH driven oxidation pathway for CH_3Cl that terminates with a 1:1 molecule production of HCl. With recorded emissions of CH_3Cl from tropical vegetation, combined with the high oxidative capacity of the rainforest, it is possible that local CH_3Cl emission followed by subsequent OH oxidation could result in the maintenance of a background HCl concentration, as recorded during this campaign. However, to confirm this idea, simultaneous measurements

of CH_3Cl and HCl concentrations would be required, with observational confirmation of Sanhuezas postulated CH_3Cl oxidation pathway.

Anthropogenic and biogenic drivers of SO_2 concentrations

This campaign presents the first tower measurements of SO_2 fluxes over tropical rainforest, and some of the few concentration measurements made at high-time resolution and sufficient sensitivity, with standard SO_2 monitors struggling to resolve such low concentrations. Although aircraft measurements (Andreae and Andreae, 1988), denuder tube (Adon *et al.*, 2013) and filter pack (Paralovo *et al.*, 2019) measurements of SO_2 exist, they lack the same time resolution as the measurements during this campaign or do not measure fluxes. This study has shown that LRT pollution episodes can significantly enhance SO_2 deposition fluxes a maximum deposition flux of -33.2 $ng\,m^{-2}\,s^{-1}$ was recorded during the most polluted period of the campaign and that even during relatively pristine conditions for the dry season, SO_2 concentrations remained above the detection limit of our wet chemistry based measurement system. As Figure 5.14 demonstrates, the close correlation between SO_2 and BC suggests that long term measurements of SO_2 over tropical rainforest may be worthwhile as a further method to identify episodes of increased pollution or biomass burning. Long term measurements would also aid in determining if concentrations of SO_2 remain above detection limits during the pristine conditions of the wet season, and to determine potential sources during these periods. It is possible that a biogenic source may account for some of the measured SO_2 during this campaign considering measurements during relatively pristine conditions. For example, SO_2 can derive from the oxidation by OH of dimethyl sulfide emitted from the rainforest (Jardine *et al.*, 2015).

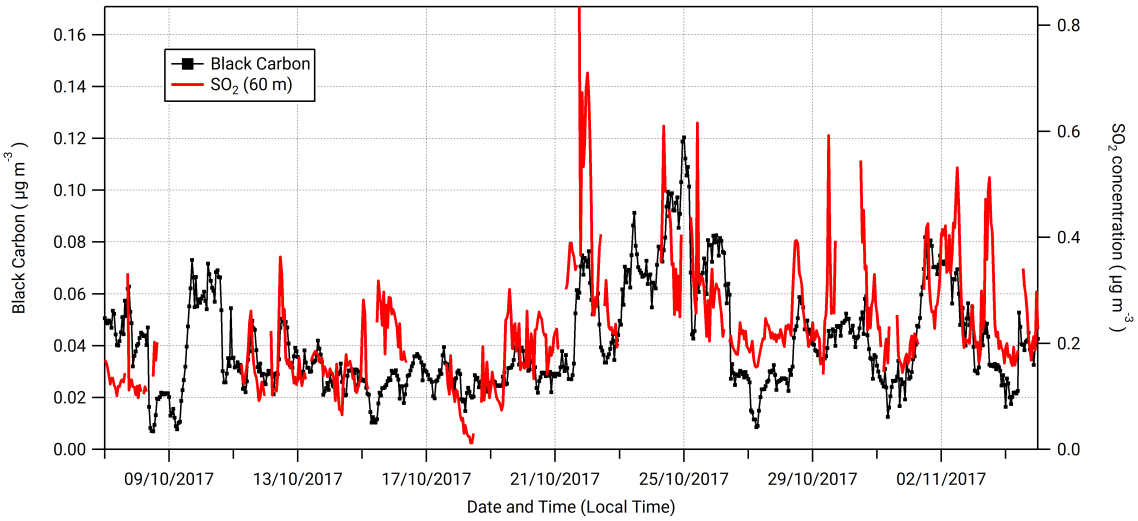

Figure 5.14: Time series of hourly SO_2 and BC concentrations, highlighting the close correlation between SO_2 and BC measurements throughout the campaign.

5.4.2 Aerosol Mass Fractions and Deposition Velocities

Aerosol mass fraction comparison with ACSM

The comparison between ACSM and GRAEGOR water-soluble aerosol concentrations in Section 5.3.2 indicates good agreement between them for SO_4^{2-} and NH_4^+, but significant divergence for NO_3^- and, in particular, Cl^-.

Long-term measurements of aerosol chemical composition at the ATTO site using an ACSM have been conducted since 2014, and the first publication of data from 2015 suggested that aerosol chemical speciation varied little across the wet and dry seasons (Andreae *et al.*, 2015). As recorded by the ACSM during this campaign, organic aerosols are always the dominant mass fraction (comprising approximately 70% of aerosol), followed by SO_4^{2-} (10 15%), BC (5 11%), NH_4^+ (5%), NO_3^- (4%) and finally Cl^- as the smallest contributor. Focusing only on the aerosol species measured by both the GRAEGOR and ACSM during this dry season campaign, the average ACSM mass fractions are 55% SO_4^{2-}, 22% NH_4^+, 18% NO_3^-

and 5% Cl^-. As Figure 5.15 demonstrates, the total mass fraction contribution to total suspended particulate as measured by the GRAEGOR suggests that the contribution of NO_3^- and Cl^- is more significant than previously thought. The relative contribution of each species to TSP as measured by the GRAEGOR in this campaign (in descending order) is: SO_4^{2-} = 34.4%, NO_3^- = 30.8%, NH_4^+ = 19.0% and Cl^- = 15.3%. In comparison to ACSM measurements, the proportion of SO_4^{2-} is reduced, NO_3^- becomes the second most dominant species with an almost equal contribution to SO_4^{2-}, and Cl^- while remaining the smallest contributor to total mass has a greater contribution to the mass of TSP.

Chemical speciation of coarse and fine aerosol

The ACSM samples only the sub-micron (< PM_1) aerosol size range, while the GRAEGOR samples TSP (< 50-100 μm particle diameter). Furthermore, the ACSM speciates only non-refractory particles, and is therefore insensitive to refractory sea-salt and crustal material (Fröhlich *et al.*, 2013). While the ACSM measures within fine aerosol fraction, the GRAEGOR measures both fine and coarse aerosol. The close similarity in SO_4^{2-} and NH_4^+ measurements between the two instruments would suggest that the majority of SO_4^{2-} and NH_4^+ during the campaign were contained within fine aerosol and represented compounds detectable by the ACSM, i.e. NH_4^+, SO_4^{2-} and bisulfate. Conversely, the difference between ACSM and GRAEGOR nitrate measurements suggests that most of the NO_3^- was contained within the coarse mode and/or represented non-volatile compounds such as $NaNO_3$ and $Ca(NO_3)_2$, and that almost all of the chloride measured by the GRAEGOR in this campaign was found in the coarse mode and/or as NaCl.

The recorded deposition velocities of the aerosol species measured are an indication that NO_3 and Cl^- aerosols were contained in the coarse fraction, while

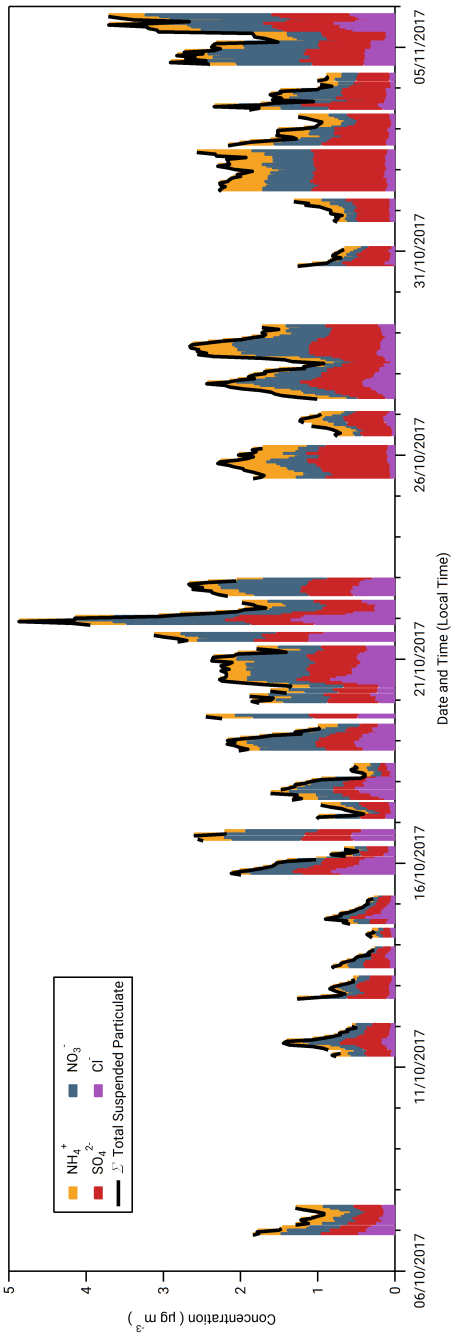

Figure 5.15: Total mass of suspended particulate recorded by the GRAEGOR at 80 m throughout period of campaign.

NH_4^+ and SO_4^{2-} were contained within fine aerosol. From a process-orientated approach (Davidson *et al.*, 1982; Slinn and Slinn, 1980), the deposition velocity of a particle is dependent upon its size. For particles above 0.1 μm, deposition velocity (normalised against u_*) increases with increasing particle diameter. As outlined in Section 5.3.2, the close agreement between measured SO_4^{2-} and NH_4^+ deposition velocities (and parametrised values for 0.1 0.2 μm size range aerosols) above tropical rainforest suggest that these aerosols were contained in the fine mode. These observed deposition velocity values also agree well with modelled deposition velocities for <1 μm diameter particles above forest with similar mean roughness lengths and u_* values as recorded at ATTO (Petroff *et al.*, 2008). Conversely, the larger observed deposition velocities for NO_3^- (5.83 mm s^{-1}) and Cl^- (7.32 mm s^{-1}) exceed the parameterised values obtained using Gallaghers formulation (Gallagher *et al.*, 2002), and fit within the modelled values given by Petroff *et al.*. for particles in the 2 10 μm diameter range above surfaces with a similar roughness length.

Potential origins for coarse Cl^- and NO_3^-

Accounting for the insensitivity of the ACSM to refractory particles, a possible source for coarse Cl^- aerosols could be sea-salt. Although a continental site, intrusions of sea salt through long-range transport have been noted previously at ATTO (Moran-Zuloaga *et al.*, 2018), although this is generally limited to the wet season. The presence of sea salt could also account for a shift in NO_3^- deposition velocities, as the reaction between HNO_3 and NaCl would result in the formation of the coarse aerosol $NaNO_3$ (Dasgupta *et al.*, 2007), a refractory particle that would not be detected by the ACSM. The reaction of HNO_3 with sea salt would also form HCl, the measured concentrations of which are closely linked to those of Cl^- in this campaign. Alternatively, the strong link between HCl and Cl^- concentrations could be accounted for by biomass burning emissions arriving at

the ATTO site, although chloride particulate from biomass burning is principally in the fine, non-refractory form of KCl (Pratt *et al.*, 2011). Other crustal material, such as dust and soil particles which are recorded in elevated amounts at ATTO during the dry season (Moran-Zuloaga *et al.*, 2018), could provide a source of coarse NO_3^-. These can include a variety of NO_3^--containing mineral species, such as $NaNO_3$, $Ca(NO_3)_2$ and $Mg(NO_3)_2$ (Karydis *et al.*, 2016). The surface of dust and suspended soil particles could also act as a sink for HCl in the marine boundary layer (Sullivan *et al.*, 2007), allowing for the heterogeneous formation of coarse Cl^- particulate.

As noted, intrusions of sea salt to the ATTO site are potentially increased during the dry season due the influence of the inter-tropical convergence zone position on trade wind transportation. Wash-out of sea salt from the troposphere due to precipitation events occurring transportation would also minimise the overall impact of sea salt intrusions on observed Cl^- concentrations. Consequently, alternative sources for coarse chloride should be considered.

It has been shown previously that primary biological aerosol particles (PBAPs) contribute to the majority of the mass fraction of measured coarse aerosol in the Amazon (Poschl *et al.*, 2010). PBAPs over the rainforest consist of a variety of different biological material, such as plant and animal matter fragments, algae, pollen and fungal spores. The latter contributor is particularly important, as fungi which actively discharge their spores through liquid jets have been identified by Elbert *et al.* (2007) to be a significant source for the concentrations of inorganic ions in air particulate matter. Fungi which actively discharge their spores do so via a liquid jet, whereby spores are forcibly discharged from a spore sac (*asci*) along with a liquid mix of sugars and ions, of which Cl^- forms a significant fraction (Trail *et al.*, 2005). The spore itself can rupture under conditions of high relative humidity, resulting in the formation of fragments containing inorganic ions (China *et al.*, 2016). In a chemical imaging analysis of such spore fragments above the

Amazon Rainforest, China *et al.* (2018) found almost 40 60% of these fragments contain Na^+ and Cl^- associated as a salt, which appeared morphologically similar to dry sea salt and which grew to super-micron sizes in conditions of high relative humidity. The contribution of fungal spores to total Na^+ mass during the wet season over the rainforest was estimated as 69% by the same study, with the conclusion that measured concentrations of coarse Na^+ and Cl^- could mistakenly be ascribed to marine sources, rather than to locally originating fungal spore emissions. As discussed in Section 5.4.3, emission fluxes for Cl^- are recorded throughout the campaign, and occurred during cooler, wetter periods at night. As noted by Elbert *et al.* (2007), fungal spore emissions also predominantly occurred under the same conditions.

Therefore, the possibility that Cl^- concentrations measured during this campaign are biogenically driven through the active discharge or rupturing of localized fungal spore emissions should not be discounted.

5.4.3 Bi-directional exchange of inorganic trace gases and aerosols

Inorganic trace gases

As detailed in Section 5.3.3., HCl, HNO_3 and SO_2 were continuously deposited with no periods where emissions were recorded. Conversely, measurements of both HONO and NH_3 flux revealed periods of emission from the rainforest, with 26% of all calculated HONO fluxes and 19% of NNH_3 fluxes recorded as emissions. Discussion of NH_3 fluxes will be considered in a separate chapter which investigates the influence of factors such as leaf wetness and modelled canopy compensation points upon NH_3 bi-directional exchange. This chapter will focus on discussing the emissions of HONO from the rainforest canopy.

The median diel fluxes of HONO in Figure 5.8 show persistent emission in the early morning after dawn (from 07:00 to 09:00), with deposition dominating throughout the rest of the day. Two possible explanations are considered here. The first considers the influence of soil emissions below the forest canopy. HONO emissions from soil have been observed by a number of studies (Sörgel *et al.*, 2011, 2015; Twigg *et al.*, 2011), with possible sources including the volatilization of HONO from soil nitrite (Su *et al.*, 2011), the temperature-dependant activity of ammonia oxidizing bacteria (Oswald *et al.*, 2013; Scharko *et al.*, 2015), or the oxidation of hydroxylamine released from soil microorganisms (Ermel *et al.*, 2018). During night-time, radiative cooling above the forest causes stable stratification, generating a nocturnal boundary layer that prevents mixing between the air below and above the canopy (Foken, 2008; Tóta *et al.*, 2008). Consequently, HONO emissions from the soil will accumulate below the canopy. At dawn, turbulent mixing starts to break up the nocturnal boundary layer, generating unstable conditions and a mixed layer. This creates a venting effect where the below-canopy accumulated HONO is transported upwards, creating a venting effect, and appears as an early morning emission flux. Such venting episodes have been noted previously in tower measurements above rainforests for CO_2 (Araújo *et al.*, 2002), methane (Querino *et al.*, 2011) and particles (Whitehead *et al.*, 2010), with Querino *et al.* recording maximum median diel CO_2 and CH_4 fluxes between 06:00 and 10:00, similar to the period of maximum median diel HONO emissions. CO_2 flux measurements taken at the ATTO site concurrently with this study also showed a characteristic early morning flux, suggesting a similar venting effect to HONO flux measurements. However, morning emissions have also been observed at short vegetation sites (Laufs *et al.*, 2017; Di Marco *et al.*, 2019), where storage effects are much smaller, and this suggests that a different mechanism is contributing to these emissions.

Alternatively, early morning HONO emissions may be a consequence of the

photolysis of HNO_3 (Zhou *et al.*, 2011). Accumulation of HNO_3 on leaf surfaces during night-time would result in a reservoir of HNO_3 within the canopy. At dawn, incoming solar radiation photolyses this reservoir, resulting in the formation of exited NO_2 radicals that in the presence of photosensitizing organics such as humic acid (George *et al.*, 2005; Stemmler *et al.*, 2007) are reduced to HONO. The concurrent breakdown of the nocturnal boundary layer again results in an upward emission flux of HONO. However, while Zhou *et al.* recorded emissions of HONO from forests between the hours just after dawn until late afternoon, with maximum fluxes recorded around solar noon, this study found emissions occurred predominately during the hours immediately after dawn. While emissions were recorded at noon and during the afternoon on certain days, median diel emissions were confined strictly to 07:00 to 09:00 hours. Future work should measure the gradients of HONO above and below the canopy to determine whether HONO accumulation below canopy during stable night time conditions is occurring, followed by venting during morning hours due to turbulent mixing.

It is important to note that measurements of HONO by the GRAEGOR system are not artefact free. As detailed by (Spindler *et al.*, 2003), the presence of SO_2 and NO_2 on wet denuder walls can introduce a positive artefact that results in an overestimate of HONO concentrations, which if using a multi-point gradient system that uses more than two wet denuders set at different heights can result in erroneous concentration gradient profiles. Correction algorithms exist for general application (Spindler *et al.*, 2003) and specifically for the GRAEGOR (see Chapter 4) that allow the influence of the artefact to be quantified using concentrations of SO_2 and NO_2. However, for this campaign, no correction was deemed necessary as the SO_2 concentration recorded during the campaign was 5 to 10 times lower than those relevant to artefact formation.

Water-soluble aerosols

As detailed in Section 5.3.3, periods of apparent particle emissions from the rainforest were recorded throughout the campaign for all aerosol species measured. Deviations from the near exclusive pattern of deposition were rare (between 1 3% of all measured fluxes), confined to one hour periods, and are unlikely to be due to measurement error. Similar to the emissions of HONO recorded during this campaign, upward particle fluxes may be caused by early morning turbulent mixing generating upward entrainment fluxes into the growing mixing layer. Whitehead *et al.* (2010) recorded a similar pattern of particle emissions at a tropical rainforest site in North Borneo, as did Ahlm *et al.* (2009) at a rainforest site in the Amazon basin located 120 km south-west of the ATTO site. However, both studies recorded a more predominant pattern of early morning emissions than here. Whitehead *et al.* recorded particle emissions for almost all mornings, while Ahlm *et al.* reported 40% of all particle fluxes as emissions. Both studies record later (08:00 09:00) emission periods. As both studies measured total particulate number which was not chemically speciated it is possible that the flux behaviour of the organic fraction of aerosol which dominates the total aerosol mass fraction over tropical rainforest is a more important driver for observed particle emissions than the aerosol species measured during this campaign.

5.4.4 Dry deposition budget of reactive nitrogen for Amazon rainforest dry season

The dry deposition of total reactive nitrogen to the ATTO site as derived from the GRAEGOR measurements (ΣN_r = NH_3 + NH_4^+ + HNO_3 + NO_3^- + HONO) during the dry season for this study relies on the assumption that

values for ΣN_r in October are indicative of the dry season overall, and that bi-directional surface-atmosphere exchange of individual ΣN_r species is occurring. With these assumptions considered, the dry deposition total for ΣN_r for the ATTO site during the dry season of the Amazon Rainforest is estimated to be 1.74 kg Nitrogen $ha^{-1}yr^{-1}$. A breakdown of the contribution of each reactive nitrogen species to this total is presented in Table 5.4.

Although dry deposition totals based on direct observation are rare for this biosphere, this value for dry ΣN_r should be considered as limited in scope due to the lack of an equivalent value of a wet ΣN_r based on direct measurement. From a previous study by Trebs *et al.* (2006), wet ΣN_r is the predominant contributor to total ΣN_r over the Amazon rainforest. Furthermore, this study presents a value of ΣN_r that does not include water soluble organic nitrogen (WSON), which can constitute up to 43% of total nitrogen in the aerosol phase during the dry season (Mace *et al.*, 2003).

Nevertheless, this studys value of -1.74 kg Nitrogen $ha^{-1}yr^{-1}$ for dry season, dry deposition only ΣN_r compares favourably with Trebs *et al.* (2006) equivalent estimate of -3.68 kg Nitrogen $ha^{-1}yr^{-1}$ over a remote pasture site situated in the Amazon Basin. While this study arrives at a lower estimate using the same methodology as Trebs et al., the stronger influence of agricultural activities and biomass burning at the pasture site in Trebs *et al.* study would account for a higher total ΣN_r.

5.4.5 Comparisons of measured concentrations of trace gases and associated aerosols with selected studies

While this was a one-month study limited to the dry season, during which local, regional and global biomass burning contributed to observed concentrations, it

Table 5.4: Contribution of reactive nitrogen species to total (Σ (NH_3 + NH_4^+ + HNO_3 + NO_3^-) reactive nitrogen dry deposition budget for ATTO in kg Nitrogen $ha^{-1}yr^{-1}$, inferred from fluxes measured during campaign.

Reactive Nitrogen Species	kg Nitrogen $ha^{-1}yr^{-1}$
NH_3	-0.74
HONO	-0.03
HNO_3	-0.25
NH_4^+	-0.41
NO_3^-	-0.31
$\Sigma N_r = NH_3 + NH_4^+ + HNO_3 + NO_3^- + HONO$	-1.74

provides some insight into the atmospheric composition of a biosphere for which there are few measurements overall. Placing these measurements in context with similar regional and local studies above tropical rainforest sites provides an impression of the spatial and temporal representativeness of this study.

For aerosols, measurements of PM_{10} concentrations (both cations and anions) taken by high-volume air samplers between 2008 and 2016 over the Cuieiras ZF2 natural reserve approximately 130 km west of the ATTO site have recently become available (Custodio *et al.*, 2019), allowing for a local comparison in measured aerosol concentrations between the GRAEGOR and filter sampling. In comparison to the measurements taken by the GRAEGOR, median dry season concentrations of Cl^- and NO_3^- for the period 2008 to 2016 are between 2.5 to 4 times greater in magnitude than those recorded by the high volume air samplers during dry seasons. Conversely, the median dry season SO_4^{2-} concentrations recorded by the GRAEGOR is 0.3 times that recorded by the high volume samplers. NH_4^+ concentrations recorded by both measurement techniques are approximately equivalent.

Discrepancies in the measurements of these aerosols species between wet-chemistry based instruments and high volume air-sampler systems has previously been noted by Trebs *et al.* (2008), who found a similar order of magnitude in difference between SO_4^{2-} measurements between a WRD-SJAC system and a high volume air sampler in tropical conditions. Similarly, the study also found that high volume air samplers measured lower concentrations of Cl^- and NO_3^- compared to wet chemistry instruments, although this pattern was only observed during periods of low overall concentrations of Cl^- and NO_3^-. Trebs *et al.* attributed higher SO_4^{2-} high volume air sampler concentrations to the decomposition of organosulfates on filters during storage, as well as environmental conditions such as high relative humidity that may have introduced both positive and negative artefacts on the filter substrate.

For the inorganic trace gases NH_3, SO_2 and HNO_3, the most comprehensive study into their concentrations over remote tropical rainforests is by Adon *et al.* (2013), who presented long term-measurements over Cameroonian rainforest using passive denuder tubes. For the dry season, Adon *et al.* reported a similar concentration of SO_2 and HNO_3, but reported a significantly higher concentration of NH_3 (a dry season average of 2.9 $\mu g\,m^{-3}$ compared to 0.28 $\mu g\,m^{-3}$ reported in this study).Adon *et al.* postulated that the NH_3 concentrations recorded over their rainforest site were driven by biomass burning, similar to the conclusion drawn in this study. It is possible that the intensity, proliferation and proximity of biomass burning at the Cameroonian site may therefore be heightened in comparison to the ATTO site, resulting in greater measurements of NH_3 concentrations.

Trebs *et al.* (2004), using a wet annular rotating denuder with steam jet aerosol collector system a prototype of the GRAEGOR instrument measured the same suite of inorganic trace gases and associated aerosols as this study, but at a pasture site located within the Amazon Basin. Measurements from the dry season of Trebs *et al.* campaign found similar mean and median concentrations of NH_3 and HNO_3

as this study, but recorded higher concentrations of HCl and HONO, with SO_2 recorded as the lowest concentration of all the inorganic trace gases measured. As a fractional contribution to acid loading, this suggests that HCl is even more dominant than at the ATTO site, which is expected for an active pasture site with local biomass burning compared with the ATTO pristine rainforest site.

5.5 Conclusions

This study employed a two-point, wet-chemistry instrument (GRAEGOR) to measure online, hourly resolved measurements of the inorganic trace gases NH_3, HCl, HONO, HNO_3 and SO_2 and their associated aerosol counterparts NH_4^+, Cl^-, NO_2^-, NO_3^- and SO_4^{2-}. While measurements of NO_2^- concentrations were below the detection limit for the instrument and consequently were not discussed, this study was able to present for the first time the concentrations, fluxes and deposition velocities for a number of species during the Amazon dry season. Some of the key findings of this study are summarised below:

1. The influence of long range transport (LRT) of pollutants on ATTO pollution burdens. Elevated concentrations of the inorganic trace gases SO_2 and NH_3, with use of the markers for anthropogenic emissions BC and c_{CO}, were noted at several periods during the campaign. Using back trajectory analysis for particularly polluted conditions, it was found that air masses arriving at the ATTO site during this period originated from the coast or interior of south west Africa. This area is a location of biomass burning during the August-October period. LRT episodes, driven by African biomass burning, could therefore contribute to an overall background of increased pollution during the Amazon dry season to elevated concentrations

of inorganic trace gases and associated aerosols observe during the dry season.

2. Bi-directional exchange of inorganic trace gases and aerosols. While the gases HCl, HNO_3 and SO_2 were uniformly deposited to the rainforest canopy, 26% of all HONO fluxes and 19% of NH_3 fluxes were recorded as emissions. Similarly, all aerosol species measured during the campaign had recorded emissions, although these constituted between 1-3% of all measured fluxes. For HONO and the aerosol species measured, the influence of venting whereby the accumulation of a gas or aerosol species below or on the canopy is swiftly entrained into the mixed layer through early morning turbulence was suggested as an explanation for the emission periods recorded.

3. Influence of coarse aerosol on total aerosol fraction above Amazon rainforest. This study presents for the first time measures of chemical differentiated aerosol concentration in the coarse fraction. Compared to long term measurements of chemically differentiated aerosol in the sub-micron fine fraction, the contribution of Cl^- and NO_3^- to the total aerosol mass is substantially higher. Consideration of the deposition velocity of the aerosols measured confirmed that Cl^- and NO_3^- particulate measurements were derived from coarse aerosol, and explanations for their presence at the ATTO site biomass burning, sea-salt, and crustal material were considered.

This study has also confirmed the applicability of Chor *et al.* (2017) flux enhancement factor (γ_F) for correcting fluxes measured using the aerodynamic gradient method within the roughness sublayer above tropical rainforest. An estimate of total reactive nitrogen dry deposition for the Amazon rainforest during the dry season has also been presented, although limited by lack of an equivalent wet deposition value.

The measurements presented here confirm the importance of measuring chemically differentiated inorganic trace gases and associated aerosols above rainforest, as by doing so, important atmosphere-exchange processes (venting from the forest floor, increased deposition during pollution episodes) and knowledge of aerosol speciation (the importance of the coarse mode on total aerosol mass) become apparent. With the implementation of the ATTO 325 m tower, the potential for further long term measurements of inorganic trace gases and aerosols using GRAEGOR or commercial GRAEGOR derivatives (such as the Monitor for Aerosols and Gases in Ambient Air, or MARGA), is now available. Replicating this study in the wet season, or by including measurements of the concentrations and fluxes of water soluble organic nitrogen through modifications to the instrumentation, are potential avenues for future investigation.

Chapter 6

Measurement and modelling of the dynamics of NH_3 surface-atmosphere exchange over Amazonian rainforest

This chapter is based on a research paper currently in preparation for submission to the journal Biogeosciences. I took the measurements of NH_3 *and processed the data with help from Dr. C.F. Di Marco, Dr. E. Nemitz and Prof. M. Heal. Meteorological data used in the campaign was taken by Dr. M. Sá and Dr. A. Arujo. Leaf wetness measurements were taken by myself and Dr. M. Srgel. With consultation with Dr. E Nemitz, I undertook the modelling of* NH_3*. I wrote the manuscript, with subsequent contributions from all co-authors.*

6.1 Introduction

The global cycling of nitrogen is of critical importance to the Earths biogeochemistry. One of the major contributors to the global atmospheric reactive nitrogen (N_r) budget is ammonia (NH_3) which is primarily generated from anthropogenic sources (Galloway *et al.*, 2003). The emission of NH_3, and the subsequent deposition of NH_3 or other forms of reactive nitrogen, have impacts on terrestrial and marine ecosystems (Erisman *et al.*, 2013). In particular, semi-natural vegetation such as forest ecosystems can be impacted through changes to N input in several ways. Fowler *et al.* (2013) detail how increased deposition of N can lead to increased vegetation growth rates in forests, leading to potentially greater carbon sequestration rates. This potential positive impact, however, is offset by the effect of N saturation on forests as detailed by Nadelhoffer (2008). Here, the combined impact of disturbance to forest soil microbial systems involved in the nitrification-denitrification cycle (Fowler *et al.*, 2009) and damage to vegetation (Krupa, 2003) leads to a sharp decrease in net primary productivity. Even at deposition rates well below the saturation values, atmospheric N_r deposition can lead to changes in plant species composition, with implication not only on biodiversity but also ecosystem services. It is therefore important that exchange models be developed for all major biomes to accurately simulate deposition rates of NH_3 to forests to predict potential environmental consequences.

NH_3 is, in small quantities, emitted from (semi-)natural sources such as wild fires and the excreta of wild animals, but also emitted from plants as a result of non-zero NH_4^+ concentrations within the leaf apoplast, and from decomposing leaf-litter; both plant sources vary with the N status of the plants. Of further importance for nitrogen modelling is therefore the determination of the extent of potential emissions from forest ecosystems and the role such NH_3 emission might play in the N_r cycle within natural forests. Once considered to be perfect sinks

for ammonia (Duyzer *et al.*, 1992), bi-directional surface exchange of NH_3 i.e., deposition to and emission from have been recorded by many studies of NH_3 fluxes from forests (Langford and Fehsenfeld, 1992; Neirynck and Ceulemans, 2008; Wyers and Erisman, 1998). Predominantly, this has occurred in forests situated close to sources of agriculturally derived N_r pollution, although Hansen *et al.* (2015) have observed bi-directional fluxes over a more remote forest site.

The modelling of regional and local surface exchange of NH_3 is based on parameterisations of the exchange which remain unverified for many biomes of global importance due to the difficulty and cost of making measurements of NH_3 fluxes. Datasets of NH_3 flux measurements have mainly been constrained to temperate agricultural areas. Consequently, very little is known about the role of NH_3 in the N cycling in remote ecosystems such as the tropics and their disturbance through anthropogenic activity. Although Flechard *et al.* (2015) identified the need for NH_3 surface exchange measurements over tropical ecosystems, and over rainforests in particular, such measurements have been limited so far. Here we present recent data from the Amazon Tall Tower Observatory site situated in remote tropical rainforest where NH_3 fluxes were measured for one month during the dry season of 2017 as part of a suite of compounds (Chapter 5). This provides the necessary data required to develop site-specific parameterisations of NH_3 surface exchange, with the potential for upscaling to the regional level.

As extensive reviews of NH_3 surface exchange models are available (Flechard *et al.*, 2015; Massad *et al.*, 2010), only a brief overview is provided here. Models of bi-directional NH_3 surface exchange consider the control of fluxes to be analogous to electrical resistances (Baldocchi, 1988; Monteith and Unsworth, 2013). Whether emission occurs from the atmosphere to the canopy or vice versa, is dependent upon the difference between ambient and canopy concentrations, with resistances acting in series or in parallel impeding the exchange. In the simplest model of

bi-directional surface exchange, all exchange is approximated to occur via the leaf stomata situated at a single notional mean height (big-leaf approach) and is restricted by two atmospheric resistances in series (the aerodynamic resistance and quasi laminar boundary layer resistance), in series with a third (stomatal) resistance (stomatal compensation point model) (Sutton *et al.*, 1993).

Increasingly complex models include further pathways of exchange (Kruit *et al.*, 2010), with the most important for the current study being the canopy compensation point model, initially proposed by (Sutton *et al.*, 1995). In this model, two parallel pathways operate at the canopy level. In the first pathway, a stomatal compensation point is introduced, which is the concentration of NH_3 in the leaf stomata and which can consequently mediate with impedance from the associated stomatal resistance the exchange of NH_3 to and from the canopy to the leaf stomata. In the parallel pathway, a unidirectional deposition flux is modelled from canopy to the leaf cuticle, with a separate cuticular resistance controlling deposition. In a modified version of this model (the cuticular capacitance model), the leaf cuticle is considered to be both a sink and source for NH_3 (Sutton *et al.*, 1998). Here, the ability of water films on the leaf cuticle surface to act as a storage of previously deposited NH_3 is introduced as an analogue of an electrical capacitor, with emission fluxes of NH_3 from the cuticle possible with the evaporation of charged water films. Further models include ones which simulate the potential for soil and leaf litter below canopy to act as emission sources of NH_3 (Nemitz *et al.*, 2000a; Sutton *et al.*, 2009).

Using existing model frameworks of NH_3 surface exchange, in combination with new NH_3 flux and meteorological data measured at a remote, tropical rainforest site, this study aims to present a series of local models using different base parameters which accurately simulate the bi-directional fluxes of NH_3 as outlined in Chapter 5. Statistical comparison between models is conducted, with the aim to determine which model and hence, which of the factors controlling

the formulation of model parameters is most able to simulate observed fluxes. Discussion includes how meteorological conditions may have influenced model performance, and how subsequent studies of NH_3 fluxes over tropical rainforest may be conducted to help increase model performance.

6.2 Methodology

6.2.1 Field site description

Measurements were conducted on an 80 m walk-up tower located at the Amazon Tall Tower Observatory site (Brazil, 2°08.637 S, 58°59.992 W,). The ATTO site lies on a level plateau 120 m a.s.l., and is situated within a region of dense, undisturbed *terra firme* rainforest, with a mean canopy height of 37.5 m (Chor *et al.*, 2017). Manaus, the nearest large urban centre, is located 150 km to the south west. A full description of the ATTO site, its permanent instrumentation and the floristic composition of the surrounding rainforest is given in Andreae *et al.* (2015).

The rainforest extends homogeneously for many hundreds of kilometres to the north and east, but gives way to shrub-forest (*campina*) 5 km to the south, where the plateau descends to meet the Uatum River. The flux fetch distance of the sites 80 m tower, as determined from the approximation given by Monteith and Unsworth (2013), is 8 km. Therefore, while NH_3 fluxes can be considered representative for *terra firme* forest for the north and east, potential perturbation effects in flux measurements may result from the limited fetch distance to the south. However, during convective daytime conditions, the fetch is much shorter, typically < 2 km.

Measurements were made between 6 October 2017 and 5 November 2017, during the regions dry season. Lasting typically from August to November, the dry season is characterised by warmer, drier conditions in comparison to the wet season which lasts from February to May. Air masses that arrive at the site during the dry season typically travel over some urban and agricultural areas located to the south and south east of the site, which can give rise to periods of elevated black carbon (BC) and carbon monoxide (CO) concentrations (Saturno *et al.*, 2018b).

6.2.2 Measurements of ammonia and meteorological parameters

Ammonia

Ammonia was measured using the Gradient of Aerosols and Gases Online Registration system (GRAEGOR), a semi-autonomous, continuous wet-chemistry instrument (ECN, The Netherlands) (Thomas *et al.*, 2009). The GRAEGOR provides online analysis of a suite of inorganic trace gases (NH_3, HCl, HONO, HNO_3 and SO_2) and their associated water-soluble aerosol counterparts (NH_4^+, Cl^-, NO_2^-, NO_3^- and SO_4^{2-}) at hourly resolution. The instrument consists of two sample boxes, which were set at two heights ($z_1 = 42\,\text{m}$,and $z_2 = 60\,\text{m}$) on the 80 m walk-up tower, with a detector box which is connected to each sample box set at ground level for online analysis of samples.

Each sample box contains a wet annular rotating denuder (WRD) connected in series to a steam jet aerosol collector (SJAC). A length of high-density polyethylene (HDPE) tubing and a HDPE filter connect the inlets of the sample boxes to the WRDs, ensuring that losses of NH_3 are minimised. The walls of each WRD are coated in a constantly replenishing sorption solution of 18.2 MΩ

double deionised (DDI) water, with 0.6 mL of H_2O_2 (9.8 M) added per 10 L of sorption solution to eliminate potential biological contamination of the WRDs. Air is drawn simultaneously through each WRD at a rate of 16.7 $L\,min^{-1}$, kept constant by a critical orifice downstream of the WRD. Gaseous NH_3 within the laminar air flow diffuses onto the sorption solution coating the walls of the WRD, and the solution is subsequently transported to the detector box at ground level for analysis.

The detector box contains a flow injection analysis unit (FIA) to analyse the concentration of NH_3 within the WRD samples. WRD samples are fed to the FIA unit, where NaOH (0.1 M) is first added to the sample to form gaseous NH_3. The gaseous NH_3 then passes through a semi-permeable polytetrafluoroethylene (PTFE) membrane to enter a counterflow of DDI water to re-form NH_4^+. The temperature-corrected conductivity of NH_4^+ is then measured in the conductivity cell of the FIA unit, from which the atmospheric concentration of NH_3 at the height from which the sample was drawn can be determined. Through a valve control system within the detector box, the WRD sample from each height is analysed for NH_3 by FIA once per hour, resulting in an hourly resolved concentration gradient of NH_3. The FIA unit is calibrated autonomously using three liquid NH_4^+ samples (0, 50, and 500 ppb NH_4^+ concentration), with the first calibration conducted 24 hours after the GRAEGOR begins measurements, and every 72 hours afterwards. A total of 10 autonomous calibrations were conducted during this campaign.

Meteorology

Wind speed (u), wind direction (w_d), frictional velocity (u_*) and sensible heat flux were measured via eddy covariance by a Gill Windmaster mounted at 46 m on the 80 m walk-up tower. Relative humidity and air temperature were measured at 22

m, 36 m and 55 m using a series of Vaisala HMP45C-L instruments. Net radiation and photosynthetically active radiation were measured at 75 m by, respectively, a net radiometer (Kipp and Zonnen NR-LITE2) and a quantum sensor (Kipp and Zonnen PAR LITE). Hourly rainfall was measured using a HS Hyquist TB4-L.

6.2.3 Modified Aerodynamic Gradient Method

In the constant flux layer over homogeneous surfaces, the flux of a chemical tracer χ (gas or aerosol species) can be determined using the aerodynamic method (AGM) if the vertical concentration gradient of χ and its diffusion coefficient are known (Foken, 2008). A modified form of the AGM, based on the vertical concentration difference (∂_χ) between measurements of NH_3 at 42 m and 60 m, a series of stability parameters determined from meteorological measurements, and u_* as measured at 46 m by eddy-covariance (Flechard, 1998), was used to determine the flux of NH_3 as follows:

$$F_\chi = -u_* \kappa \frac{\chi_2 - \chi_1}{\ln\left(\frac{z_2-d}{z_1-d}\right) - \Psi_H\left(\frac{z_2-d}{L}\right) + \Psi_H\left(\frac{z_1-d}{L}\right)} \tag{6.1}$$

where κ is the von Krmn constant ($\kappa = 0.41$) and d is the zero-plane displacement height, determined as $0.9h_c = 33.4$ m. The integrated form of the heat stability correction term, ΨH, is included to account for deviations from the log-linear wind profile, while the term $(z - d)/L$, where L is the Obukhov Length, is a dimensionless measure of atmospheric stability.

The aerodynamic gradient method strictly holds for measurements made within the inertial sublayer. Corrections must be applied to fluxes calculated using the AGM if measurements are made close to the canopy and within the roughness sublayer, as was the case in this study. Fluxes were corrected using a correction

factor, γ_F, whose magnitude was determined from the stability conditions present at the time of measurement (Chor *et al.*, 2017) The validity of this correction was assessed for HNO_3 and HCl in Chapter 5.

6.2.4 Bi-directional flux models

The basic resistance model approximates the ability of the surface to mediate NH_3 deposition through a canopy resistance, R_c, which can be calculated from the inverse of the deposition velocity (V_d) of NH_3 at a reference height z minus the atmospheric aerodynamic resistance, R_a, and the quasi-laminar boundary layer resistance, R_b, (Fowler and Unsworth, 1979; Garland, 1977):

$$R_c = \frac{1}{v_d(z-d)} - R_a(z-d) - R_b \tag{6.2}$$

R_a and R_b can be determined from Eq. (6.3) and (6.4), respectively (Garland, 1977):

$$R_a(z-d) = \frac{u(z-d)}{u_*^2} - \frac{\Psi_H(\zeta) - \Psi_M(\zeta)}{\kappa u_*} \tag{6.3}$$

$$R_b = (Bu_*)^{-1} \tag{6.4}$$

where B is the sublayer Stanton number (Foken, 2008). This canopy resistance approach, however, can only strictly be applied if there is no bi-directional exchange. Since both emission and deposition of NH_3 was observed in this study, a bi-directional exchange model in which the exchange between the canopy and

the atmosphere is controlled by a conceptual canopy compensation point (χc) was required to simulate surface atmosphere exchange of NH_3.

In this static canopy compensation point model, the total surface-atmosphere exchange of NH_3 (F_t) is the sum of two constituent fluxes, the unidirectional deposition of NH_3 to the cuticle surface (F_w), and a bidirectional flux of NH_3 through the leaf stomata (F_s) (Sutton *et al.*, 1995):

$$F_t = F_w + F_s \tag{6.5}$$

where

$$F_w = \frac{-\chi_c}{R_w} \tag{6.6}$$

and

$$F_s = \frac{(\chi_s - \chi_c)}{R_s} \tag{6.7}$$

For the stomatal exchange flux, the difference between the canopy compensation point concentration (χ_c) and the stomatal compensation point concentration (χ_s) provides the numerator on the right-hand-side term in Eq. (6.7). When χ_s exceeds χ_c, emission occurs. χ_s is proportional to the ratio of dissolved NH_4^+ to H^+ in the leaf apoplast, which represents a dimensionless emission potential (Γ), via a temperature function that describes the combined Henry and solubility equilibrium (Nemitz *et al.*, 2004b):

$$\chi_s = \frac{161,500}{T} \exp\left(-\frac{10380}{T}\right) \Gamma_s \tag{6.8}$$

Here T is the temperature of the canopy in K.

The stomatal resistance, R_s, is dependent upon air temperature and the global radiation. The following generalised function for bulk stomatal resistance as per Wesely (1989) is used to calculate the stomatal resistance for NH_3 ($R_s(NH_3)$):

$$R_s\left(NH_3\right) = R_i \left\{1 + \left(200\left(S_t + 0.1\right)^{-1}\right)^2\right\} \left\{400\left[T'_{z0}\left(400 - T'_{z0}\right)\right]^{-1}\right\} \tag{6.9}$$

where R_i represents the minimum bulk resistance stomatal resistance for water vapour (in this study, $R_i = 45$ sm^{-1}); S_t is the global radiation in Wm^{-2}; and $T_{Z'_0}$ is the temperature in °C at the mean canopy height.

This model treats the flux to the leaf cuticle (F_w) to be unidirectional to a perfectly absorbing sink, given by the ratio of the canopy compensation point (χ_c) and the cuticular resistance (R_w). R_w can be described by a number of empirically derived parameterisations (Massad *et al.*, 2010), with most dependent on either relative humidity or water vapour pressure deficit. The term R_w is discussed further in Section 6.3.4.

The canopy compensation point (χ_c) is the conceptual mean concentration of NH_3 inside the canopy, at which the stomatal, cuticular and above-canopy fluxes balance each other. It is therefore dependent upon the ambient concentration of NH_3 (χ_a) and various physical and chemical parameters, both on the surface of the leaf and the surrounding atmosphere, as described by the resistances (stomatal,

cuticular, aerodynamic and quasi-laminar boundary layer) and the stomatal compensation point previously described. In this study, χ_c was calculated as:

$$\chi_c = \frac{\chi_s \times R_w \times (R_a + R_b) + \chi_a \times R_w \times R_s}{R_w \times R_s + R_a + R_b \times R_w + R_a + R_b \times R_s} \tag{6.10}$$

Prompted by the observation of morning emissions of NH_3 which could not be explained by stomatal exchange alone, this model was further extended by (Sutton *et al.*, 1998) to account for bi-directional exchange with leaf surfaces, by allowing NH_3 to be absorbed and desorbed to/from leaf water layers. That model calculated the NH_3 holding capacity by estimating the leaf water amount in relation to RH, which was implemented into the resistance framework by analogy to an electric capacitor, the charge of which depended dynamically on previously deposited NH_3 and tended to be released as dew dried out in the morning.

6.2.5 Determination of $T_{z'_0}$, $RH_{z'_0}$, $VPD_{z'_0}$ and $\chi_{z'_0}$

The aerodynamic resistance R_a and the quasi-laminar boundary layer R_b can be used to determine the temperature and NH_3 concentration at the mean canopy height, z'_0, if their respective values at a reference height are known (Nemitz *et al.*, 2009b):

$$T_{z'_0} = T(z-d)\frac{H}{\rho c_p}\left(R_a(z-d) + R_b\right) \tag{6.11}$$

$$\chi_{z'_0} = \chi(z-d) + F_\chi\left(R_a(z-d) + R_b\right) \tag{6.12}$$

The relative humidity at z_0' can be determined if the saturation pressure at z_0' ($\varepsilon\,\mathrm{sat}\,(z_0')$) and the water vapour pressure at $z_0{}'$ ($\varepsilon\,(z_0')$) are known:

$$RH_{z_0'} = \frac{\varepsilon\,(z_0')}{\varepsilon_{\mathrm{sat}(z_0')}} \times 100 \tag{6.13}$$

From measurements of $T_{z_0'}$ and $RH_{z_0'}$, the vapour pressure deficit (VPD) in kPa was determined.

6.2.6 Leaf wetness measurements

Leaf surface wetness was measured using a sensor array as first described by Burkhardt and Eiden (1994). Six sensors arranged in pairs of two, each consisting of gold-plated electrodes arranged as a clip, were each attached to a leaf situated 30 m above ground level and within the canopy surrounding the 80 m walk-up tower. Each clip measured the electrical conductivity in mV between the two electrodes. Data were recorded using a Raspberry Pi Model 2 B (Raspberry Pi Foundation, Cambridge) at a resolution of one minute. The sensor array was checked daily to ensure good contact between the clips and the leaf. Leaf wetness was measured from 6 October to 5 November 2017. Unlike conventional (Boolean) wetness grid sensors, this approach provides some graduation between fully dry and fully wet canopies.

Raw values from each sensor pair were converted to a leaf wetness parameter value, ranging from 0 to 1, according to the methodology outlined by Klemm *et al.* (2002). During periods of significant precipitation (0.1 mm rainfall per hour), the leaf is considered wet and the raw signal from the sensor is at a maximum value. During prolonged dry periods the leaf is considered to be dry, and the lowest recorded conductivity of the sensor pair during these periods is designated

as a zero signal. The net signal from each sensor pair is then determined by subtracting the corresponding zero signal from the raw signal for each period of data considered. The cumulative time period of precipitation is then determined from rainfall measurements. For this study, precipitation occurred during 15% of the total campaign time. Consequently, the signal percentile for each sensor that represents periods of precipitation was 85% in this study. Finally, the zero corrected net signals are divided by the value of signal percentile to give a finalised leaf wetness parameter whose values range from 0 (dry) to 1 (wet).

6.3 Results

6.3.1 Temperature, relative humidity, VPD and LWP at canopy

The time series of calculations of $T_{z_0'}$, $RH_{z_0'}$ and $VPD_{z_0'}$, together with measurements of leaf wetness parameter, are shown in Figure 6.1. The measurements can broadly be split into four distinct periods of warmer, drier conditions and cooler, wetter conditions. Period One, from 6 October to 18 October, is typified by an average leaf wetness at the canopy of 0.7, with an average RH of 82%, suggesting the prevalence of humid, wet conditions. Period Two extends from 19 October to 25 October, where leaf wetness at the canopy decreases, while VPD increases, which is paired with a drop in average RH. Conditions resume the same pattern from 6 October to 18 October during Period Three, which lasts between 26 October and 1 November, but gives way to drier, warmer conditions (Period Four) from 2 November until the end of the campaign.

A distinct lag exists between the relative humidity at the canopy level and the leaf wetness measurements, particularly during the drier conditions from 17 October

to 25 October. Minima in RH, which occur on average between 11:00 and 13:00, are not reflected in leaf wetness measurements until several hours later. Minima leaf wetness measurements during this period are recorded between 13:00 and 16:00.

6.3.2 Overview of NH_3 measurements

Figure 6.2 shows the time-series of the measured fluxes, together with model results (Section 6.3.5). Both (positive) emission and (negative) deposition fluxes were recorded during the campaign, ranging from $+9.47\ \mathrm{ng\,m^{-2}\,s^{-1}}$ to $-30.2\ \mathrm{ng\,m^{-2}\,s^{-1}}$. Figure 6.3 presents calculated NH_3 fluxes as scatter-plots for the duration of the campaign against paired measurements of temperature, relative humidity and leaf wetness parameter extrapolated to the canopy height. Shaded contour areas from green to red for, respectively, areas from low to high density of measurements - are added to the scatter-plots to highlight temperature, relative humidity and leaf wetness conditions where measurements of NH_3 fluxes were particularly concentrated. A statistical summary of linear regression models for calculated NH_3 flux and the respective metrological parameter plotted is given for each subplot.

While emission and deposition occur across the full range of temperatures recorded during the campaign, with a weak correlation ($R^2 = 0.02$; $p = 0.02$) in the linear regression model of NH_3 flux against temperature, emissions were more likely to be observed during warmer conditions. Relative humidity appears to be a somewhat stronger driver of NH_3 surface exchange behaviour ($R^2 = 0.08$; $p = 3.98 \times 10^{-4}$) than temperature. The slope and density contours suggest that with decreasing relative humidity, emissions are more likely. The strongest predictor of the three meteorological parameters investigated is leaf wetness parameter ($R^2 = 0.19$; $p = 2.72 \times 10^{-5}$). Emissions predominately occur during periods where leaf

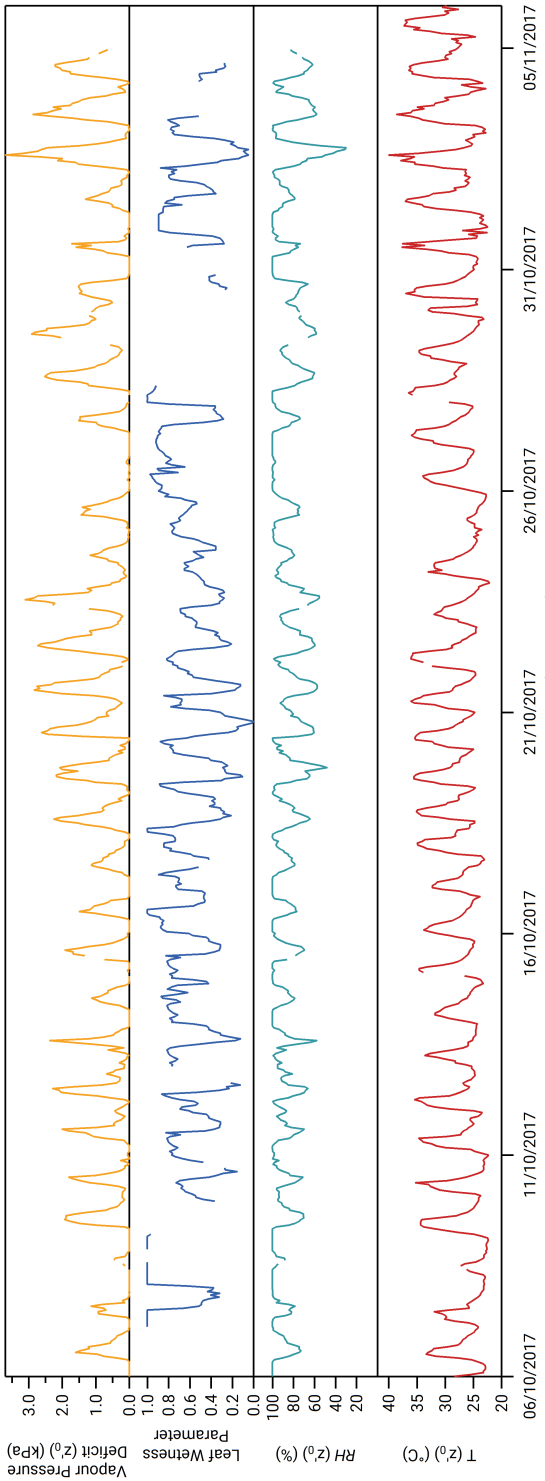

Figure 6.1: Time series of (from top to bottom) vapour pressure deficit at z'_0, leaf wetness parameter, relative humidity at z'_0, and air temperature at z'_0 throughout the period of NH_3 flux measurements.

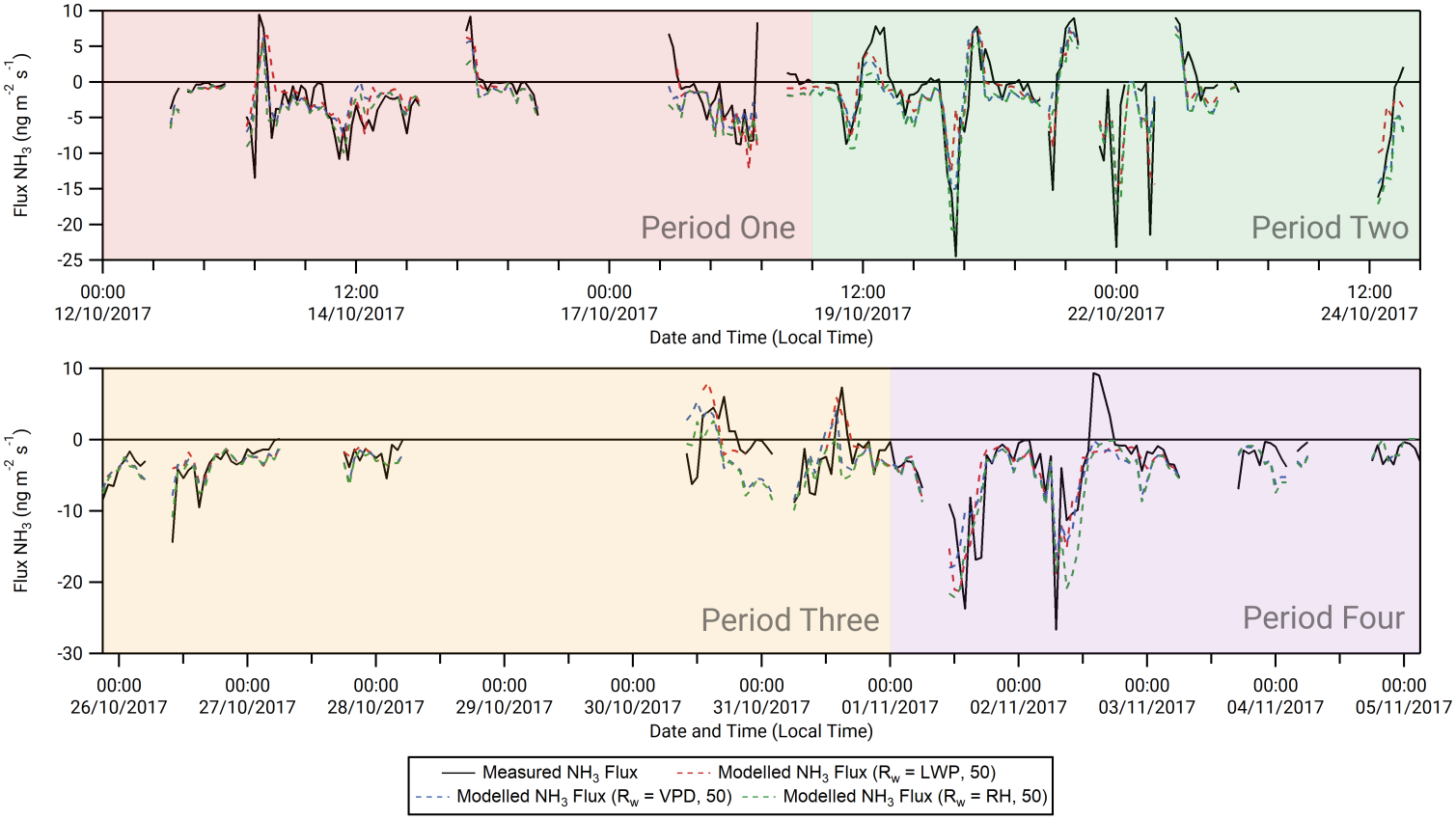

Figure 6.2: Time series of measured ammonia fluxes and simulated values produced by three single-layer canopy resistance models: in red, R_w = LWP, $\Gamma = 50$; in blue, R_w = VPD, $\Gamma = 50$; and in green, R_w = RH, $\Gamma = 50$. Periods of differing meteorological conditions are shaded in different colours.

wetness parameter values fall below 0.5, with deposition occurring predominately during periods where the leaf surface is wet (>0.6) or completely saturated (1).

6.3.3 Determination of stomatal compensation points and emission potentials

The modelling of NH_3 flux through the static canopy compensation point model is conditional upon the stomatal flux (F_s), which, from Eq. (6.7), is further dependent on the canopy concentration of NH_3 (χ_c) and the stomatal compensation point (χ_s). χ_s is determined by the leaf surface temperature (in this study, taken as $T_{z_0'}$) and the apoplastic ratio (Γ). If Γ is known, which varies with vegetation type (Hoffmann *et al.*, 1992; Mattsson *et al.*, 2009), environmental stressors such as drought (Sharp and Davies, 2009) and nitrogen nutrition (Massad *et al.*, 2008), then χ_s and subsequently F_s can be modelled.

Γ can be inferred from measurements if the NH_3 surface exchange is judged to be driven by stomatal exchange, rather than from desorption of NH_3 from the leaf surface. For the measurements of NH_3 surface exchange during this campaign, stomatal exchange is likely to be the driving force for observed emissions, due to emissions occurring during drier, warmer conditions as per analysis of Figure 6.3. Consequently, it can be considered that the ambient NH_3 concentration (χ_a) at which a zero-net flux (i.e., when the difference between χ_c and χ_s is 0) occurs is implicitly equal to χ_c and χ_s if R_w is very large compared with R_s. Therefore, if NH_3 surface exchange is driven by stomatal exchange, χ_s may be determined from the values of χ_a at which the flux changes from deposition to emission, or vice versa (Nemitz *et al.*, 2004a). Figure 6.4 presents the ambient NH_3 concentrations measured during the campaign at which such flux sign changes occurs as a function of $T_{z_0'}$, for conditions under which R_w is expected to be fairly large (RH $< 65\%$).

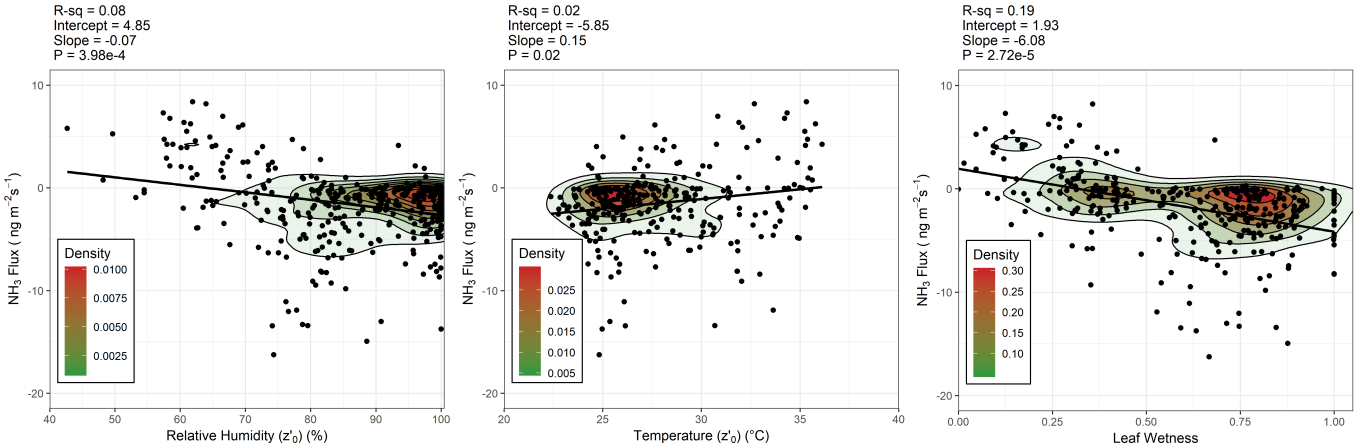

Figure 6.3: Scatter-plots with line of best fit and number density shadings for NH_3 flux against (from left to right) relative humidity at z_0', temperature at z_0', and leaf wetness parameter.

Eq. (6.8) can therefore be rearranged to give an expression for Γ that is dependent upon $T_{z'_0}$ and χ_s, where χ_s can be substituted with a value of χ_a at which a sign change in the flux of

$$\Gamma_s = \frac{1}{\left[\frac{161500}{T_{z'_0}+273} \exp\left(-\frac{10380}{T_{z'_0}+273}\right)\left(\frac{1}{\chi_s}\right)\right]} \tag{6.14}$$

Using the values of χ_a measured in this campaign which are inferred to be equal to χ_s, an apoplastic ratio applicable to the period of measurement was determined as 38.5 ± 15.8. From this value, a temperature response curve of the apoplastic ratio was generated, which is plotted in Figure 6.4, and shows reasonable fit for the values of χ_a which are inferred to be equal to χ_s. Consequently, modelled values of χ_s based on a value of $\Gamma = 38.5$ were determined for the campaign period, and subsequently used to determine values of χ_c and total modelled flux. With consideration of the standard deviation, and subsequent model comparisons with NH_3 fluxes derived from observations, a value of $\Gamma = 50$ was also used to develop further parameterisations for comparison. Furthermore, with this approach, all emissions from the leaf surface are implicitly considered to originate from leaf stomata, rather than cuticular desorption or other potential sources of NH_3 emissions, such as soil or leaf litter.

6.3.4 Determination of the three R_w parameterisations

Considering the observed drivers for NH_3 surface exchange discussed in Section 6.3.2, three different parametrizations for the cuticular resistance R_w were developed for this study based upon three alternative proxies of the NH_3 holding capacity of the leaf water layers: $RH_{z'_0}$, $VPD_{z'_0}$, and leaf wetness. Subsequently, each parameterisation of R_w was used to develop three distinct values for F_w,

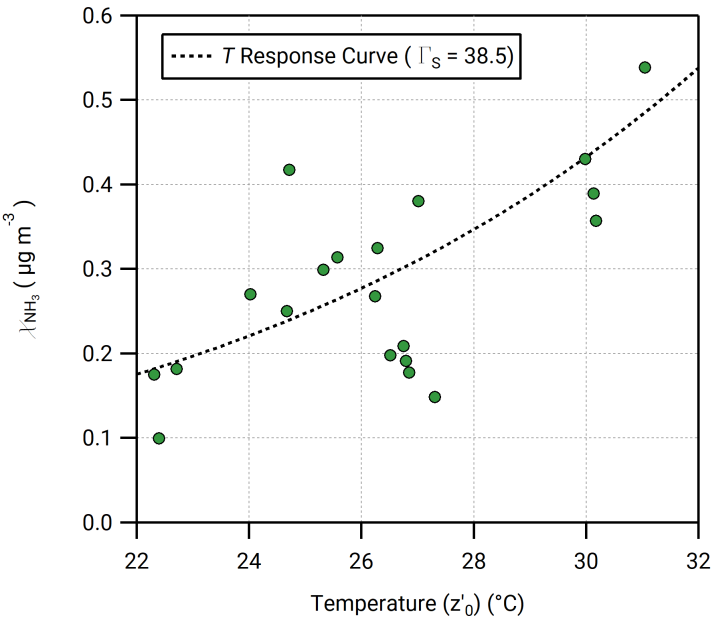

Figure 6.4: Estimating the stomatal compensation point from the ambient NH_3 concentrations at which the flux changed signs as a function of the temperature at z'_0. The dotted line shows the temperature response curve calculated using an apoplastic ratio of 38.5.

the unidirectional flux component of the cuticular-resistance-based, single-layer model, each describing the surface atmosphere exchange of NH_3 at the ATTO site.

The first parameterisation was based on measurements of $RH_{z'_0}$ using the following equation (Sutton *et al.*, 1993):

$$R_w = \alpha + \exp\left(\frac{100 - RH}{\beta}\right) \tag{6.15}$$

Here, α, or $R_{w(min)}$, is the minimum cuticular resistance, while β is a constant scaling coefficient controlling the increase of R_w with decreasing relative humidity. The coefficients α and β were fitted by least squares optimisation with the

measured, observed values of NH_3 flux taken during the campaign to arrive at values of $\alpha = 2\ \mathrm{s\,m^{-1}}$ and $\beta = 9$, which were used for the modelling R_w based on $RH_{z'_0}$ for the entirety of the campaign.

The second parameterisation was based on measurements of the vapour pressure deficit, using the formulation for R_w employed by (Flechard *et al.*, 1999):

$$R_w = \alpha + \beta \left(1 - \exp^{-\gamma(\mathrm{VPD})}\right) \tag{6.16}$$

As with the parameterisation of R_w in Eq. (6.15), the coefficient α is the minimum value for R_w at zero VPD, set at $2\ \mathrm{s\,m^{-1}}$. β and γ are constant scaling coefficients which, respectively, control the scaling of the exponential term and the scaling of the vapour pressure deficit. Through least square optimisation, a value of 5 was used for β and 1.7 for γ, for the determination of R_w based on Eq. (6.16) for the entirety of the campaign.

Finally, a novel parameterisation for R_w based upon measurements of leaf wetness was developed for this campaign based on least square optimisation:

$$R_w = \alpha + \beta \left[\exp^{\gamma(1-LWP)} - 1\right] \tag{6.17}$$

As with the parameterisations of R_w described in Eq. (6.15) and (6.16), α is the minimum value of R_w at maximum leaf wetness, set at $2\ \mathrm{s\,m^{-1}}$, β is a scaling coefficient, similar to that of the parameterisation in Eq. (6.16), set at a value of 5, and γ is a scaling coefficient controlling the increase in R_w with the decrease in leaf wetness, set in this study to 4.8.

6.3.5 Comparison of modelled with observed NH_3 fluxes

Six discrete models of NH_3 surface exchange developed using Eqs. (6.5), (6.6) and (6.7) were produced using the two values of apoplastic ratio ($\Gamma = 38.5$ and $\Gamma = 50$) and the three parameterisations for R_w (relative humidity RH, vapour pressure deficit VPD, and leaf wetness parameter LWP) described above. These models are: a. (R_w = LWP,$\Gamma = 38.5$), b. (R_w = LWP,$\Gamma = 50$), c. (R_w = RH,$\Gamma = 38.5$), d. (R_w = RH,$\Gamma = 50$), e. (R_w = VPD,$\Gamma = 38.5$), and f. (R_w = VPD,$\Gamma = 50$).

Table 6.1 presents a summary of the model results, with average mean modelled fluxes for the overall campaign, together with day (06:00 17:00) and night-time (18:00 05:00) average mean values for the four separate periods of the campaign discussed in Section 6.3.1. Also presented are average mean values for calculated fluxes based on NH_3 measurements during the campaign, and the percentage of modelled values which agree in flux direction with observed values. Modelled mean values highlighted in bold signify where the model value deviates by more than 25% from the corresponding observed mean average. The models which differ least and most from the observed values are models b and c, respectively. Models which use the calculated apoplastic ratio of 38.5 differ more from the observed values than those which use an apoplastic ratio of 50 (near 1-σ from calculated). Modelled daytime values tend to differ less from their corresponding observed value in comparison to night-time values. Modelled values during Period One have the least divergence from the observed overall (day and night), while the greatest divergence in modelled values occurs during Period Four, particularly at night. 90.6% of model b values agree with the observed direction of fluxes, the best performing model using this parameter. Conversely, model c values agree with only 82.4% of the observed direction of fluxes.

Figure 6.2 shows the full time series of modelled NH_3 fluxes from models b, d, and

Table 6.1: Summary of model results, with comparison to measured hourly NH_3 fluxes (in $ng\,m^{-2}\,s^{-1}$). Presented are the overall mean average flux for measured and modelled NH_3 fluxes, the correctness of modelled flux direction in comparison to the measured values, and mean average values for modelled and measured NH_3 fluxes during day (06:00 17:00) and night (18:00 05:00) for the four periods of the measurement campaign. Values in bold signify average model values which differs by ± 25% from corresponding measured average value.

	Overall	Correctness	Period One		Period Two		Period Three		Period	Four
		of direction (%)	Day	Night	Day	Night	Day	Night	Day	Night
Measured	-2.83	-	-2.80	-1.47	-3.36	-2.14	-4.74	-1.97	-6.61	-2.02
Model a. R_w, LWP, 38.5	-3.03	87.2	-3.19	-1.86	-3.33	**-2.81**	-4.55	**-2.58**	-5.99	-2.90
Model b. R_w, LWP, 50	-2.69	90.6	-2.36	-1.86	-3.25	**-2.80**	-3.93	-2.37	-5.94	-2.89
Model c. R_w, RH, 38.5	**-3.97**	82.4	**-4.76**	**-2.45**	**-5.05**	**-3.74**	**-6.35**	**-3.52**	**-4.28**	**-2.76**
Model d. R_w, RH, 50	**-3.73**	86.8	**-4.14**	**-2.45**	**-4.15**	**-3.73**	**-5.89**	**-3.52**	**-4.22**	**-2.75**
Model e. R_w, VPD, 38.5	-3.48	84.8	-3.45	**-2.28**	-3.55	**-3.58**	-4.62	**-3.32**	-5.83	-3.35
Model f. R_w, VPD, 50	-3.16	89.1	-2.64	**-2.28**	**-2.50**	**-3.58**	-4.01	**-3.32**	-5.78	**-3.34**

f alongside the measured flux for the entirety of the campaign. The four periods of differing meteorological conditions are highlighted by different shadings. In general, periods of emission and deposition are modelled well by all three models. Two exceptions exist: the emission period from 12:00 to 16:00 on 30 October, where modelled fluxes suggest an earlier emission from 11:00 which lasts for fewer hours; and from 13:00 to 15:00 on 2 November, where no model predicts an emission, in contrast to the measurements. The magnitude of modelled fluxes generally agree well with the observed flux, although model d, which uses a R_w parameterisation based on RH, tends to estimate smaller emissions in comparison to model f (R_w = VPD). Model b (R_w = LWP) comes closest to replicating the magnitudes of the measured emissions, although as with the other two models underestimates the magnitude of the measured deposition.

6.4 Discussion

The observed bidirectional surface exchange of NH_3 from a remote tropical rainforest site was modelled using a series of canopy compensation point, cuticular resistance based models using a variety of different R_w parameterisations and apoplastic ratios.

As mentioned in the Introduction, measurements of NH_3 surface exchange over natural ecosystems such as forests remain sparse. This is particularly true for measurements over tropical vegetation, which to this study's knowledge, are limited to those by (Trebs *et al.*, 2004) and Adon *et al.* (2010, 2013). Bi-directional exchange of NH_3 has been reported previously at temperate forest sites: for example, Langford and Fehsenfeld (1992) noted daytime emission from a remote forest near Boulder, Colorado; Neirynck and Ceulemans (2008) observed bidirectional NH_3 exchange (with median diel emissions recorded between 12:00

and 16:00) over a Scots Pine (*Pinus sylvestris*) forest in Flanders, Belgium; while Wyers and Erisman (1998) noted daytime emissions from Douglas Fir forest at Speuld in the Netherlands. When using models to determine the drivers of surface exchange above forest sites, these studies often stress the importance of cuticular desorption as a further process that dominated in the morning when emission could not have originated from stomatal compensation points. Indeed, in the case of Neirynck and Ceulemans, the static canopy compensation point model (CCP) was unable to simulate their observed emissions.

At ATTO, there is no such indication that the single layer static CCP model was unable to reproduce the dynamics of the measured NH_3 surface exchange. Indeed, an exploratory application of the dynamic CCP model did not result in an improvement in model performance and therefore the modelling work here focussed on the static model as the simpler model able to reproduce the measurements. The absence of morning desorption peaks at the ATTO forest is likely due to the small night-time adsorption of NH_3 into leaf water layers associated with the low NH_3 concentrations at this site. In addition, given the high RH, the water layers may not dry out as rapidly and completely as at other sites. The measured median NH_3 atmospheric concentration at the canopy height during the measurement period was 0.23 $\mu g\,m^{-3}$, with an estimated annual total N_r input of 1.74 kg Nitrogen ha^{-1} (Chapter 5). This is far lower than reported by Neirynck and Ceulemans (2008) and by Wyers and Erisman (1998), both of whose sites were subject to high levels of agriculturally sourced pollution. As noted by Massad *et al.* (2010) and Zhang *et al.* (2010), higher atmospheric inputs of nitrogen to forest systems lead to an increase in the stomatal emission potential. Conversely, with lower atmospheric NH_3 concentrations, the potential for forests to act as a source of NH_3 is increased, as the likelihood of the canopy compensation point exceeding the ambient concentration increases.

The consistently warmer noon-time conditions at the leaf canopy during measurements at the ATTO site would also favour stomatal exchange. An increase in leaf temperature leads to greater gas exchange through increased stomatal openings (Urban *et al.*, 2017), while alterations to the Henry and solubility equilibria would lead to a change in the stomatal compensation point favouring increased stomatal emissions. Similarly, the unstable conditions at noon above the canopy over tropical rainforest leads to reductions in R_a, which would increase any emissions occurring at the time that were driven by stomatal exchange ((Flechard *et al.*, 2015). In the study of forest NH_3 emissions that is most similar in ambient NH_3 concentrations, canopy compensation points and apoplast ratios to this study, Hansen *et al.* (2017) comes to a similar conclusion on the observed daytime emissions from a remote, temperate forest in Indiana, USA.

Despite the low N inputs and apoplastic NH_4^+/H^+ ratio, significant emission periods were observed above the ATTO site. One driver is clearly the high daytime leaf temperatures. Nevertheless, over infinitely large areas and in the absence of other sources and sinks, the concentration in the air should adjust to the emission potential of the terrestrial landscape and, once this equilibrium is established, fluxes should go to zero. This argument has been used to assume that oceanic NH_3 emissions should be small. The observed flux dynamics of emission and deposition above the Amazon rainforest therefore suggest that such steady state equilibrium is not reached. The average flux amounted to a small deposition of -2.83 $\mathrm{ng\,m^{-2}\,s^{-1}}$ suggesting that, on average, the site receives more nitrogen as NH_3 than it loses. Possible sources include small-scale farming and biomass burning.

6.4.1 Apoplastic Ratio

The apoplastic ratio of NH_4^+/H^+ (Γ) derived from measurements in this study was 38.5 ± 15.8; the models investigated used either a value of 38.5 or 50 (close to one standard deviation from inferred value). Both values are significantly lower than the majority of Γ values obtained for other forest sites. Wang *et al.* (2011) gives a value of $\Gamma = 400$ for green temperate forest canopies, which is also used by Hansen *et al.* (2017). Massad *et al.* (2010) reviews a range of Γ values derived from measurements of NH_3 surface exchange over forest, which range from $\Gamma =$ 27 to $\Gamma = 5604$. The study by Neirynck and Ceulemans (2008) used a value of 3300 in spring and 1375 in summer.

The disparity in the emission potentials between other forest sites and the tropical rainforest site at ATTO is linked, as with the canopy compensation point, to nitrogen input. With larger N inputs where nitrogen is deposited in excess, the stomatal concentration is increased (Schjoerring *et al.*, 1998). Consequently, at polluted areas such as the forest sites studied by Neirynck and Ceulemans (2008), apoplastic ratios are increased, while at sites with lower nitrogen input, such as semi natural vegetation with low ambient NH_3 concentrations (Hanstein *et al.*, 1999), values of Γ can be as low as 5 10. The species of vegetation is also critical (Mattsson *et al.*, 2009), with plants which are reliant on mixed nitrogen sources (ammonium, nitrate, and organic nitrogen), and which are more reliant on root rather than shoot assimilation of nitrogen, exhibiting lower apoplast ratios than nitrate reliant, shoot assimilating species Hoffmann *et al.* (1992). While not established if the tree species constituting the canopy layer at the ATTO site assimilate nitrogen predominantly through roots or shoots, and whether they are reliant on NO_3^- or mixed sources of nitrogen, the nitrogen poor status of the soil substrate would potentially impact on overall apoplastic ratio through diminished intracellular NH_4^+ concentrations. Considering this, the value of 38.5 which was

inferred from measurements lies comfortably in the range of Γ values exhibited by semi-natural vegetation with low N inputs, and in the lower range of overall forest values, as quoted by Massad *et al.* (2010).

6.4.2 Model Performance

An assessment of the performance of the individual parameterisations against calculated NH_3 fluxes is included in Figure 6.5, which displays the results of simple linear regression models for the simulated values of each NH_3 flux model against observed NH_3 fluxes. With regards to the coefficient of determination (R^2), the rank of models from most strongly correlated with observed NH_3 fluxes to least correlated is model b, model a, model f, model e, model d, model c. The R_w parameterisation was a stronger determinant of model-measurement correlation than the choice of Γ. Correlation with measurements is highest for the models using an R_w based upon LWP, followed by those which use VPD and finally RH. Within each grouping, models using $\Gamma = 50$ provide simulated values which have a better correlated fit with observed values than $\Gamma = 38.5$.

The predominance of R_w parameterisation over apoplastic ratio as a factor governing good model fit is more visibly noted from the Taylor diagram (Figure 7.1) of model performance which summarises in one diagram the three complementary model-measurement performance statistics of (i) correlation coefficient (R), (ii) centred root mean squared error (RMSE), and (iii) within-model and within-measurement standard deviations (SD) (Taylor, 2001). The statistical metrics visualised in Figure 7.1 are summarised in Table 6.2.

The standard deviation in the observed dataset is 3.65 $\mathrm{ng\,m^{-2}\,s^{-1}}$. The model which comes closest to replicating this same variability is model b (2.65 $\mathrm{ng\,m^{-2}\,s^{-1}}$), with model e (2.24 $\mathrm{ng\,m^{-2}\,s^{-1}}$) replicating observed values least well,

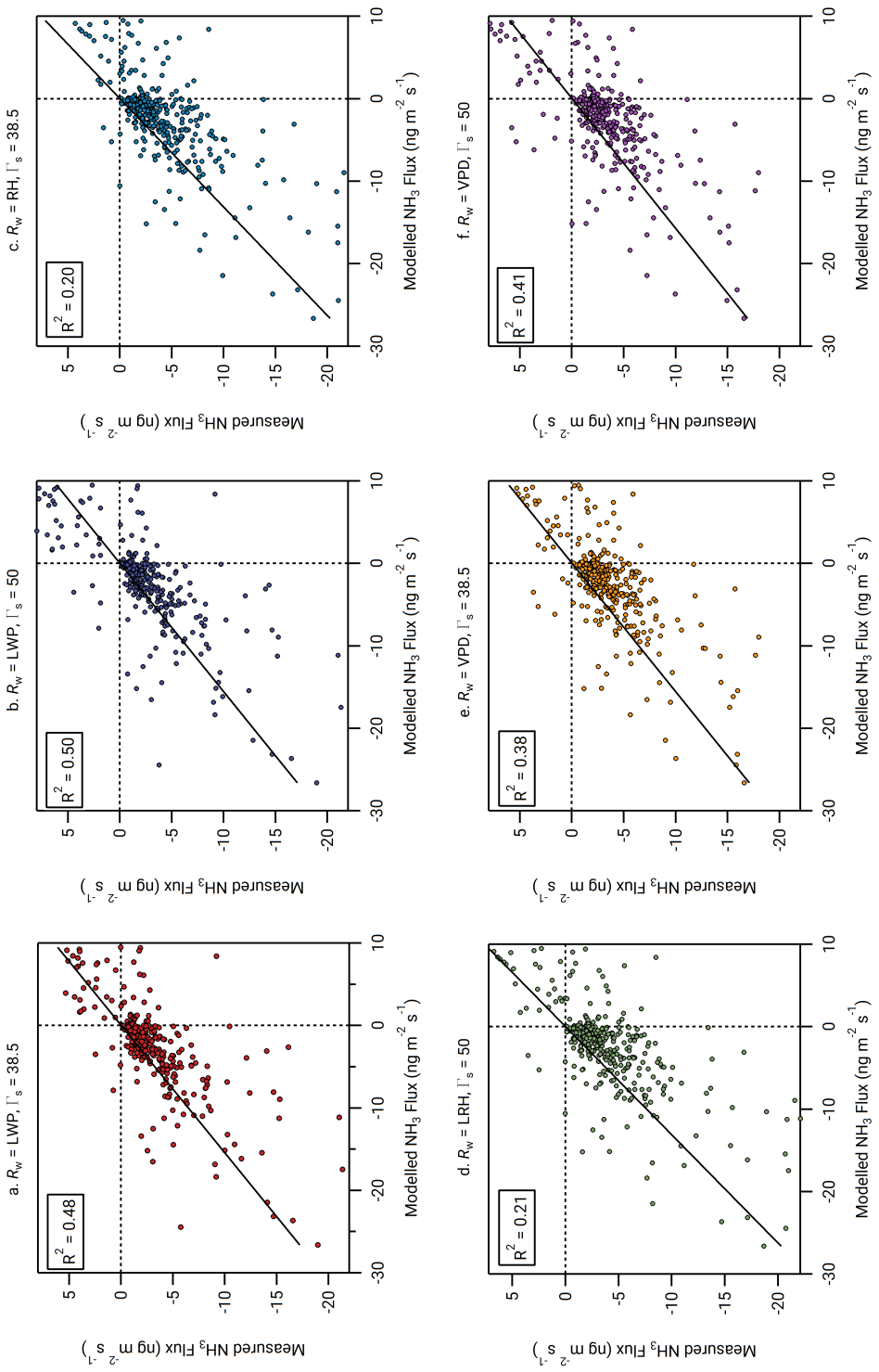

Figure 6.5: Linear regressions between measured NH_3 fluxes and six models, a - f, of NH_3 fluxes differing in the approach used to derive a value for the cuticular resistance R_w and in the value used for the apoplastic ratio Γ, as noted above each panel.

although the overall range between model standard deviation is broadly similar. It should be borne in mind, however, that the standard deviation of the measured flux includes error variability in addition to real variability. With regards to R, model b simulated values produce the highest correlation with the observed values at 0.71, in comparison to model c, which performs the worst at 0.45. Finally, the model with the lowest root mean square error from the observed is model b at 2.79 $\mathrm{ng\,m^{-2}\,s^{-1}}$, with the highest error found in model c, at 3.31 $\mathrm{ng\,m^{-2}\,s^{-1}}$. Therefore, from these values and the ability of the parameterisations to reproduce the measured average fluxes (Table 6.1) it can be concluded that parameterisation b, in which the value R_w is parametrised using leaf wetness parameter values and where the apoplastic ratio is set to 50, is the best performing model in simulating NH_3 surface-atmosphere exchange at the ATTO site, while model c is the worst performing. However, it is important to note, as is visually apparent in Figure 7.1, that the influence of the apoplastic ratio is relatively minimal for reproducing flux variability in comparison to the effect of R_w parameterisation. However, the choice of Γ does affect the models ability to reproduce the overall magnitude of the fluxes during daytime (Table 6.1).

All three parameters explored for the parameterisation of R_w leaf wetness, vapour pressure deficit and relative humidity at the canopy level should be closely linked. Even after optimisation of the models, however, extensive differences in model output remain, principally between leaf wetness parameter and RH. Figure 6.7 presents a scatter plot of leaf wetness measurements against RH normalised to the canopy height. The relationship between them is best described through a power equation, which suggests that leaf wetness decreases far more sharply than RH across the campaign. Indeed, considering Figure 6.1, there exists a distinct lag between observed RH (as well as VPD) and the leaf wetness parameter. While RH minima are detected between 11:00 and 13:00, and ranges in a fairly narrow band between 100% to 80%, leaf wetness reaches minima between 13:00

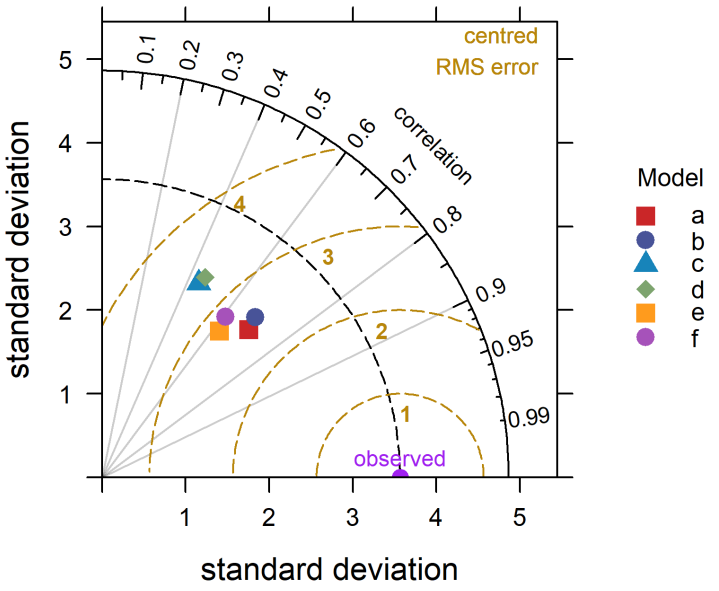

Figure 6.6: A Taylor diagram summarising the statistical comparisons between the modelled NH_3 fluxes from six models and the measured NH_3 fluxes.

to 16:00, and can decrease significantly, particularly during Period Two of the campaign. Considering the measurements of leaf wetness take place directly at the leaf surface, and are therefore more responsive to the actual changes occurring in leaf desiccation, the response of NH_3 surface exchange models using the leaf wetness parameter are likely to be more sensitive, and better simulate values in relation to the observed, than models using leaf-wetness proxies such as $RH(z_0')$ or $VPD(z_0')$ as the basis for R_w.

The results therefore indicate that there is significant value in making direct measurements of leaf wetness using leaf wetness clip sensors of the type used here, for interpreting field measurements. However, such a parameter is not typically available in chemistry and transport models and here the results would favour VPD based of RH based parameterisations.

Table 6.2: Summary of model statistical performance (correlation coefficient R, centred root mean square error, and standard deviation) as presented in Figure 7.1.

	R	RMSE ($\mathrm{ng\,m^{-2}\,s^{-1}}$)	Standard Deviation within model ($\mathrm{ng\,m^{-2}\,s^{-1}}$)
Model a. R_w, LWP, $\Gamma = 38.5$	0.69	2.81	2.49
Model b. R_w, LWP, $\Gamma = 50$	0.71	2.79	2.65
Model c. R_w, RH, $\Gamma = 38.5$	0.45	3.31	2.60
Model d. R_w, RH, $\Gamma = 50$	0.46	3.27	2.62
Model e. R_w, VPD, $\Gamma = 38.5$	0.62	2.92	2.24
Model f. R_w, VPD, $\Gamma = 50$	0.64	2.90	2.49

Choice of Γ value

Although modelled values are not as greatly affected to the same extent as with which R_w parameterisation was used, the choice of which apoplastic ratio was used did have a small but significant effect between agreement of modelled values and observations. Models which used the Γ value of 50 (b, d and f) simulated values better in agreement with observations in comparison to their paired R_w models (respectively, a, c, and e) which used the value of 38.5. In particular, the use of 38.5 as a value led to models underestimating the scale of the emissions.

The discrepancy highlights a potential problem with using the method outlined in Section 6.3.3 in tropical conditions. As outlined by (Nemitz *et al.*, 2004a), the validity of equating χ_a to χ_c only holds for dry conditions (e.g. RH $< 50\%$), when R_w can reliably be expected to be large. At higher humidity values, leaf cuticles may start to become a small sink and χ_c becomes an underestimate of χ_s. At the ATTO site, where median humidity at the canopy level throughout the campaign was 87%, with only a few occurrences during the drier Periods Two and Four where it fell below 60%, this approach of inferring Γ from NH_3

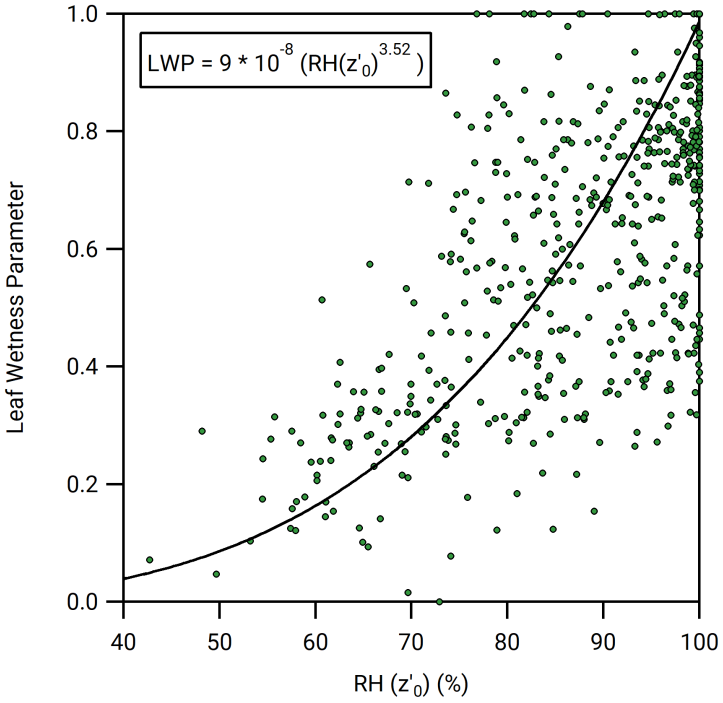

Figure 6.7: Scatter plot of hourly leaf wetness parameter and relative humidity z'_o measurements taken during campaign, with a fitted power relation curve.

measurements was likely affected. However, the impact does not appear to have completely invalidated the use of the method, as the somewhat larger value of 50 that resulted in models with best agreement still lies within one standard deviation of the inferred Γ value. However, while suitable for this campaign in modelling NH_3 surface exchange, the need for an accurate determination of apoplastic ratio for tropical rainforest remains an important concern, particularly for larger scale surface exchange models.

Period of measurement

Modelled values diverge significantly from observations at several points during the campaign. In particular, every model on 30 October predicts an earlier, less sustained emission in comparison to the observation, while on 2 November, no

model predicts any emission, contrary to observations which suggest a strong emission of NH_3 from 13:00 to 15:00. With regards to the divergence in models from the observations on 2 November, the possibility of other sources of NH_3 emission could be considered that would not be accounted using the single layer model. For example, from the evening of 31 October to the early morning of 2 November, heavy periods of precipitation were recorded, coupled with increased deposition fluxes of NH_3 on 1 November. Increased wet deposition of N through NH_4^+ in rainwater and washed from the canopy (Nemitz *et al.*, 2000a) to the forest floor would lead to an increase in soil or leaf litter microbial activity below canopy. Subsequently, the drying of the soil and leaf litter throughout 2 November might have led to an evaporation of NH_3 from the littler or soil layer from the forest floor (Hansen *et al.*, 2017), leading to observed emissions of NH_3 in the afternoon. This potentiality would not be modelled with the single layer canopy resistance model, and as a result, models would not capture this source of emission. The additional impact of soil or leaf litter emissions could further explain the slight underestimation of emissions of all models throughout the campaign.

Average modelled values for daytime tended to agree better with their corresponding period of observations than night-time values. Overall, the six models tended to overestimate nocturnal NH_3 deposition, particularly during Period Two and Four when all six models overestimated the average deposition by over 25% from the corresponding average observations. A possible reason for this discrepancy could be incomplete stomatal closing at night due to the absence of water stress (Caird *et al.*, 2007). A resultant higher stomatal conductance could suppress the deposition of NH_3, leading to differences between observed and modelled NH_3 surface exchange. Of course, the flux measurement itself is not without error, especially during the calmer and more stable night-time conditions.

6.5 Summary and Conclusions

Observations of the bi-directional, surface atmosphere exchange of NH_3 at a tropical rainforest site have been successfully replicated using single layer, canopy resistance based models. Cuticular capacitance models, however, were unsuccessful at simulating the observations, which in combination with the meteorological conditions under which emissions occurred led to the conclusion that the observed flux behaviour was governed by stomatal exchange. Models which used a single layer canopy resistance approach, where the cuticular resistance was governed either by RH, VPD or a measurement of leaf wetness, were able to replicate the pattern of observed NH_3 deposition with frequent periods of afternoon emissions. Of all the models used, the most successful was a cuticular resistance modelling approach based on using leaf wetness measurements, and where modelled χ_c was governed by an apoplast $\Gamma = NH_4^+ / H^+$ ratio of 50.

The absence of desorption emission fluxes of NH_3 from drying water films is surprising considering the warm, humid conditions that prevail at this rainforest site. The general conditions would, from first principles, seem to favour a surface exchange of NH_3 predicted upon the formation of water films on leaves, which upon evaporation during early morning would discharge captured NH_3 from previous deposition or stomatal exchange. Past studies above forests have noted similar behaviour, and while stomatal exchange has been noted as being the dominant process of NH_3 surface exchange in many of these studies, this has occurred in areas with high ambient NH_3 concentrations, forests with high Γ values, and in combination with desorption fluxes, factors which were absent during this campaign.

However, the periods where the most frequent emissions of NH_3 occurred, and which were successfully modelled by cuticular resistance models, are typified by conditions that diverge from the overall expected climate. The question

arises, then, if these periods are frequent annually over tropical South American rainforest. This campaign took place in the dry season, and so comparison with the surface exchange of NH_3 during the wet season would be a necessary first step in determining if stomal exchange is the principal driver of NH_3 surface exchange throughout the year. Long term observations would also be required to note if the temperature increases, drought conditions and elevated ambient NH3 concentrations that are to be expected in time with climate change and human development over this region have any impact on NH_3 surface exchange.

One of the results of this study has been in establishing the suitability of leaf wetness measurements, converted to a suitable parameter, as a factor for modelling cuticular resistance in NH_3 surface exchange modelling. While the use of leaf wetness values in NH_3 modelling has been used previously, this has primarily been used to convert to an associated value of RH and then to use in R_w parameters which use RH rather than leaf wetness directly. Through the use of contact sensors, leaf wetness can be used directly, with a R_w parametrisation that, in this study, proved to be the most sensitive and accurate in simulating NH_3 surface exchange. However, VPD may be the parameter of choice for chemistry and transport models as it is more readily simulated.

The Γ value which led to the best modelling of χ_c values, and hence to the best fit with observed values, was 50. While within one standard deviation from the inferred values of 38.5, this did highlight that the method used to infer apoplastic ratio perhaps suffered under the high humidity conditions present at the rainforest site. An accurate determination of emission potential for this region is required for global scale modelling, necessitating accurate measurements of apoplast ratio. Future studies of NH_3 surface exchange above rainforest should therefore seek to incorporate accurate determination of leaf apoplastic ratio as a necessary part of their methodology.

Finally, periods of divergence between the models and observed values highlights that other sources of NH_3 surface exchange (such as soil or leaf litter exchange) should be incorporated into future investigation, while also emphasising the difficulty in measuring and modelling NH_3 surface exchange in remote, challenging conditions. For a full-scale understanding of NH_3 surface exchange dynamics at rainforest sites, a full suite of instruments measurements, incorporating in-canopy measurements of NH_3 concentration gradients, trunk space flux measurements and characterisation of leaf and soil NH_4^+ pools would be required. With increasingly sensitive and cost-effective measurements of NH_3 becoming available, and the growing diversity of measurements conducted at the ATTO site, long-term measurements of NH_3 surface exchange over rainforest will likely become more feasible.

Chapter 7

Conclusions, synthesis, and future work

7.1 Conclusions and synthesis

This work has presented the concentrations of the inorganic trace gas species NH_3, HCl, HONO, HNO_3 and SO_2, and their associated aerosol counterparts, NH_4^+, Cl^-, NO_3^-, and SO_4^{2-} as measured over agricultural grassland and tropical rainforest. Measurements over agricultural grassland were taken from May 2016 to June 2016 at the Easter Bush agricultural grassland site (Midlothian, United Kingdom), while measurements over tropical rainforest were taken from October 2017 to November 2017 at the Amazon Tall Tower Observatory site (Amazonas, Brazil). In both measurement campaigns, the Gradient of Aerosols and Gases Online Registration (GRAEGOR) instrument was used to measure the concentrations of the aforementioned species at two discrete heights (0.6 m and 2.4 m over agricultural grassland, and 42 m and 60 m over tropical rainforest). From these two-point concentration measurements, the fluxes of the trace gas

species and aerosols measured were determined using a modified form of the aerodynamic gradient method. With regards to the fundamental task of this study then, which was to measure the concentrations and surface-atmosphere exchange of trace gases and associated aerosols above two distinct biomes, the principal aim of this work has been achieved. One month of trace gas and aerosol concentration and flux values are now available for an agricultural grassland site and for a tropical rainforest site, which can be compared to the results of other instruments measuring the concentrations of the same species present during both campaigns (the LOPAP and QCL for Easter Bush, and the ToF-ACSM for ATTO). For the measurements taken at the ATTO site, the acquisition of such a dataset is novel in itself, as the measurements of hourly resolved fluxes for the inorganic trace gases and associated aerosols are the first taken over the Amazon rainforest.

The more pertinent aim of this work, however, has been to advance understanding of surface-atmosphere exchange processes, particularly for areas where measurements of the surface-exchange of trace gases and aerosols are lacking. Based on the conclusions that can be drawn from the datasets of concentrations and fluxes gathered at both sites, this aim has also been achieved to a degree.

7.1.1 Easter Bush

Consideration will first be given to the conclusions that have been drawn from the concentration and flux measurements at the Easter Bush site. One observation that is particularly of relevance to later discussion of the conclusions drawn from the measurements made at the tropical rainforest site was the observed emission of HONO from the grassland to the atmosphere at several periods during the campaign. Emissions six to eight hours post-fertilisation of the site were observed, while pre-fertilisation emission events were observed occurring regularly from 07:00 to 09:00 hours in the morning. Emissions of HONO at rural and agricultural

areas had been observed previously, as with Twigg *et al.* (2011) at the same site post-fertilisation. However, the regularity of non-negligible emissions before dawn and during the pre-fertilisation period, with periods where emissions reached $+1.15\ \mathrm{ng\,m^{-2}\,s^{-1}}$, is interesting for the potential impact on tropospheric hydroxyl chemistry. As outlined in Chapter 1 of this work, HONO rapidly photolyses to OH during the day. Emissions from the surface to the atmosphere before dawn, resulting in an increase of HONO in the inertial sublayer, would result in a pulse of OH radical production as photolysis of HONO occurs. The source of this HONO emission from the surface is likely to be from the soil of the grassland site, as outlined by Di Marco *et al.* (2019) who using the LOPAP instrument also present at the Easter Bush site during this campaign also recorded morning emissions of HONO from bare, agricultural soils. The principal implication of such emissions would therefore be in considering the budget of hydroxyl radicals present in the troposphere, with ramifications for the understanding of how tropospheric oxidative capacity is sustained.

It is also important to note that HONO concentrations during the campaign at Easter Bush were always above the detection limit of the instrument, even during the day. This has been reported in previous studies (Laufs *et al.*, 2017; Sörgel *et al.*, 2011), but the use of the GRAEGOR which confirms a consistent deposition of HONO to the surface during the day suggests that the source of daytime HONO must be confined to in situ pathways in the troposphere.

The ability of the GRAEGOR to measure multiple species, both gas and particulate, at 1 hour resolution allowed for the observation at the Easter Bush site of ammonium nitrate formation post-fertilisation Measurement of all three species of the NH_3 HNO_3 NH_4NO_3 triad is critical to making informed conclusions regarding their behaviour and interaction. Only through the use of the conservative fluxes tot-NH_4^+ and tot-NO_3^- (developed from the individual fluxes of these species) can the gas particle interactions that would otherwise invalidate

the condition of flux conservation be accounted for. By using the GRAEGOR instrument to measure all three species, and then developing the conservative fluxes of tot-NH_4^+ and tot-NO_3^-, it was noted that the observed formation of NH_4NO_3 was driven by emissions of HNO_3 post fertilisation. The excess of NH_3 at the site post fertilisation a consequence of the loss of NH_3 from the fertiliser via volatilization rapidly scavenged the emitted HNO_3, resulting in NH_4NO_3 formation. This remains an enigmatic result worth considering for future work, because the reason why the application of fertiliser on particularly acidic soil (for example, the soils at the Easter Bush site) would result in the emission of HNO_3 remains unknown.

Finally, the calculation of aerosol deposition velocities based on concentration and flux measurements allowed for the development of a relationship between the deposition velocities of Cl^-, NO_3^-, and SO_4^{2-} containing aerosols and a proxy for particle size. An exponential relationship linked the measured deposition velocity (once normalised for turbulence) of each of the three species with a proxy for particle size, namely, the ratio of $PM_{2.5}/PM_{10}$ as measured by a nearby MARGA system. Naturally, the use of a proxy measurement for aerosol size does not lead to a direct confirmation between particle size and deposition velocity, but as a first stage in illustrating that such a relationship can be empirically determined, this conclusion can serve as an impetus for future work. Furthermore, the pathway which was considered to have driven coarse particle formation observed through this analysis has relevance to results found at the ATTO site, and for biosphere-atmosphere interactions in general. Namely, this is the observed interaction between biogenically derived air masses in this case, a marine source of NaCl sea-salt - with anthropogenic emissions, such as NO_x emissions resulting in the formation of HNO_3. Together, the interaction between biogenic and anthropogenic sources of gases and aerosols results in changes to atmospheric

composition, such as the formation of $NaNO_3$ coarse aerosol, with the potential to affect the biosphere upon deposition.

7.1.2 Amazon Tall Tower Observatory

Periodic intrusions of anthropogenically-driven pollution, as at Easter Bush, was noted to occur at the Amazon Tall Tower Observatory. From 18 October to 26 October, elevated deposition fluxes of the gas SO_2 and HNO_3 were observed, with concurrent deposition of associated aerosols containing SO_4^{2-} and NO_3^-. For SO_2, deposition fluxes reached a maximum of -33.2 ng m^{-2} s^{-1} at 11:00 on 21 October, which in comparison to the baseline observed throughout the campaign was particularly high. Through the use of back trajectory analysis in combination with fire data counts, as well as considering the correlation with markers for biomass burning (M_{BC} and c_{CO}) with SO_2, it was found that these periods of elevated SO_2 deposition originated either from local, regional, or potentially global, sources of biomass burning. Periods of elevated HNO_3 deposition were linked to local and regional urban air pollution. The influence of long range transport of pollutants to the ATTO site had previously been noted by Pöhlker *et al.* (2016) for Saharan dust and Saturno *et al.* (2018b) for black and brown carbon particulate, but this study has confirmed that trace gases such as SO_2 can also be transported in this manner, resulting in potentially deleterious effects on ecosystem health in the Amazon rainforest. In addition, the potential for these anthropogenically-driven perturbations to the atmosphere above the rainforest particularly with regards to the maintenance of oxidative capacity, or the potential for the formation of scattering aerosols must now be considered in light of the evidence presented by this study of periodic intrusions of these trace gas species.

Mirroring the result found at the Easter Bush site was the observation made at

ATTO of regular morning emissions of HONO. 26% of all recorded fluxes of HONO at the ATTO site were emissions, and of those, 97% occurred between the hours of 07:00 to 09:00, replicating the hours of HONO emissions observed at the Easter Bush site. The conclusion drawn from this surface-exchange behaviour is similar to that for the Easter Bush site as well. At ATTO, it was theorised that at night, HONO emissions from the soil of the forest floor accumulated below canopy. Mixing with the air above canopy was prevented due to stable stratification, which creates a nocturnal boundary layer cap between the air below and above canopy. At dawn, turbulent mixing would remove this cap, allowing mixing between the air above and below canopy. The accumulated HONO is then transported and mixed with the air above canopy, in a venting effect that leads to an observed morning emission. As with the conclusion drawn from HONO behaviour at the Easter Bush site, the emission of nitrous acid from the surface to the atmosphere would result in an increase of OH concentrations as photolysis of HONO occurred. Considering the importance of the oxidative capacity of the troposphere above the rainforest, this injection of early morning OH radicals may have profound implications for overall maintenance of oxidation cycles. The study of Taraborrelli *et al.* (2012) into the buffering of OH radicals by isoprene oxidation above Amazon rainforest was informed by the need to explain why observed OH radical concentrations were maintained in contradiction to the suggestion of modelling. This studys observation of early morning HONO emissions may go some way in explaining this OH concentration gap above the Amazon rainforest.

Emissions were observed for all aerosol species measured, with emissions occurring in 3% of all the measured fluxes of Cl^-. As mentioned in the introduction to this study, the contribution of primary biological aerosol to the overall particulate burden over the rainforest is a topic of ongoing investigation. Part of that investigation is into the inorganic ions such as Cl^-, which China *et al.* (2018) confirms as being present in the form of NaCl in PBAP derive spore fragments

released during spore fragmentation or transport. While this study can not directly state that the observed emissions of Cl^- derive from this PBAP spore route, confirmations of Cl^- emissions should give impetus to further work in determining their origin. While Ahlm *et al.* (2009) found 40% of all measured aerosol fluxes in their study above the Amazon rainforest were emissions, this was for non-chemically speciated aerosols.

Finally, as discussed in Chapter 6, emissions of NH_3 were also recorded at the ATTO site. Due to the lack of local modelling of NH_3 surface-exchange for this biosphere, the results were used to develop a single layer, canopy compensation point model for NH_3 bi-directional fluxes, using a novel parameterisation of the cuticular resistance, R_w, based on leaf wetness measurements. The single layer model based on this parameterisation was capable of simulating the observations well, and was better at doing so in comparison to R_w parameterisations based upon vapour pressure deficit or relative humidity. Considering the periods in which emissions of NH_3 were observed, it was concluded that particularly dry, warm conditions were responsible for driving stomatal exchange of NH_3 between surface and the atmosphere. While the overall averaged flux for NH_3 during the campaign was -2.78 ng ng m^{-2} s^{-1}, confirming that the rainforest is a net sink for NH_3, these occasional periods of emission which are expected to become more frequent with climate change induced drought conditions in the Amazon Basin can lead to significant losses of total leaf nitrogen in the form of NH_3.

7.1.3 Contrasts between biomes and context of work within wider research

While similarities exist between the measurements taken over the agricultural grassland site at Easter Bush and the near-pristine rainforest site at ATTO (such as similar observations of early morning HONO emissions), the difference

in the observed pollution climates at both biomes leads to stark differences in the concentrations and ratios of the measured trace gases and aerosols. The most striking difference between the two sites, as illustrated in the summary of results shown in Table 7.1, is between the overall measured mean concentrations of NH_3. At Easter Bush, a mean concentration of 1.48 $\mu g\,m^{-3}$ was measured, in contrast to the value of 0.28 $\mu g\,m^{-3}$ measured at ATTO. Furthermore, the negative mean deposition velocity of NH_3 observed at Easter Bush, suggesting an overall emission throughout the campaign, contrasts with the overall pattern of deposition, as evidenced by a mean positive deposition velocity of NH_3, recorded at ATTO. The differences in NH_3 concentrations, and consequently between the ratios of NH_3 and the trace acidic gases measured at both sites, suggests an "excess" of NH_3 at Easter Bush, and a comparative "dearth" at ATTO, when considering NH_3 as a rate limiting reactant. The larger concentrations of NH_3 at Easter Bush leads to the efficient scavenging of the acidic trace gases present. The result is the formation of fine aerosols at Easter Bush, which was inferred during the period immediately after fertilisation from considering the deposition velocity of the aerosol NO_3^-. Furthermore, this leads to a trace gas to respective aerosol ratio that favours the respective aerosol (i.e. as noted in Table 7.1, where the ratio of HNO_3 to NO_3^- is 1:8). In contrast, the ratio of NH_3 to the acidic trace gases measured at ATTO favours the latter. As a consequence, gas to respective aerosol ratios are less than those observed at Easter Bush.

The differences in pollution climates reflects the difference in the sources of the pollutants at each site. Atmospheric composition is driven at Easter Bush by the volatilization of NH_3 from the application of fertilisers and from livestock waste at the site itself. As a consequence, trace gas and aerosol concentrations are determined in part by the efficient scavenging of acidic trace gases by NH_3. In contrast, the pollution climate at ATTO is characterised by periodic intrusions from regional sources, either urban pollutants dominated by NOx, or from

regional biomass burning which is characterised by elevated levels of SO_2 and aerosols. Summarized, the pollution climate at Easter Bush can be considered as a consequence of gas particle interconversion occurring on, or locally to, the site, while the pollution climate of ATTO is typified by the deposition of pollutants which have been regionally transported from their source of origin. Consequently, strategies to tackle pollution at both sites, and extrapolated to a wider strategy for agricultural grasslands and remote biomes, must consider either, respectively, the influence of on site emissions and subsequent gas particle interconversion, or the influence of regional (and potentially global, as evidenced by back trajectory analysis at ATTO) pollution.

The results presented for both studies can be placed with the context of wider research. For example, the modelling of bulk dry deposition velocity is necessary for the prediction of regional and global pollution budgets. To improve these models, empirically derived dry deposition velocities are required for as many biomes as possible. The ATTO site, lying within a region of near pristine rainforest, is a region lacking such measurements. Similarly, while measurements of bulk deposition velocity have been conducted for grassland sites, they still remain few in number, and any addition to the prior research further refines the model's predictive capabilities. The model of dry deposition velocity developed by Gallagher *et al.* (2002), previously cited in Chapter 5, can be further improved with the addition of surface dry deposition velocities for NH_4^+ developed from the measurements at Easter Bush and ATTO. As an illustration, this highlights the context of wider empirical studies in which both studies reside within, while also reflecting the continuum on which both sites lie on – divergent landscapes with noticeable differences in dry deposition velocity, but which are linked through process orientated modelling.

Table 7.1: Summary table comparing the mean concentrations (μ_A) and mean deposition velocities (V_d) for the trace gases and aerosols measured at the Easter Bush agricultural grassland and the Amazon Tall Tower Observatory.

Species		Easter Bush		Amazon Tall Tower Observatory	
		μ_A ($\mu g\,m^{-3}$)	V_d ($mm\,s^{-1}$)	μ_A ($\mu g\,m^{-3}$)	V_d ($mm\,s^{-1}$)
Trace Gases	NH_3	1.48	−8.99	0.28	10.5
	HCl	0.2	15.1	0.13	15.2
	HONO	0.04	8.8	0.07	4.49
	HNO_3	0.19	13.6	0.25	12.4
	SO_2	0.24	11.7	0.23	10.4
Aerosols	NH_4^+	0.74	0.93	0.30	2.86
	Cl^-	0.91	3.65	0.23	7.83
	NO_3^-	1.53	1.97	0.47	7.04
	SO_4^{2-}	1.29	1.89	0.51	3.72

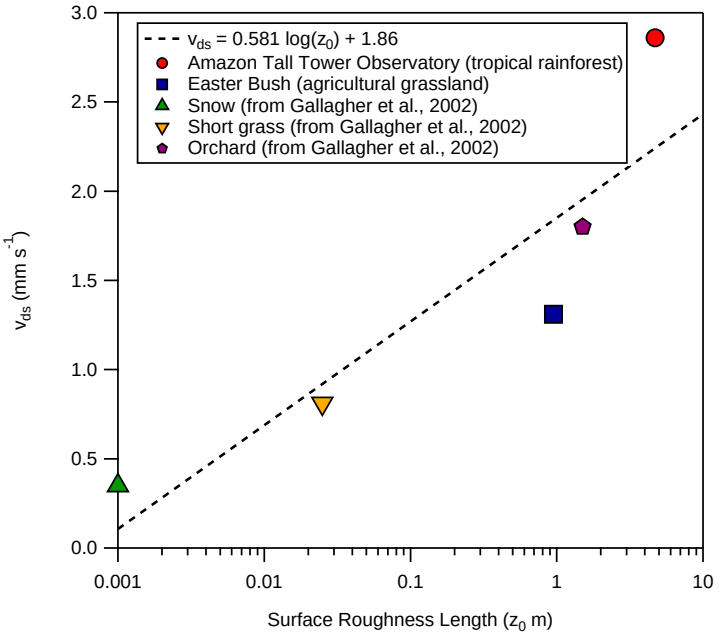

Figure 7.1: Variation in the small particle deposition velocity as a function of surface roughness length, with values of NH_4^+ V_{ds} for Easter Bush and ATTO placed in context of previous research.

7.2 Recommendations for future work

One of the species which this study intended to measure as part of the suite of inorganic trace gases and aerosols was nitrite (NO_2^-) containing aerosol. However, during both campaigns, the measured concentrations of NO_2^- at no point exceeded the limits of detection of the GRAEGOR. All studies which have used the GRAEGOR instrument in field measurements (Wolff *et al.*, 2010a; Twigg *et al.*, 2011) have similarly not been able to quantify NO_2^- aerosol for the same reason. The surface exchange dynamics of NO_2^- containing aerosol as measured by the GRAEGOR therefore remain elusive. Measurements of the tropospheric concentrations and fluxes of NO_2^- containing aerosol, such as $ClNO_2$ (a product of the reaction between N_2O_5 and NaCl as detailed in Chapter 1 of this study), are currently lacking, and the GRAEGOR (or derivatives of the GRAEGOR, such

as the MARGA) is an instrument that could potentially be well placed to take such measurements. Investigation should therefore be focused on increasing the sensitivity of the GRAEGOR with regards to NO_2^- containing aerosol, lowering the detection limit so that measurements can be made.

As detailed in Chapter 1, K^+ containing aerosol has been noted as a component of PBAP fragments and spore *ascii* fluid. Na^+ is also important with regards to PBAPs, but also as part of sea-salt and other coarse aerosol such as $NaNO_3$. Measurements of the tropospheric concentrations and fluxes of these species could therefore elucidate on more of the surface-atmosphere exchange pathways occurring over different biospheres, especially if measurements were taken in tandem with the anion species which the GRAEGOR measures already. The current IC analytical column used in the GRAEGOR, the Dionex AS12, is limited to measurements of the anions Cl^-, NO_2^-, NO_3^- and SO_4^{2-}. As such, it is not capable of taking concentration measurements and hence, incapable of giving fluxes for cation species such as K^+ or sodium Na^+. However, the GRAEGOR has the capacity to measure cations, by either replacing the Dionex AS12 anion column currently used by the GRAEGOR with a Metrosep C Supp 1 - 150/4.0 Metrohm cation column. Alternatively, a cation IC analytical column with separate detector unit, in parallel with the current anion IC analytical column, may be designed in order to give a full complement of both cations and anions. While an attempt was made during this study to install a column to the IC system of the GRAEGOR which would have allowed measurement of cations, the radical alteration to the original GRAEGOR architecture which would have been required including implementing a heating system for the column, a new valve control design, and the installation of a secondary power system with a parallel IC detector was considered too intensive for the time constraints of this study. However, the proof of concept has been developed, and implementation is possible. Future work could aim to incorporate a parallel IC system to the

GRAEGOR which measures the concentrations and fluxes of cation containing aerosol species.

Another potential area for investigation would be to measure the concentrations and fluxes of water-soluble organic nitrogen (WSON) and water-soluble organic carbon (WSOC) in the troposphere. WSOC is particularly relevant to the Amazon rainforest, where the majority of measured aerosol is secondary organic aerosol, formed from the oxidation of organic carbon species such as isoprene (Poschl *et al.* 2010; China *et al.* 2018). Furthermore, as discussed in Section 5.4.3 of Chapter 5, WSON forms a significant proportion of wet and dry deposited nitrogen to the Amazon rainforest. Therefore, to make a complete inventory of total nitrogen deposition to the rainforest, measurements of WSON fluxes and deposition rates are required. The current design of the GRAEGOR can potentially be modified to measure WSOC and WSON by the inclusion of a total organic carbon/total nitrogen (TOC/TN) detector to the overall GRAEGOR architecture. This concept follows from a study by Lin *et al.* (2010) who connected a TOC/TN detector to a single height SJAC/WRD combination in order to determine the total organic nitrogen concentration above an oak forest. In Lin *et al.* study, the air sample to be analysed was drawn through a WRD where water soluble gas species would be absorbed by the WRD feeding solution, and then be pumped through a SJAC where aerosol particles underwent deliquescence. The eluent from the WRD and SJAC then underwent IC analysis, similar to the GRAEGOR. The IC units which measured cations and anions, including inorganic nitrogen aerosols and ammonium gave a total reading for the overall inorganic nitrogen component present in the sample analysed. In addition to IC analysis, a portion of the sample was be pumped to a TOC/TN detector; in the case of Lin *et al.* study, this was a high sensitivity Shimadzu TOC-Vesh Unit, which measured total nitrogen via chemiluminescence detection of the excitation of nitric oxide (generated by catalytically combustion of the sample) with ozone.

Thus, the TOC/TN gives a value for the total nitrogen concentration of the sample, while the IC units give a value for the total inorganic concentration of the sample. From this, the total concentration of organic nitrogen in the sample can be determined by subtracting the inorganic nitrogen fraction from the total nitrogen fraction.

As part of the work conducted in this study, such an instrument was attached to the GRAEGOR (the Skalar Formacs HT/TN) during both campaigns, and preliminary measurements of both total organic carbon and total nitrogen at both heights was made. However, time constraints, difficulty with maintaining performance, and balancing the demands of competing objectives, resulted in only very few measurements being made. The concept, however, has been demonstrated in this study, and can be further developed for future use. Considering the importance WSON and WSOC play in tropospheric chemistry, future work involving the GRAEGOR should therefore aim - as a high priority - to refine the methodology as developed here to include measurements of WSOC and WSON concentrations and fluxes.

Delays with instrument delivery and faults with instruments occurred during the study which particularly affected the ATTO campaign. It was originally intended that measurements at ATTO would occur during the dry season of 2016 (from October to November), and the wet season of 2017 (from February to April). Due to the instrument not arriving before October 2016, the dry season campaign was postponed to October 2017, while the wet season campaign would be the first campaign to be conducted. While the wet season campaign did occur, faults with instrumentation (principally, the break down of the GRAEGORs IC unit), combined with high water column pressure between the GRAEGOR sample boxes and detector unit which led to faults with the valve control systems, led to only spurious data being collected. Resultantly, only one campaign at the ATTO site was conducted. With consideration that this campaign was the last chance this

study had for measurement over tropical rainforest, objectives were narrowed, so that other potential investigations such as the aforementioned measurements of TOC and TN were abandoned.

The lack of a corresponding wet season dataset is unfortunate. The wet season of the Amazon is known for near pristine, almost marine like, atmospheric conditions, with occasional intrusions of long range transport of Saharan Dust (Pöhlker *et al.*, 2016). To compare dry season background concentrations to the wet season, or to have had the GRAEGOR measure during a long range transport episode, would have resulted in further discussion, and potentially have extended the knowledge of surface-atmosphere exchange for tropical rainforest during these periods of near-pristine conditions. This study, from just dry season measurements, has developed interesting insights and new knowledge on the surface-exchange of inorganic trace gases and associated aerosols, particularly with regards to the bi-directional flux of NH_3 and early morning emissions of HONO. The methodology is now refined for tower measurements at the ATTO site using the GRAEGOR, and so the impetus should now be on gaining a paired wet season dataset, with potentially an extension to the transitional periods which occur between the wet and dry seasons.

References

Acker, K., Möller, D., Wieprecht, W., Meixner, F.X., Bohn, B., Gilge, S., Plass-Dülmer, C. and Berresheim, H. (2006). Strong daytime production of OH from HONO at a rural mountain site. *Geophysical Research Letters*, **33**.

Adams, P.J., Seinfeld, J.H. and Koch, D.M. (1999). Global concentrations of tropospheric sulfate, nitrate, and ammonium aerosol simulated in a general circulation model. *Journal of Geophysical Research: Atmospheres*, **104**, 13791–13823.

Adon, M., Galy-Lacaux, C., Yoboué, V., Delon, C., Lacaux, J.P., Castera, P., Gardrat, E., Pienaar, J., Al Ourabi, H., Laouali, D., Diop, B., Sigha-Nkamdjou, L., Akpo, A., Tathy, J.P., Lavenu, F. and Mougin, E. (2010). Long term measurements of sulfur dioxide, nitrogen dioxide, ammonia, nitric acid and ozone in Africa using passive samplers. *Atmos. Chem. Phys.*, **10**, 7467–7487.

Adon, M., Galy-Lacaux, C., Delon, C., Yoboue, V., Solmon, F. and Kaptue Tchuente, A.T. (2013). Dry deposition of nitrogen compounds NO_2, HNO_3, NH_3, sulfur dioxide and ozone in west and central African ecosystems using the inferential method. *Atmos. Chem. Phys.*, **13**, 11351–11374.

Ahlm, L., Nilsson, E.D., Krejci, R., Mårtensson, E.M., Vogt, M. and Artaxo, P. (2009). Aerosol number fluxes over the Amazon rain forest during the wet season. *Atmos. Chem. Phys.*, **9**, 9381–9400.

Akiyama, H., McTaggart, I.P., Ball, B.C. and Scott, A. (2004). N_2O, NO, and NH_3 emissions from Soil after the Application of Organic Fertilizers, Urea and Water. *Water, Air, and Soil Pollution*, **156**, 113–129.

Allen, A.G., Harrison, R.M. and Nicholson, K.W. (1991). Dry deposition of fine aerosol to a short grass surface. *Atmospheric Environment. Part A. General Topics*, **25**, 2671–2676.

Andersen, H.V. and Hovmand, M.F. (1999). Review of dry deposition measurements of ammonia and nitric acid to forest. *Forest Ecology and Management*, **114**, 5–18.

Andreae, M.O. and Andreae, T.W. (1988). The cycle of biogenic sulfur compounds over the Amazon Basin: 1. Dry season. *Journal of Geophysical Research: Atmospheres*, **93**, 1487–1497.

Andreae, M.O., Berresheim, H., Bingemer, H., Jacob, D.J., Lewis, B.L., Li, S.M. and Talbot, R.W. (1990). The atmospheric sulfur cycle over the Amazon Basin: 2. Wet season. *Journal of Geophysical Research: Atmospheres*, **95**, 16813–16824.

Andreae, M.O., Elbert, W., Cai, Y., Andreae, T.W. and Gras, J. (1999). Non-sea-salt sulfate, methanesulfonate, and nitrate aerosol concentrations and size distributions at Cape Grim, Tasmania. *Journal of Geophysical Research: Atmospheres*, **104**, 21695–21706.

Andreae, M.O., Artaxo, P., Beck, V., Bela, M., Freitas, S., Gerbig, C., Longo, K., Munger, J.W., Wiedemann, K.T. and Wofsy, S.C. (2012). Carbon monoxide and related trace gases and aerosols over the Amazon Basin during the wet and dry seasons. *Atmos. Chem. Phys.*, **12**, 6041–6065.

Andreae, M.O., Acevedo, O.C., Araùjo, A., Artaxo, P., Barbosa, C.G.G., Barbosa, H.M.J., Brito, J., Carbone, S., Chi, X., Cintra, B.B.L., da Silva, N.F., Dias, N.L., Dias-Júnior, C.Q., Ditas, F., Ditz, R., Godoi, A.F.L., Godoi, R.H.M., Heimann, M., Hoffmann, T., Kesselmeier, J., Könemann, T., Krüger, M.L., Lavric, J.V., Manzi, A.O., Lopes, A.P., Martins, D.L., Mikhailov, E.F., Moran-Zuloaga, D., Nelson, B.W., Nölscher, A.C., Santos Nogueira, D., Piedade, M.T.F., Pöhlker, C., Pöschl, U., Quesada, C.A., Rizzo, L.V., Ro, C.U., Ruckteschler, N., Sá, L.D.A., de Oliveira Sá, M., Sales, C.B., dos Santos, R.M.N., Saturno, J., Schöngart, J., Sörgel, M., de Souza, C.M., de Souza, R.A.F., Su, H., Targhetta, N., Tóta, J., Trebs, I., Trumbore, S., van Eijck, A., Walter, D., Wang, Z., Weber, B., Williams, J., Winderlich, J., Wittmann, F., Wolff, S. and Yáñez-Serrano, A.M. (2015). The Amazon Tall Tower Observatory (ATTO): overview of pilot measurements on ecosystem ecology, meteorology, trace gases, and aerosols. *Atmos. Chem. Phys.*, **15**, 10723–10776.

Andreae, M.O., Afchine, A., Albrecht, R., Holanda, B.A., Artaxo, P., Barbosa, H.M.J., Borrmann, S., Cecchini, M.A., Costa, A., Dollner, M., Fütterer, D., Järvinen, E., Jurkat, T., Klimach, T., Konemann, T., Knote, C., Krämer, M., Krisna, T., Machado, L.A.T., Mertes, S., Minikin, A., Pöhlker, C., Pöhlker, M.L., Pöschl, U., Rosenfeld, D., Sauer, D., Schlager, H., Schnaiter, M., Schneider, J., Schulz, C., Spanu, A., Sperling, V.B., Voigt, C., Walser, A., Wang, J., Weinzierl, B., Wendisch, M. and Ziereis, H. (2018). Aerosol characteristics and particle production in the upper troposphere over the Amazon Basin. *Atmos. Chem. Phys.*, **18**, 921–961.

Appel, B.R., Wall, S.M., Tokiwa, Y. and Haik, M. (1980). Simultaneous nitric

acid, particulate nitrate and acidity measurements in ambient air. *Atmospheric Environment (1967)*, **14**, 549–554.

Appel, B.R., Winer, A.M., Tokiwa, Y. and Biermann, H.W. (1990). Comparison of atmospheric nitrous acid measurements by annular denuder and differential optical absorption systems. *Atmospheric Environment. Part A. General Topics*, **24**, 611–616.

Araújo, A.C., Nobre, A.D., Kruijt, B., Elbers, J.A., Dallarosa, R., Stefani, P., von Randow, C., Manzi, A.O., Culf, A.D., Gash, J.H.C., Valentini, R. and Kabat, P. (2002). Comparative measurements of carbon dioxide fluxes from two nearby towers in a central Amazonian rainforest: The Manaus LBA site. *Journal of Geophysical Research: Atmospheres*, **107**, LBA 58–1–LBA 58–20.

Arneth, A., Harrison, S.P., Zaehle, S., Tsigaridis, K., Menon, S., Bartlein, P.J., Feichter, J., Korhola, A., Kulmala, M., O'Donnell, D., Schurgers, G., Sorvari, S. and Vesala, T. (2010). Terrestrial biogeochemical feedbacks in the climate system. *Nature Geoscience*, **3**, 525.

Artaxo, P., Rizzo, L.V., Brito, J.F., Barbosa, H.M.J., Arana, A., Sena, E.T., Cirino, G.G., Bastos, W., Martin, S.T. and Andreae, M.O. (2013). Atmospheric aerosols in Amazonia and land use change: from natural biogenic to biomass burning conditions. *Faraday Discussions*, **165**, 203–235.

Aruffo, E., Biancofiore, F., Di Carlo, P., Busilacchio, M., Verdecchia, M., Tomassetti, B., Dari-Salisburgo, C., Giammaria, F., Bauguitte, S., Lee, J., Moller, S., Hopkins, J., Punjabi, S., Andrews, S.J., Lewis, A.C., Palmer, P.I., Hyer, E., Le Breton, M. and Percival, C. (2016). Impact of biomass burning emission on total peroxy nitrates: fire plume identification during the BORTAS campaign. *Atmos. Meas. Tech.*, **9**, 5591–5606.

Aurela, M., Beukes, J., van Zyl, P., Vakkari, V., Teinilä, K., Saarikoski, S. and Laakso, L. (2016). The composition of ambient and fresh biomass burning aerosols at a savannah site, South Africa. *South African Journal of Science*, **112**.

Baccini, A., Goetz, S.J., Walker, W.S., Laporte, N.T., Sun, M., Sulla-Menashe, D., Hackler, J., Beck, P.S.A., Dubayah, R., Friedl, M.A., Samanta, S. and Houghton, R.A. (2012). Estimated carbon dioxide emissions from tropical deforestation improved by carbon-density maps. *Nature Climate Change*, **2**, 182.

Baldocchi, D. (1988). A Multi-layer model for estimating sulfur dioxide deposition to a deciduous oak forest canopy. *Atmospheric Environment (1967)*, **22**, 869–884.

Bardouki, H., Liakakou, H., Economou, C., Sciare, J., Smolk, J., Ždmal, V., Eleftheriadis, K., Lazaridis, M., Dye, C. and Mihalopoulos, N. (2003). Chemical composition of size-resolved atmospheric aerosols in the eastern Mediterranean during summer and winter. *Atmospheric Environment*, **37**, 195–208.

Behera, S.N., Sharma, M., Aneja, V.P. and Balasubramanian, R. (2013). Ammonia in the atmosphere: a review on emission sources, atmospheric chemistry and deposition on terrestrial bodies. *Environmental Science and Pollution Research*, **20**, 8092–8131.

Blei, E., Hardacre, C.J., Mills, G.P., Heal, K.V. and Heal, M.R. (2010). Identification and quantification of methyl halide sources in a lowland tropical rainforest. *Atmospheric Environment*, **44**, 1005 – 1010.

Brost, R.A., Delany, A.C. and Huebert, B.J. (1988). Numerical modeling of concentrations and fluxes of HNO_3 , NH_3 , and NH_4NO_3 near the surface. *Journal of Geophysical Research: Atmospheres*, **93**, 7137–7152.

Brown, S.S. and Stutz, J. (2012). Nighttime radical observations and chemistry. *Chemical Society Reviews*, **41**, 6405–6447.

Burkhardt, J. and Eiden, R. (1994). Thin water films on coniferous needles: A new device for the study of water vapour condensation and gaseous deposition to plant surfaces and particle samples. *Atmospheric Environment*, **28**, 2001–2011.

Burling, I.R., Yokelson, R.J., Griffith, D.W.T., Johnson, T.J., Veres, P., Roberts, J.M., Warneke, C., Urbanski, S.P., Reardon, J., Weise, D.R., Hao, W.M. and de Gouw, J. (2010). Laboratory measurements of trace gas emissions from biomass burning of fuel types from the southeastern and southwestern United States. *Atmos. Chem. Phys.*, **10**, 11115–11130.

Caird, M.A., Richards, J.H. and Hsiao, T.C. (2007). Significant transpirational water loss occurs throughout the night in field-grown tomato. *Functional Plant Biology*, **34**, 172–177.

Carslaw, D.C. and Ropkins, K. (2012). openair An R package for air quality data analysis. *Environmental Modelling & Software*, **27-28**, 52–61.

Charlson, R.J., Lovelock, J.E., Andreae, M.O. and Warren, S.G. (1987). Oceanic phytoplankton, atmospheric sulphur, cloud albedo and climate. *Nature*, **326**, 655–661.

China, S., Wang, B., Weis, J., Rizzo, L., Brito, J., Cirino, G.G., Kovarik, L., Artaxo, P., Gilles, M.K. and Laskin, A. (2016). Rupturing of Biological Spores As a Source of Secondary Particles in Amazonia. *Environmental Science & Technology*, **50**, 12179–12186.

China, S., Burrows, S.M., Wang, B., Harder, T.H., Weis, J., Tanarhte, M., Rizzo, L.V., Brito, J., Cirino, G.G., Ma, P.L., Cliff, J., Artaxo, P., Gilles, M.K. and Laskin, A. (2018). Fungal spores as a source of sodium salt particles in the Amazon basin. *Nature Communications*, **9**, 4793.

Chor, T.L., Dias, N.L., Araújo, A., Wolff, S., Zahn, E., Manzi, A., Trebs, I., Sá, M.O., Teixeira, P.R. and Sörgel, M. (2017). Flux-variance and flux-gradient relationships in the roughness sublayer over the Amazon forest. *Agricultural and Forest Meteorology*, **239**, 213–222.

Chow, J.C. (1995). Measurement Methods to Determine Compliance with Ambient Air Quality Standards for Suspended Particles. *Journal of the Air & Waste Management Association*, **45**, 320–382.

Costanza, R., D'Arge, R., de Groot, R., Farber, S., Grasso, M., Hannon, B., Limburg, K., Naeem, S., O'Neill, R.V., Paruelo, J., Raskin, R.G., Sutton, P. and van den Belt, M. (1997). The value of the world's ecosystem services and natural capital. *Nature*, **387**, 253–260.

Cowan, N.J., Norman, P., Famulari, D., Levy, P.E., Reay, D.S. and Skiba, U.M. (2015). Spatial variability and hotspots of soil N_2O fluxes from intensively grazed grassland. *Biogeosciences*, **12**, 1585–1596.

Custodio, D., Alves, C., Jomolca, Y. and de Castro Vasconcellos, P. (2019). Carbonaceous components and major ions in PM10from the Amazonian Basin. *Atmospheric Research*, **215**, 75–84.

Dasgupta, P.K., Campbell, S.W., Al-Horr, R.S., Ullah, S.M.R., Li, J., Amalfitano, C. and Poor, N.D. (2007). Conversion of sea salt aerosol to $NaNO_3$ and the production of HCl: Analysis of temporal behavior of aerosol chloride/nitrate and gaseous HCl/HNO_3 concentrations with AIM. *Atmospheric Environment*, **41**, 4242–4257.

Davidson, C.I., Miller, J.M. and Pleskow, M.A. (1982). The influence of surface structure on predicted particle dry deposition to natural grass canopies. *Water, Air, and Soil Pollution*, **18**, 25–43.

Davidson, E.A. and Kingerlee, W. (1997). A global inventory of nitric oxide emissions from soils. *Nutrient Cycling in Agroecosystems*, **48**, 37–50.

Davidson, E.A., Ishida, F.Y. and Nepstad, D.C. (2004). Effects of an experimental drought on soil emissions of carbon dioxide, methane, nitrous oxide, and nitric oxide in a moist tropical forest. *Global Change Biology*, **10**, 718–730.

Davidson, E.A., de Araújo, A.C., Artaxo, P., Balch, J.K., Brown, I.F., C. Bustamante, M.M., Coe, M.T., DeFries, R.S., Keller, M., Longo, M., Munger,

J.W., Schroeder, W., Soares-Filho, B.S., Souza, C.M. and Wofsy, S.C. (2012). The Amazon basin in transition. *Nature*, **481**, 321.

De Ridder, K. (2010). Bulk Transfer Relations for the Roughness Sublayer. *Boundary-Layer Meteorology*, **134**, 257–267.

Dellwik, E. and Jensen, N.O. (2005). FluxProfile Relationships Over a Fetch Limited Beech Forest. *Boundary-Layer Meteorology*, **115**, 179.

Di Marco, C., Skiba, U., Weston, K., Hargreaves, K. and Fowler, D. (2004). Field Scale N_2O flux Measurements from Grassland Using Eddy Covariance. *Water, Air, & Soil Pollution: Focus*, **4**, 143–149.

Di Marco, C.F., Kramer, L.J., Twigg, M.M., Crilley, L., Ramsay, R., Cowan, N., Coyle, M., Jones, M.R., Leeson, S.R., Bloss, W.J. and Nemitz, E. (2019). Characterisation of HONO fluxes over grassland.

Dias-Jnior, C.Q., Dias, N.L., dos Santos, R.M.N., Srgel, M., Arajo, A., Tsokankunku, A., Ditas, F., de Santana, R.A., von Randow, C., S, M., Phlker, C., Toledo Machado, L.A., de S, L.D., Moran-Zuloaga, D., Janssen, R., Acevedo, O., Oliveira, P., Fisch, G., Chor, T. and Manzi, A. (2019). Is there a classical inertial sublayer over the amazon forest? *Geophysical Research Letters*, **46**, 5614–5622.

Dimmock, N.A. and Marshall, G.B. (1987). The determination of hydrogen chloride in ambient air with diffusion/denuder tubes. *Analytica Chimica Acta*, **202**, 49–59.

Dollard, G.J., Atkins, D.H.F., Davies, T.J. and Healy, C. (1987). Concentrations and dry deposition velocities of nitric acid. *Nature*, **326**, 481–483.

Dong, H.B., Zeng, L.M., Hu, M., Wu, Y.S., Zhang, Y.H., Slanina, J., Zheng, M., Wang, Z.F. and Jansen, R. (2012). Technical Note: The application of an improved gas and aerosol collector for ambient air pollutants in China. *Atmos. Chem. Phys.*, **12**, 10519–10533.

Duffy, P.B., Brando, P., Asner, G.P. and Field, C.B. (2015). Projections of future meteorological drought and wet periods in the Amazon. *Proceedings of the National Academy of Sciences*, **112**, 13172 LP – 13177.

Duyzer, J.H., Verhagen, H.L.M., Weststrate, J.H. and Bosveld, F.C. (1992). Measurement of the dry deposition flux of NH3 on to coniferous forest. *Environmental Pollution*, **75**, 3–13.

Eatough, D.J., White, V.F., Hansen, L.D., Eatough, N.L. and Ellis, E.C. (1985). Hydration of nitric acid and its collection in the atmosphere by diffusion denuders. *Analytical Chemistry*, **57**, 743–748.

Elbert, W., Taylor, P.E., Andreae, M.O. and Pöschl, U. (2007). Contribution of fungi to primary biogenic aerosols in the atmosphere: wet and dry discharged spores, carbohydrates, and inorganic ions. *Atmos. Chem. Phys.*, **7**, 4569–4588.

Elliott, K.J., Vose, J.M., Knoepp, J.D., Johnson, D.W., Swank, W.T. and Jackson, W. (2008). Simulated Effects of Sulfur Deposition on Nutrient Cycling in Class I Wilderness Areas. *Journal of Environmental Quality*, **37**, 1419–1431.

Erisman, J.W. and Wyers, G. (1993). Continuous measurements of surface exchange of SO_2 and NH_3; Implications for their possible interaction in the deposition process. *Atmospheric Environment. Part A. General Topics*, **27**, 1937–1949.

Erisman, J.W., Galloway, J.N., Seitzinger, S., Bleeker, A., Dise, N.B., Petrescu, A.M.R., Leach, A.M. and de Vries, W. (2013). Consequences of human modification of the global nitrogen cycle. *Philosophical transactions of the Royal Society of London. Series B, Biological sciences*, **368**, 20130116.

Ermel, M., Behrendt, T., Oswald, R., Derstroff, B., Wu, D., Hohlmann, S., Stönner, C., Pommerening-Röser, A., Könneke, M., Williams, J., Meixner, F.X., Andreae, M.O., Trebs, I. and Sörgel, M. (2018). Hydroxylamine released by nitrifying microorganisms is a precursor for HONO emission from drying soils. *Scientific Reports*, **8**, 1877.

Famulari, D., Fowler, D., Hargreaves, K., Milford, C., Nemitz, E., Sutton, M.A. and Weston, K. (2004). Measuring Eddy Covariance Fluxes of Ammonia Using Tunable Diode Laser Absorption Spectroscopy. *Water, Air, & Soil Pollution: Focus*, **4**, 151–158.

Fan, J., Rosenfeld, D., Zhang, Y., Giangrande, S.E., Li, Z., Machado, L.A.T., Martin, S.T., Yang, Y., Wang, J., Artaxo, P., Barbosa, H.M.J., Braga, R.C., Comstock, J.M., Feng, Z., Gao, W., Gomes, H.B., Mei, F., Pöhlker, C., Pöhlker, M.L., Pöschl, U. and de Souza, R.A.F. (2018). Substantial convection and precipitation enhancements by ultrafine aerosol particles. *Science*, **359**, 411 LP – 418.

Farmer, D.K. and Cohen, R.C. (2008). Observations of HNO_3, Sigma-AN, Sigma-PN and NO_2 fluxes: evidence for rapid HO_x chemistry within a pine forest canopy. *Atmos. Chem. Phys.*, **8**, 3899–3917.

Febo, A., Perrino, C. and Allegrini, I. (1996). Measurement of nitrous acid in Milan, Italy, by DOAS and diffusion denuders. *Atmospheric Environment*, **30**, 3599–3609.

Ferm, M. (1986). A Na_2CO_3-coated denuder and filter for determination of gaseous HNO_3 and particulate NO_3^- in the atmosphere. *Atmospheric Environment (1967)*, **20**, 1193–1201.

Ferm, M. (1998). Atmospheric ammonia and ammonium transport in Europe and critical loads: a review. *Nutrient Cycling in Agroecosystems*, **51**, 5–17.

Fiedler, V., Arnold, F., Ludmann, S., Minikin, A., Hamburger, T., Pirjola, L., Dörnbrack, A. and Schlager, H. (2011). African biomass burning plumes over the Atlantic: aircraft based measurements and implications for H₂SO₄ and HNO₃ mediated smoke particle activation. *Atmos. Chem. Phys.*, **11**, 3211–3225.

Fiore, A.M., Naik, V. and Leibensperger, E.M. (2015). Air Quality and Climate Connections. *Journal of the Air & Waste Management Association*, **65**, 645–685.

Flechard, C.R. (1998). *Turbulent Exchange of Ammonia Above Vegetation*. Ph.D. thesis, University of Nottingham.

Flechard, C.R., Fowler, D., Sutton, M.A. and Cape, J.N. (1999). A dynamic chemical model of bi-directional ammonia exchange between semi-natural vegetation and the atmosphere. *Quarterly Journal of the Royal Meteorological Society*, **125**, 2611–2641.

Flechard, C.R., Massad, R.S., Loubet, B., Personne, E., Simpson, D., Bash, J.O., Cooter, E.J., Nemitz, E. and Sutton, M.A. (2015). Advances in understanding, models and parameterizations of biosphere-atmosphere ammonia exchange. In R.S. Massad and B. Loubet, eds., *Review and Integration of Biosphere-Atmosphere Modelling of Reactive Trace Gases and Volatile Aerosols*, 11–84, Springer Netherlands, Dordrecht.

Foken, T. (2006). 50 Years of the MoninObukhov Similarity Theory. *Boundary-Layer Meteorology*, **119**, 431–447.

Foken, T. (2008). *Micrometeorology*. Springer Berlin Heidelberg, Berlin, Heidelberg, 1st edn.

Foken, T., Meixner, F.X., Falge, E., Zetzsch, C., Serafimovich, A., Bargsten, A., Behrendt, T., Biermann, T., Breuninger, C., Dix, S., Gerken, T., Hunner, M., Lehmann-Pape, L., Hens, K., Jocher, G., Kesselmeier, J., Lüers, J., Mayer, J.C., Moravek, A., Plake, D., Riederer, M., Rütz, F., Scheibe, M., Siebicke, L., Sörgel, M., Staudt, K., Trebs, I., Tsokankunku, A., Welling, M., Wolff, V. and Zhu, Z. (2012). Coupling processes and exchange of energy and reactive and non-reactive trace gases at a forest site results of the EGER experiment. *Atmospheric Chemistry and Physics*, **12**, 1923–1950.

Foley, J.A., Ramankutty, N., Brauman, K.A., Cassidy, E.S., Gerber, J.S., Johnston, M., Mueller, N.D., O'Connell, C., Ray, D.K., West, P.C., Balzer, C., Bennett, E.M., Carpenter, S.R., Hill, J., Monfreda, C., Polasky, S., Rockström,

J., Sheehan, J., Siebert, S., Tilman, D. and Zaks, D.P.M. (2011). Solutions for a cultivated planet. *Nature*, **478**, 337.

Fowler, D. and Unsworth, M.H. (1979). Turbulent transfer of sulphur dioxide to a wheat crop. *Quarterly Journal of the Royal Meteorological Society*, **105**, 767–783.

Fowler, D., Pilegaard, K., Sutton, M.A., Ambus, P., Raivonen, M., Duyzer, J., Simpson, D., Fagerli, H., Fuzzi, S., Schjoerring, J.K., Granier, C., Neftel, A., Isaksen, I.S.A., Laj, P., Maione, M., Monks, P.S., Burkhardt, J., Daemmgen, U., Neirynck, J., Personne, E., Wichink-Kruit, R., Butterbach-Bahl, K., Flechard, C., Tuovinen, J.P., Coyle, M., Gerosa, G., Loubet, B., Altimir, N., Gruenhage, L., Ammann, C., Cieslik, S., Paoletti, E., Mikkelsen, T.N., Ro-Poulsen, H., Cellier, P., Cape, J.N., Horváth, L., Loreto, F., Niinemets, Ü., Palmer, P.I., Rinne, J., Misztal, P., Nemitz, E., Nilsson, D., Pryor, S., Gallagher, M.W., Vesala, T., Skiba, U., Brüggemann, N., Zechmeister-Boltenstern, S., Williams, J., O'Dowd, C., Facchini, M.C., de Leeuw, G., Flossman, A., Chaumerliac, N. and Erisman, J.W. (2009). Atmospheric composition change: EcosystemsAtmosphere interactions. *Atmospheric Environment*, **43**, 5193–5267.

Fowler, D., Coyle, M., Skiba, U., Sutton, M.A., Cape, J.N., Reis, S., Sheppard, L.J., Jenkins, A., Grizzetti, B., Galloway, J.N., Vitousek, P., Leach, A., Bouwman, A.F., Butterbach-Bahl, K., Dentener, F., Stevenson, D., Amann, M. and Voss, M. (2013). The global nitrogen cycle in the twenty-first century. *Philosophical Transactions of the Royal Society B: Biological Sciences*, **368**, 20130164.

Fröhlich, R., Cubison, M.J., Slowik, J.G., Bukowiecki, N., Prévôt, A.S.H., Baltensperger, U., Schneider, J., Kimmel, J.R., Gonin, M., Rohner, U., Worsnop, D.R. and Jayne, J.T. (2013). The ToF-ACSM: a portable aerosol chemical speciation monitor with TOFMS detection. *Atmos. Meas. Tech.*, **6**, 3225–3241.

Galanter, M., Levy II, H. and Carmichael, G.R. (2000). Impacts of biomass burning on tropospheric CO, NO x , and O3. *Journal of Geophysical Research: Atmospheres*, **105**, 6633–6653.

Gallagher, M.W., Nemitz, E., Dorsey, J.R., Fowler, D., Sutton, M.A., Flynn, M. and Duyzer, J. (2002). Measurements and parameterizations of small aerosol deposition velocities to grassland, arable crops, and forest: Influence of surface roughness length on deposition. *Journal of Geophysical Research: Atmospheres*, **107**, AAC 8–1–AAC 8–10.

Galloway, J.N., Aber, J.D., Erisman, J.W., Seitzinger, S.P., Howarth, R.W., Cowling, E.B. and Cosby, B.J. (2003). The Nitrogen Cascade. *BioScience*, **53**, 341–356.

Ganzeveld, L. and Lelieveld, J. (2004). Impact of Amazonian deforestation on atmospheric chemistry. *Geophysical Research Letters*, **31**.

Garland, J.A. (1977). The Dry Deposition of Sulphur Dioxide to Land and Water Surfaces. *Proceedings of the Royal Society A: Mathematical, Physical and Engineering Sciences*, **354**, 245–268.

Garratt, J.R. (1980). Surface influence upon vertical profiles in the atmospheric near-surface layer. *Quarterly Journal of the Royal Meteorological Society*, **106**, 803–819.

Garratt, J.R. (1994). The atmospheric boundary layer. *International Journal of Climatology*, **14**, 112–113.

Gebhardt, S., Colomb, A., Hofmann, R., Williams, J. and Lelieveld, J. (2008). Halogenated organic species over the tropical South American rainforest. *Atmos. Chem. Phys.*, **8**, 3185–3197.

George, C., Strekowski, R.S., Kleffmann, J., Stemmler, K. and Ammann, M. (2005). Photoenhanced uptake of gaseous NO_2 on solid organic compounds: a photochemical source of HONO? *Faraday discussions*, **130**, 164–195,519–524.

Gloor, M., Gatti, L., Brienen, R., Feldpausch, T.R., Phillips, O.L., Miller, J., Ometto, J.P., Rocha, H., Baker, T., de Jong, B., Houghton, R.A., Malhi, Y., Aragão, L.E.O.C., Guyot, J.L., Zhao, K., Jackson, R., Peylin, P., Sitch, S., Poulter, B., Lomas, M., Zaehle, S., Huntingford, C., Levy, P. and Lloyd, J. (2012). The carbon balance of South America: a review of the status, decadal trends and main determinants. *Biogeosciences*, **9**, 5407–5430.

Godfray, H.C.J., Beddington, J.R., Crute, I.R., Haddad, L., Lawrence, D., Muir, J.F., Pretty, J., Robinson, S., Thomas, S.M. and Toulmin, C. (2010). Food Security: The Challenge of Feeding 9 Billion People. *Science*, **327**, 812 LP – 818.

Graedel, T.E. and Keene, W.C. (1995). Tropospheric budget of reactive chlorine. *Global Biogeochemical Cycles*, **9**, 47–77.

Gutzwiller, L., Arens, F., Baltensperger, U., Gäggeler, H.W. and Ammann, M. (2002). Significance of Semivolatile Diesel Exhaust Organics for Secondary HONO Formation. *Environmental Science & Technology*, **36**, 677–682.

Hansen, K., Pryor, S.C., Boegh, E., Hornsby, K.E., Jensen, B. and Sørensen, L.L. (2015). Background concentrations and fluxes of atmospheric ammonia over a deciduous forest. *Agricultural and Forest Meteorology*, **214-215**, 380–392.

Hansen, K., Personne, E., Skjøth, C.A., Loubet, B., Ibrom, A., Jensen, R., Sørensen, L.L. and Boegh, E. (2017). Investigating sources of measured forest-atmosphere ammonia fluxes using two-layer bi-directional modelling. *Agricultural and Forest Meteorology*, **237-238**, 80–94.

Hanstein, S., Mattsson, M., Jaeger, H.J. and Schjoerring, J.K. (1999). Uptake and utilization of atmospheric ammonia in three native Poaceae species: Leaf conductances, composition of apoplastic solution and interactions with root nitrogen supply. *New Phytologist*, **141**, 71–83.

Harman, I.N. and Finnigan, J.J. (2007). A simple unified theory for flow in the canopy and roughness sublayer. *Boundary-Layer Meteorology*, **123**, 339–363.

Harrison, R.M., Peak, J.D. and Collins, G.M. (1996). Tropospheric cycle of nitrous acid. *Journal of Geophysical Research: Atmospheres*, **101**, 14429–14439.

Harriss, R.C., Garstang, M., Wofsy, S.C., Beck, S.M., Bendura, R.J., Coelho, J.R.B., Drewry, J.W., Hoell Jr., J.M., Matson, P.A., McNeal, R.J., Molion, L.C.B., Navarro, R.L., Rabine, V. and Snell, R.L. (1990). The Amazon Boundary Layer Experiment: Wet season 1987. *Journal of Geophysical Research: Atmospheres*, **95**, 16721–16736.

Hoffmann, B., Flänker, R. and Mengel, K. (1992). Measurements of pH in the apoplast of sunflower leaves by means of fluorescence. *Physiologia Plantarum*, **84**, 146–153.

Högström, U. (1996). Review of Some Basic Characteristics of the Atmospheric Surface Layer. In J.R. Garratt and P.A. Taylor, eds., *Boundary-Layer Meteorology 25th Anniversary Volume, 19701995*, 215–246, Springer Netherlands, Dordrecht.

Holton, J.R. and Hakim, G.J. (2012). *An introduction to dynamic meteorology*. Elsevier, 5th edn.

Horst, T.W. and Weil, J.C. (1994). How far is far enough? The fetch requirements for micrometeorological measurement of surface fluxes. *Journal of Atmospheric & Oceanic Technology*, **11**, 1018–1025.

Houghton, R.A., Lawrence, K.T., Hackler, J.L. and Brown, S. (2001). The spatial distribution of forest biomass in the Brazilian Amazon: a comparison of estimates. *Global Change Biology*, **7**, 731–746.

Jaenicke, R. (2005). Abundance of cellular material and proteins in the atmosphere. *Science*, **308**, 73.

Jardine, K., Yañez-Serrano, A.M., Williams, J., Kunert, N., Jardine, A., Taylor, T., Abrell, L., Artaxo, P., Guenther, A., Hewitt, C.N., House, E., Florentino,

A.P., Manzi, A., Higuchi, N., Kesselmeier, J., Behrendt, T., Veres, P.R., Derstroff, B., Fuentes, J.D., Martin, S.T. and Andreae, M.O. (2015). Dimethyl sulfide in the Amazon rain forest. *Global Biogeochemical Cycles*, **29**, 19–32.

Jones, S.K., Helfter, C., Anderson, M., Coyle, M., Campbell, C., Famulari, D., Di Marco, C., van Dijk, N., Tang, Y.S., Topp, C.F.E., Kiese, R., Kindler, R., Siemens, J., Schrumpf, M., Kaiser, K., Nemitz, E., Levy, P.E., Rees, R.M., Sutton, M.A. and Skiba, U.M. (2017). The nitrogen, carbon and greenhouse gas budget of a grazed, cut and fertilised temperate grassland. *Biogeosciences*, **14**, 2069–2088.

Karydis, V.A., Tsimpidi, A.P., Pozzer, A., Astitha, M. and Lelieveld, J. (2016). Effects of mineral dust on global atmospheric nitrate concentrations. *Atmos. Chem. Phys.*, **16**, 1491–1509.

Keuken, M.P., Schoonebeek, C.A.M., van Wensveen-Louter, A. and Slanina, J. (1988). Simultaneous sampling of NH3, HNO3, HCl, SO2 and H2O2 in ambient air by a wet annular denuder system. *Atmospheric Environment (1967)*, **22**, 2541–2548.

Khlystov, A., Wyers, G.P. and Slanina, J. (1995). The steam-jet aerosol collector. *Atmospheric Environment*, **29**, 2229–2234.

Kim, P. (2013). Processes regulating nitric oxide emissions from soils. *Philosophical Transactions of the Royal Society B: Biological Sciences*, **368**, 20130126.

Kleffmann, J. (2007). Daytime Sources of Nitrous Acid (HONO) in the Atmospheric Boundary Layer. *ChemPhysChem*, **8**, 1137–1144.

Kleffmann, J. and Wiesen, P. (2008). Technical Note: Quantification of interferences of wet chemical HONO LOPAP measurements under simulated polar conditions. *Atmos. Chem. Phys.*, **8**, 6813–6822.

Kleffmann, J., Lörzer, J.C., Wiesen, P., Kern, C., Trick, S., Volkamer, R., Rodenas, M. and Wirtz, K. (2006). Intercomparison of the DOAS and LOPAP techniques for the detection of nitrous acid (HONO). *Atmospheric Environment*, **40**, 3640–3652.

Klemm, O., Milford, C., Sutton, M.A., Spindler, G. and van Putten, E. (2002). A climatology of leaf surface wetness. *Theoretical and Applied Climatology*, **71**, 107–117.

Klockow, D., Jablonski, B. and Nieβner, R. (1979). Possible artifacts in filter sampling of atmospheric sulphuric acid and acidic sulphates. *Atmospheric Environment (1967)*, **13**, 1665–1676.

Kramm, G. and Dlugi, R. (1994). Modelling of the vertical fluxes of nitric acid, ammonia, and ammonium nitrate. *Journal of Atmospheric Chemistry*, **18**, 319–357.

Kritz, M.A. and Rancher, J. (1980). Circulation of Na, Cl, and Br in the tropical marine atmosphere. *Journal of Geophysical Research: Oceans*, **85**, 1633–1639.

Kruit, R.J.W., van Pul, W.A.J., Sauter, F.J., van den Broek, M., Nemitz, E., Sutton, M.A., Krol, M. and Holtslag, A.A.M. (2010). Modeling the surfaceatmosphere exchange of ammonia. *Atmospheric Environment*, **44**, 945–957.

Krupa, S.V. (2003). Effects of atmospheric ammonia (NH3) on terrestrial vegetation: a review. *Environmental Pollution*, **124**, 179–221.

Kuhn, U., Andreae, M.O., Ammann, C., Araújo, A.C., Brancaleoni, E., Ciccioli, P., Dindorf, T., Frattoni, M., Gatti, L.V., Ganzeveld, L., Kruijt, B., Lelieveld, J., Lloyd, J., Meixner, F.X., Nobre, A.D., Pöschl, U., Spirig, C., Stefani, P., Thielmann, A., Valentini, R. and Kesselmeier, J. (2007). Isoprene and monoterpene fluxes from Central Amazonian rainforest inferred from tower-based and airborne measurements, and implications on the atmospheric chemistry and the local carbon budget. *Atmos. Chem. Phys.*, **7**, 2855–2879.

Kuhn, U., Ganzeveld, L., Thielmann, A., Dindorf, T., Schebeske, G., Welling, M., Sciare, J., Roberts, G., Meixner, F.X., Kesselmeier, J., Lelieveld, J., Kolle, O., Ciccioli, P., Lloyd, J., Trentmann, J., Artaxo, P. and Andreae, M.O. (2010). Impact of Manaus City on the Amazon Green Ocean atmosphere: ozone production, precursor sensitivity and aerosol load. *Atmos. Chem. Phys.*, **10**, 9251–9282.

Kutsuna, S. and Ibusuki, T. (1994). Fourier transform infrared measurement of the formation of nitrogen compounds on sodium chloride particles exposed to the ambient air in the Arctic. *Journal of Geophysical Research*, **99**, 25479.

Langford, A.O. and Fehsenfeld, F.C. (1992). Natural vegetation as a source or sink for atmospheric ammonia: A case study. *Science*, **255**, 581–583.

Langford, B., Acton, W., Ammann, C., Valach, A. and Nemitz, E. (2015). Eddy-covariance data with low signal-to-noise ratio: time-lag determination, uncertainties and limit of detection. *Atmos. Meas. Tech.*, **8**, 4197–4213.

Laufs, S., Cazaunau, M., Stella, P., Kurtenbach, R., Cellier, P., Mellouki, A., Loubet, B. and Kleffmann, J. (2017). Diurnal fluxes of HONO above a crop rotation. *Atmos. Chem. Phys.*, **17**, 6907–6923.

Lee, J.D., Whalley, L.K., Heard, D.E., Stone, D., Dunmore, R.E., Hamilton, J.F., Young, D.E., Allan, J.D., Laufs, S. and Kleffmann, J. (2016). Detailed budget

analysis of HONO in central London reveals a missing daytime source. *Atmos. Chem. Phys.*, **16**, 2747–2764.

Lelieveld, J. and Crutzen, P.J. (1991). The role of clouds in tropospheric photochemistry. *Journal of Atmospheric Chemistry*, **12**, 229–267.

Lelieveld, J., Peters, W., Dentener, F.J. and Krol, M.C. (2002). Stability of tropospheric hydroxyl chemistry. *Journal of Geophysical Research: Atmospheres*, **107**, ACH 17–1–ACH 17–11.

Lelieveld, J., Butler, T.M., Crowley, J.N., Dillon, T.J., Fischer, H., Ganzeveld, L., Harder, H., Lawrence, M.G., Martinez, M., Taraborrelli, D. and Williams, J. (2008). Atmospheric oxidation capacity sustained by a tropical forest. *Nature*, **452**, 737.

Lenton, T.M., Held, H., Kriegler, E., Hall, J.W., Lucht, W., Rahmstorf, S. and Schellnhuber, H.J. (2008). Tipping elements in the Earth's climate system. *Proceedings of the National Academy of Sciences*, **105**, 1786 LP – 1793.

Lin, M., Walker, J., Geron, C. and Khlystov, A. (2010). Organic nitrogen in $PM_{2.5}$ aerosol at a forest site in the Southeast US. *Atmos. Chem. Phys.*, **10**, 2145–2157.

Mace, K.A., Artaxo, P. and Duce, R.A. (2003). Water-soluble organic nitrogen in Amazon Basin aerosols during the dry (biomass burning) and wet seasons. *Journal of Geophysical Research: Atmospheres*, **108**.

Malhi, Y., Roberts, J.T., Betts, R.A., Killeen, T.J., Li, W. and Nobre, C.A. (2008). Climate Change, Deforestation, and the Fate of the Amazon. *Science*, **319**, 169 LP – 172.

Mannschreck, K., Gilge, S., Plass-Duelmer, C., Fricke, W. and Berresheim, H. (2004). Assessment of the applicability of NO-NO₂-O₃ photostationary state to long-term measurements at the Hohenpeissenberg GAW Station, Germany. *Atmos. Chem. Phys.*, **4**, 1265–1277.

Martin, S.T., Andreae, M.O., Althausen, D., Artaxo, P., Baars, H., Borrmann, S., Chen, Q., Farmer, D.K., Guenther, A., Gunthe, S.S., Jimenez, J.L., Karl, T., Longo, K., Manzi, A., Müller, T., Pauliquevis, T., Petters, M.D., Prenni, A.J., Pöschl, U., Rizzo, L.V., Schneider, J., Smith, J.N., Swietlicki, E., Tota, J., Wang, J., Wiedensohler, A. and Zorn, S.R. (2010a). An overview of the Amazonian Aerosol Characterization Experiment 2008 (AMAZE-08). *Atmos. Chem. Phys.*, **10**, 11415–11438.

Martin, S.T., Andreae, M.O., Artaxo, P., Baumgardner, D., Chen, Q., Goldstein, A.H., Guenther, A., Heald, C.L., Mayol-Bracero, O.L., McMurry, P.H., Pauliquevis, T., Pöschl, U., Prather, K.A., Roberts, G.C., Saleska, S.R., Silva

Dias, M.A., Spracklen, D.V., Swietlicki, E. and Trebs, I. (2010b). Sources and properties of Amazonian aerosol particles. *Reviews of Geophysics*, **48**.

Martin, S.T., Artaxo, P., Machado, L.A.T., Manzi, A.O., Souza, R.A.F., Schumacher, C., Wang, J., Andreae, M.O., Barbosa, H.M.J., Fan, J., Fisch, G., Goldstein, A.H., Guenther, A., Jimenez, J.L., Pöschl, U., SilvaDias, M.A., Smith, J.N. and Wendisch, M. (2016). Introduction: Observations and Modeling of the Green Ocean Amazon (GoAmazon2014/5). *Atmos. Chem. Phys.*, **16**, 4785–4797.

Massad, R.S., Loubet, B., Tuzet, A. and Cellier, P. (2008). Relationship between ammonia stomatal compensation point and nitrogen metabolism in arable crops: Current status of knowledge and potential modelling approaches. *Environmental Pollution*, **154**, 390–403.

Massad, R.S., Nemitz, E. and Sutton, M.A. (2010). Review and parameterisation of bi-directional ammonia exchange between vegetation and the atmosphere. *Atmos. Chem. Phys.*, **10**, 10359–10386.

Mattsson, M., Herrmann, B., David, M., Loubet, B., Riedo, M., Theobald, M.R., Sutton, M.A., Bruhn, D., Neftel, A. and Schjoerring, J.K. (2009). Temporal variability in bioassays of the stomatal ammonia compensation point in relation to plant and soil nitrogen parameters in intensively managed grassland. *Biogeosciences*, **6**, 171–179.

McMeeking, G.R., Kreidenweis, S.M., Baker, S., Carrico, C.M., Chow, J.C., Collett Jr., J.L., Hao, W.M., Holden, A.S., Kirchstetter, T.W., Malm, W.C., Moosmüller, H., Sullivan, A.P. and Wold, C.E. (2009). Emissions of trace gases and aerosols during the open combustion of biomass in the laboratory. *Journal of Geophysical Research: Atmospheres*, **114**.

Medinets, S., Skiba, U., Rennenberg, H. and Butterbach-Bahl, K. (2015). A review of soil NO transformation: Associated processes and possible physiological significance on organisms. *Soil Biology and Biochemistry*, **80**, 92–117.

Milford, C., Theobald, M.R., Nemitz, E. and Sutton, M.A. (2001). Dynamics of Ammonia Exchange in Response to Cutting and Fertilising in an Intensively-Managed Grassland. *Water, Air and Soil Pollution: Focus*, **1**, 167–176.

Mölder, M., Grelle, A., Lindroth, A. and Halldin, S. (1999). Flux-profile relationships over a boreal forest roughness sublayer corrections. *Agricultural and Forest Meteorology*, **98-99**, 645–658.

Monin, A. and Obukhov, A. (1954). Osnovnye zakonomernosti turbulentnogo peremeshivanija v prizemnom sloe atmosfery [Basic Laws of Turbulent Mixing in the Atmosphere near the Ground]. *Trudy Geofizicheskogo Instituta, Akademiya Nauk SSSR*, **24**, 163 – 187.

Monteith, J. and Unsworth, M. (2013). *Principles of Environmental Physics: Plants, Animals, and the Atmosphere: Fourth Edition*. Elsevier.

Moore, R.M., Gut, A. and Andreae, M.O. (2005). A pilot study of methyl chloride emissions from tropical woodrot fungi. *Chemosphere*, **58**, 221–225.

Moran-Zuloaga, D., Ditas, F., Walter, D., Saturno, J., Brito, J., Carbone, S., Chi, X., Hrabě de Angelis, I., Baars, H., Godoi, R.H.M., Heese, B., Holanda, B.A., Lavrič, J.V., Martin, S.T., Ming, J., Pöhlker, M.L., Ruckteschler, N., Su, H., Wang, Y., Wang, Q., Wang, Z., Weber, B., Wolff, S., Artaxo, P., Pöschl, U., Andreae, M.O. and Pöhlker, C. (2018). Long-term study on coarse mode aerosols in the Amazon rain forest with the frequent intrusion of Saharan dust plumes. *Atmos. Chem. Phys.*, **18**, 10055–10088.

Mozurkewich, M. (1993). The dissociation constant of ammonium nitrate and its dependence on temperature, relative humidity and particle size. *Atmospheric Environment. Part A. General Topics*, **27**, 261–270.

Myhre, G., Grini, A. and Metzger, S. (2006). Modelling of nitrate and ammonium-containing aerosols in presence of sea salt. *Atmos. Chem. Phys.*, **6**, 4809–4821.

Nadelhoffer, K.J. (2008). The Impacts of Nitrogen Deposition on Forest Ecosystems. In J.L. Hatfield and Follett, eds., *Nitrogen in the Environment*, 463–482, Academic Press, San Diego.

Neftel, A., Blatter, A., Hesterberg, R. and Staffelbach, T. (1996). Measurements of concentration gradients of HNO2 and HNO3 over a semi-natural ecosystem. *Atmospheric Environment*, **30**, 3017–3025.

Neirynck, J. and Ceulemans, R. (2008). Bidirectional ammonia exchange above a mixed coniferous forest. *Environmental Pollution*, **154**, 424–438.

Nemitz, E. and Sutton, M.A. (2004). Gas-particle interactions above a Dutch heathland: III. Modelling the influence of the NH_3 - HNO_3 - NH_4NO_3 equilibrium on size-segregated particle fluxes. *Atmos. Chem. Phys.*, **4**, 1025–1045.

Nemitz, E., Sutton, M.A., Schjoerring, J.K., Husted, S. and Paul Wyers, G. (2000a). Resistance modelling of ammonia exchange over oilseed rape. *Agricultural and Forest Meteorology*, **105**, 405–425.

Nemitz, E., Sutton, M.A., Wyers, G., Otjes, R.P., Schjoerring, J.K., Gallagher, M.W., Parrington, J., Fowler, D. and Choularton, T.W. (2000b). Surface/atmosphere exchange and chemical interaction of gases and aerosols over oilseed rape. *Agricultural and Forest Meteorology*, **105**, 427–445.

Nemitz, E., Sutton, M.A., Wyers, G.P. and Jongejan, P.A.C. (2004a). Gas-particle interactions above a Dutch heathland: I. Surface exchange fluxes of NH_3, SO_2, HNO_3 and HCl. *Atmos. Chem. Phys.*, **4**, 989–1005.

Nemitz, E., Sutton, M.A., Wyers, G.P., Otjes, R.P., Mennen, M.G., van Putten, E.M. and Gallagher, M.W. (2004b). Gas-particle interactions above a Dutch heathland: II. Concentrations and surface exchange fluxes of atmospheric particles. *Atmos. Chem. Phys.*, **4**, 1007–1024.

Nemitz, E., Dorsey, J.R., Flynn, M.J., Gallagher, M.W., Hensen, A., Erisman, J.W., Owen, S.M., Dämmgen, U. and Sutton, M.A. (2009a). Aerosol fluxes and particle growth above managed grassland. *Biogeosciences*, **6**, 1627–1645.

Nemitz, E., Hargreaves, K.J., Neftel, A., Loubet, B., Cellier, P., Dorsey, J.R., Flynn, M., Hensen, A., Weidinger, T., Meszaros, R., Horvath, L., DäCurrency Signmmgen, U., Frühauf, C., Löpmeier, F.J., Gallagher, M.W. and Sutton, M.A. (2009b). Intercomparison and assessment of turbulent and physiological exchange parameters of grassland. *Biogeosciences*, **6**, 1445–1466.

Neuman, J.A., Huey, L.G., Ryerson, T.B. and Fahey, D.W. (1999). Study of Inlet Materials for Sampling Atmospheric Nitric Acid. *Environmental Science & Technology*, **33**, 1133–1136.

Norman, M., Spirig, C., Wolff, V., Trebs, I., Flechard, C., Wisthaler, A., Schnitzhofer, R., Hansel, A. and Neftel, A. (2009). Intercomparison of ammonia measurement techniques at an intensively managed grassland site (Oensingen, Switzerland). *Atmos. Chem. Phys.*, **9**, 2635–2645.

Obukhov, A. (1946). Turbulentnost' v temperaturnoj neodnorodnoj atmosfere [Turbulence in an Atmosphere with a Non uniform Temperature]. *Trudy Geofizicheskogo Instituta, Akademiya Nauk SSSR*, **1**, 95 – 115.

O'Dowd, C. and de Leeuw, G. (2007). Marine aerosol production: a review of the current knowledge. *Philosophical Transactions of the Royal Society A: Mathematical, Physical and Engineering Sciences*, **365**, 1753–1774.

Oswald, R., Behrendt, T., Ermel, M., Wu, D., Su, H., Cheng, Y., Breuninger, C., Moravek, A., Mougin, E., Delon, C., Loubet, B., Pommerening-Röser, A., Sörgel, M., Pöschl, U., Hoffmann, T., Andreae, M.O., Meixner, F.X. and Trebs, I. (2013). HONO Emissions from Soil Bacteria as a Major Source of Atmospheric Reactive Nitrogen. *Science*, **341**, 1233 LP – 1235.

Pagsberg, P., Bjergbakke, E., Ratajczak, E. and Sillesen, A. (1997). Kinetics of the gas phase reaction OH + NO(+M)HONO(+M) and the determination of the UV absorption cross sections of HONO. *Chemical Physics Letters*, **272**, 383–390.

Panofsky, H.A. (1963). Determination of stress from wind and temperature measurements. *Quarterly Journal of the Royal Meteorological Society*, **89**, 85–94.

Paralovo, S.L., Barbosa, C.G.G., Carneiro, I.P.S., Kurzlop, P., Borillo, G.C., Schiochet, M.F.C., Godoi, A.F.L., Yamamoto, C.I., de Souza, R.A.F., Andreoli, R.V., Ribeiro, I.O., Manzi, A.O., Kourtchev, I., Bustillos, J.O.V., Martin, S.T. and Godoi, R.H.M. (2019). Observations of particulate matter, NO2, SO2, O3, H2S and selected VOCs at a semi-urban environment in the Amazon region. *Science of the Total Environment*, **650**, 996–1006.

Petroff, A., Mailliat, A., Amielh, M. and Anselmet, F. (2008). Aerosol dry deposition on vegetative canopies. Part I: Review of present knowledge. *Atmospheric Environment*, **42**, 3625–3653.

Phillips, G.J., Makkonen, U., Schuster, G., Sobanski, N., Hakola, H. and Crowley, J.N. (2013). The detection of nocturnal N_2O_5 as HNO_3 by alkali- and aqueous-denuder techniques. *Atmos. Meas. Tech.*, **6**, 231–237.

Pio, C.A. and Harrison, R.M. (1987). The equilibrium of ammonium chloride aerosol with gaseous hydrochloric acid and ammonia under tropospheric conditions. *Atmospheric Environment (1967)*, **21**, 1243–1246.

Pöhlker, C., Wiedemann, K.T., Sinha, B., Shiraiwa, M., Gunthe, S.S., Smith, M., Su, H., Artaxo, P., Chen, Q., Cheng, Y., Elbert, W., Gilles, M.K., Kilcoyne, A.L.D., Moffet, R.C., Weigand, M., Martin, S.T., Pöschl, U. and Andreae, M.O. (2012). Biogenic Potassium Salt Particles as Seeds for Secondary Organic Aerosol in the Amazon. *Science*, **337**, 1075 LP – 1078.

Pöhlker, M.L., Pöhlker, C., Ditas, F., Klimach, T., Hrabe de Angelis, I., Araújo, A., Brito, J., Carbone, S., Cheng, Y., Chi, X., Ditz, R., Gunthe, S.S., Kesselmeier, J., Könemann, T., Lavrič, J.V., Martin, S.T., Mikhailov, E., Moran-Zuloaga, D., Rose, D., Saturno, J., Su, H., Thalman, R., Walter, D., Wang, J., Wolff, S., Barbosa, H.M.J., Artaxo, P., Andreae, M.O. and Pöschl, U. (2016). Long-term observations of cloud condensation nuclei in the Amazon rain forest Part 1: Aerosol size distribution, hygroscopicity, and new model parametrizations for CCN prediction. *Atmos. Chem. Phys.*, **16**, 15709–15740.

Pöhlker, M.L., Ditas, F., Saturno, J., Klimach, T., Hrabě de Angelis, I., Araùjo, A.C., Brito, J., Carbone, S., Cheng, Y., Chi, X., Ditz, R., Gunthe, S.S., Holanda, B.A., Kandler, K., Kesselmeier, J., Könemann, T., Krüger, O.O., Lavrič, J.V., Martin, S.T., Mikhailov, E., Moran-Zuloaga, D., Rizzo, L.V., Rose, D., Su, H., Thalman, R., Walter, D., Wang, J., Wolff, S., Barbosa, H.M.J., Artaxo, P., Andreae, M.O., Pöschl, U. and Pöhlker, C. (2018). Long-term observations of cloud condensation nuclei over the Amazon rain forest

Part 2: Variability and characteristics of biomass burning, long-range transport, and pristine rain forest aerosols. *Atmos. Chem. Phys.*, **18**, 10289–10331.

Poschl, U., Martin, S.T., Sinha, B., Chen, Q., Gunthe, S.S., Huffman, J.A., Borrmann, S., Farmer, D.K., Garland, R.M., Helas, G., Jimenez, J.L., King, S.M., Manzi, A., Mikhailov, E., Pauliquevis, T., Petters, M.D., Prenni, A.J., Roldin, P., Rose, D., Schneider, J., Su, H., Zorn, S.R., Artaxo, P., Andreae, M.O., Pöschl, U., Martin, S.T., Sinha, B., Chen, Q., Gunthe, S.S., Huffman, J.A., Borrmann, S., Farmer, D.K., Garland, R.M., Helas, G., Jimenez, J.L., King, S.M., Manzi, A., Mikhailov, E., Pauliquevis, T., Petters, M.D., Prenni, A.J., Roldin, P., Rose, D., Schneider, J., Su, H., Zorn, S.R., Artaxo, P. and Andreae, M.O. (2010). Rainforest Aerosols as Biogenic Nuclei of Clouds and Precipitation in the Amazon. *Science*, **329**, 1513 LP – 1516.

Pratt, K.A., Murphy, S.M., Subramanian, R., DeMott, P.J., Kok, G.L., Campos, T., Rogers, D.C., Prenni, A.J., Heymsfield, A.J., Seinfeld, J.H. and Prather, K.A. (2011). Flight-based chemical characterization of biomass burning aerosols within two prescribed burn smoke plumes. *Atmos. Chem. Phys.*, **11**, 12549–12565.

Prueger, J.H. and Kustas, W.P. (2005). Aerodynamic Methods for Estimating Turbulent Fluxes. In *Micrometeorology in Agricultural Systems*, Agronomy Monograph SV - 47, 407–436, American Society of Agronomy, Crop Science Society of America, and Soil Science Society of America, Madison, WI.

Querino, C.A.S., Smeets, C.J.P.P., Vigano, I., Holzinger, R., Moura, V., Gatti, L.V., Martinewski, A., Manzi, A.O., de Araújo, A.C. and Röckmann, T. (2011). Methane flux, vertical gradient and mixing ratio measurements in a tropical forest. *Atmos. Chem. Phys.*, **11**, 7943–7953.

Raupach, M.R. and Legg, B.J. (1984). The uses and limitations of flux-gradient relationships in micrometeorology. *Agricultural Water Management*, **8**, 119–131.

Roberts, G., Wooster, M.J. and Lagoudakis, E. (2009). Annual and diurnal african biomass burning temporal dynamics. *Biogeosciences*, **6**, 849–866.

Roberts, G.C., Andreae, M.O., Zhou, J. and Artaxo, P. (2001). Cloud condensation nuclei in the Amazon Basin: marine conditions over a continent? *Geophysical Research Letters*, **28**, 2807–2810.

Robertson, G.P., Bruulsema, T.W., Gehl, R.J., Kanter, D., Mauzerall, D.L., Rotz, C.A. and Williams, C.O. (2013). Nitrogenclimate interactions in US agriculture. *Biogeochemistry*, **114**, 41–70.

Rumsey, I.C. and Walker, J.T. (2016). Application of an online ion-chromatography-based instrument for gradient flux measurements of speciated nitrogen and sulfur. *Atmos. Meas. Tech.*, **9**, 2581–2592.

Sanhueza, E. (2001). Hydrochloric acid from chlorocarbons: a significant global source of background rain acidity. *Tellus B: Chemical and Physical Meteorology*, **53**, 122–132.

Saturno, J., Ditas, F., Penning de Vries, M., Holanda, B.A., Pöhlker, M.L., Carbone, S., Walter, D., Bobrowski, N., Brito, J., Chi, X., Gutmann, A., Hrabe de Angelis, I., Machado, L.A.T., Moran-Zuloaga, D., Rüdiger, J., Schneider, J., Schulz, C., Wang, Q., Wendisch, M., Artaxo, P., Wagner, T., Pöschl, U., Andreae, M.O. and Pöhlker, C. (2018a). African volcanic emissions influencing atmospheric aerosols over the Amazon rain forest. *Atmos. Chem. Phys.*, **18**, 10391–10405.

Saturno, J., Holanda, B.A., Pöhlker, C., Ditas, F., Wang, Q., Moran-Zuloaga, D., Brito, J., Carbone, S., Cheng, Y., Chi, X., Ditas, J., Hoffmann, T., Hrabe de Angelis, I., Könemann, T., Lavrič, J.V., Ma, N., Ming, J., Paulsen, H., Pöhlker, M.L., Rizzo, L.V., Schlag, P., Su, H., Walter, D., Wolff, S., Zhang, Y., Artaxo, P., Pöschl, U. and Andreae, M.O. (2018b). Black and brown carbon over central Amazonia: long-term aerosol measurements at the ATTO site. *Atmos. Chem. Phys.*, **18**, 12817–12843.

Scharko, N.K., Schütte, U.M.E., Berke, A.E., Banina, L., Peel, H.R., Donaldson, M.A., Hemmerich, C., White, J.R. and Raff, J.D. (2015). Combined Flux Chamber and Genomics Approach Links Nitrous Acid Emissions to Ammonia Oxidizing Bacteria and Archaea in Urban and Agricultural Soil. *Environmental Science & Technology*, **49**, 13825–13834.

Schjoerring, J.K., Husted, S. and Mattsson, M. (1998). Physiological parameters controlling plantatmosphere ammonia exchange. *Atmospheric Environment*, **32**, 491–498.

Seinfeld, J. and Pandis, S. (2006). *Atmospheric Chemistry and Physics: From Air Pollution to Climate Change*. John Wiley & Sons, New York, 2nd edn.

Sharp, R.G. and Davies, W.J. (2009). Variability among species in the apoplastic pH signalling response to drying soils. *Journal of Experimental Botany*, **60**, 4363–4370.

Shaw, R.H. and Pereira, A.R. (1982). Aerodynamic roughness of a plant canopy: A numerical experiment. *Agricultural Meteorology*, **26**, 51–65.

Simpson, I.J., Thurtell, G.W., Neumann, H.H., Den Hartog, G. and Edwards, G.C. (1998). The Validity of Similarity Theory in the Roughness Sublayer Above Forests. *Boundary-Layer Meteorology*, **87**, 69–99.

Slanina, J., ten Brink, H.M., Otjes, R.P., Even, A., Jongejan, P., Khlystov, A., Waijers-Ijpelaan, A., Hu, M. and Lu, Y. (2001). The continuous analysis of nitrate and ammonium in aerosols by the steam jet aerosol collector (SJAC): extension and validation of the methodology. *Atmospheric Environment*, **35**, 2319–2330.

Slinn, S.A. and Slinn, W.G.N. (1980). Predictions for particle deposition on natural waters. *Atmospheric Environment (1967)*, **14**, 1013–1016.

Slinn, W.G.N. (1982). Predictions for particle deposition to vegetative canopies. *Atmospheric Environment (1967)*, **16**, 1785–1794.

Sommer, S.G. and Hutchings, N.J. (2001). Ammonia emission from field applied manure and its reductioninvited paper. *European Journal of Agronomy*, **15**, 1–15.

Sörgel, M., Trebs, I., Serafimovich, A., Moravek, A., Held, A. and Zetzsch, C. (2011). Simultaneous HONO measurements in and above a forest canopy: influence of turbulent exchange on mixing ratio differences. *Atmos. Chem. Phys.*, **11**, 841–855.

Sörgel, M., Trebs, I., Wu, D. and Held, A. (2015). A comparison of measured HONO uptake and release with calculated source strengths in a heterogeneous forest environment. *Atmos. Chem. Phys.*, **15**, 9237–9251.

Soussana, J.F., Allard, V., Pilegaard, K., Ambus, P., Amman, C., Campbell, C., Ceschia, E., Clifton-Brown, J., Czobel, S., Domingues, R., Flechard, C., Fuhrer, J., Hensen, A., Horvath, L., Jones, M., Kasper, G., Martin, C., Nagy, Z., Neftel, A., Raschi, A., Baronti, S., Rees, R.M., Skiba, U., Stefani, P., Manca, G., Sutton, M., Tuba, Z. and Valentini, R. (2007). Full accounting of the greenhouse gas (CO_2, N_2O, CH_4) budget of nine European grassland sites. *Agriculture, Ecosystems & Environment*, **121**, 121–134.

Spindler, G., Hesper, J., Brüggemann, E., Dubois, R., Müller, T. and Herrmann, H. (2003). Wet annular denuder measurements of nitrous acid: laboratory study of the artefact reaction of NO_2 with S(IV) in aqueous solution and comparison with field measurements. *Atmospheric Environment*, **37**, 2643–2662.

Stein, A.F., Draxler, R.R., Rolph, G.D., Stunder, B.J.B., Cohen, M.D. and Ngan, F. (2015). NOAA's HYSPLIT Atmospheric Transport and Dispersion Modeling System. *Bulletin of the American Meteorological Society*, **96**, 2059–2077.

Stemmler, K., Ndour, M., Elshorbany, Y., Kleffmann, J., D'Anna, B., George, C., Bohn, B. and Ammann, M. (2007). Light induced conversion of nitrogen dioxide into nitrous acid on submicron humic acid aerosol. *Atmos. Chem. Phys.*, **7**, 4237–4248.

Stone, D., Whalley, L.K. and Heard, D.E. (2012). Tropospheric OH and HO2 radicals: field measurements and model comparisons. *Chemical Society Reviews*, **41**, 6348–6404.

Stull, R.B., ed. (1988). *An Introduction to Boundary Layer Meteorology*. Springer Netherlands, Dordrecht.

Su, H., Cheng, Y.F., Shao, M., Gao, D.F., Yu, Z.Y., Zeng, L.M., Slanina, J., Zhang, Y.H. and Wiedensohler, A. (2008). Nitrous acid (HONO) and its daytime sources at a rural site during the 2004 PRIDE-PRD experiment in China. *Journal of Geophysical Research: Atmospheres*, **113**.

Su, H., Cheng, Y., Oswald, R., Behrendt, T., Trebs, I., Meixner, F.X., Andreae, M.O., Cheng, P., Zhang, Y. and Pöschl, U. (2011). Soil Nitrite as a Source of Atmospheric HONO and OH Radicals. *Science*, **333**, 1616 LP – 1618.

Sullivan, R.C., Guazzotti, S.A., Sodeman, D.A., Tang, Y., Carmichael, G.R. and Prather, K.A. (2007). Mineral dust is a sink for chlorine in the marine boundary layer. *Atmospheric Environment*, **41**, 7166 – 7179.

Suter, H., Sultana, H., Turner, D., Davies, R., Walker, C. and Chen, D. (2013). Influence of urea fertiliser formulation, urease inhibitor and season on ammonia loss from ryegrass. *Nutrient Cycling in Agroecosystems*, **95**, 175–185.

Sutton, M.A., Moncrieff, J.B. and Fowler, D. (1992). Deposition of atmospheric ammonia to moorlands. *Environmental Pollution*, **75**, 15–24.

Sutton, M.A., Flower, D. and Moncrieff, J.B. (1993). The exchange of atmospheric ammonia with vegetated surfaces. I: Unfertilized vegetation. *Quarterly Journal of the Royal Meteorological Society*, **119**, 1023–1045.

Sutton, M.A., Schjørring, J.K., Wyers, G.P., Duyzer, J.H., Ineson, P., Powlson, D.S., Fowler, D., Jenkinson, D.S., Monteith, J.L. and Unsworth, M.H. (1995). Plantatmosphere exchange of ammonia. *Philosophical Transactions of the Royal Society of London. Series A: Physical and Engineering Sciences*, **351**, 261–278.

Sutton, M.A., Burkhardt, J.K., Guerin, D., Nemitz, E. and Fowler, D. (1998). Development of resistance models to describe measurements of bi-directional ammonia surfaceatmosphere exchange. *Atmospheric Environment*, **32**, 473–480.

Sutton, M.A., Miners, B., Tang, Y.S., Milford, C., Wyers, G.P., Duyzer, J.H. and Fowler, D. (2001). Comparison of low cost measurement techniques for long-term monitoring of atmospheric ammonia. *Journal of Environmental Monitoring*, **3**, 446–453.

Sutton, M.A., Nemitz, E., Erisman, J.W., Beier, C., Bahl, K.B., Cellier, P., de Vries, W., Cotrufo, F., Skiba, U., Di Marco, C., Jones, S., Laville, P., Soussana, J.F., Loubet, B., Twigg, M., Famulari, D., Whitehead, J., Gallagher, M.W., Neftel, A., Flechard, C.R., Herrmann, B., Calanca, P.L., Schjoerring, J.K., Daemmgen, U., Horvath, L., Tang, Y.S., Emmett, B.A., Tietema, A., Peñuelas, J., Kesik, M., Brueggemann, N., Pilegaard, K., Vesala, T., Campbell, C.L., Olesen, J.E., Dragosits, U., Theobald, M.R., Levy, P., Mobbs, D.C., Milne, R., Viovy, N., Vuichard, N., Smith, J.U., Smith, P., Bergamaschi, P., Fowler, D. and Reis, S. (2007). Challenges in quantifying biosphereatmosphere exchange of nitrogen species. *Environmental Pollution*, **150**, 125–139.

Sutton, M.A., Nemitz, E., Milford, C., Campbell, C., Erisman, J.W., Hensen, A., Cellier, P., David, M., Loubet, B., Personne, E., Schjoerring, J.K., Mattsson, M., Dorsey, J.R., Gallagher, M.W., Horvath, L., Weidinger, T., Meszaros, R., Dämmgen, U., Neftel, A., Herrmann, B., Lehman, B.E., Flechard, C. and Burkhardt, J. (2009). Dynamics of ammonia exchange with cut grassland: synthesis of results and conclusions of the GRAMINAE Integrated Experiment. *Biogeosciences*, **6**, 2907–2934.

Swinbank, W.C. and Dyer, A.J. (1967). An experimental study in micrometeorology. *Quarterly Journal of the Royal Meteorological Society*, **93**, 494–500.

Taraborrelli, D., Lawrence, M.G., Crowley, J.N., Dillon, T.J., Gromov, S., Groß, C.B.M., Vereecken, L. and Lelieveld, J. (2012). Hydroxyl radical buffered by isoprene oxidation over tropical forests. *Nature Geoscience*, **5**, 300.

Taylor, K.E. (2001). Summarizing multiple aspects of model performance in a single diagram. *Journal of Geophysical Research: Atmospheres*, **106**, 7183–7192.

Thom, A.S. (1972). Momentum, mass and heat exchange of vegetation. *Quarterly Journal of the Royal Meteorological Society*, **98**, 124–134.

Thomas, R.M., Trebs, I., Otjes, R., Jongejan, P.A.C., ten Brink, H., Phillips, G., Kortner, M., Meixner, F.X. and Nemitz, E. (2009). An Automated Analyzer to Measure Surface-Atmosphere Exchange Fluxes of Water Soluble Inorganic Aerosol Compounds and Reactive Trace Gases. *Environmental Science & Technology*, **43**, 1412–1418.

Thompson, A.M. (1992). The Oxidizing Capacity of the Earth's Atmosphere: Probable Past and Future Changes. *Science*, **256**, 1157 LP – 1165.

Tóta, J., Fitzjarrald, D.R., Staebler, R.M., Sakai, R.K., Moraes, O.M.M., Acevedo, O.C., Wofsy, S.C. and Manzi, A.O. (2008). Amazon rain forest subcanopy flow and the carbon budget: Santarém LBA-ECO site. *Journal of Geophysical Research: Biogeosciences*, **113**.

Trail, F., Gaffoor, I. and Vogel, S. (2005). Ejection mechanics and trajectory of the ascospores of gibberella zeae (anamorph fuarium graminearum). *Fungal Genetics and Biology*, **42**, 528 – 533.

Trebs, I., Meixner, F.X., Slanina, J., Otjes, R., Jongejan, P. and Andreae, M.O. (2004). Real-time measurements of ammonia, acidic trace gases and water-soluble inorganic aerosol species at a rural site in the Amazon Basin. *Atmos. Chem. Phys.*, **4**, 967–987.

Trebs, I., Lara, L.L., Zeri, L.M.M., Gatti, L.V., Artaxo, P., Dlugi, R., Slanina, J., Andreae, M.O. and Meixner, F.X. (2006). Dry and wet deposition of inorganic nitrogen compounds to a tropical pasture site (Rondônia, Brazil). *Atmos. Chem. Phys.*, **6**, 447–469.

Trebs, I., Andreae, M.O., Elbert, W., Mayol-Bracero, O.L., Soto-García, L.L., Rudich, Y., Falkovich, A.H., Maenhaut, W., Artaxo, P., Otjes, R. and Slanina, J. (2008). Aerosol Inorganic Composition at a Tropical Site: Discrepancies Between Filter-Based Sampling and a Semi-Continuous Method. *Aerosol Science and Technology*, **42**, 255–269.

Trebs, I., Mayol-Bracero, O.L., Pauliquevis, T., Kuhn, U., Sander, R., Ganzeveld, L., Meixner, F.X., Kesselmeier, J., Artaxo, P. and Andreae, M.O. (2012). Impact of the Manaus urban plume on trace gas mixing ratios near the surface in the Amazon Basin: Implications for the NO-NO_2-O_3 photostationary state and peroxy radical levels. *Journal of Geophysical Research: Atmospheres*, **117**.

Twigg, M.M., House, E., Thomas, R., Whitehead, J., Phillips, G.J., Famulari, D., Fowler, D., Gallagher, M.W., Cape, J.N., Sutton, M.A. and Nemitz, E. (2011). Surface/atmosphere exchange and chemical interactions of reactive nitrogen compounds above a manured grassland. *Agricultural and Forest Meteorology*, **151**, 1488–1503.

Twigg, M.M., Di Marco, C.F., Leeson, S., van Dijk, N., Jones, M.R., Leith, I.D., Morrison, E., Coyle, M., Proost, R., Peeters, A.N.M., Lemon, E., Frelink, T., Braban, C.F., Nemitz, E. and Cape, J.N. (2015). Water soluble aerosols and gases at a UK background site Part 1: Controls of $PM_{2.5}$ and PM_{10} aerosol composition. *Atmos. Chem. Phys.*, **15**, 8131–8145.

Urban, J., Ingwers, M.W., McGuire, M.A. and Teskey, R.O. (2017). Increase in leaf temperature opens stomata and decouples net photosynthesis from stomatal conductance in Pinus taeda and Populus deltoides x nigra. *Journal of experimental botany*, **68**, 1757–1767.

Van der Eerden, L.J., Lekkerkerk, L.J.A., Smeulders, S.M. and Jansen, A.E. (1992). Effects of atmospheric ammonia and ammonium sulphate on Douglas fir (Pseudotsuga menziesii). *Environmental Pollution*, **76**, 1–9.

van Dijk, S.M. and Meixner, F.X. (2001). Production and Consumption of NO in Forest and Pasture Soils from the Amazon Basin. *Water, Air and Soil Pollution: Focus*, **1**, 119–130.

Van Oss, R., Duyzer, J. and Wyers, P. (1998). The influence of gas-to-particle conversion on measurements of ammonia exchange over forest. *Atmospheric Environment*, **32**, 465–471.

van Son, M., Schothorst, R.C. and den Boef, G. (1983). Determination of total ammoniacal introgen in water by flow injection analysis and a gas diffusion membrane. *Analytica Chimica Acta*, **153**, 271–275.

VanDamme, M., WichinkKruit, R., Schaap, M., Clarisse, L., Clerbaux, C., Coheur, P.F., Dammers, E., Dolman, A. and Erisman, J. (2014). Evaluating 4 years of atmospheric ammonia (NH_3) over Europe using IASI satellite observations and LOTOS-EUROS model results. *Journal of Geophysical Research: Atmospheres*, **119**, 9549–9566.

Verhoeven, J.T.A., Beltman, B., Dorland, E., Robat, S.A. and Bobbink, R. (2011). Differential effects of ammonium and nitrate deposition on fen phanerogams and bryophytes. *Applied Vegetation Science*, **14**, 149–157.

Vieno, M., Heal, M.R., Hallsworth, S., Famulari, D., Doherty, R.M., Dore, A.J., Tang, Y.S., Braban, C.F., Leaver, D., Sutton, M.A. and Reis, S. (2014). The role of long-range transport and domestic emissions in determining atmospheric secondary inorganic particle concentrations across the UK. *Atmos. Chem. Phys.*, **14**, 8435–8447.

von Bobrutzki, K., Braban, C.F., Famulari, D., Jones, S.K., Blackall, T., Smith, T.E.L., Blom, M., Coe, H., Gallagher, M., Ghalaieny, M., McGillen, M.R., Percival, C.J., Whitehead, J.D., Ellis, R., Murphy, J., Mohacsi, A., Pogany, A., Junninen, H., Rantanen, S., Sutton, M.A. and Nemitz, E. (2010). Field intercomparison of eleven atmospheric ammonia measurement techniques. *Atmos. Meas. Tech.*, **3**, 91–112.

Vong, R.J., Vickers, D. and Covert, D.S. (2004). Eddy correlation measurements of aerosol deposition to grass. *Tellus B*, **56**, 105–117.

Wang, J. and Bras, R.L. (1998). A new method for estimation of sensible heat flux from air temperature. *Water Resources Research*, **34**, 2281–2288.

Wang, L., Xu, Y. and Schjoerring, J.K. (2011). Seasonal variation in ammonia compensation point and nitrogen pools in beech leaves (Fagus sylvatica). *Plant and Soil*, **343**, 51–66.

Wesely, M.L. (1989). Parameterization of surface resistances to gaseous dry deposition in regional-scale numerical models. *Atmospheric Environment (1967)*, **23**, 1293–1304.

Wesely, M.L., Cook, D.R., Hart, R.L. and Speer, R.E. (1985). Measurements and parameterization of particulate sulfur dry deposition over grass. *Journal of Geophysical Research: Atmospheres*, **90**, 2131–2143.

Wexler, A.S. and Seinfeld, J.H. (1992). Analysis of aerosol ammonium nitrate: Departures from equilibrium during SCAQS. *Atmospheric Environment. Part A. General Topics*, **26**, 579–591.

Whitburn, S., Van Damme, M., Kaiser, J.W., van der Werf, G.R., Turquety, S., Hurtmans, D., Clarisse, L., Clerbaux, C. and Coheur, P.F. (2015). Ammonia emissions in tropical biomass burning regions: Comparison between satellite-derived emissions and bottom-up fire inventories. *Atmospheric Environment*, **121**, 42–54.

Whitehead, J.D., Twigg, M., Famulari, D., Nemitz, E., Sutton, M.A., Gallagher, M.W. and Fowler, D. (2008). Evaluation of Laser Absorption Spectroscopic Techniques for Eddy Covariance Flux Measurements of Ammonia. *Environmental Science & Technology*, **42**, 2041–2046.

Whitehead, J.D., Gallagher, M.W., Dorsey, J.R., Robinson, N., Gabey, A.M., Coe, H., McFiggans, G., Flynn, M.J., Ryder, J., Nemitz, E. and Davies, F. (2010). Aerosol fluxes and dynamics within and above a tropical rainforest in South-East Asia. *Atmos. Chem. Phys.*, **10**, 9369–9382.

Whitehead, J.D., Darbyshire, E., Brito, J., Barbosa, H.M.J., Crawford, I., Stern, R., Gallagher, M.W., Kaye, P.H., Allan, J.D., Coe, H., Artaxo, P. and McFiggans, G. (2016). Biogenic cloud nuclei in the central Amazon during the transition from wet to dry season. *Atmos. Chem. Phys.*, **16**, 9727–9743.

Williams, E., Rosenfeld, D., Madden, N., Gerlach, J., Gears, N., Atkinson, L., Dunnemann, N., Frostrom, G., Antonio, M., Biazon, B., Camargo, R., Franca, H., Gomes, A., Lima, M., Machado, R., Manhaes, S., Nachtigall, L., Piva, H., Quintiliano, W., Machado, L., Artaxo, P., Roberts, G., Renno, N., Blakeslee, R., Bailey, J., Boccippio, D., Betts, A., Wolff, D., Roy, B., Halverson, J., Rickenbach, T., Fuentes, J. and Avelino, E. (2002). Contrasting convective regimes over the Amazon: Implications for cloud electrification. *Journal of Geophysical Research: Atmospheres*, **107**, LBA 50–1–LBA 50–19.

Wolff, V., Trebs, I., Ammann, C. and Meixner, F.X. (2010a). Aerodynamic gradient measurements of the NH_3 - HNO_3 - NH_4NO_3 triad using a wet chemical instrument: an analysis of precision requirements and flux errors. *Atmos. Meas. Tech.*, **3**, 187–208.

Wolff, V., Trebs, I., Foken, T. and Meixner, F.X. (2010b). Exchange of reactive nitrogen compounds: concentrations and fluxes of total ammonium and total nitrate above a spruce canopy. *Biogeosciences*, **7**, 1729–1744.

Wyers, G. and Erisman, J.W. (1998). Ammonia exchange over coniferous forest. *Atmospheric Environment*, **32**, 441–451.

Wyers, G.P., Otjes, R.P. and Slanina, J. (1993). A continuous-flow denuder for the measurement of ambient concentrations and surface-exchange fluxes of ammonia. *Atmospheric Environment. Part A. General Topics*, **27**, 2085–2090.

Yeatman, S.G., Spokes, L.J. and Jickells, T.D. (2001). Comparisons of coarse-mode aerosol nitrate and ammonium at two polluted coastal sites. *Atmospheric Environment*, **35**, 1321–1335.

Yokelson, R.J., Burling, I.R., Urbanski, S.P., Atlas, E.L., Adachi, K., Buseck, P.R., Wiedinmyer, C., Akagi, S.K., Toohey, D.W. and Wold, C.E. (2011). Trace gas and particle emissions from open biomass burning in Mexico. *Atmos. Chem. Phys.*, **11**, 6787–6808.

Yokouchi, Y., Ikeda, M., Inuzuka, Y. and Yukawa, T. (2002). Strong emission of methyl chloride from tropical plants. *Nature*, **416**, 163–165.

Yokouchi, Y., Takenaka, A., Miyazaki, Y., Kawamura, K. and Hiura, T. (2015). Emission of methyl chloride from a fern growing in subtropical, temperate, and cool-temperate climate zones. *Journal of Geophysical Research: Biogeosciences*, **120**, 1142–1149.

Zahn, E., Dias, N.L., Araújo, A., Sá, L.D.A., Sörgel, M., Trebs, I., Wolff, S. and Manzi, A. (2016). Scalar turbulent behavior in the roughness sublayer of an Amazonian forest. *Atmos. Chem. Phys.*, **16**, 11349–11366.

Zhang, L., Wright, L.P. and Asman, W.A. (2010). Bi-directional air-surface exchange of atmospheric ammonia: A review of measurements and a development of a big-leaf model for applications in regional-scale air-quality models. *Journal of Geophysical Research Atmospheres*, **115**.

Zhou, X., Zhang, N., Teravest, M., Tang, D., Hou, J., Bertman, S., Alaghmand, M., Shepson, P., Anne Carroll, M., Griffith, S., Dusanter, S. and Stevens, P. (2011). Nitric acid photolysis on forest canopy surface as a source for tropospheric nitrous acid. *Nature Geoscience*, **4**, 440–443.

Zöll, U., Brümmer, C., Schrader, F., Ammann, C., Ibrom, A., Flechard, C.R., Nelson, D.D., Zahniser, M. and Kutsch, W.L. (2016). Surfaceatmosphere exchange of ammonia over peatland using QCL-based eddy-covariance measurements and inferential modeling. *Atmos. Chem. Phys.*, **16**, 11283–11299.